Ocean Circulation and Variability in the Solomon Sea

Cyril Germineaud

Université Fédérale

Toulouse Midi-Pyrénées

THÈSE

En vue de l'obtention du

DOCTORAT DE L'UNIVERSITÉ DE TOULOUSE

Délivré par :

Université Toulouse 3 Paul Sabatier (UT3 Paul Sabatier)

Présentée et soutenue par :

Cyril Germineaud

le mercredi 7 décembre 2016

Titre :

Circulation Océanique et Variabilité en Mer des Salomon

École doctorale et discipline ou spécialité**:**

ED SDU2E : Océan, Atmosphère et Surfaces Continentales

Unité de recherche :

Laboratoire d'Études en Géophysique et Océanographie Spatiales

Directeur/trice(s) de Thèse :

Alexandre Ganachaud, Sophie Cravatte et Janet Sprintall

Jury :

Sabrina Speich	Professeure des universités	PRESIDENTE
Jérôme Vialard	Directeur de recherche	RAPPORTEUR
Angélique Melet	Scientifique Projet	EXAMINATRICE
Christophe Maes	Chargé de recherche	EXAMINATEUR
Alexandre Ganachaud	Directeur de recherche	DIRECTEUR
Sophie Cravatte	Chargée de recherche	DIRECTRICE
Janet Sprintall	Research Oceanographer	DIRECTRICE

Remerciements

Je voudrais commencer par dire que ces trois années de thèses furent une expérience très enrichissante, autant d'un point de vue scientifique que personnel, et qui reflètent le fruit d'un travail collaboratif entre de nombreuses personnes : des techniciens, des ingénieurs et des chercheurs issus d'une large communauté scientifique à l'échelle internationale.

Je souhaite tout d'abord remercier Alex et Sophie pour leur encadrement, leur soutien et surtout de m'avoir donné l'opportunité de faire cette thèse. J'ai grâce à vous pu réaliser un de mes rêves les plus chers, faire une campagne en mer, dans cette région fascinante qu'est le Pacifique Sud-ouest. Un grand merci aussi à Janet pour son éternelle bonne humeur, et pour m'avoir accueilli et encadré lors de mes deux séjours au sein de la Scripps Institution of Oceanography à San Diego. Merci sincèrement à tous les trois, vous avez toujours été présents, à l'écoute, et je tiens à vous dire que j'ai énormément appris à vos cotés.

Je souhaite aussi remercier les autres membres du jury, mes deux rapporteurs, Jérôme Vialard et Sabrina Speich et mes deux examinateurs, Christophe Maes et Angélique Melet. Merci à vous quatre pour votre lecture attentive de mon manuscrit, et d'avoir montré autant d'intérêt pour mes travaux de thèse. J'en profite également pour remercier Marion, ce fut un véritable plaisir de travailler avec toi tout au long de cette thèse, mais aussi Gérard, Thierry, Lionel et Catherine pour nos divers échanges autour de la mer des Salomon. Un grand merci aussi à tout le personnel du LEGOS, et notamment à vous Martine, Brigitte, Agathe et Nadine, vous avez toujours été à l'écoute et d'une aide précieuse pour surmonter les petites embûches du quotidien. Je n'oublie pas non plus mes collègues de l'IRAP : Philippe, Camille, Damien, David et Jesse avec qui j'ai largement partagé cette belle aventure.

Je remercie aussi mes amis, sans qui ces trois années n'auraient pu être aussi agréables : Teddy, Lucas, Adriana, Valter, Clément, J-B, Eric, Adrien, Romain et tous les autres, merci à vous ! Pour finir, je souhaite remercier toute ma famille et plus particulièrement ma mère, pour son soutien sans faille tout au long de mes études et de cette thèse.

Abstract

The Low Latitude Western Boundary Currents (LLWBCs) of the Southwest Pacific establish a major connection between the subtropics and the equator. They cross the semi-enclosed Solomon Sea southeast of Papua New Guinea, resulting in a large variability due to the strong boundary currents encountering rough topography. As a result, the water mass properties are influenced during their transit with downstream effect on equatorial water properties. Two oceanographic multidisciplinary cruises have been conducted in July-August 2012 and March 2014 to characterize currents, water properties and their modifications in the Solomon Sea as part of a France-U.S. collaboration. For this purpose, hydrographic data collected during both cruises were analyzed to depict an unprecedented picture of the near full-depth pathways and associated water mass transformations along with an inverse box model result. On the equator side of the Solomon sea, Mooring arrays in key straits provide a 1.5-year time series to assess the flow variability and associated transports from intraseasonal to annual time scales.

During July-August 2012, the season of strong southeasterly trade winds, an intense flow of 36 $\pm$ 3 Sv from the surface down to 1000 m is entering the Solomon Sea, that falls to 11 $\pm$ 3 Sv (70% reduction) in March 2014 when the winds over the sea are weaker. Most of the volume transport occurs at the thermocline level ($\sim$65%) although the LLWBCs flowing below 500 m exhibit a significant contribution (20-25%) to the total transport.

The LLWBCs are associated with distinct water mass properties (i.e. salinity, dissolved oxygen, nutrients) across the Solomon Sea that can be tracked along their pathways, and undergo significant modifications between the southern entrance and the northern exits of the sea. Both salinity extrema of the South Pacific Tropical Water (SPTW) and the Antarctic Intermediate Water (AAIW) are eroded ($\sim$0.05), associated with stronger salinity gradients within the Solomon Sea than within the subtropical Pacific.

Below 2000 m, the Upper Circumpolar Deep Water (UCDW) emanating from the New Caledonia Trench and the South Fiji Basin transports 2-3 $\pm$ 2 Sv into the Solomon Sea, associated with high salinity, low oxygen and high nutrients characteristics. The UCDW carries 2-3 $\pm$ 2 Sv northward through the Solomon Strait, before joining the Deep Western Boundary Current (DWBC) and ultimately the western equatorial Pacific.

The analysis of the mooring timeseries gives some insights into the LLWBC variability through the northern exits of the Solomon Sea. Seasonal variations in both intensity and vertical extent occur following the annual march of the trade winds. Thermocline pathways of the LLWBCs vary coherently and in phase at intraseasonal to seasonal time scales, though other physical processes that influence the ocean variability are at stake east of the Solomon Strait. The intermediate flow is coherent at both monthly and intraseasonal time scales between Vitiaz and St Georges moorings, while the flow between the pairs Vitiaz-Solomon M1 and Vitiaz-Solomon M3 are seasonally coherent and in phase.

Résumé

Dans le Pacifique sud-ouest, le cheminement des eaux depuis la gyre subtropicale vers l'équateur est réalisé via les courants de bord ouest (WBCs), jouant ainsi un rôle clé dans la circulation méridienne du Pacifique. Ces WBCs traversent la mer des Salomon située au sud de la Papouasie Nouvelle-Guinée, et pourraient moduler le climat aux échelles décennales en fonction des anomalies des caractéristiques des masses d'eau transportées jusqu'à la bande équatoriale. Dans le cadre d'une collaboration internationale, deux campagnes en mer ont été réalisées pendant deux périodes contrastées de la saison des alizés : en Juillet-Août 2012 et Mars 2014. Les objectifs de cette thèse étaient de déterminer la circulation océanique à différentes profondeurs en mer des Salomon, d'évaluer les flots entrants et sortants et leurs transports au niveau des détroits, ainsi que les transformations des masses d'eau associées. Pour ce faire, les données hydrologiques et courantométriques collectées pendant les deux campagnes sont analysées à l'aide d'un modèle inverse dit "en boîte". Pour obtenir la variabilité temporelle de cette circulation, une série de mouillages a été déployée pendant les deux campagnes aux passages clés de la mer des Salomon, incluant des courantomètres et des capteurs de température, de pression et de salinité.

En Juillet-Août 2012, pendant la saison de forts alizés, les courants de bord ouest transportent 36 ± 3 Sv à travers l'entrée sud de la mer des Salomon depuis la surface jusqu'à 1000 m de profondeur, mais seulement 11 ± 3 Sv en Mars 2014 (réduction de 70%) quand les alizés faiblissent. L'essentiel du transport a lieu au niveau de la thermocline ($\sim$65%) même si les WBCs qui s'écoulent en-dessous de 500 m de profondeur contribuent de 20 à 25% au transport total. Les WBCs sont par ailleurs associés à des propriétés de masses d'eau distinctes (i.e. salinité, oxygène dissous et sels nutritifs), caractérisées par la South Pacific Tropical Water (SPTW) au niveau des eaux de thermocline et de l'Antarctic Intermediate Water (AAIW) au niveau des eaux intermédiaires. La SPTW et l'AAIW subissent des transformations significatives au cours de leur passage en mer des Salomon, comme peut l'attester l'érosion de leur extrema de salinité ($\sim$0.05) entre les eaux situées à l'entrée sud et celles qui traversent les détroits au nord de la mer des Salomon.

La circulation profonde en mer des Salomon voit le passage de l'Upper Circumpolar Deep Water (UCDW) entre 2000 et 3200 m, caractérisée par des distributions distinctes de salinité, d'oxygène et de silica. L'UCDW est tracée depuis le bassin de Fidji et la fosse de la Nouvelle-Calédonie avant d'atteindre la mer des Salomon, où 2 à 3 ± 2 Sv traversent le détroit des Salomon, pour finalement rejoindre le courant de bord ouest profond (DWBC) qui alimente le Pacifique équatorial ouest. L'étude des mouillages a permis d'identifier une modulation de l'intensité et de la structure verticale des WBCs en mer des Salomon en relation avec les fluctuations saisonnières des alizés. Les eaux de la thermocline entre les différents mouillages varient de manière cohérente et en phase à l'échelle intra-saisonnière et saisonnière, sauf à l'est du détroit des Salomon où d'autres processus physiques affectent la variabilité de la circulation.

Table of Contents

Introduction

The oceans are a major component of the climate system, covering near 70% of the Earth's surface. They can store large amounts of thermal energy and carbon dioxide from the atmosphere. Over the last 50 years, about 93% of the excess heat stored by the Earth is observed in the oceans (*Levitus et al.*, 2012; *Stocker et al.*, 2013). This excess heat can be transported all around the world via ocean currents, and then released into the atmosphere months or years later after being stored. The oceanic circulation is mainly driven by wind stress near the surface and density contrasts in the deeper part, although it is much slower than the atmospheric circulation. In addition, most of the total exchange of water between the Earth's surface and the atmosphere (i.e. precipitation and evaporation) occurs over the oceans. As such, the ocean can be seen as a regulator of the Earth's climate, and is an important source of natural climate variability at different time scales. Examples of this variability at interannual time scales are the El Niño fluctuations, the North Atlantic Oscillation (NAO) and the Southern Annular Mode (SAM), resulting from a coupling between the ocean and the atmosphere. This coupling is strongly dependent on the surface temperature of the ocean, especially in the tropics, where some of the warmest waters are observed.

In the tropical Pacific, the ocean-atmosphere interactions are responsible for the largest climate fluctuation at global scale: the El Niño Southern Oscillation (ENSO). El Niño corresponds to the warm phase of this oscillation, with high surface temperature in the central and eastern parts of the tropical Pacific. The opposite phase is associated with cold sea surface temperatures, and is referred to as la Niña. These swings in temperature are accompanied by changes in the atmospheric circulation, and lead to variations in local weather patterns in the tropical Pacific but also in many other regions of the world. During El Niño, the position of the atmospheric convection is shifted eastward, inducing severe droughts in Southeast Asia and Oceania with impacts on agriculture and freshwater supplies. On the eastern side of the Pacific, heavy precipitation is observed along the western coast of South America traversed by the Andes, causing major floods in these mountainous regions. Moreover, cold and nutrient-rich waters that usually upwell along the Peruvian and Chilean coasts are blocked during El Niño, leading to a massive drop in fisheries resources. Thus, El Niño events are strongly related with socio-economics issues and can have severe environmental and human consequences, as during the strong amplitude events of 1982-83, 1997-98 and the recent 2015-2016.

Moreover, since the late 1950s, global warming induced by human activities has been observed (*Stocker et al.*, 2013), linked to climate changes (e.g. the precipitation distribution, sea level rise) or a modification of the pre-existing natural climate variability (*Cai et al.*, 2012, 2014). It is not clear yet how present-day weather and climate fluctuations such as ENSO would evolve in this climate change context. Do they proceed as before, superimposed by a global warming background? Or will they be modified in term of amplitude, spatial patterns or timescales?

In the recent decades, intense research on ENSO cycle has led to a good understanding of its basic physical features. As part of the Tropical Ocean-Global Atmosphere (TOGA, 1985-1994) program, an observing system dedicated to ENSO was initiated in the tropical Pacific to provide near real-time observations (*McPhaden et al.*, 1998). This system includes moored buoys (TAO-TRITON array), drifting buoys, volunteer observing ship measurements and a global network of tide gauges. In addition to these ocean-based measurements, satellite observations (i.e. surface wind, sea surface temperature and sea level variations) are used to monitor with high precision the ENSO-related climate swings at the ocean surface, while the deployment of Argo floats since the mid-2000s, has permitted a better description of the subsurface ocean down to 2000 m.

Moreover, the recent development of complex coupled global circulation models (CGCMs) has allowed major scientific progress in ENSO forecasting (*Collins et al.*, 2010). These CGCMs have became powerful tools to explain its physical mechanisms and associated variability, although it remains quite challenging to simulate ENSO due to the stochastic nature of the ocean-atmosphere system, as suggested by the aborted El Niño in 2014 and the unforeseen one in 2015 (*McPhaden*, 2015).

Despite these significant efforts in monitoring, understanding and forecasting ENSO, many features of its dynamics remain unresolved, especially its low frequency modulation at decadal timescales (*McPhaden and Zhang*, 2002). Furthermore, each ENSO event remains somewhat unique, and is strongly influenced by the oceanic conditions of the equatorial Pacific. The interplay between trade wind intensity and sea surface temperature (SST), associated with equatorial waves drive the amplitude and the spatial extent of ENSO, but also the frequency between each event (*McPhaden et al.*, 2006). The volume of warm water (WWV) in the equatorial Pacific (i.e. waters $> 20°C$ between 5°N and 5°S) is tightly related with both ENSO phases, as suggested by the well known theory of the recharge oscillator (*Jin*, 1997). Changes in WWV involves a meridional discharge of warm waters at the end of El Niño and a meridional recharge of those at the end of La Niña (e.g. *Meinen and McPhaden*, 2000, 2001). Thus, understanding the physical mechanisms controlling the supply of warm waters into the equatorial region is of great importance to explain the fluctuations of ENSO.

Within the Pacific Ocean, water mass exchange between subtropical regions and the equator is carried out by the subtropical cell (STC) (*McCreary and Lu*, 1994), that can be seen as a shallow meridional circulation cell. Changes in either temperature or amount of water carried at the equator from the subtropics are associated with the STC, inducing decadal SST variability in the tropics that will in turn, influence ENSO dynamics. As part of the STC, waters from the subtropical gyres in both Southern and Northern hemispheres, travel westward across the tropical Ocean before feeding the equator through Low-Latitude Western Boundary Currents (LLWBCs) or the interior ocean. Several studies underline the significant contributions of both pathways (e.g. *Lee and Fukumori*, 2003; *Zilberman et al.*, 2013) that were found to be anti-correlated to each other at interannual to decadal timescales.

Thus, the WWV transports in the western boundary and interior regions are crucial to understand the equatorial WWV variability, and therefore the low-frequency modulation of ENSO. Since the last decade, interior pathway variations have been well documented from both observations (e.g. *McPhaden and Zhang*, 2002, 2004) and numerical simulations (e.g. *McPhaden et al.*, 2006; *Cheng et al.*, 2007; *Lengaigne et al.*, 2012), while the western boundary transports and their variability remain poorly quantified, particularly in the southern hemisphere.

The international OceanObs'09[1] conference and the on going international TPOS2020[2] project identified the lack of observations associated with the western boundary currents as a major weak point of the present observing system that needs to be improved. Hence, as a key component of the equatorial water mass budget, the understudied western boundary currents triggered recent interests from the scientific community through two dedicated international research programs (*Hu et al.*, 2015), the Northwestern Pacific Ocean Circulation and Climate Experiment (NPOCE) and Southwest Pacific Ocean Circulation and Climate Experiment (SPICE).

Within the SPICE[3] research program (*Ganachaud et al.*, 2014), scientific efforts were made to understand the Southwest Pacific ocean circulation and its influence on the equatorial current system. Significant advancements were achieved including an unprecedented description of the South Pacific WBC route across the Solomon, Coral and Tasman Seas. The equatorward branches of these WBCs transit through the semi-enclosed Solomon Sea, identified as a choke point to study the direct connections between the subtropics and the equator (e.g. *Melet et al.*, 2010a; *Cravatte et al.*, 2011; *Davis et al.*, 2012; *Hristova and Kessler*, 2012), and their downstream effects on the whole equatorial current system (*Grenier et al.*, 2011). Furthermore, the equatorward redistribution of waters flowing across the Solomon Sea is of prime importance, as Papua New Guinea coastal margins were identified as a major source of key micronutrients (*Grenier et al.*, 2013; *Qin et al.*, 2016), with direct implications on the equatorial oceanic primary production.

Despite their major importance, knowledge about the LLWBC transports and associated water properties within the Solomon Sea, are mostly based on numerical simulations and scattered measurements collected since the mid-1980s. As part of SPICE, this thesis work aims to improve our understanding of the circulation and its variability in the Solomon Sea, from two exploratory oceanographic cruises conducted through a France-U.S. collaboration in July-August 2012 and March 2014.

[1] http://www.oceanobs09.net
[2] http://tpos2020.org
[3] http://spice.legos.obs-mip.fr

Introduction générale

Les océans sont une composante majeure du système climatique, couvrant près de 70% de la surface de la Terre. Ils ont la possibilité d'emmagasiner de grandes quantités d'énergie thermique et de dioxide de carbone depuis l'atmosphère, avant de les restituer ultérieurement après des mois voire des années de cheminement autour du globe via les courants océaniques. En surface, les vents exercent une forte contrainte sur l'océan global contrôlant ainsi la distribution et l'intensité des courants alors que plus en profondeur, ce sont des contrastes de temperature et de salinité qui prédominent : la circulation thermohaline. Les océans jouent donc un rôle primordial dans la régulation du climat, et ceci à différentes échelles spatio-temporelles. Les fluctuations climatiques majeures comme El Niño aux échelles interannuelles sont le résultat d'étroites interactions entre l'océan et l'atmosphère qui dépendent essentiellement de la température de surface des océans, notamment dans la ceinture tropicale ou le rayonnement solaire est le plus important.

Dans le Pacifique tropical, ce couplage donne lieu au phénomène climatique le plus important à l'échelle du globe : "El Niño Southern Oscillation". El Niño correspond à la phase chaude de ce phénomène qui est associée à des anomalies positives de température dans la partie centrale et Est de la bande équatoriale. Inversement, des anomalies négatives de température sont générées pendant la phase opposée du phénomène, appelée La Niña. Ces oscillations de température ont une périodicité de 2 à 7 ans et conduisent à des modifications locales, mais aussi globales de la circulation océanique, des régimes de vents et donc des zones de précipitations. Pendant El Niño, la position des zones de convection atmosphérique est décalée vers l'Est, ce qui engendre de sévères sécheresses en Asie du Sud-Est et en Océanie. De l'autre côté du Pacifique, de fortes précipitations s'abattent sur l'Amérique du Sud entraînant des inondations et des glissements de terrain dans les régions montagneuses. Par ailleurs, les remontées d'eaux froides et riches en nutriments le long des côtes chiliennes et péruviennes se retrouvent bloquées durant El Niño, provoquant une chute importante des ressources halieutiques et donc des dommages socio-économiques majeurs. Ce fut par exemple le cas au cours des évènements de fortes amplitudes en 1982-83, 1997-98 et récemment en 2015-2016.

En outre, depuis le début des années 50, le réchauffement global induit par les activités anthropiques (*Stocker et al.*, 2013) engendre d'évidentes modifications du climat, telles que l'augmentation de catastrophes naturelles (tempêtes tropicales, inondations, sécheresses) ou la hausse du niveau de la mer. Cependant, les interactions entre les fluctuations climatiques de grandes ampleurs comme ENSO, et ces variations d'origine anthropique du climat restent profondément méconnues. Vont-elles continuer à évoluer comme par le passé ou vont-elles être modifiées en terme d'amplitude, intensité voire même d'échelles spatio-temporelles ?

Depuis les années 80, des efforts considérables ont été déployés par la communauté scientifique pour mieux comprendre les différents mécanismes associés à ENSO. Dans le cadre du programme "Tropical Ocean-Global Atmosphere" (TOGA, 1985-1994), un système d'observations dédié à l'étude d'ENSO a été initié (*McPhaden et al.*, 1998). Ce système inclut les bouées fixes TAO-TRITON, des bouées dérivantes, des campagnes de mesures en mer et un réseau global de marégraphes. En plus de ces mesures in situ, ce sont rajoutés au cours du temps les données satellites et les flotteurs Argo pour assurer un suivi en quasi temps réel d'ENSO. A partir des années 90, l'essor des modèles numériques couplés a permis une meilleure compréhension de la dynamique physique d'ENSO et de sa variabilité. En revanche, la nature stochastique du système océan-atmosphère est difficilement prise en compte dans les modèles, tout comme le forçage exercé par le réchauffement global.

Malgré ces avancées significatives, plusieurs aspects de la dynamique d'ENSO sont toujours mal compris, comme notamment sa modulation à basse fréquence aux échelles interannuelles et décennales (*McPhaden and Zhang*, 2002). De plus, chaque évènement demeure unique, tout en étant fortement influencé par les conditions océaniques du Pacifique équatorial. Les variations de régime des vents, la température de surface des océans et la propagation d'ondes équatoriales régissent l'amplitude et l'extension spatiale d'ENSO, mais aussi la fréquence entre chaque évènement (*McPhaden et al.*, 2006). Le réservoir d'eaux chaudes ($> 20°$C entre $5°$N and $5°$S) est étroitement lié avec les deux phases d'ENSO, comme suggéré dans la théorie de l'oscillateur rechargé proposée par *Jin* (1997). Ce réservoir, communément appelé le "warm water volume" (i.e. WWV), est déchargé pendant El Niño et rechargé pendant La Niña (e.g. *Meinen and McPhaden*, 2000, 2001). Il apparaît donc nécessaire d'appréhender les mécanismes qui contrôlent cet apport d'eaux chaudes au niveau de l'équateur pour mieux comprendre les variations d'ENSO.

Dans l'Océan Pacifique, l'échange des masses d'eau entre la région subtropicale et l'équateur est effectué via la cellule subtropicale (STC) (*McCreary and Lu*, 1994), associée à des changements de température ou de quantité d'eau à différentes échelles de temps pouvant impacter ENSO. Au sein de la STC, les eaux transportées depuis les gyres subtropicales rejoigent l'équateur via l'océan intérieur ou les courants de bord ouest de basses latitudes (LLWBCs). Plusieurs études ont mis en évidence une anti-corrélation de ces deux chemins aux échelles interannuelles et décennales (e.g. *Lee and Fukumori*, 2003; *Zilberman et al.*, 2013), influençant les transports associés au WWV et donc potentiellement ENSO. Depuis les années 2000, des études basées sur des observations (*McPhaden and Zhang*, 2002, 2004, e.g.) et des simulations numériques (e.g. *McPhaden et al.*, 2006; *Cheng et al.*, 2007; *Lengaigne et al.*, 2012) ont permis de décrire les variations du chemin intérieur, cependant celles associées aux transports des LLWBCs restent peu documentées, surtout dans l'hémisphère sud.

Identifiés comme une faiblesse majeure du système global d'observations des océans, les courants de bord ouest ont suscité un récent intérêt de la part de la communauté scientifique (*Hu et al.*, 2015), notamment à travers deux programmes internationaux : NPOCE[4] pour l'hémisphère nord et SPICE[5] pour l'hémisphère Sud.

[4]Northwestern Pacific Ocean Circulation and Climate Experiment
[5]Southwest Pacific Ocean Circulation and Climate Experiment

Dans le cadre de SPICE (*Ganachaud et al.*, 2014), les efforts se sont portés sur la circulation dans le Pacifique Sud-ouest, permettant une meilleure description du cheminement des LLWBCs à travers notamment les mers de Corail et de Tasmanie. Au niveau de la Papouasie Nouvelle-Guinée, les courants de bord ouest traversent la mer des Salomon, identifiée comme un passage clé pour étudier les connections entre les régions subtropicale et équatoriale (e.g. *Melet et al.*, 2010a; *Cravatte et al.*, 2011; *Davis et al.*, 2012; *Hristova and Kessler*, 2012). Par ailleurs, les marges continentales de la Papouasie Nouvelle-Guinée ont été identifiées comme une source majeure d'éléments nutritifs comme le fer (*Grenier et al.*, 2013; *Qin et al.*, 2016), avec des implications directes sur la production primaire équatoriale.

Malgré leur importance, les transports et propriétés des masses d'eau associés aux LLWBCs de la mer des Salomon reposent essentiellement sur des simulations numériques et quelques observations in situ depuis les années 80. Au sein du programme SPICE, ce travail de thèse a pour objectif d'améliorer nos connaissances de la circulation océanique et de sa variabilité en mer des Salomon, à partir de données collectées lors de deux campagnes en mer conduites en Juillet-Août 2012 et Mars 2014 via une collaboration entre le LEGOS[6] et la Scripps Institution of Oceanography.

[6]Laboratoire d'Etudes en Géophysique et Océanographie Spatiales

Chapter 1

Scientific Context and Key Issues

Contents

1.1 The Tropical Pacific Ocean

In the tropics, the zonal extension of the Pacific Ocean reaches half of the Earth's circumference, allowing strong ocean-atmosphere interactions without the influence of landmasses, unlike in the Atlantic Ocean. The warmest waters on the planet are found in the tropical Pacific Ocean with temperatures exceeding 28°C, mostly confined in the western side of the basin. These waters usually referred as the warm pool, extends from the surface down to 100 m, inducing a slope at the sea surface between both sides of the Equatorial Pacific Ocean that is maintained in the presence of easterlies. Forced by atmospheric features, the warm pool is tightly involved in the largest climate oscillation, the ENSO phenomenon. Despite major progress in understanding ENSO variability, its modulation at different time scales still remains an import scientific issue, especially in the actual global warming context. The connections between the tropics and subtropical regions in both hemispheres, appear to strongly influence the equatorial Pacific dynamics, and so potentially ENSO, as suggested by major scientific studies (e.g. *Fukumori et al.*, 2004; *Ishida et al.*, 2008; *Zilberman et al.*, 2013).

This chapter will provide a detailed background to explain why the Solomon Sea is considered in many studies, as a hotspot to study the connections between the subtropics and the tropics in the Pacific Ocean. For this purpose, the tropical Pacific dynamics will be introduced through both mean atmospheric and oceanic circulations, as well as the associated seasonal and interannual variations (ENSO). The physical mechanisms of ENSO will be briefly exposed, followed by its low frequency modulation through the meridional subtropical cell. The western boundary route of the STC, which is thought to play a key role in the equatorial Pacific climate will be presented, especially in the southern hemisphere through the international SPICE program. Particular attention will be finally given to the Solomon Sea region, as a complex system of boundary currents flowing through three narrow straits establish a direct connection between the subtropics and the tropics.

1.1.1 The atmospheric circulation

The solar radiation is not uniform over the planet, with largest incoming solar heat flux at the surface in the tropics on annual average. At the equator, warm air arises in the lower atmosphere and subsides near 30°N and °S, creating a high-pressure area. As a result, there is a pressure gradient from the equatorial low pressure (due to arising air) towards the subtropical highs, where cooler air has been subsided before returning to the equator. This meridional circulation cell known as the Hadley cell, is associated with easterly winds in the lower atmosphere from high to low pressure areas that are called the trade winds (Figure 1.1a). As Earth rotates, these winds are deflected in both southern and northern hemispheres towards the equator via the Coriolis force. Historically, the winds are named in term of where they are blowing from, and both North and South components of the trade winds are referred as the northeasterly and southeasterly trades, respectively. Within the Hadley cell, both trades converge towards two main regions over the tropical Pacific Ocean, associated with deep convection and large rain bands (Figure 1.1b).

The first region, the Intertropical Convergence Zone (ITCZ), extends zonally from East to West, along the equator with an annual position centered on 5°N.

The second region, the South Pacific Convergence Zone (SPCZ), is the predominant atmospheric feature in the South Pacific and is somewhat unique as it the only convergence zone existing all year around in the southern hemisphere (*Vincent et al.*, 2011). Its mean annual position extends from the western equatorial Pacific Ocean to French Polynesia along a south-eastward axis (see review by *Vincent*, 1994). Its location is dependent on regional SST gradients that determine moisture convergence patterns related with the SPCZ (*Vincent et al.*, 2011). The SST distribution itself is impacted by near surface wind patterns, so the parameters SST, wind and rainfall are tightly related, and can not be easily divided to examine the SPCZ variations at seasonal or interannual time scales (*Takahashi and Battisti*, 2007).

Furthermore, as the easterly trade winds blow over the Tropical Pacific, the warm surface waters are pilled up in the western part of the basin to feed the warm pool (Figure 1.1a). Upwelling occurs on the eastern side, associated with colder waters off South America, referred as the cold tongue (e.g. *Wyrtki*, 1981). This zonal SST gradient strongly influences atmospheric patterns, inducing a zonal atmospheric circulation known as the Walker cell. Clouds and rainfall are found over the warm pool, induced by warm and moist arising air, while the eastern tropical Pacific is dominated by the subsidence of dry air from the upper atmosphere.

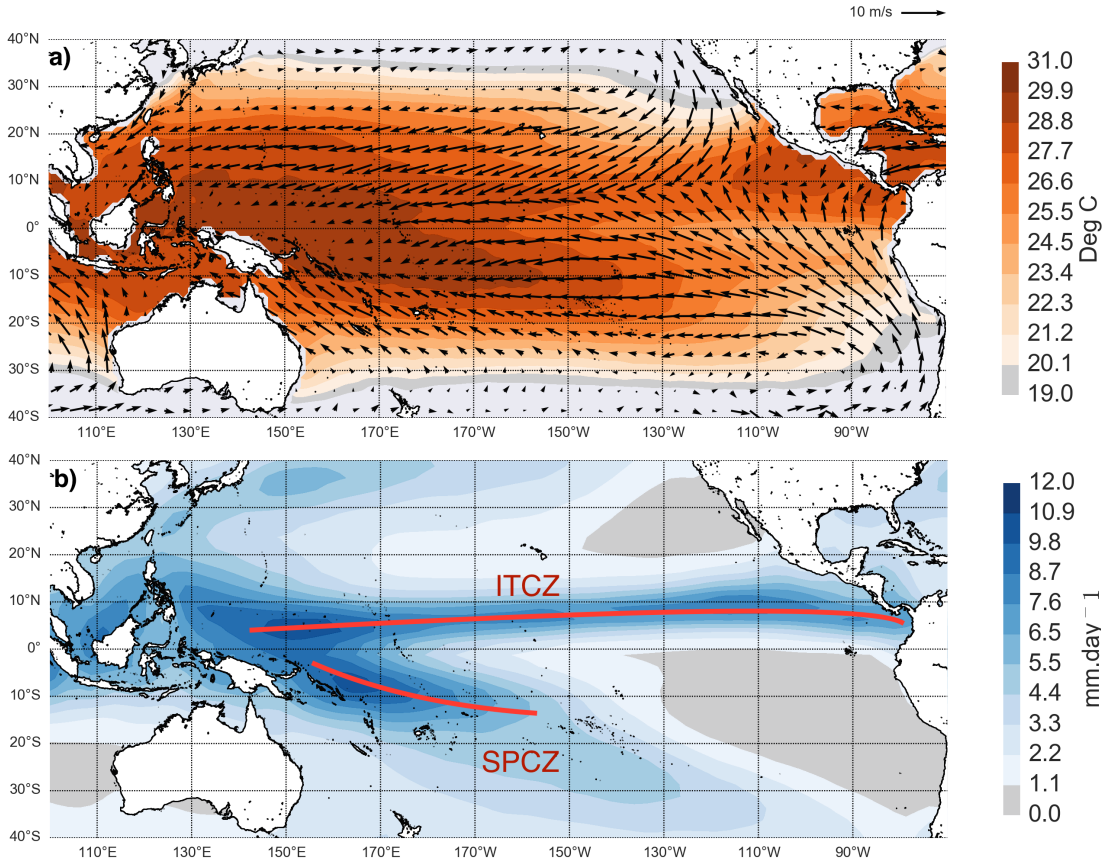

Figure 1.1 – (a) Mean sea surface temperature (°C, color scale) overlaid by near-surface winds (10 m) from ICOADS climatology. Note the unit vector in the upper right of the panel. (b) CPC Merged Analysis of Precipitation (CMAP) precipitations (mm.d^{-1}, color scale) averaged over January 1979 through July 2016. Note the superimposed annual mean positions of the ITCZ and SPCZ (red lines).

1.1.2 The oceanic circulation

The zonal trade winds blowing over the intertropical belt induce zonal currents with opposite directions in the tropical Pacific Ocean (Figure 1.2). The North and the South Equatorial Currents (SEC and NEC, respectively) are two main features generated by the trades, flowing westward from both sides of the ITCZ. Both currents feed the western branch of the anticyclonic subtropical gyres in both hemispheres, before reaching the western boundary, or the interior ocean. Under Sverdrup dynamics (*Sverdrup and Munk*, 1947), fast and intense Low-Latitude Western Boundary Currents (LLWBCs) redistribute waters to the equatorial current system through the Mindanao Current (MC) in the Northern Hemisphere and New Guinea Coastal Current and Undercurrent (NGCC/NGCU) in the southern hemisphere. Within the interior ocean, waters transported by the NEC and SEC pilled up in the western basin, before feeding counter-currents where the winds are weaker (Figure 1.2). In the northern hemisphere, both the North Equatorial Counter Current (NECC) and North Subsurface Counter Currents (NSCC) flow eastward between the NEC and the equator (doldrums), while a less prominent counter flow, the South Subsurface Counter Current (SSCC) is identified in the southern hemisphere near 10°S.

Along the equatorial Pacific, the narrow Equatorial Undercurrent (EUC) flows eastward from the western part of the basin, north of Papua New Guinea (PNG) to the coast of South America (Figure 1.2). It carries distinct water properties, mostly with southwestern origins (e.g. *Blanke and Raynaud*, 1997; *Izumo et al.*, 2002; *Grenier et al.*, 2011). On the western boundary, the EUC is centered on 200 m and gradually shoals along its pathway following the thermocline. Finally it upwells in the eastern Pacific into the SEC, and feeds the equatorial cold tongue.

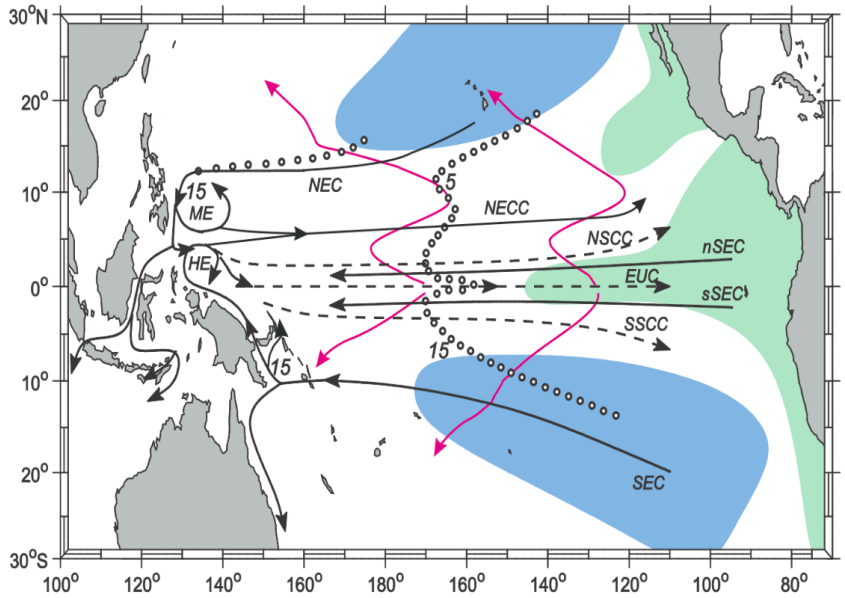

Figure 1.2 – Schematic representation of major surface (solid arrows) and subsurface (dash arrows) currents (NEC and SEC=North and South Equatorial Currents; nSEC and sSEC=north, south South Equatorial Currents; NECC=South Equatorial Counter Currents; NSCC and SSCC=North and South Subsurface Counter Currents; EUC=Equatorial Undercurrent; ME=Mindanao Eddy; HE=Halmahera Eddy).Subtropical subduction (blue shading) zones and equatorial/eastern upwellings (green shading) involved in the STC are indicated. Interior equatorward thermocline pathways are dotted, along with corresponding transport estimates (in Sv). Surface poleward pathways from the central equatorial region are overlaid (magenta lines). From *Schott et al.* (2007).

1.2 The Seasonal cycle in the Tropical Pacific

As solar radiation varies seasonally over the Pacific Ocean, changes in wind patterns are observed, associated with latitudinal migrations of both the ITCZ and SPCZ in the northern and southern hemispheres, respectively. In December-May (Figure 1.3a), the ITCZ is shifted equatorward near 2°N and the trade winds weaken. Meanwhile, the SPCZ consists of a zonal band over the western equatorial Pacific region and a diagonal portion oriented along a northwest-southeast axis east of 170°E, 10°S (*Vincent*, 1994). The annual march of the SPCZ influences the South Pacific climate, controlling rainfall, ocean circulation and the development of tropical cyclones (*Cai et al.*, 2012). In June-November (Figure 1.3b), the southeasterly trades are strengthened due to a northward migration of the ITCZ near 10°N, whereas the SPCZ is zonally shifted over the warm pool and its diagonal feature is less marked. As an oceanic response to this seasonal wind forcing, a spinup (in August-October) and a spindown (February-April) of the South Pacific subtropical gyre is induced (*Kessler and Gourdeau*, 2007; *Melet et al.*, 2010a), impacting the mass redistribution carried out by the currents between the subtropics and the tropics.

During June-November, as the strong and dry trade season prevails and the subtropical gyre spins up, the inflow to the Coral Sea is enhanced and the NVJ is found to be maximum, feeding more waters to the NGCU while the GPC is minimum. A strong SEC is observed near 10°S, as well as a strong eastward flow at the equator (*Hristova and Kessler*, 2012). In this season, the NGCU is found to be maximum in several studies based on observational (*Cravatte et al.*, 2011; *Hristova and Kessler*, 2012) and model results (*Melet et al.*, 2010a,b), as it flows northward across the Solomon Sea. In December-May, the weak and wet trade season coincides with the slowdown of the subtropical gyre. South of 13°S, along the Australian coast, the northward GPC is weakened whereas the southward EAC is enhanced (*Kessler and Gourdeau*, 2007). As a consequence, the NGCU is weakened along its equatorward pathways and the EUC flowing at the equator is found to be minimum (*Melet et al.*, 2010a).

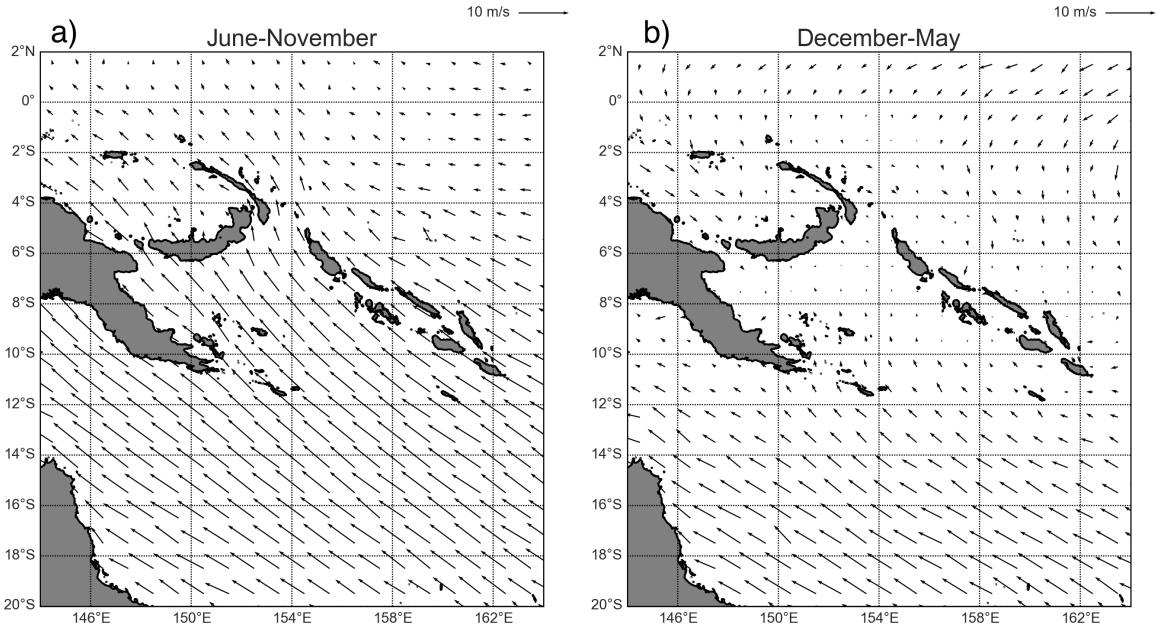

Figure 1.3 – Seasonally averaged wind velocity (unit vectors, upper right) over the Solomon Sea during (a) June-November (the strong trade season) and (b) December-May (the weak trade season), based on the ICOADS climatology.

1.3 Interannual variability in the Tropical Pacific

The dominant climate signal on interannual time scales is the El Niño Southern Oscillation (ENSO), alternating between warm El Niño and cold La Niña events. The ENSO phenomenon originates in the tropical Pacific Ocean based on ocean-atmosphere interactions, but its influence is worldwide associated with major environmental and socio-economics impacts. El Niño and La Niña fluctuations typically occur every 2 to 7 years, associated with swings in the Southern Oscillation (SO), an atmospheric pattern discovered by Sir Gilbert Walker in the early twentieth century, between the Indian and Pacific Oceans. This oscillation is characterized by an internannual seesaw in sea level pressure between the western (low pressure) and eastern (high pressure) sides of the tropical Pacific, inducing a weakening or a strengthening of the easterly trade winds. The strength of the SO is typically determined through a dedicated index, the Southern Oscillation Index (SOI, Figure 1.4), based on mean sea level pressure differences between Tahiti and Darwin.

The negative phase of the SOI corresponds to air pressure below the normal state at Tahiti and above-normal pressure at Darwin, where extended negative periods agree well with warm SSTs typical of El Niño events. Conversely, the positive phase of the SOI coincides with prolonged cold periods related with La Niñas.

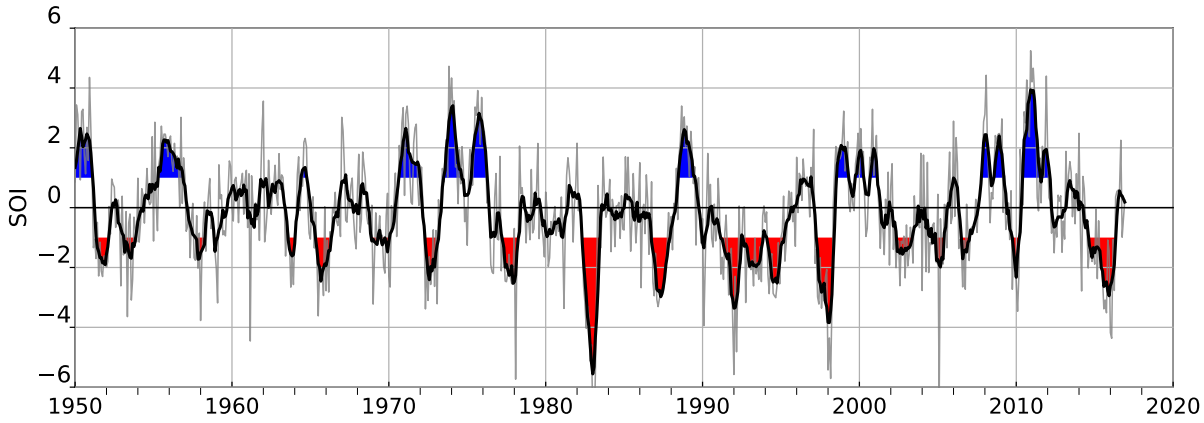

Figure 1.4 – Southern Oscillation Index (SOI) from 1950 through January 2017 (grey line); overlaid by a 6-month moving average of the SOI (black line), where red and blue shading indicate El Niños (SOI less than -1) and La Niñas (SOI greater than +1), respectively.

Bjerknes (1969) highlighted a key feature of ENSO physics: the interactions between the tropical zonal SST anomalies, linked to El Niño and La Niña phases, and the trade wind intensity (referred as the Bjerknes feedback). The easterly trade winds pile up warm waters in the western Pacific where strong convection (precipitation) occurs, associated with a zonal sea level pressure (SLP) gradient that in turn, drives the trade winds.

On a oceanic point of view, the easterly trades shoal the equatorial thermocline shoals in the east and induce upwelling of cold waters occurs along the equator and off the west coast of South America. Since, Bjerknes, the scientific community has made considerable effort in observing ENSO and understanding its mechanisms, especially after the strong unforeseen El Niño event of 1982-83 (*McPhaden et al.*, 1998, 2006).

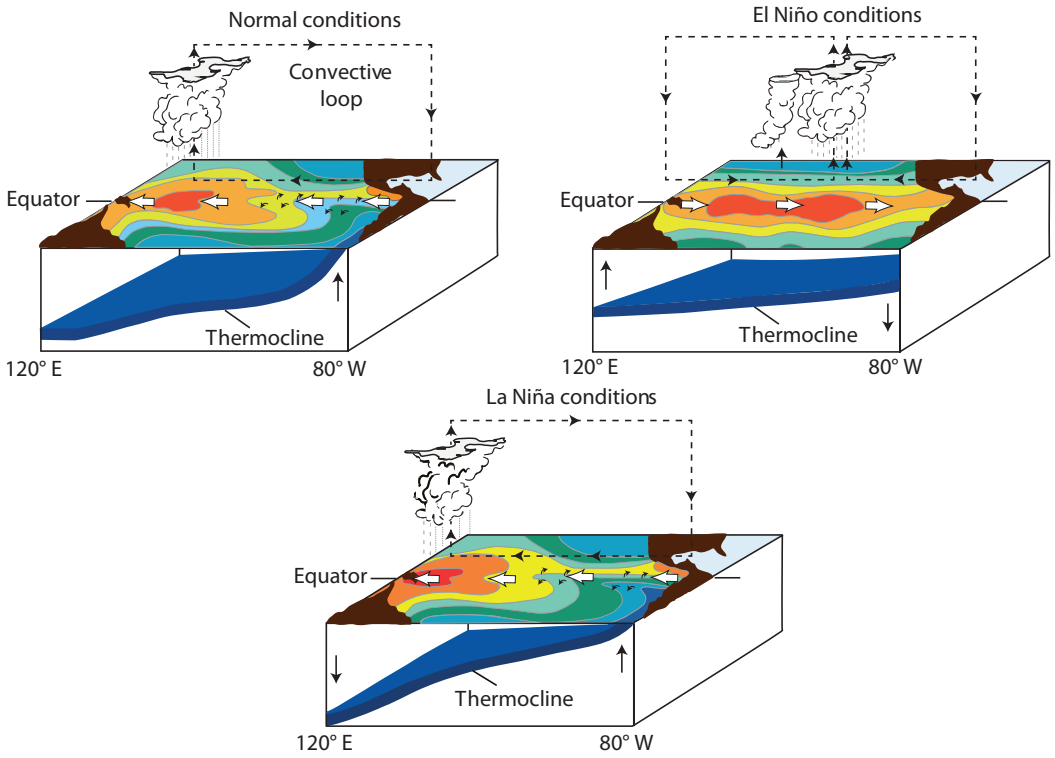

Figure 1.5 – Schematic representation of normal (left panel), El Niño (middle panel) and La Niña conditions (bottom panel) of the El Niño Southern Oscillation. Arrows denote the direction of the winds and surface currents (from *McPhaden*, 2015).

Despite good knowledge of the conceptual framework of ENSO (Figure 1.5), some important questions remain about its dynamics, variability and forecasting, especially in a global warming context. Another yet-unresolved question is related with the nature of the phenomenon itself, is it a cycle in which each fluctuation between both phases is a self-sustained oscillation, or a series of events resulting from stochastic forcing? The next section provides a basic description of ENSO physics, as well as the mechanisms controlling the development of El Niño, and its counterpart La Niña.

1.3.1 Physical mechanisms of ENSO

Every few years, the trades weaken along the equator under the influence of episodic westerly wind bursts (WWBs). These WWBs generate an oceanic response that sets warm SST anomalies in the central Pacific, leading to convective anomalies that can generate in turn, westerly wind anomalies in the central and western Pacific. The atmospheric pressure rises in the western Pacific and falls in the eastern part, leading to a reverse Bjerknes feedback that maintains the convective anomaly and westerly winds (Gill response), associated with a weakening of the trades and strengthened initial SST anomalies.

As a consequence, equatorial basin-scale waves are generated, supporting the growth of anomalously warm SSTs and generating an El Niño event. At the end of El Niño, negative feedbacks are required to shut off the warming, and potentially trigger a La Niña event. Based on a combination of Bjerknes and equatorial wave feedbacks, four main oscillating theories (see review by *Wang and Picaut*, 2004) have been suggested since the late 1980s: (1) the delayed oscillator (*Suarez and Schopf*, 1988; *Battisti and Hirst*, 1988), (2) the recharge oscillator (*Jin*, 1997), (3) the western Pacific oscillator (*Weisberg and Wang*, 1997; *Wang et al.*, 1999a) and (4) the advective-reflective oscillator (*Picaut et al.*, 1997).

However, ENSO can be considered as a multi-mechanism phenomenon, where these oscillators may act in concert in nature. An unified theory was proposed by *Wang* (2001), taking into account different delayed negative feedbacks to turn around the warm state of ENSO (Figure 1.6). This unified oscillator considers the reflected Kelvin waves on the western boundary (i.e. Rossby waves) firstly introduced through the delayed oscillator, meridional discharge/recharge processes due to Sverdrup transport (recharge oscillator), western Pacific wind-forced Kelvin waves (western Pacific oscillator) and reflected Rossby wave at the eastern boundary (advective-reflective oscillator). For example, in the recharge oscillator theory (Figure 1.7), the warm phase of ENSO is associated with the discharge of equatorial heat content (the warm water volume) via the divergence of Sverdrup transport, leading to an anomalously shallow thermocline depth in the entire equatorial Pacific. This anomalous shallow thermocline (the warm to cold transition phase) induces upwelling of cold waters at the equator and then potentially leads to the cold phase, associated with strengthened trade winds (*Jin*, 1997; *Wang and Picaut*, 2004).

The cold phase of the ENSO oscillation, referred as La Niña, is related with cold SST anomalies in the eastern and central equatorial Pacific, and strengthened easterly trades. As a result, the warm pool is confined near the western boundary, while the Bjerknes feedback reinforces the trades. Ultimately, the cooling terminates following the unified oscillator theory to reach the neutral state, or even trigger an El Niño. However, a significant asymmetry between life cycles of El Niño and La Niña has been evident in the past decades. Much stronger El Niño events than La Niñas were observed between the mid-1970s to the late 1990s (*McPhaden et al.*, 2006), suggesting a decadal to interdecadal variability of ENSO. The duration and the evolution of La Niña events are also much less understood, and appear to be more irregular than El Niños.

Recent studies have also argued that different types of ENSO might occur based on spatial variations of SST patterns (e.g. *Larkin and Harrison*, 2005b,a; *Ashok et al.*, 2007; *Kug et al.*, 2009). Particularly, *Ashok et al.* (2007) identified anomalous warming events in the central equatorial Pacific that are not related with classical El Niños. They named these events El Niño Modoki [1] (pseudo-El Niño), corresponding to the second empirical orthogonal function (EOF) mode of variability of tropical Pacific SST anomalies from observed data sets between 1979-2005.

[1] word in Japanese that means "a similar but different thing"

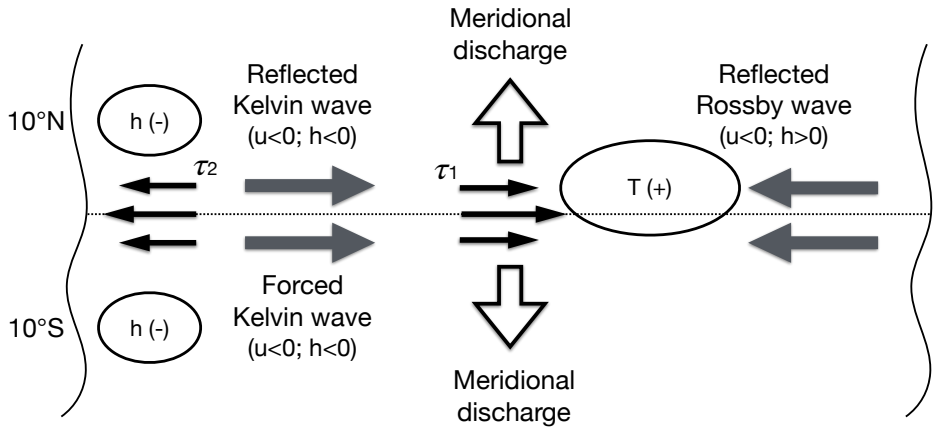

Figure 1.6 – Diagram of the unified oscillator for ENSO, including the negative feedbacks introduced through the four oscillator models. (1) the delayed oscillator, (2) the recharge oscillator, (3) the western pacific oscillator and (4) the advective-reflective oscillator. In this unified theory, the four ENSO oscillators are seen as special cases that may operate together to generate ENSO fluctuations. T corresponds to the SST anomaly in the equatorial eastern Pacific, h is thermocline depth anomaly in the off-equatorial western Pacific, while $\tau 1$ and $\tau 2$ correspond to the zonal wind stress anomalies in the equatorial central Pacific and in the equatorial western Pacific, respectively. Adapted from *Wang and Picaut* (2004).

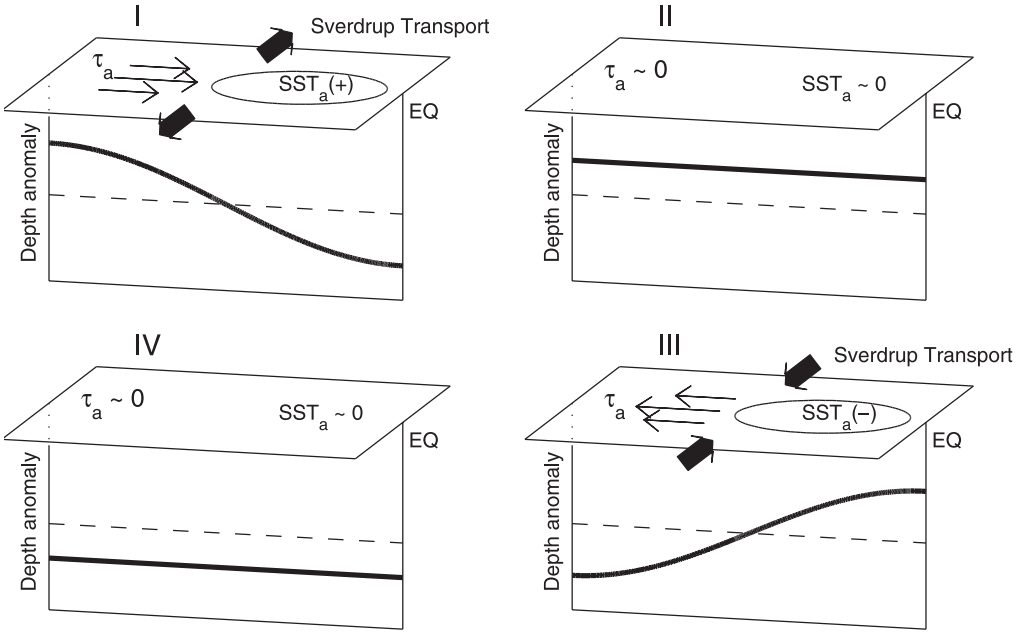

Figure 1.7 – Schematic diagram of the four phases of the recharge oscillator theory. (I) The warm phase, (II) the warm to cold transition phase, (III) the cold phase and (IV) the cold to warm transition phase. From *Wang and Picaut* (2004).

1.3.2 Low frequency variability of ENSO

Variations of ENSO characteristics have been observed at decadal to multidecadal time scales, with major influences on climate. In the North Pacific, evident ocean-atmosphere variability is related with the Pacific Decadal Oscillation (PDO) (*Mantua et al.*, 1997), corresponding to the leading EOF mode of SST north of 20°N. The PDO signature is mostly found in the extratropics with no dominant periodicity, as it is more characterized by a red spectrum typical of stochastic climate models (e.g. *Rudnick and Davis*, 2003). It has been argued that PDO variations are part of a basin-wide feature (e.g. *Power et al.*, 1999; *Folland et al.*, 2002) referred as the Interdecadal Pacific Oscillation (IPO) with again, no dominant periodicity in observations (and most models), and defined as the third unrotated EOF of 13 year low pass filtered on global SST fluctuations from 1911 to 1995 (*Power et al.*, 1999; *Salinger et al.*, 2001). Several studies have shown that ENSO influences both oscillations (e.g. *Newman et al.*, 2003), while the reverse has been suggested but not demonstrated.

Furthermore, PDO and IPO are not the only two climate features able to impact ENSO variability at such time scales. In the tropics, decadal to mutidecadal SST variations can be generated through processes with tropical origins only, such as stochastic atmospheric features (e.g. *Latif*, 1998; *Thompson and Battisti*, 2001), non linear interactions between the seasonal and interannual cycles (*Wang et al.*, 1999b), while some numerical simulations suggested the role of the asymmetry between El Niño and La Niña (*Timmermann et al.*, 2003; *Rodgers et al.*, 2004). Some studies (e.g. *Vimont*, 2002; *Vimont et al.*, 2003a,b) also suggest an influence of the midlatitudes on the tropics through the atmosphere, and more precisely via the "seasonal footprint mechanism" (SFM). During the winter season, the atmospheric variability in the midlatitudes induces an SST "footprint" on the ocean that is maintained until the late spring and summer seasons. This footprint (the subtropical portion, 0°-20°N) generates atmospheric circulation anomalies, associated with equatorial wind stress anomalies that can generate in turn, ENSO-like features of variability.

Changes might also originate from the subtropics, via a shallow meridional overturning circulation that consists of subducted midlatitude surface waters, flowing equatorward all the way to the EUC. More details of this circulation are given in the next section.

1.3.3 Subtropical-tropical connections

Within the Pacific Ocean, water mass exchange between subtropical regions and the equator is carried out by the subtropical cell (STC) (Figure 1.8), that can be seen as a shallow meridional circulation cell (*McCreary and Lu*, 1994). Many studies, from observations and models, lead to an advanced picture of the different pathways and mechanisms associated with the STC (e.g. *Lu and McCreary*, 1995; *Harper*, 2000; *Lee and Fukumori*, 2003; *Schott et al.*, 2007). In the subtropics, surface waters are subducted into the main thermocline and are transported towards the equator through low latitude western boundary currents or the interior ocean, where they travel eastward in the Equatorial Undercurrent (EUC). These waters are then upwelled to the surface into the eastern Pacific, before returning to the subtropical regions via Ekman transport.

Hence, understanding the variability of the STC appears to be a major issue to explain how subtropical heat content is transmitted to the tropics.

A first mechanism is based on the advection of temperature anomalies emanating from the subtropics (the vt' hypothesis; *Gu and Philander*, 1997) that could affect the equatorial sea surface temperature and tropical wind, leading to changes in poleward Ekman transport (*Alexander et al.*, 2002). Some studies observed changes in temperature at decadal time scales between the subtropics and the tropics (e.g. *Deser et al.*, 1996; *Zhang et al.*, 1998, 1999; *Luo et al.*, 2005), however it is not clear how these temperature anomalies travel along the equator (*Schneider et al.*, 1999; *Hazeleger et al.*, 2001). A second mechanism based on fluctuations in the intensity of the cells (the $v't$ hypothesis) was proposed by (*Kleeman et al.*, 1999), where the rate at which waters are transported into the tropics is modified rather than the temperature of those waters.

Studies based on observations (*McPhaden and Zhang*, 2002) and numerical simulations (*Zhang and McPhaden*, 2006) found consistent results, and have shown a slowdown of the subtropical cell at decadal time scale from 1970 to 1999, associated with consistent heat content variations. Since the late 1990s, an intensification of the STC was observed (*McPhaden and Zhang*, 2004; *Cheng et al.*, 2007), but the physical processes that initiated this shift remain poorly understood. Some studies using analytical and numerical models (*Lysne et al.*, 1997; *Liu et al.*, 1999; *Wang et al.*, 2003a,b) mentioned a third mechanism, the interplay between Rossby and Kelvin waves forced by extra-tropical wind stress variations to modulate SST anomalies across the subtropical-tropical basin.

The STC controls mass and heat transports between the subtropics and the equator, and therefore plays a key role in redistributing water properties in the Pacific Ocean via interior and western boundary pathways (*Johnson and McPhaden*, 1999; *McPhaden and Zhang*, 2002) with significant differences between both hemispheres. According to (*Johnson and McPhaden*, 1999), interior pathways in the Southern Hemisphere exhibit water mass transports from the subtropics three times higher than those in the Northern Hemisphere.

Moreover, some numerical simulations (*Lee and Fukumori*, 2003; *Fukumori et al.*, 2004; *Schott et al.*, 2007; *Ishida et al.*, 2008) suggested anti-correlated variations at interannual to decadal time scales between interior and western boundary transports, consistent with an Argo-based study focused on the South Pacific (*Zilberman et al.*, 2013). Pertinent transport estimates of the interior flow were determined at interannual to decadal time scales, but those associated with the western boundary flows remain relatively uncertain, as few observations are available, particularly in the South Pacific.

1.3.4 The Pacific western boundary currents

The Pacific western boundary currents (WBCs) are major oceanic currents that are poorly understood and observed, although their influence on climate variability is well established (*Hu et al.*, 2015). As a key feature of the STC, they establish a direct connection between the subtropics and the tropics, transporting mass and heat into the equatorial current system. These currents can therefore, critically influence the recharge/discharge of the warm water volume (WWV), also referred to as the equatorial heat content for waters warmer than 28-29°C. The tropical belt of these currents, referred to as the low-latitude WBCs, encompasses the Mindanao Current (MC) in the North Pacific and the New Guinea Coastal Undercurrent (NGCU) in the South Pacific. They originate from two zonal westward currents that bifurcate along western boundaries, the North Equatorial Current (NEC) in the northern hemisphere and the South Equatorial Current (SEC) in the southern hemisphere.

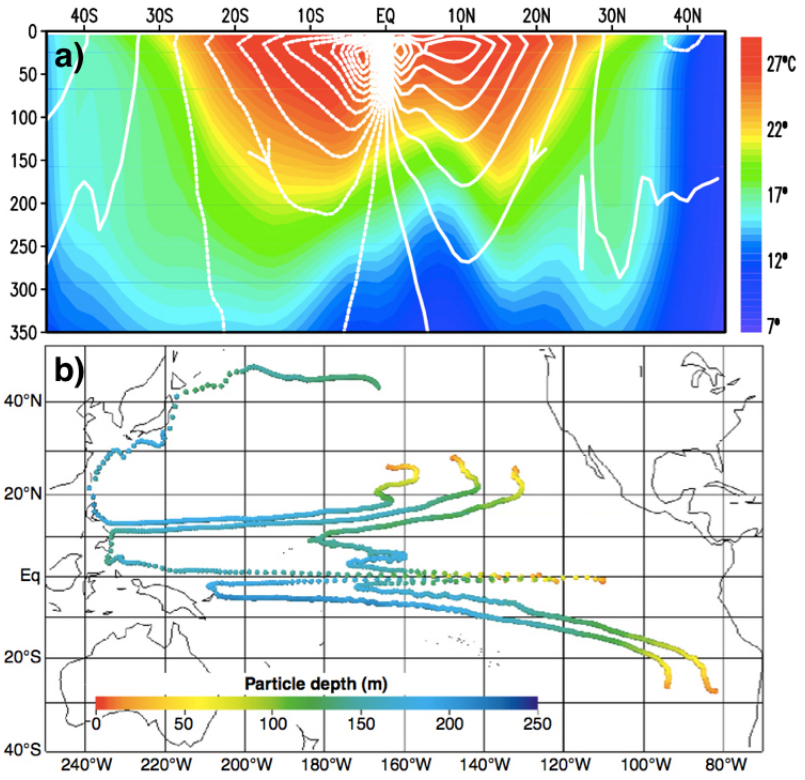

Figure 1.8 – Numerical representations of the Pacific Subtropical cell from (a) Latitude-depth section of the mean temperature at 170°W (color scale), overlaid by the meridional streamfunction (white contours). From *Nonaka et al.* (2002). (b) Particle pathways across over 16 years from a Lagrangian model analysis. Particle depth (color scale) is indicated, with evident subduction off the coasts of California and South America, and upwelling in the central equatorial Pacific. From *Gu and Philander* (1997).

The latitude and the partitioning of both bifurcations is influenced by different climate related features, such as monsoonal winds, or ENSO. During the positive phase of ENSO (Figure 1.9a), the bifurcation is shifted northward in both hemispheres, resulting in enhanced equatorward transports of the MC (*Qiu and Lukas*, 1996; *Qiu and Chen*, 2011) and NGCU (*Davis et al.*, 2012; *Melet et al.*, 2013); although NGCU variability is mostly due to increased transports entering the Solomon Sea, particularly in the NVJ, rather than excursions of the SEC bifurcation. An opposite tendency is expected during the cold phase of ENSO with decreased MC and NGCU equatorward transports.

The responses of the Mindanao current and the New Guinea Coastal Undercurrent to ENSO discharge/recharge fluctuations are critical, with downstream effects on the EUC and the Indonesian Throughflow (ITF). During the El Niño phase, a weakening or even the disappearance of the EUC is typically observed in the central and eastern Pacific (e.g. *Kessler and McPhaden*, 1995; *Johnson et al.*, 2000; *Izumo*, 2005). In contrast, as La Niña develops (Figure 1.9a), a weaker NGCU from the South Pacific is expected from observations (*Davis et al.*, 2012; *Kessler and Cravatte*, 2013a) and a modeling study (*Melet et al.*, 2013).

Regarding the ITF, observational studies have suggested oscillating transports in phase with ENSO, smaller during El Niño and larger during La Niña (*Fieux et al.*, 1996; *Gordon and Fine*, 1996; *Gordon and McClean*, 1999). However, a recent modeling study (*van Sebille et al.*, 2014) depicted a more complex picture, where the response in transports relative to ENSO can differ for the different straits in the Indonesian Seas.

At decadal and multidecadal time scales, the variations of the Pacific WBCs are also related with shifts in latitude of the NEC and the SEC bifurcations, but they are not consistent with ENSO-related changes (*Hu et al.*, 2015). These variations of the Pacific WBCs can strongly influence the air-sea interactions, such as the latent and sensible heat contents to the atmosphere. At seasonal time scales, the North Pacific WBCs are known to be tightly related with the Asian monsoon (*Qu and Lukas*, 2003) and the storm track activities (*Frankignoul and Sennéchael*, 2007; *Taguchi et al.*, 2009), however climatic impacts are less understood in the South Pacific. Some studies suggest an influence of the poleward branch of the South Pacific WBCs, called the East Australian Current (EAC), on Australia (*Shi et al.*, 2008) and New Zeland (*Sprintall et al.*, 1995) climates, but little is known at lower latitudes between the subtropics and the tropics.

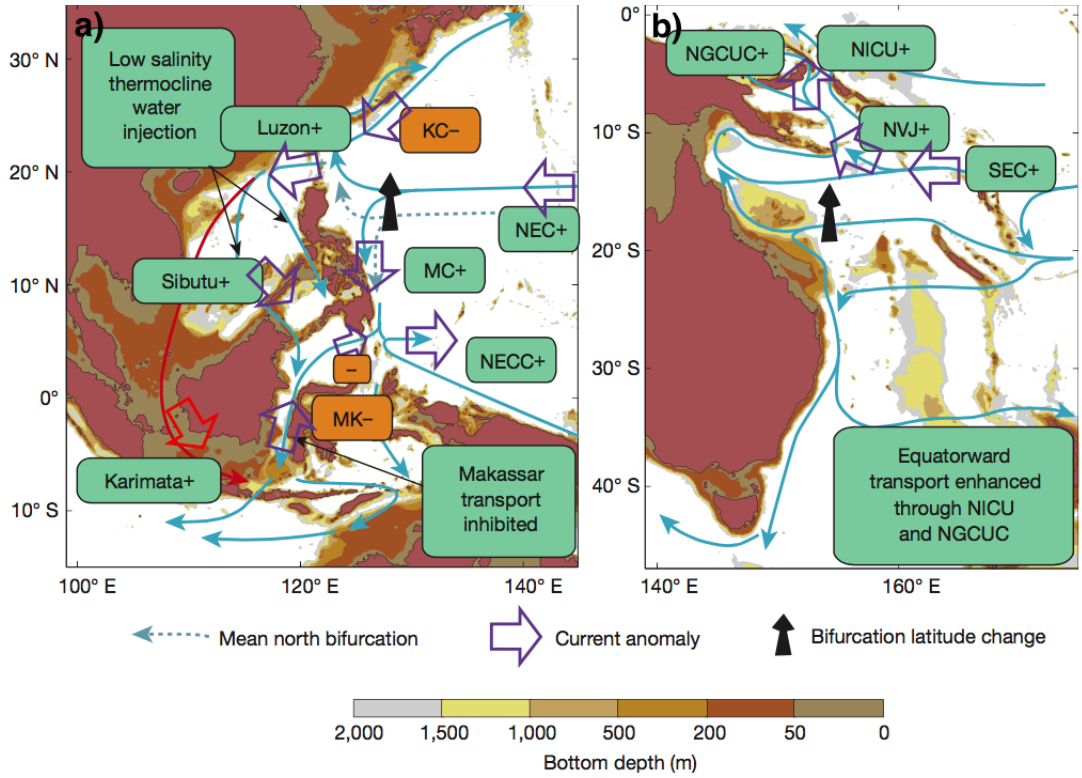

Figure 1.9 – Schematic of the Pacific western boundary currents (blue arrows) in the northern hemisphere (a) and southern hemisphere (b), color shading shows depths shallower than 2000 m. Black arrows indicate northward shifts of the northern (a) and southern bifurcations (b) during El Niño. Increased (green boxes) and decreased (orange boxes) volume transports are indicated as El Niño develops, along with associated current anomalies (large arrows). KC=Kuroshio Current; Luzon=flow through Luzon Strait; Sibutu=flow through Sibutu Passage; Karimata=flow through Karimata Strait; MK=flow through Makassar Strait; MC=Mindanao Current; NGCUC=New Guinea Coastal Undercurrent; NEC=North Equatorial Current; NICU=New Ireland Coastal Undercurrent; NVJ=North Vanuatu Jet. From *Hu et al.* (2015).

1.4 The international SPICE program

At the outset of the CLIVAR international Southwest Pacific Ocean Circulation and Climate Experiment program (*Ganachaud et al.*, 2014), only few observations were available, mostly because the region is difficult to work in. Indeed, the region is dominated by strong narrow currents through complex topography, and associated with a large temporal variability. Despite serious challenges, intense in situ observational and modeling efforts were conducted within SPICE, to improve our knowledge of the Southwest Pacific Ocean circulation and its role on climate.

The main objective of this program involved specific efforts on:

- The circulation in the Coral, Solomon and Tasman Seas, with specific attention to the strong boundary currents and associated jets
- The transformation and mixing undergone by the different water masses during their transit
- The variability of the circulation and its relation with the SPCZ dynamics
- The impact of the EAC variations on Tasman Sea water properties and regional climate
- Maintain and develop an integrated observational program (e.g. cruises, HR XBT lines, gliders or mooring arrays) to monitor key currents and associated transports

Within SPICE, the successful numerical simulations coupled with repeated measurements (Figure 1.10a) lead to significant advances, including an unprecedented description of the South Pacific WBC route across the Solomon, Coral and Tasman Seas (Figure 1.10b). Particular attention was given to the Solomon Sea through a France-U.S. collaboration that encompasses the Solwara project and the MoorSPICE program. The Solwara project is a french component of SPICE and GEOTRACES[2] that aims to provide a complete picture of the circulation and associated water properties in the Solomon Sea. A combined approach including ocean modeling and exploratory observations was implemented for an optimal survey of the inflow and outflow across the sea, as well as their time-variability.

More specifically, Solwara[3] involves in situ measurements through a multi-disciplinary oceanographic cruise (Pandora), mooring deployments in the Solomon Strait and high-resolution numerical simulations (1/12° to 1/36°). The MoorSPICE program consists in mooring deployments of current meter and T-S sensors in Vitiaz Strait and St Georges Channel as part of Pandora cruise. It also includes an oceanographic cruise (MoorSPICE) that sampled both the Solomon and Bismarck Seas, and recovered the moorings deployed during Pandora before a last redeployment in Vitiaz and Solomon Straits.

Refined oceanic pathways flowing across the Southwest Pacific are shown in the next section, as well as the distribution of water properties over the water column.

[2] http://www.geotraces.org

[3] Solwara means "salt water", the sea, in pidgin languages from Papua New Guinea and the Solomon Islands

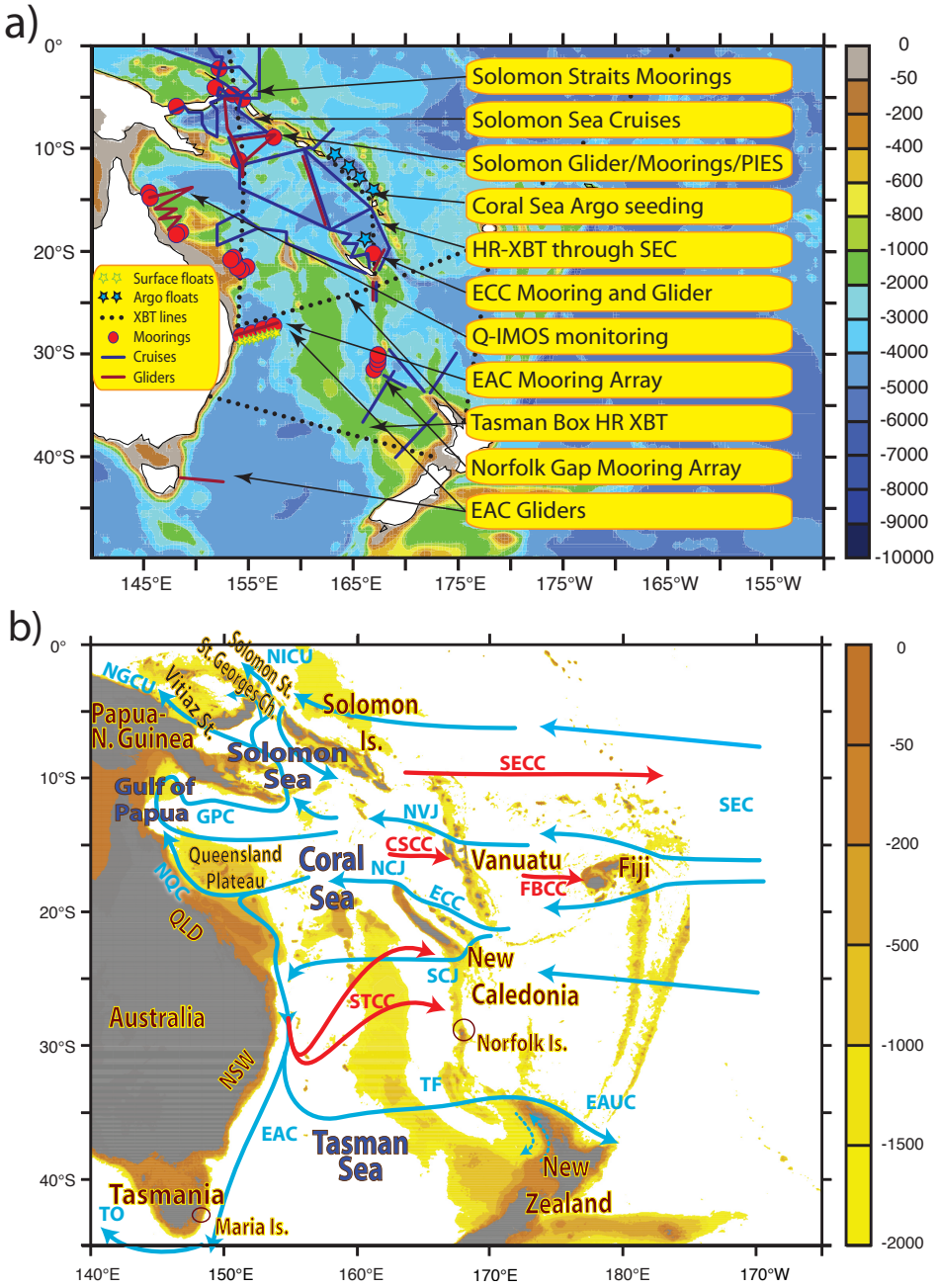

Figure 1.10 – (a) Main elements of the SPICE field program and background map indicates ocean depth (color scale, meters). Note that PIES=Pressure Inverted Echo Sounder; HR-XBT=High resolution XBTs; Q-IMOS= Integrated Marine Observing System. (b) Southwest Pacific topography (color scale, meters), countries and islands are indicated in red, as the Queensland (QLD) and New South Wales (NSW). Blue arrows denote the main currents, integrated over 0-1000 m (SEC=South Equatorial Current; NVJ=North Vanuatu Jet; ECC=East Caledonian Current; NCJ=North Caledonian Jet; SCJ=South Caledonian Jet; GPC=Gulf of Papua Current; NGCU=New Guinea Coastal Undercurrent; NICU=New Ireland Coastal Undercurrent; EAC=East Australia Current; TF=Tasman Front; EAUC=East Auckland Current; TO=Tasman Outflow). The red arrows indicate the main surface-trapped counter-currents (STCC=South Pacific Subtropical Counter Current; CSSC=Coral Sea Counter Current; FBCC=Fiji Basin Counter Current; and SECC=South Equatorial Counter Current). From *Ganachaud et al.* (2014).

1.4.1 Major oceanic pathways

The southwest Pacific circulation (Figure 1.10b) emanates from the westward flowing South Equatorial Current across the Pacific Ocean, carrying dynamical and water properties influences from the subtropical gyre to the western boundary (*Kessler and Gourdeau*, 2007; *Melet et al.*, 2010a). The SEC is characterized by two bands a few hundred kilometers wide centered near 3° and 14°S. The northern SEC stream splits near Solomon Strait, where most of the flow is deflected equatorward. South, a myriad of narrow jets are generated as the southern SEC stream encounters numerous islands along its way to Australia through the Coral Sea, such as the North Vanuatu Jet (NVJ), the North Caledonian Jet (NCJ) and the South Caledonian Jet (SCJ). At the Australian coast, the SEC bifurcates into the poleward East Australian Current and the North Queensland Current (NQC) that flows northward across the Coral Sea to become the Gulf of Papua Current (GPC) (e.g. *Kessler and Cravatte*, 2013b). North, the GPC enters the Solomon Sea, becoming the New Guinea Coastal Undercurrent that flows equatorward around a complex topography before exiting through three narrow straits: the Vitiaz Strait, Solomon Strait and St. Georges channel, and ultimately reach the equatorial current system (e.g. *Melet et al.*, 2010a; *Cravatte et al.*, 2011; *Grenier et al.*, 2011).

1.4.2 Vertical structure and water properties

Measured salinity and dissolved oxygen in the Southwest Pacific can be tracked along the LLWBCs from the Coral Sea to the equator through two prominent features. An upper salinity maximum near 150 m (*Qu and Lindstrom*, 2002), identified as the South Pacific Tropical Water (SPTW) that originates in the Southeast Pacific gyre (e.g. *Kessler*, 1999; *Hasson et al.*, 2013; *Qu et al.*, 2013). Near 800 m, the Antarctic Intermediate Water (AAIW) is characterized by a salinity minimum and a marked oxygen maximum, with southeast origins (*Tsuchiya*, 1991; *Qu and Lindstrom*, 2004). Two other water masses are sandwiched between these two layers, the Subtropical Mode Water (STMW) and the Subantarctic Mode Water (SAMW). The primer emanates mostly from north of the Tasman Sea (*Donguy and Henin*, 1977) and partly northeast of New Zealand (*Tsuchiya*, 1981; *Qu et al.*, 2008), while the SAMW can be traced back into the Southern Ocean, north of the Antarctic Circumpolar Current (*McCartney*, 1977; *Hanawa and Talley*, 2001).

Below 1000 m, increasing salinity and decreasing oxygen, associated with high silica marks the transition with the deep waters. The Upper Circumpolar Deep Water (UCDW) ranges approximately from 1000 to 2000 m in the Antarctic Circumpolar Current (*Orsi et al.*, 1995), and originates from the Southern Ocean with relatively low oxygen and high nutrients (i.e. nitrate, phosphate and silica) (*Callahan*, 1972). UCDW pathways are still poorly documented across the Pacific Ocean, mainly based on scattered observations from the World Ocean Circulation Experiment (WOCE) conducted in the 1990s (e.g. *Reid*, 1997; *Tsimplis et al.*, 1998; *Kawabe and Fujio*, 2010).

Underneath the UCDW, the deep and bottom Lower Circumpolar Deep Water (LCDW) is identified as a remnant of the North Atlantic Deep Water (NAPDW), with a salinity maximum and a silica minimum (*Orsi et al.*, 1999; *Kawabe and Fujio*, 2010). According to *Johnson* (2008), this deep water encompasses Antarctic Bottom Water (AABW), and flows northward from the Antarctic Circumpolar Current (ACC) to the North Pacific via intricate pathways largely constrained by complex bathymetry (e.g. *Roemmich et al.*, 1996; *Kawabe et al.*, 2003, 2006).

Within the Southwest Pacific Ocean, the Solomon Sea is a key location to study the direct connections between the subtropics and the equator via low-latitude western boundary currents. Our current knowledge of the circulation in this region is given in the next section.

1.5 The Solomon Sea: a hotspot to examine equatorward LLWBCs

The main features and scientific interests related with the Solomon Sea are firstly introduced, following with a description of the surface and thermocline pathways, and their associated water properties. A last section will focus on unresolved issues, as well as recent operations related with the Solomon Sea.

1.5.1 Presentation

The western boundary from 12° to 5°S encompasses the semi-enclosed Solomon Sea (Figure 1.11a). This sea, located north of the Coral Sea, is bounded on the west by the Papua New Guinea (PNG), on the north by the islands of New Britain (NB) and New Ireland (NI), and on the east by the Solomon Island chain. The Solomon Sea is connected to the equator by three narrow passages: the Vitiaz Strait, which is around 1000 m deep and about 42 km wide at 200 m, St. Georges Channel, which is deeper but only about 15 km wide, and Solomon Strait, which is deeper an much wider (about 170 km). Its intricate topography exhibits many different features, from shallow reefs with many channels near the coasts and Archipelagos, to deep ocean trenches.

The LLWBCs of the Solomon Sea travel equatorward following intricate routes through narrow passages before joining the equatorial region. Each pathway potentially means different time scales for water to transit across the Solomon Sea, including some differences in water properties. Thus, a major issue related with the Solomon Sea is to provide a quantitative view of equatorward transports and property fluxes through each passage, as well as their time variability at different time scales. In addition, intense mixing induced by internal waves and submesoscale to mesoscale activity is expected to occur within the Solomon Sea from a tracer model study *Melet et al.* (2011).

As a result, significant reduction of the vertical salinity and temperature gradients are suggested across the water column, especially at the thermocline and intermediate levels. The high salinity water mass flowing at the upper thermocline is identified as the SPTW, and appears to be eroded along its equatorward pathways whereas a low salinity core, associated with the AAIW gets saltier at intermediate depth levels. A quite good data coverage mostly based on Argo profiles, at the southern entrance and northern exits of the Solomon Sea depict a coherent picture with this modeling study (Figure 1.11a).

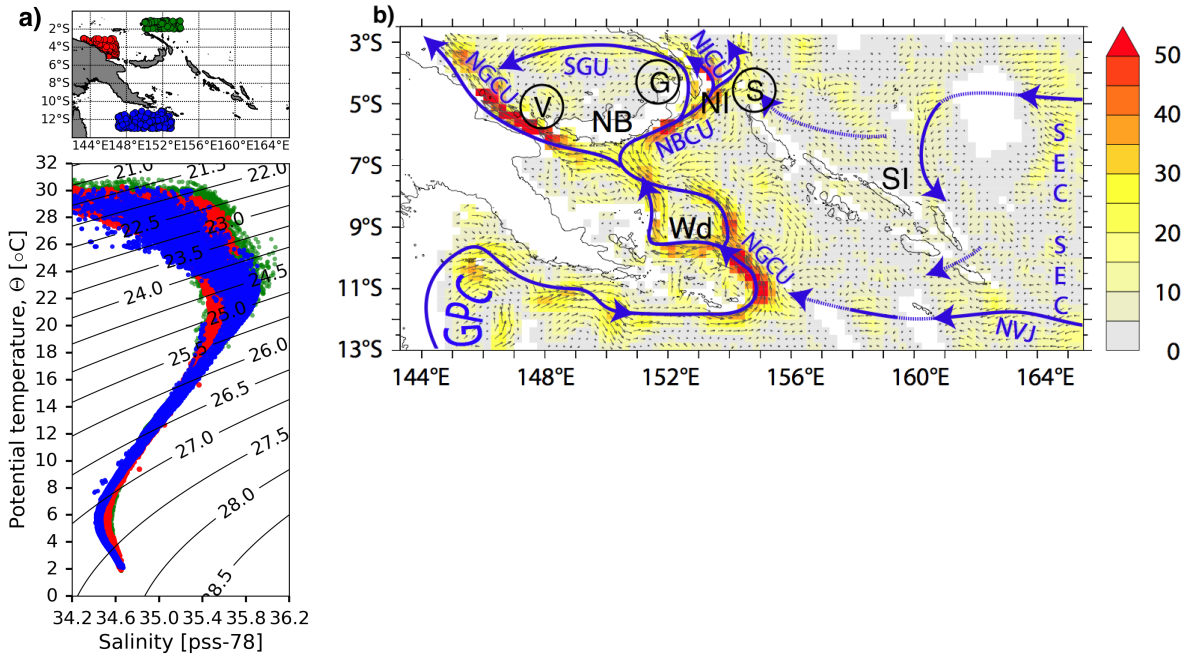

Figure 1.11 – (a) Θ–S diagrams from the Coriolis database upstream (blue dots; 11.5°–13°S, 147°–153°E), downstream off Vitiaz Strait (red dots; 3°–5°S, 143°–147°E) and downstream off Solomon Strait (green dots; 1°–2°S, 150°–154°E) of the Solomon Sea. Only profiles flagged as "good data" were extracted from the Coriolis database, from January 2005 through August 2016. (b) Mean circulation in the Solomon Sea averaged over 100-300 m based on historical S-ADCP data from *Cravatte et al.* (2011). Main current pathways are indicated (blue arrows), as well as their velocity (color scale, cm.s^{-1}). Names of Islands are in black (NB=New Britain; NI=New Ireland; SI=Solomon Islands; Wd=Woodlark Island), while circled "V", "S" and "G" indicate Vitiaz and Solomon Straits, and St Georges Channel, respectively.

1.5.2 Circulation in the Solomon Sea

Recent studies based on numerical simulations (*Melet et al.*, 2010a; *Djath et al.*, 2014) and a 20-year shipboard ADCP[4] velocity climatology (*Cravatte et al.*, 2011) provided a first description of the mean circulation above 300 m depth (Figure 1.11b). As briefly introduced in Section 1.4.1, the LLWBCs coming from the Coral Sea transit through the Solomon Sea before joining the equatorial current system via the NGCC near the surface and the NGCU at deeper depths. (*Cravatte et al.*, 2011) found similar mean current patterns between the subsurface (20-100 m) and thermocline depth level (100-300 m) that agreed well with the modeling study of *Melet et al.* (2010a).

[4]Acoustic Doppler Current Profiler (ADCP): Instrument that obtains water current velocity profiles by transmitting sound waves of known frequency over a depth range and measuring the Doppler shift of reflections scattered back from particles, which are assumed to be passively moving within the water column

At the thermocline, the GPC enters the Solomon Sea through and around the Louisiade Archipelago, feeding the NGCU. A direct portion of the NVJ also enters the sea, and merge into the NGCU as it flows along the Papua New Guinea coast. South of Woodlark Island, the NGCU splits into two streams that merge again north of Woodlark, before splitting again into two streams south of New Britain. At Vitiaz Strait, the western NGCU exits the Solomon Sea, while the eastern NGCU turns east into the New Britain Coastal Undercurrent (NBCU). In turn, the NBCU splits to form the St Georges Undercurrent (SGU) as it exits St Georges Channel, and to form the New Ireland Coastal Undercurrent through the Solomon Strait. Below the thermocline, the low-latitude western boundary pathways remain unobserved, as well as their transport partition across the northern exit straits.

Seasonally, several studies (*Melet et al.*, 2010a,b; *Cravatte et al.*, 2011; *Hristova and Kessler*, 2012) identified major changes in the surface inflow and outflow partitions across the Solomon Sea, influenced by the reversal of the trades. At the thermocline level, most of the seasonal variability is associated with a strengthening or a weakening of the NGCU, that is minimum in austral fall and maximum in austral spring (*Melet et al.*, 2010a; *Cravatte et al.*, 2011). At interannual time scales, LLWBC transport variations are found to be as strong as the mean (*Davis et al.*, 2012), associated with enhanced transports during El Niño and decreased transports during La Niña (*Melet et al.*, 2010b, 2013).

1.5.3 Unresolved issues

Full-depth equatorward LLWBC transports and water property fluxes (e.g. heat and salt) through each narrow exit passage still need to be quantified, especially between St Georges Channel and Solomon Strait. Furthermore, the water mass transformations undergone along the LLWBC pathways remain unknown within the sea, as only few scattered in situ observations were available before SPICE. Indeed, the Solomon Sea is poorly documented, and mostly based on the past Western Equatorial Pacific Ocean Climate Studies (WEPOCS) cruises conducted in 1985-1986 (*Lindstrom et al.*, 1987, 1990), and sparse ADCP and XBT surveys.

The significant mixing suggested in numerical tracer studies (*Melet et al.*, 2011; *Grenier et al.*, 2011) within the Solomon Sea, warrants further investigation, although in situ measurements such as those from microstructure profilers are not available to confirm results from these two simulations. Determining the tidal forcing in the narrow straits of the sea is also an interesting issue that needs to be quantified.

Thus, two exploratory oceanographic cruises were recently conducted in the region (see Chapter 2), including hydrographic measurements and mooring deployments that are presently analyzed, and constitute most of the data set used in this thesis.

1.6 Summary

Interactions between the ocean and the atmosphere within the tropical Pacific contribute to the major climate fluctuation on the planet with a period of 2 to 7 years, the ENSO phenomenon. Intensive scientific effort was made since the 1980s to understand the causes and worldwide consequences of its warm phase, El Niño and its cold counterpart La Niña. Despite advanced theories, models and field programs, many aspects of ENSO dynamics remain unexplained, as its evolution in response to greenhouse warming.

Variations of ENSO signatures have been observed over a broad spectrum of time scales, involving major changes in the Pacific equatorial budget. Water mass influx conveyed by the Subtropical Cell from the subtropics have been demonstrated to be strongly involved in those changes through two main mechanisms, (1) the equatorward advection of temperature anomalies (vt') formed by subduction or (2) variations in STC volume transports ($v't$), which cause equatorial SST anomalies. Within the STC, waters join the equatorial region in both hemispheres either through low-latitude western boundary currents or the interior ocean.

Direct observations and modeling studies suggest that the two pathways are generally anti-correlated, with large variations at interannual to decadal time scales. While the change of interior transport has been well documented since the last decade, transport through the western boundary is less constrained due to larger uncertainties in transport estimates, as only few observations are available. Several studies identify the southwest Pacific western boundary currents as a major source of the equatorial waters, but the region is remote with serious technical challenges to implement suitable surveys.

As part of SPICE, scientific efforts were made to monitor the southwest Pacific inflows, outflows and associated western boundary currents through a well-defined field program, resulting in a better picture of these flows, mostly in the Coral Sea. However, unresolved issues remain, especially in the Solomon Sea that appears to be a choke point in the southwest Pacific, as it provides a direct connection between the subtropics and the equator. Only scattered observations were available in this sea before SPICE, making the water mass transformations and pathways in this last portion of the LLWBCs before the equator uncertain.

1.7 Objectives of the thesis

In this thesis, I aim to assess the circulation and associated water properties in the poorly documented Solomon Sea region, despite its importance in the southwest Pacific climate. Estimating the variability of this circulation at different time scales is also a major objective of this thesis. More specifically, the major objectives of this thesis are:

1. Determine a refined picture of the LLWBC pathways and associated transport across the Solomon Sea, from in situ observations collected during two exploratory cruises as part of the SPICE program

2. Characterize the water mass properties and their modification along those LLWBCs from both hydrographic measurements and ocean climatology

3. Estimate the representativeness of the flows during both cruises with respect to the synoptic scale variability (seasonal and interannual), as well as mesoscale structure (eddies) at the subsurface based on available global mean products

4. Assess the intraseasonal to seasonal flow variability at the northern exit passages of the sea, particularly for thermocline and intermediate waters, through preliminary analyses of an unprecedented 1.5-year mooring timeseries

The next chapters of the thesis are organized as follows. First, detailed information about the Pandora and MoorSPICE cruises are given along with complete details about the collected data. The method used to estimate the circulation and transports in the Solomon Sea is then described (Chapter 2). A regional climatic study to determine sea surface conditions during both cruises follows in Chapter 3. A first estimate of the oceanic circulation in the Solomon Sea, with particular insights on thermocline and intermediate waters, is provided in Chapter 4.

A second estimate of the circulation depicts a first picture of the deep pathways and associated water properties (Chapter 5). The time variability of the flow at the northern exits of the Solomon Sea is then analyzed in Chapter 6, after presenting all mooring instrumentation and associated quality control. A final chapter gives a general summary of the thesis along with conclusion remarks and future work perspectives.

Chapter 2

Methodological Approach

Contents

2.1 Introduction and scientific motivations

Chapter 1 presented the key role of the Solomon Sea, including downstream effects on the equatorial current system. To improve our knowledge of the circulation, two exploratory oceanographic cruises took place inside the Solomon and Bismarck Seas as part of SPICE (*Ganachaud et al.*, 2016). The first cruise, named Pandora, occurred from 27 June to 6 August 2012, on the French research vessel R/V L'Atalante. It aimed at documenting the region with a multi-disciplinary approach, combining physics, geochemistry and biogeochemistry (Figure 2.1a). The second cruise, named MoorSPICE, focused on physics and biogeochemistry from 28 February to 31 March 2014, on the U.S. vessel R/V Thomas G. Thompson. The cruise partly repeated the Pandora hydrographic transects, and explored the Bismarck Sea northwest of the Solomon Sea (Figure 2.1b). In addition, nine subsurface mooring instruments were deployed in the northern straits of the sea during Pandora, then recovered and redeployed during MoorSPICE before a final recovery in August 2015. I had the chance to be onboard of MoorSPICE, and greatly benefited from this experience at sea.

One of the motivations of these two cruises is to depict a mean picture of the equatorward South Pacific western boundary currents across the Solomon Sea, from the surface down to deep layers (below 2000 m). The transport partitions through the narrow exit passages of the sea are also a key motivation to obtain a quantitative view of the mean circulation. Furthermore, the water properties associated with those currents are expected to undergo significant changes when transiting through the Solomon Sea, as suggested by a modeling study (*Melet et al.*, 2011), but mostly unobserved before these two SPICE cruises. The northern exit pathways might also be supplied by different water mass combinations that vary in time, with potential downstream effects on equatorward property fluxes.

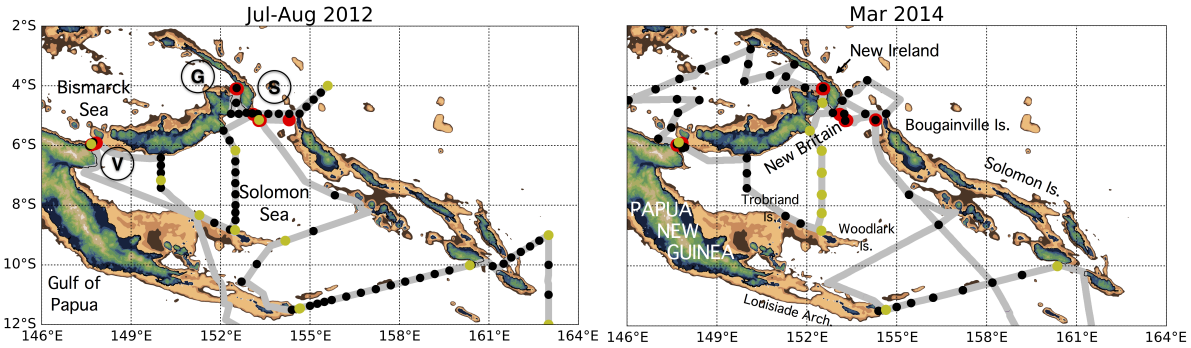

Figure 2.1 – Shallow bathymetry at 100, 500 and 1000 m (brown shading), station positions (black dots) and repeat stations (yellow dots) along cruise tracks (grey background) during (left) the Pandora cruise (July-August 2012) and (right) the MoorSPICE cruise (March 2014). Mooring locations (red dots) deployed during Pandora and retrieved during MoorSPICE. Circled "V" and "S" represent Vitiaz and Solomon straits, while "G" abbreviates St Georges Channel.

2.2 Description of the two SPICE exploratory cruises

This section provides a description of the cruises, including detailed information about the in situ observations measured along the hydrographic transects. The mooring instruments will be presented in Chapter 6, along with required instrument quality control.

2.2.1 The July-August 2012 cruise: Pandora

Having departed from Nouméa on 28 June 2012 on board of the R/V L'Atalante, Pandora lasted 40 days and returned to port on 6 August (Figure 2.1a; a larger-scale map with station numbers is shown in Figure A1a). Hydrographic transects, including repeat 28-36h time series stations, were carried out using CTD-O_2 sensors to measure temperature, conductivity[1] and oxygen. Niskin bottles were used to collect discrete samples at specific depths to measure salinity, oxygen, inorganic nutrients (nitrite, nitrate, phosphate and silica) and other biogeochemical parameters. Currents were measured using a pair of RDI Lowered-Acoustic Doppler Current Profilers (L-ADCPs) attached to the *standard* CTD rosette (150 kHz and 300 kHz, down- and up-looking, respectively). Currents were also measured along the ship track, using two shipboard ADCPs (S-ADCPs) with vertical ranges of 1300-1350 m and 300-350 m, respectively. A titanium *clean* CTD body along with Go-Flo bottles was used to obtain uncontaminated samples for trace metals.

During Pandora, the cruise track included first, a latitudinal transect between 18°-9°S, along 163°E to sample waters from the westward SEC, entering the Coral Sea. At the southern entrance of the Solomon Sea, a transect repeated the FLUSEC cruise conducted in August 2007 (*Gasparin et al.*, 2012). Then, three transects were carried out within the Solomon Sea to sample as much as possible the LLWBC pathways. A transect sampled water masses northeast of Bougainville Island, while two other transects were conducted across Solomon Strait to St Georges Channel, and Vitiaz Strait. In total, measurements were collected at 83 stations, including 170 casts, most to 2000 m depth.

The nine subsurface moorings were deployed, more or less simultaneously, over the narrow exit passages of Vitiaz Strait (U.S), St Georges Channel (U.S) and Solomon Strait (France) in July 2012.

2.2.2 The March 2014 cruise: MoorSPICE

MoorSPICE departed also from Nouméa, aboard the R/V Thomas G. Thompson from 28 February to 31 March 2014 (Figure 2.1b; a larger-scale map with station numbers is shown in Figure A1b). As during Pandora, some repeat 28-36h time series stations were surveyed, along with CTD-O_2 hydrographic transects and Niskin bottle measurements (salinity, oxygen and nutrients). Currents were also measured using a pair of down- and up-looking 300 kHz RDI L-ADCPs, and a shipboard ADCP working in both broadband and narrowband modes with vertical ranges of 700-750 m and 850-900 m, respectively.

The cruise began with the mooring recovery at Solomon Strait and St Georges Channel, along with station surveys. The ship continued northwestward into the Bismarck Sea, where measurements were collected following a saw-tooth pattern. Then, the last moorings located at Vitiaz Strait were recovered, before entering again into the Solomon Sea. Within the sea, similar transects than those of Pandora were performed but in a reverse pattern, including the repeat transect at the southern entrance during both FLUSEC and Pandora cruises. Overall, measurements were made at 57 stations, with 78 casts and including the deployment of six Argo floats, nine moorings recovery and four additional mooring redeployments in Vitiaz and Solomon Straits (Figure 2.2).

[1]Salinity is calculated from conductivity

Figure 2.2 – Pictures during the MoorSPICE cruise, on the R/V Thomas G. Thompson from 28 February to 31 March 2014. Subsurface mooring instruments including T-S sensors, up-and down-looking ADCPs (right) and current meters (bottom), were firstly recovered and then deployed (upper left) at the narrow exit passages of the Solomon Sea. CTD measurements and bottle samples were carried out using a rosette system (bottom) along the cruise track (photos: C. Germineaud and S. Cravatte).

Figure 2.3 – Pictures of the ship laboratory during MoorSPICE. Materials for measuring dissolved oxygen are shown in both left and middle panels. Salinity and other measurements such as phytoplankton pigments (right panel), were also carried out (photos: C. Germineaud).

2.3 Hydrographic data processing

The rosette system provides samples that were directly measured at sea in order to calibrate the CTD-O_2 sensors, and to collect samples for biogeochemistry analyses. Water sampling required a lot of care to avoid contamination or sample degradation, especially for oxygen as it could have been easily contaminated through gas exchanges, particulates or aerosols. Salinity and oxygen collected at discrete depths were analyzed at sea (Figure 2.3) along with a basic quality assessment of the data. A first check was the comparison between CTD-O_2 and bottle measurements for each cast, which was also a first approach to identify potential CTD sensor drifts over time. Ideally, the nutrient samples should be analyzed onboard to avoid any possible biological growth or decay, as during Pandora cruise, but they were in practice pasteurized and carefully stored during MoorSPICE for later analyses in laboratory.

After both expeditions, CTD-O_2 records were compiled and corrected from sensor time drifts while bottle measurements were gathered into a separate file by the technical team. Both data sets required a meticulous quality control, where full-depth profiles for the different casts and parameters were visually inspected, and flagged using IGOSS[2] quality code schemes. A specific calibration was carried out for oxygen data by the scientific and technical teams, following the GO-SHIP procedure.

Outliers were carefully examined from inter-comparisons between different parameters, and turned to be rather simple key entry errors or unusual anomalies related with several properties (e.g. phosphate or nitrate and oxygen). Temperature, salinity, and oxygen profiles are then filtered using a 5-m median to remove spikes. Vertical hydrographic sections were plotted to provide a spatial perspective of the data from both cruises, as shown as an example for oxygen across the southern entrance of the Solomon Sea (Figure 2.4). By scanning through the different parameters, we could have profitably explored both cruise data sets and identified apparent water characteristics.

[2]Integrated Global Ocean Services System

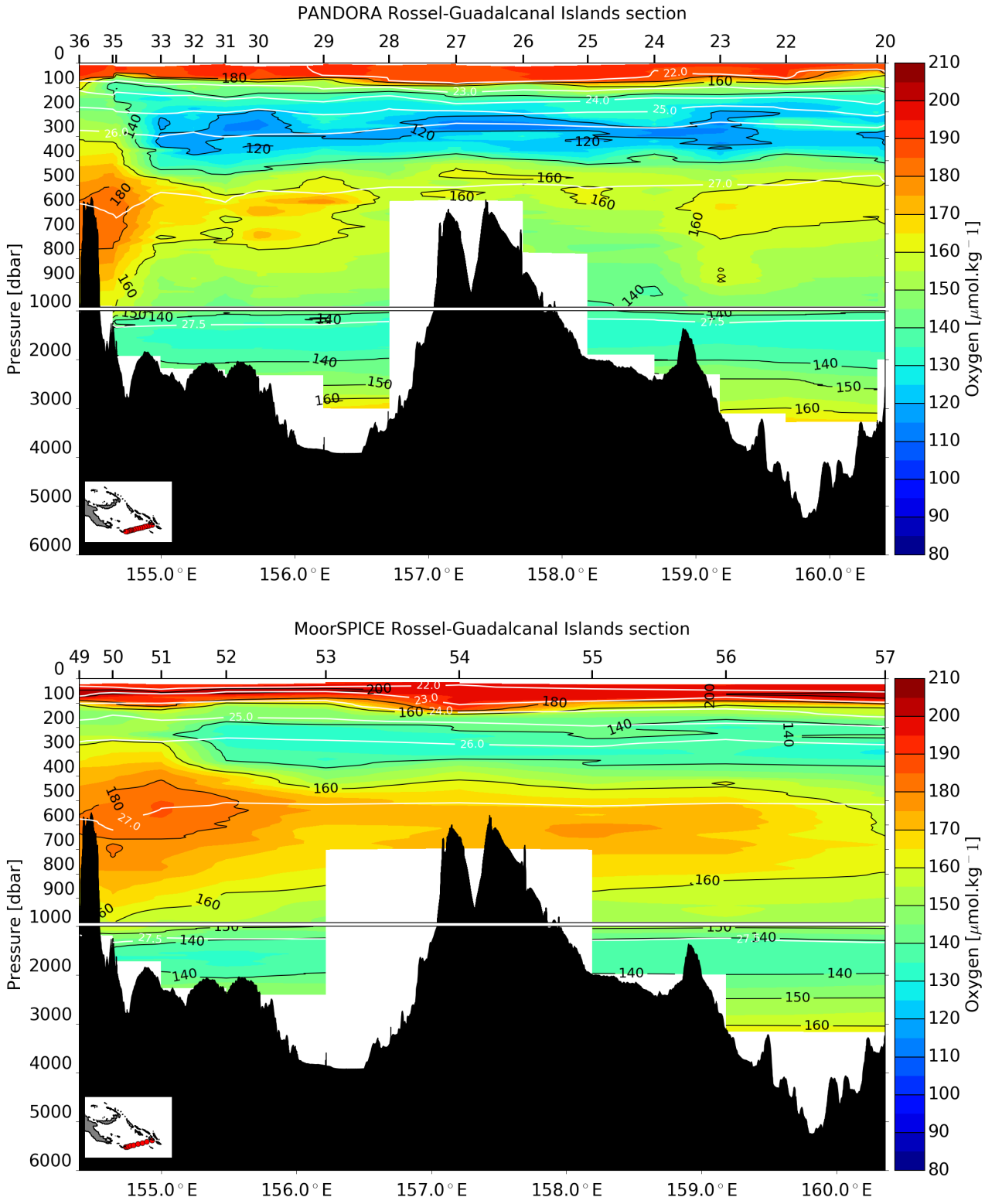

Figure 2.4 – Dissolved oxygen concentration (color scale) across the southern entrance of the Solomon Sea during (upper) Pandora cruise in July-August 2012 and (lower) MoorSPICE cruise in March 2014.

2.4 Velocity data processing

Currents recorded with two S-ADCPs and the pair of L-ADCPs on station were processed and quality controlled by the scientific team, using the standard CODAS[3] processing. Each S-ADCP instrument needed to be processed independently following several calibration steps to build a data set of averaged (every 10-min) and edited ocean velocities for each ping[4] profile (*Hummon and Firing*, 2003). These single-ping data included axial velocity components for each beam[5] that were transformed to Cartesian coordinates using corrected gyro headings. The pair of L-ADCPs were processed following *Visbeck* (2002) method, where relative velocity profiles are primarily obtained by integrating vertical shear profiles along each cast. Absolute velocities are then estimated using a least-squares framework, including constraints on bottom velocity estimates from bottom-track pulses, navigational data and upper ocean velocities from S-ADCP measurements.

Both hydrographic and ADCP velocity data were used within an inverse box model to depict a mean state of the oceanic circulation, including quantitative transport estimates and associated errors. We arranged two different configurations for each cruise along hydrographic transects that form a closed box to ensure basic conservation requirements. The following section provides inside information about inverse methods, while Section 2.5.3 gives some insight of the two model configurations.

2.5 The Inverse Box Model: how does it works?

Linear inverse box methods applied to hydrographic measurements were first introduced by *Wunsch* (1978) to estimate ocean circulation and associated transports within a finite ocean volume, divided in different layers from the surface to the bottom (Figure 2.4), and usually chosen to encompass major water masses. The classical procedure (e.g. *Wunsch et al.*, 1983; *Ganachaud et al.*, 2000; *Macdonald et al.*, 2009) uses pairs of temperature and salinity profiles along hydrographic transects to calculate an initial guess of geostrophic flow relative to a given reference level (2.1), along with a priori velocity uncertainties, which are usually obtained from current meters. One can then use an inverse method to estimate an adjusted velocity field and corresponding uncertainties to depict a more synoptic representation of the ocean circulation than the one inferred from the initial velocity snapshots. Moreover, the inverse box models allow the determination of a circulation that conserves mass and other properties (e.g. heat content, salt or silica) within individual layers. The model allows advective and diffusive exchanges between layers, referred as diapycnal fluxes.

2.5.1 Background: the model theory

To determine an initial velocities from discrete temperature and salinity measurements over the water column, the circulation is assumed to be in geostrophic balance as a good approximation. The velocity field is then calculated from by integrating the thermal wind equation,

$$v_{abs}(x,z) = v_{rel}(x,z) + b(x) = -\frac{g}{\rho f}\int_{z_0(x)}^{z} \frac{\partial \rho}{\partial x} dz + b(x) \tag{2.1}$$

[3]Common Ocean Data Access System database developed in the late 1980s

[4]sound pulse generated by the transducer for a single measurement cycle

[5]main lobe of energy generated by a transducer spreading as an acoustic wave front

where z is the vertical coordinate, x is the horizontal coordinate along the section, $z_0(x)$ is an arbitrary reference depth, $v_{rel}(x,z)$ is the thermal wind relative to $z_0(x)$ computed at station pair, $b(x)$ is the unknown reference velocity at $z_0(x)$. g is the local gravitational acceleration, ρ is the in situ density at station from hydrographic measurements and f the Coriolis parameter.

The reference depth $z_0(x)$ is specified at each station pair according to an optimal guess of $b(x)$, that is in practice, estimated from deep current meters or L-ADCP profiles. Classically, the reference depth is chosen at which b is expected to be minimal (*Ganachaud*, 2003a). The inverse box model provides an adjustment of this initial guess of $b(x)$, referred as $\tilde{\mathbf{b}}$, along with its error covariance matrix $\mathbf{P}$. This estimated solution satisfies the different constraints on the circulation, such than those on mass, heat or salt conservation, and the a priori variance of b. Steady state mass conservation (i.e. continuity) is commonly written as

$$\nabla \cdot (\rho \mathbf{v}) = FW + \Delta T_{Ek}, \tag{2.2}$$

and a tracer conservation, such as heat or salt, may be written as

$$\nabla \cdot (\rho C \mathbf{v}) = \nabla \cdot \kappa \nabla (\rho C) + Q + \Delta (C T_{Ek}), \tag{2.3}$$

where $\mathbf{v}$ is the three-dimensional velocity vector, FW is the net freshwater flux across the area (set to zero as, in the Solomon Sea, the net FW fluxes are much lower than conservation uncertainties), C is the tracer concentration per unit of mass, κ is the eddy diffusion tensor and Q is a source or sink term. In addition, the inverse box model provides an estimate of the Ekman transport T_{Ek}^{esti} from an initial Ekman transport (T_{Ek}^{init}), calculated from satellite winds or climatology, along with its a priori uncertainty (ΔT_{Ek}):

$$T_{abs}^{esti} = T_{Ek}^{init} + \Delta T_{Ek} \tag{2.4}$$

with

$$T_{Ek}(x,t) = -\rho \frac{\tau^x(x,t)}{f} \tag{2.5}$$

where $T_{Ek}(x,t)$ is the meridional Ekman transport and $\tau^x(x,t)$ is the zonal wind stress over time (t).

The different equations use to set up the inverse box model are rearranged into a single matrix equation

$$\mathbf{A}\mathbf{x} + \mathbf{n} = \mathbf{y} \tag{2.6}$$

where $\mathbf{A}$ is the inversion matrix (M X N matrix with M, the number of equations, N the number of unknowns), $\mathbf{x}$ is a column vector containing the unknowns b at each station pair and other parameters (e.g. diapycnal terms, adjustments to Ekman transport), $\mathbf{n}$ is the noise vector and $\mathbf{y}$ is the vector containing the observations.

Solutions and uncertainties estimated through inversion by linear approximation methods are described in (*Wunsch*, 1996). In this thesis, we used the well-known Gauss-Markov estimator (*Wunsch*, 1996, page 184), a particular case of the ordinary least squares method.

2.5.2 The Gauss-Markov estimator

The solution, $\tilde{\mathbf{x}}$ is estimated, such as the expectation $\mathbf{E} = \left\langle (\tilde{\mathbf{x}} - \mathbf{x}_{True}) \right\rangle$ is minimized (the $\langle\rangle$ operator stands for ensemble average). A priori knowledge of the size of the solution, $\tilde{\mathbf{x}}$ is $\mathbf{R_{xx}} = \langle \mathbf{x}\mathbf{x}^{\mathbf{T}} \rangle$, while $\mathbf{R_{nn}} = \langle \mathbf{n}\mathbf{n}^{\mathbf{T}} \rangle$ denotes the a priori noise related with the different conservation equations. A condensed linear combination of $\tilde{\mathbf{x}}$ is given by

$$\tilde{\mathbf{x}} = \mathbf{K}\mathbf{y} \tag{2.7}$$

$$with \quad \mathbf{K} = \mathbf{R_{xx}}\mathbf{A}^{\mathbf{T}}(\mathbf{A}\mathbf{R_{xx}}\mathbf{A}^{\mathbf{T}} + \mathbf{R_{xx}})^{-}\mathbf{1} \tag{2.8}$$

where (2.7) is referred as the Best Linear Unbiased Estimator (BLUE) if there is no bias (i.e. $\left\langle (\tilde{\mathbf{x}} - \mathbf{x}_{True}) \right\rangle = 0$).

The associated error covariance may be written as

$$\mathbf{P} = \left\langle (\tilde{\mathbf{x}} - \mathbf{x}_{True})(\tilde{\mathbf{x}} - \mathbf{x}_{True})^{\mathbf{T}} \right\rangle = \mathbf{R_{xx}} - \mathbf{K}\mathbf{A}\mathbf{R_{xx}} \tag{2.9}$$

The error estimate takes into account the part of the solution that is not resolved by the matrix equation (i.e. the null-space). The residuals and uncertainties are determined from (2.6). After inversion, particular attention was given to the residuals, as they are required to be indistinguishable from zero within a two standard deviation uncertainty (*Wunsch*, 1996). A priori uncertainties associated with $\mathbf{R_{xx}}$ and $\mathbf{R_{nn}}$ are determined as suggested by an investigation of the error budget of inverse box models (*Ganachaud*, 2003a), and a priori knowledge of the circulation in the region of study (e.g. in the Coral Sea, *Ganachaud et al.*, 2008; *Gasparin et al.*, 2012).

2.5.3 Inversions in the Solomon Sea

As briefly introduced, the circulation in the Solomon Sea is suggested to be dominated by other processes than geostrophic flow, especially at the narrow northern passages where strong internal wave activity is identified. To depict detailed pictures of LLWBC route across the sea over the upper 1000 m, we set up a "*shallow*" model configuration based on S-ADCP velocity transects as a first guess, rather than geostrophic flow derived from hydrographic measurements. Complete details regarding this inversion study are presented in Chapter 4, as part of a scientific article published in Journal of Physical Oceanography.

To assess the circulation below 1000 m, a "*deep*" configuration is designed from three hydrographic transects that form a closed box (see Chapter 5). A first attempt was to use a merged velocity field based on S-ADCP velocity in surface layers and L-ADCP profiles where the S-ADCP depth range is limited. However, for the transect closing the southern entrance of the box, large uncertainties in bottom track velocity estimates from the L-ADCP led to spurious strong velocities (>10 $cm.s^{-1}$) at the deepest measurements (most to 3000 m).

We built for this purpose, another merged velocity field that includes S-ADCP for the upper layers and geostrophic velocities below 1000 m. Chapter 5 provides more details about this *deep*" configuration, including an unprecedented description of the deep flow in the Solomon Sea region.

2.5.4 The standard solution

For the "shallow" and "deep" configurations, mass, heat, salt and silica conservation constraints (Table 2.1) were applied over evenly spaced isopycnal layers (Figure 2.5) from the surface to 1000 m (see Chapter 4) and from the surface down to ∼3200 m (see Chapter 5). All constraints were met within uncertainties, and both selected solutions appears to be statistically and dynamically acceptable.

Table 2.1 – Conservation constraints for the standard solution for both inverse configurations.

	Top to bottom	Individual layers
Mass	yes	yes
Heat	no	below surface
Salinity	yes	yes
Silica	yes	no

A number of solutions were explored by changing the model configurations to conserve the tracer combination, "PO" ($170PO_4 + O_2$; *Anderson and Sarmiento* (1994)) or "NO" ($9.1NO_3 + O_2$; *Broecker* (1974)). "PO" and "NO" equations are typically used to correct the oxygen concentrations for the influence of biological processes ("biological pump"), and to only reflect air-sea exchanges ("solubility pump"). In both configurations, we tried to conserve "PO" or "NO" below the surface layers (non conservative at the surface because of oxygen exchanges with the atmosphere). However, we obtained unrealistic negative oxygen utilization rates (OUR) that would imply a net production of oxygen. We could not find a suitable explanation to this issue that warrants further investigation, although it might be related with an inappropriate representation of biology by the tracer combination equations, or unaccounted physical processes within the inverse model.

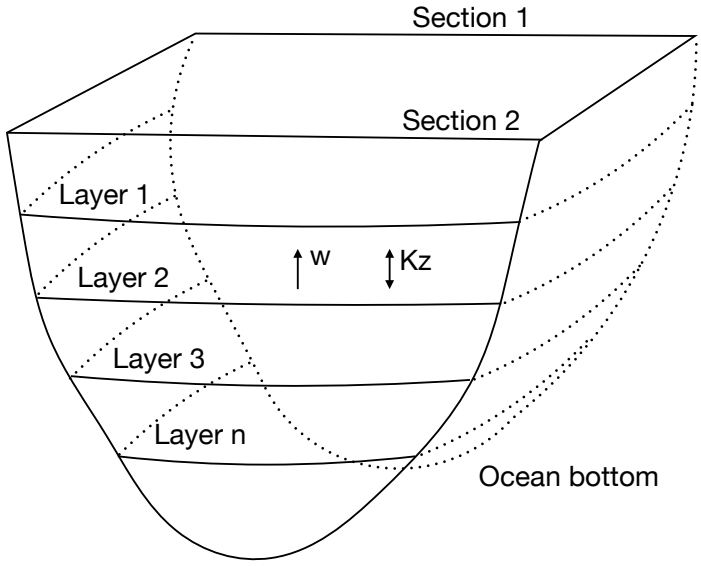

Figure 2.5 – Schematic of the inverse model structure. The velocity field is estimated so that conservation requirements are met within isopycnal layers. Advective (w) and diffusive (κ_z) exchanges are allowed between layers.

Chapter 3

Regional Context and Mean Surface Circulation during July-August 2012 and March 2014

Contents

3.1 Introduction

This chapter aims at giving a broader regional context to the Pandora and MoorSPICE cruises, using satellite-derived products and in situ observations collected during both cruises along hydrographic transects. The two cruises were undertaken in July-August 2012 and March 2014, coinciding with the two extrema of the trade seasons. Significant variations in sea surface properties, near-surface currents and mesoscale activity are expected between both cruises, and will be analyzed after presenting the climatic context associated with the two SPICE cruises.

3.2 Presentation of the datasets

The data used in this chapter combine different types of measurements, including sea surface temperature and salinity data, wind speed records, Outgoing Longwave Radiation (OLR) data, and near-surface currents from satellite altimetry.

3.2.1 Sea surface temperature and salinity products

The Operational Sea Surface Temperature and Sea Ice Analysis (OSTIA; *Donlon et al.*, 2012) provides on daily basis a global high resolution SST at a spatial resolution of 1/20°, combining satellite and in situ SST from the Group for High Resolution SST (GHRSST) and Global Telecommunications System (GTS), respectively. The SST from OSTIA is obtained through an optimal interpolation specifically designed for ocean forecasting purposes, and undergoes continuous monitoring and quality control to be operationally integrated in numerical weather predictions. Sea Surface Salinity (SSS) is investigated through the "L4aSSS In situ Match-up products" generated by the Centre d'Expertise Ifremer du CATDS-Ocean Salinity (CECI-OS). They combine satellite data from the SMOS Level 4 SSS products and a match-up database based on quality controlled in situ measurements from ARGO floats, ship Thermosalinograph (TSG), surface drifters, tropical moorings and sea seals data provided by the CORIOLIS, GOSUD, SAMOS and LOCEAN data centers. The L4aSSS products are weekly composites at a spatial resolution of 0.5° x 0.5° from May 2010 to December 2014. Despite a good data coverage over the northwestern part of the Coral Sea, only scarce or no data is available in the less accessible Solomon Sea. Along track direct SST measurements from the hull recorded during both cruises are used, as well as along track SSS records from the ship TSG. A Gaussian filter is applied to remove artifact gradients in both SST and SSS induced by the non-moving ship on station.

3.2.2 Meteorological products

The satellite Advanced Scatterometer (ASCAT) winds at a spatial resolution of 0.25° x 0.25° are temporally averaged during July-August 2012 and March 2014. Along track in situ winds recorded at 10 m during both Pandora and MoorSPICE cruises, are averaged every hour. The Outgoing Longwave Radiation satellite product from the National Oceanic and Atmospheric Administration (NOAA) provides two gridded estimates at 2.5° lateral resolution per day (i.e. daytime and nighttime orbits) (*Liebmann*, 1996; *Lee*, 2014). After a basic quality control, a temporal 1-day interpolation is completed for both daytime and nighttime grids. Then, missing data are spatially interpolated with a nearest neighbor method.

3.2.3 Surface currents products

We primary investigated mean velocity fields during each cruise using the altimetric Geostrophic and Ekman Current Observatory (GEKCO) surface currents (*Sudre et al.*, 2013), with a spatial resolution of 0.25° x 0.25°, to identify the contributions of both Geostrophic and Ekman components. In the Solomon Sea region, the mean surface currents attributed to Ekman were found to be negligible during both cruises, and during the 6-year period from 2007 to 2013. In addition, we found significant discrepancies near the equator, at the narrow straits and along the NGCU pathways in the Solomon Sea. We thus decided to examine the typical AVISO-DUACS velocity field, which only includes a geostrophic component, for each cruise period. However, we recognized similar discrepancies, probably attributed to the difficulty of getting geostrophic current in coastal areas from altimetric observations, leading to a poor representation of the western boundary currents within the mean velocity field averaged over 1993 through January 2016. In order to overcome this difficulty and depict a better picture of the mean surface currents, we decided to use instead, the annual mean near-surface currents (1979 through March 2015) from the satellite-tracked drifters of the Global Drifter Program (GDP; *Lumpkin and Johnson*, 2013).

My approach was first to use the mean near-surface geostrophic velocity anomalies, derived from the AVISO-DUACS mean sea surface height (SSH) anomalies, to extract the surface circulation variability during July-August 2012 and March 2014. The data anomaly compiles along-track measurements from several altimeter missions, on a 0.25° x 0.25° latitude-longitude grid with a 7-day temporal resolution (*Ducet et al.*, 2000). As a next step, I interpolated the drifter annual mean velocities (spatial resolution of 0.5° x 0.5°) on the same grid than the AVISO-DUACS velocity anomalies. I finally combined both data set to obtain mean surface current estimates. A similar operation was conducted with the GEKCO product, resulting in comparable mean surface currents, and so are not shown.

3.3 Results

Most of the results presented in this section have been submitted for publication (*Ganachaud et al.*, 2016) as part of a background study that provides an overview of the climatic context and different measurements carried out during both SPICE cruises (Appendix F). I specifically contributed to the climatic context section by providing the Niño3.4 SST anomaly index timeseries, satellite SST, SSS, winds and OLR mean distributions during each cruise. I also examined the along-track sea surface temperature, salinity and wind patterns, as well as the mean sea surface currents in two dedicated subsections. Finally, I presented an overview of the main water masses encountered in the region, as well as an atlas of water property sections available in supplemental material (not shown).

3.3.1 Climatic regional context

In July-August 2012, strong southeasterly trade winds are observed over the Solomon Sea (Figure 3.2a), corresponding to the height of the dry southeast trade season. Pandora coincides with a neutral phase of the ENSO cycle following the 2011 La Niña event and the associated cooling phase (Figure 3.1).

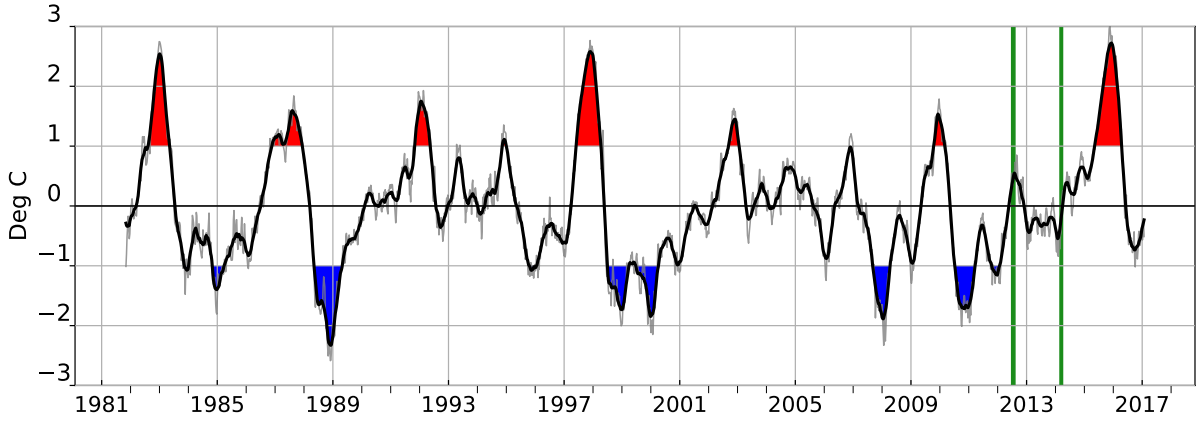

Figure 3.1 – The Niño3.4 SST anomaly index from 1982 through January 2017 (grey line); overlaid by a 3-month moving average (black line), where red and blue shading indicate El Niño (Niño3.4 anomalies greater than +1) and La Niñas (Niño3.4 anomalies less than -1), respectively. Green lines indicate the dates of the Pandora (July-August 2012) and MoorSPICE (March 2014) cruises.

Warm and salty waters (T >29°C; S >34.5) are found in the tropics (Figure 3.2a,c), where highest SSTs are mostly confined in the Bismarck Sea and the tropics (2°-4°S), potentially transported by the expected strong eastward branch of the SEC that flows along the equatorial band. The Gulf of Papua is dominated by cooler and much saltier waters, likely originating from the South Pacific subtropical gyre. The freshest waters are found north of the Solomon Sea about 2°N where data is available, and along the equator. Conversely, the winds are much weaker in March 2014, as expected by the seasonal trade reversal (Figure 3.2b), where the winds become northwesterly northeast of the Solomon Islands and northwest of Vitiaz Strait. The warmest and salty waters are found northeast of the Solomon Islands, with similar high SSTs observed within the Solomon Sea. This is probably due to a surface inflow across the Solomon Strait, where the winds are the weakest. SST is largely above 28°C in the whole region, even in the Coral Sea which was cooler in July-August 2012. These warm SSTs in March 2014 are related with the onset of the aborted 2014 El Niño, induced by weaker ocean-atmosphere interactions than during typical El Niño years (*McPhaden*, 2015).

The Solomon Sea is usually a region of high interannual variability, where large wind stress anomalies develop in the western and central tropical Pacific a few months after the peak of ENSO (e.g. *Melet et al.*, 2013; *Kessler and Cravatte*, 2013a). These anomalies produce strong interannual sea level anomalies (SLAs) that are closely related to migrations of the SPCZ (northeastward during El Niño and southwestward during La Niñas). The oceanic circulation is strongly impacted by the large-scale ENSO forcing, as shown by previous studies based on repeated glider transects (*Davis et al.*, 2012) and a numerical simulation (*Melet et al.*, 2013). Volume transports across the Solomon Sea vary in phase with ENSO (strengthened during El Niños and weakened during La Niñas), associated with large variations that can reach ∼100% of the mean. Transport partitions between the narrow exit straits of the Solomon Sea is also impacted by ENSO variability. The *Melet et al.* (2013) modeling study suggested that transports through Solomon Strait are enhanced during El Niño due to bathymetric constraints imposed by the narrowness of Vitiaz Strait.

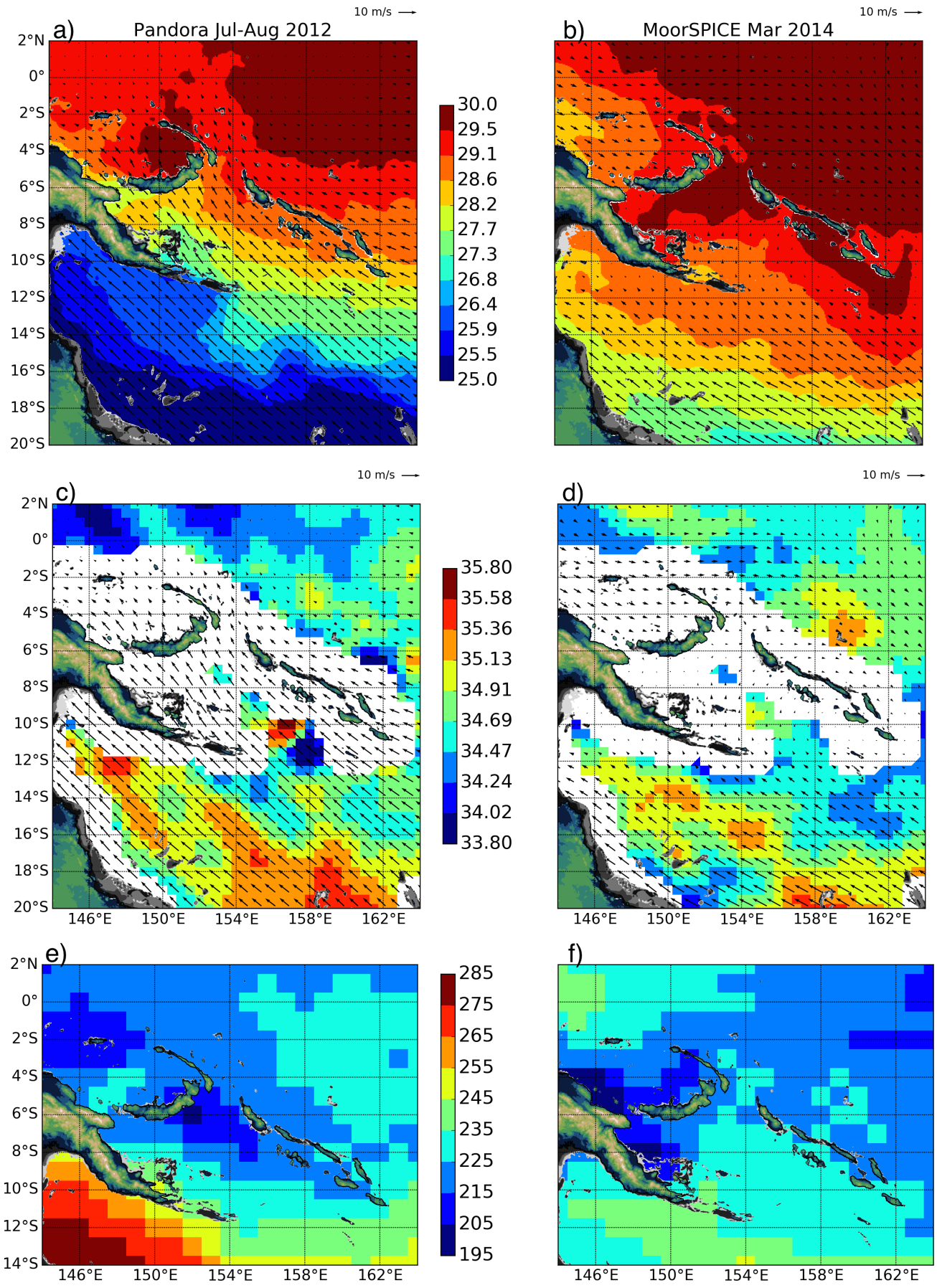

Figure 3.2 – (top panels) SST (°C) from OSTIA during (a) Pandora and (b) MoorSPICE cruises. (middle panels) SSS (pss-78) from the "L4aSSS In situ Match-up products" during (c) Pandora and (d) MoorSPICE cruises. Satellite wind vectors averaged during each cruise from ASCAT are overlaid. Note the unit vector in the upper right of the top panels. (bottom panels) daily gridded OLR ($W.m^{-2}$) averaged during (e) Pandora and (f) MoorSPICE cruises.

On intraseasonal time scale, the ocean-atmosphere interactions over the Solomon Sea are strongly influenced by the Madden-Julian Oscillation (MJO). This climate feature is characterized by interlinked atmospheric convection processes and winds patterns that can block solar radiations (*Madden and Julian*, 1972), inducing a cooling of the sea surface waters. The satellite-observed outgoing longwave radiation (OLR), which are a suitable proxy for deep convection and so cloud coverage, exhibit quite similar patterns between July-August 2012 and March 2014 (Figure 3.2e,f) with monthly-averaged values of around 205-245 W.m^{-2} over the region. Nevertheless, low OLR (i.e. cloudier) are detected northwest of Vitiaz Strait and south of New Ireland during Pandora, related with the seasonal cycle of convection over land. During MoorSPICE, we observe low OLR northeast of the Solomon Islands that likely correspond to the diagonal portion of the SPCZ, which is more pronounced during austral summer.

In order to assess the representativeness of the mean OLR distributions during the two cruises, we examined corresponding OLR anomalies (Figures 3.3a,b). During Pandora, cloudier regions are mostly found in the northern hemisphere (west of 170°E, 0°-20°N) and along the ITCZ axis (Figure 3.3a), which suggest a more expansive and convectively active cloud band over the western Pacific than typical July-August conditions. During MoorSPICE, cloudiness is higher than typical March conditions along the southeastward SPCZ axis (170°E-130°W; Figure 3.3b), suggesting a more intense and extensive SPCZ.

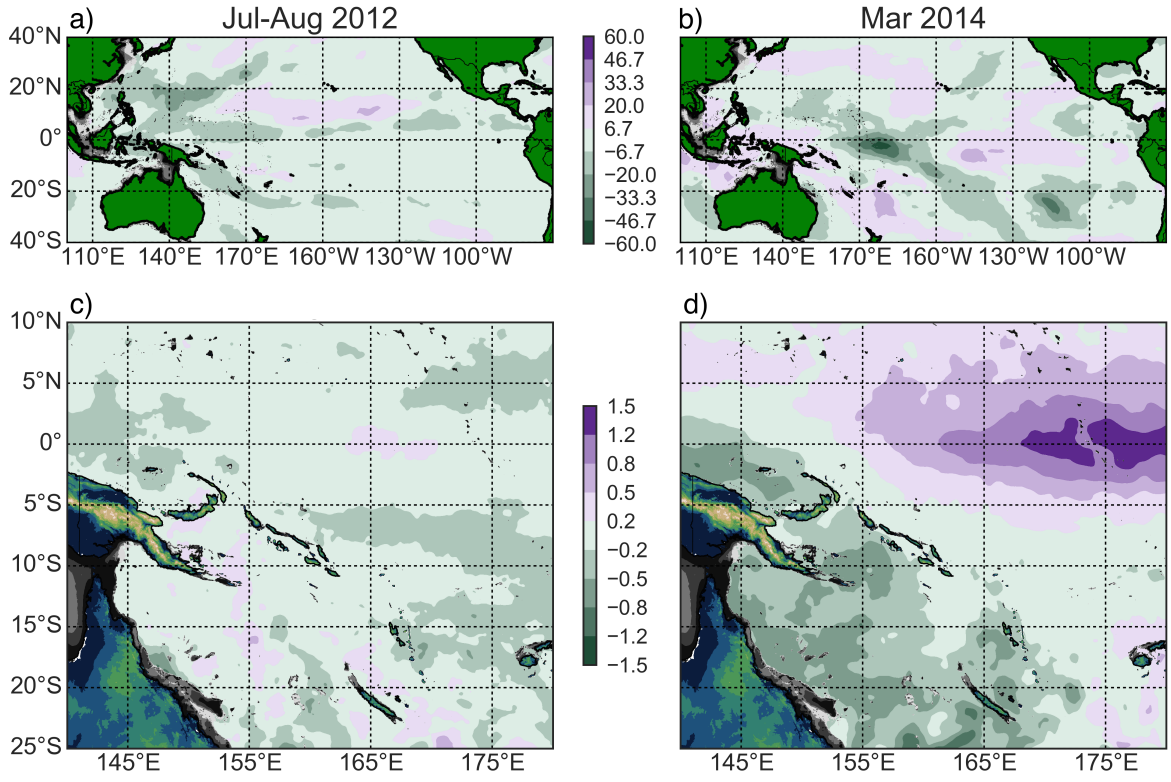

Figure 3.3 – Mean OLR anomalies (W.m^{-2}) during (a) July-August 2012 and (b) March 2014, minus the 1979-2014 climate average for July-August and March, respectively. Negative values (green shading) represent above normal cloudiness while positive values (purple shading) represent below normal cloudiness. Mean SST anomalies (°C) from OSTIA during (c) July-August 2012 and (d) March 2014, minus the 2007-2015 monthly average for July and March, respectively. Positive values (green shading) represent above normal SSTs while negative values (purple shading) represent below normal SSTs

The distributions of SST anomaly during the cruises (Figures 3.3c,d) were also examined to provide some insights into the physical processes that controlled the location, orientation and strength of both convergence zones. No major SST variations are seen during the Pandora cruise ($<$0.5°C), although lower temperature anomalies are found east of the Solomon Sea and northwest of Vitiaz Strait (Figure 3.3c). During MoorSPICE, it is seen that temperature anomalies (attributed to the 2014 El Niño that failed to materialize) are much higher in the equatorial Pacific region (east of 155°E), coinciding with the zonal portion of the SPCZ (Figure 3.3d), which is usually anchored to the warm SST from January to March (*Haffke and Magnusdottir*, 2013). However, the subtropical part of the SPCZ is less dependent on the underlying SST patterns and is more pronounced in November-December. Intraseasonal variability of the SPCZ (area, location and intensity) is associated with the different phases of the MJO (e.g. *Matthews*, 2012). The enhanced SPCZ activity progress eastward following the propagation of the MJO in the tropics, where the MJO can influence the different components of the SPCZ as far as 30°S (*Haffke and Magnusdottir*, 2013).

A seasonally independent index has been determined to monitor the MJO: the Wheeler and Hendon Index (*Wheeler and Hendon*, 2004). This index is based on the empirical orthogonal functions (EOFs) of near-equatorially averaged zonal winds at upper (200-hPa) and lower levels (850-hPa) of the atmosphere, and satellite OLR data. The MJO is defined as the leading pair of the multiple-variable EOFs after removing the annual cycle and longer time scale variability. In real time, projection of the daily wind fields and OLR data onto these two EOFs leads to principal component (PC) timeseries that vary on the intraseasonal time scale, and provide a measure of the location and strength of the MJO. To illustrate the progression of the MJO, *Wheeler and Hendon* (2004) defined a diagram that splits the MJO cycle into eight phases (Figure 3.4a,b). When the Wheeler and Hendon index is within the center circle, the MJO is considered weak whereas outside of this circle the index is stronger.

In July-August 2012, the MJO phase diagram suggests a weak active phase during July-August 2012 (Figure 3.4a) over the western Pacific (phases 6 and 7), while a much stronger phase of the MJO is only observed in late February 2014, just before MoorSPICE (Figure 3.4b). During both cruises, MJO is mostly active in the western hemisphere and Africa (phases 1 and 8), and over the Indian Ocean (phases 2 and 3), suggesting little influence of MJO and intraseasonal wind forcing on the upper ocean circulation and variability in the Solomon Sea region.

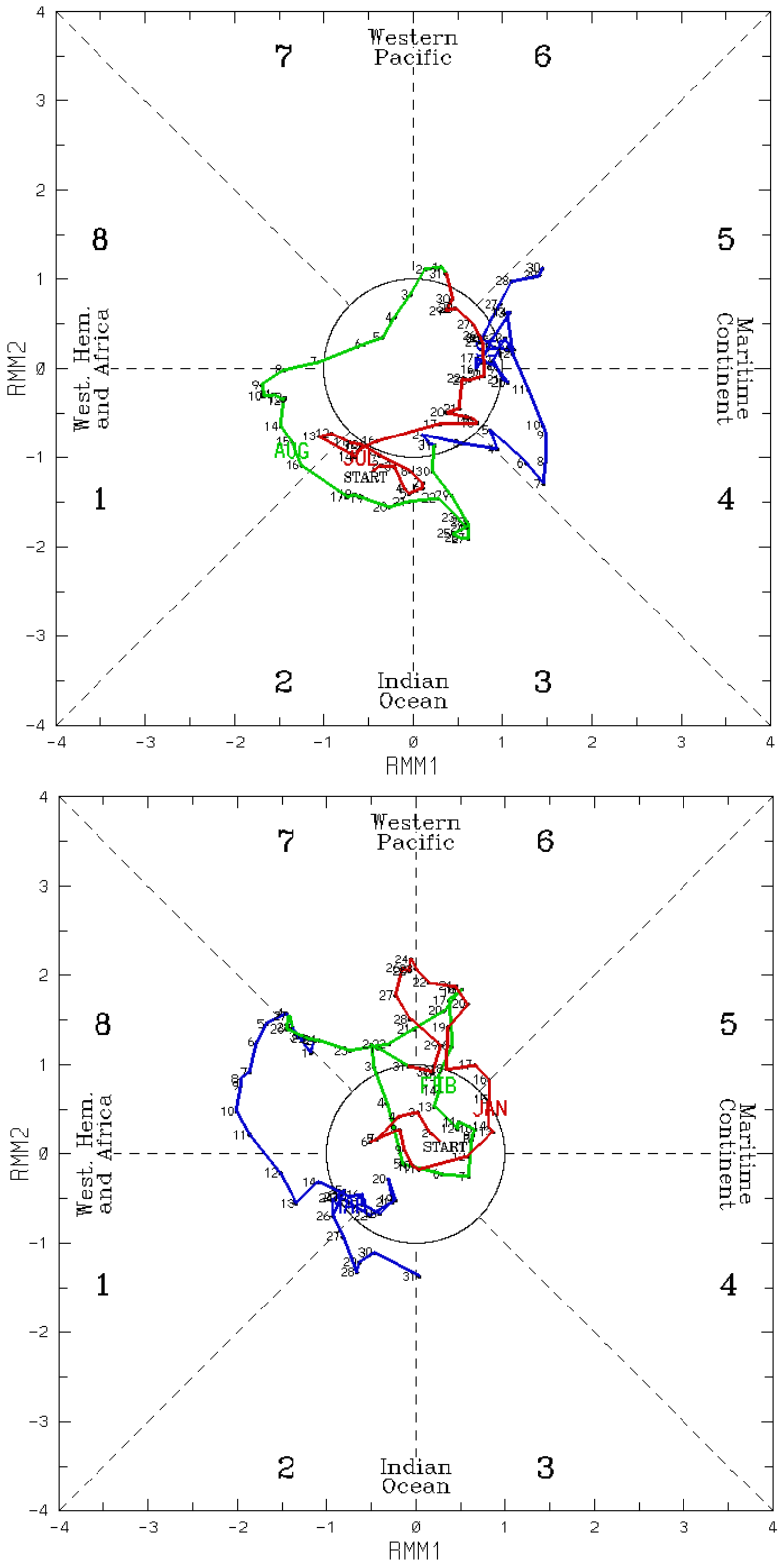

Figure 3.4 – Diagram of the MJO phases during (a) July-September 2012 and (b) January-March 2014. The Real-time Multivariate MJO series 1 (RMM1) and 2 (RMM2) are a pair of principal component (PC) time series that combine cloud amount and winds at upper (200-hPa) and lower levels (850-hPa) of the atmosphere. Note labeled dots for each day, while color corresponds to each month as indicated in diagrams (a) and (b). From the Bureau of Meteorology, Commonwealth of Australia.

3.3.2 Sea surface properties during the Pandora and MoorSPICE cruises

The sea surface conditions during both cruises are investigated using the along-track direct measurements of in situ winds, SSS and SST (Figure 3.5). During Pandora, we observe strong ($\sim$20 m.s^{-1}) and unidirectional winds oriented equatorward along the prevalent trade wind axis. During MoorSPICE, the winds are much weaker ($\sim$5 m.s^{-1}) along an identical axis, and are poleward to the north of 6°S and equatorward to the south of this latitude. In situ winds agree well with the mean satellite wind patterns during both cruises (see Figure 3.2), though they appear to be even weaker in March 2014.

Sea surface waters in the Solomon Sea appear to be saltier and colder during Pandora compared to MoorSPICE except northeast of Bougainville Island, where opposite patterns are observed. The in situ SSS is dominated by small scale gradients during Pandora, while during MoorSPICE salinity features were much more cohesive on a large scale, especially within the northern exit straits of the Solomon Sea. The in situ SST exhibits a stronger zonal cross-basin gradient during Pandora compared to MoorSPICE (Figure 3.5c,d), with lower temperature on the western part of the Solomon Sea. Similar patterns were found in the monthly mean satellite SST for both cruises (Figure 3.2a,b), and are found to be consistent with seasonal SST and SSS patterns described in *Delcroix et al.* (2014). These colder and saltier waters carried into the Solomon Sea during Pandora are consistent with northwestward advection impulsed by the strong equatorward winds.

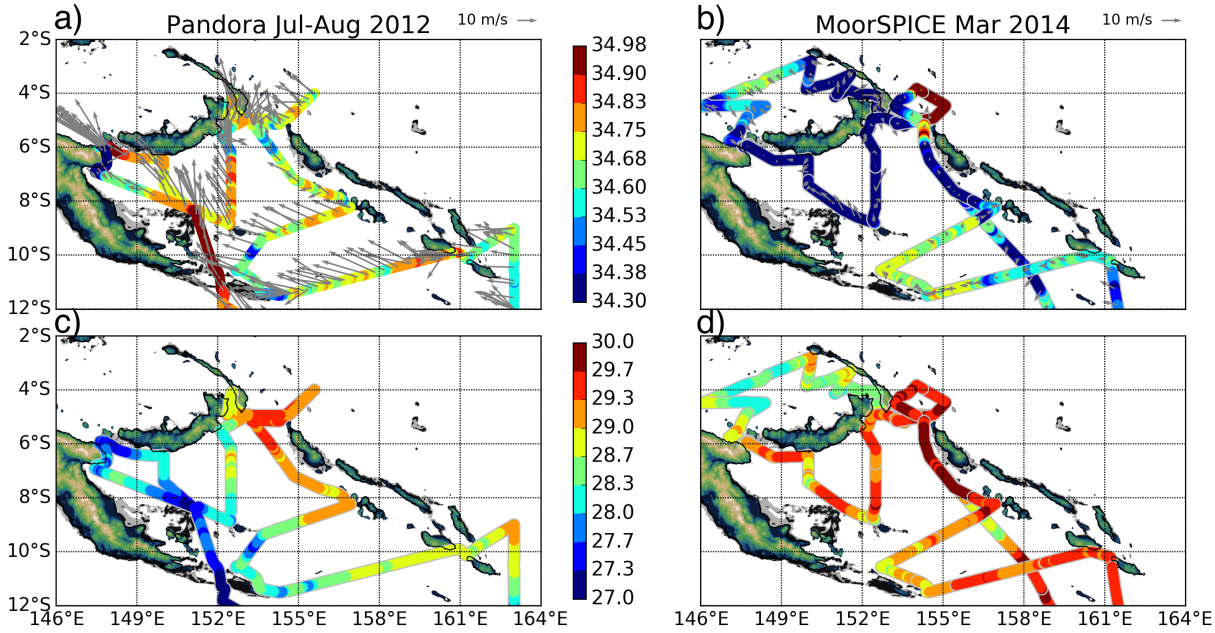

Figure 3.5 – Observed along-track sea surface salinity (color scale, pss-78) from the Thermosalinograph (TSG) and in situ winds during (a) Pandora (July-August 2012) and (b) MoorSPICE (March 2014) cruises. Along track sea surface temperature (color scale, °C) from the hull during (c) Pandora and (d) MoorSPICE. Note the unit vector in the upper right of the top panels.

3.3.3 Surface Mean currents during the Pandora and MoorSPICE cruises

Mean surface currents based on satellite velocity anomalies combined with the mean GDP drifter velocity field, suggest a surface circulation dominated by a northwestward flow in most of the Solomon Sea during July-August 2012 (Figure 3.6a). At Solomon Strait, a moderate surface flow into the sea is observed, which then bifurcates northwestward and exits through Vitiaz Strait with enhanced velocities ($\sim$50 cm.s^{-1}). At the southern entrance near 12°S, we observed a strong westward zonal NVJ emanating from the southern SEC branch. It feeds the New Guinea Coastal Current (NGCC) within the Solomon Sea, as it flows equatorward along the Papua New Guinea Coast before exiting through Vitiaz Strait.

However, the junction with the NGCC near the most southern tip of Papua New Guinea is not clearly identified, probably attributed to the lack of data near the coastlines in both drifters and altimetric SSH anomalies. We observed a southward flow in the eastern part of the basin and within the gaps of the Solomon Islands chain, that is deflected northwestward further south as it encounters the NVJ. East of the Solomon Islands (north of 6°S), a persistent cyclonic eddy is identified, whereas an anticyclonic feature is found at the mouth of Solomon Strait, as a northwestward current flows along the east coast of Bougainville Island (155°E, 6°S). In addition, an eastward current identified as a southern stream of the SEC, flows east of the Solomon Islands at 4°S while a westward flow is observed further south, near 8°S.

During March 2014, the surface circulation (Figure 3.6b) is reversed but much weaker across Vitiaz Strait, although a northwestward flow is recognized confined along Papua New Guinea (146°E, 4°S). The southward current through Solomon Strait is intensified, and seems to flow southward to feed the large cyclonic eddies at the southern entrance rather than turning westward towards Vitiaz Strait. East of Solomon Islands, the eastward SECC flows at 8°S, sandwiched by large propagating eddies centered at 6°S and 10°S. During both cruises, we also observe a persistent cyclonic circulation in the Gulf of Papua (12°S, 148°E), as the GPC turns northeastward and approaches the Papua New Guinea Coast.

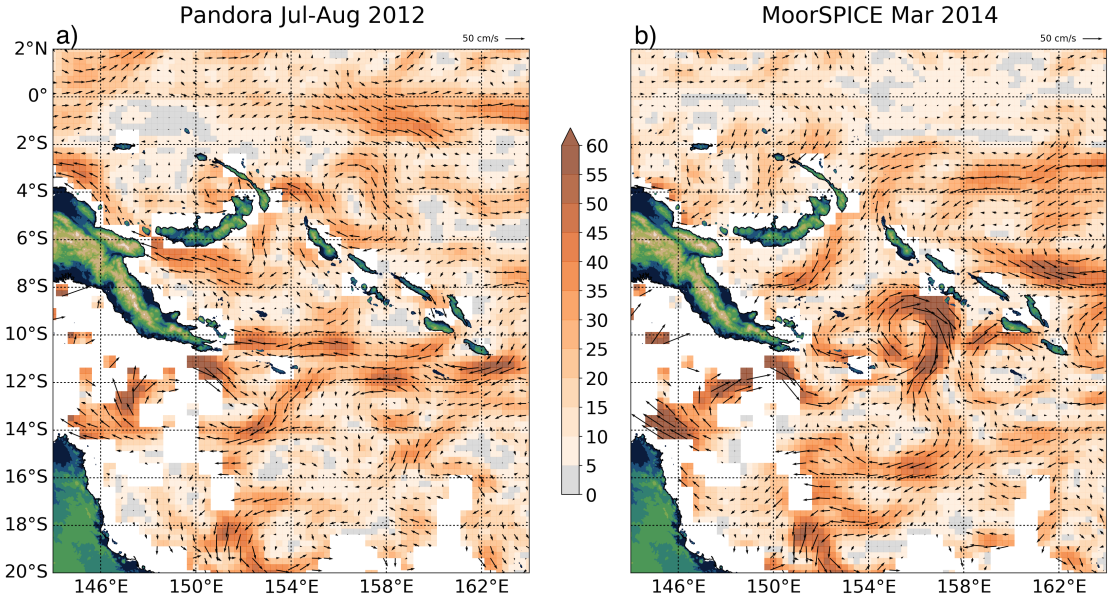

Figure 3.6 – Combined sea surface currents (color scale and black arrows, cm.s^{-1}) derived from the AVISO-DUACS mean geostrophic velocity anomalies during a) July-August 2012, b) March 2014 and the annual GDP drifter mean from 1979 through March 2015. Note the unit vector in the upper right of both panels.

Furthermore, previous studies identify the Solomon Sea as a region of high mesoscale activity, associated with strong variations at seasonal to interannual time scales (*Hristova and Kessler*, 2012; *Gourdeau et al.*, 2014). The location of maximum variability within the region also appears to change seasonally. During both cruises, the observed currents were generally strong, with many transient eddies that provide some evidence of high energy at submesoscale (∼10 km) and mesoscale (∼100 km).

3.3.4 Mean eddy kinetic energy during the Pandora and MoorSPICE cruises

As a measure of the mesoscale activity, the mean eddy kinetic energy (MEKE) was computed from the altimetric current anomalies through the classical formulation:

$$\mathbf{MEKE} = \frac{\mathbf{1}}{\mathbf{2}}(\overline{\mathbf{u'^2}} + \overline{\mathbf{v'^2}}) \tag{3.1}$$

where $\mathbf{u'}$ and $\mathbf{v'}$ denote the geostrophic current anomalies during both Pandora and MoorSPICE cruises.

During July-August 2012, the MEKE (Figure 3.7a) reaches high values (280-560 $cm^2.s^{-2}$) in the Solomon Sea basin, while the highest values (>700 $cm^2.s^{-2}$) are mostly located near 4°S at Solomon Strait and northeast of Solomon Islands, following the SEC pathway as suggested by previous MEKE estimates in the region (e.g. *Melet et al.*, 2010b; *Hristova and Kessler*, 2012). The NGCU route along Papua New Guinea appears to be associated with low MEKE values (<280 $cm^2.s^{-2}$) as well as further downstream within the Bismarck Sea, although high MEKE is observed at Vitiaz Strait.

During March 2014, the MEKE (Figure 3.7b) is much higher within the Solomon Sea, where values exceed 700 $cm^2.s^{-2}$ in the mid-basin and at the southern entrance. The highest MEKE levels (>1400 $cm^2.s^{-2}$) reflect the large and persistent cyclonic circulation near 10°S, 156°E. Outside the Solomon Sea, large MEKE is related with the westward flowing SECC at 8°S (also identified by *Qiu and Chen*, 2004), whereas moderate MEKE values are principally obtained along the SEC pathway, centered on 2°S. These MEKE estimates reveal significant differences in magnitude but also in the location of maximum variability between both cruises that agree well with *Hristova and Kessler* (2012). The authors identified large MEKE variability within the Solomon Sea during March-April where values can exceed 700 $cm^2.s^{-2}$.

More recent studies (*Gourdeau et al.*, 2014; *Hristova et al.*, 2014) identified a pronounced annual cycle of the mesoscale activity in the Solomon Sea, with maximum surface EKE in May-June and minimum ones near September. They found that cyclonic eddies are typically generated in the south basin of the Solomon Sea and then advected northward via the surface LLWBC system, while the anticyclonic eddies are less abundant (*Gourdeau et al.*, 2014). In addition, *Hristova et al.* (2014) identified seasonal fluctuations of "small scale" and "large scale" surface EKE, associated with a large number of small eddies (<80 km) in austral winter, whereas fewer but larger eddies are found in austral summer, with the largest in March. This annual cycle of surface eddies is consistent with the mesoscale variability observed during each cruise period, although the abundance of small scales in July-August 2012 is not clearly identified with altimetry because of strong detection limitations, and also because they might be related with unaccounted ageostrophic processes.

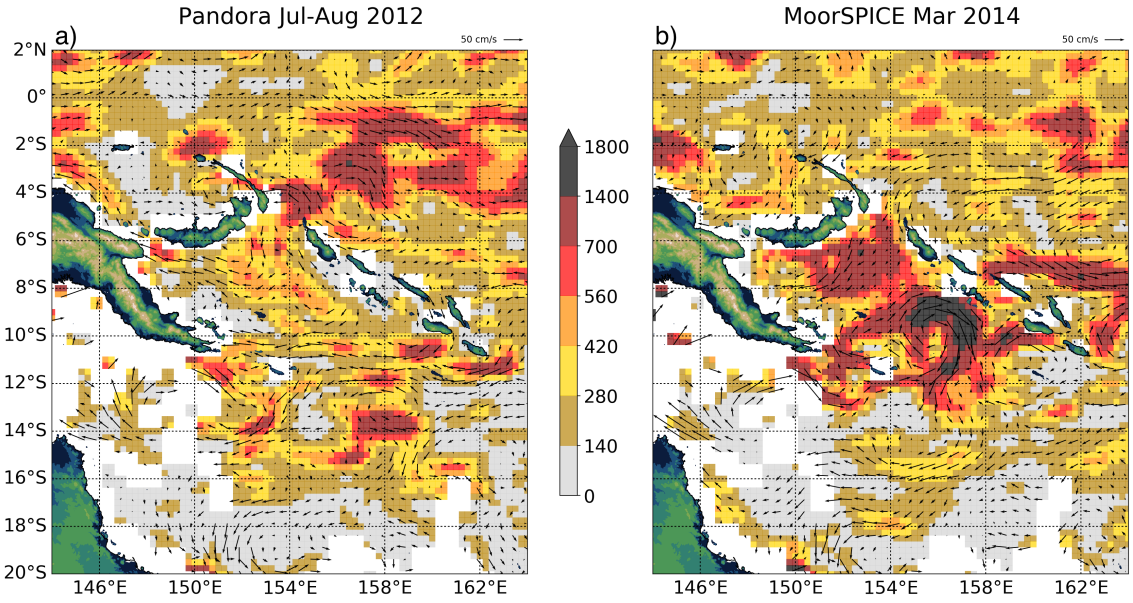

Figure 3.7 – Mean eddy kinetic energy (color scale, $cm^2.s^{-2}$) derived from the AVISO-DUACS mean geostrophic velocity anomalies and the annual GDP drifter mean from 1979 through March 2015 during a) July-August 2012 and b) March 2014. Black arrows indicate the combined sea surface currents averaged over each cruise period. Note the unit vector in the upper right of both panels.

These seasonal changes in eddy properties are potentially the consequence of surface instabilities during late winter when small mesoscale prevail, while the fewer large scale eddies are suggested to be generated from barotropic instabilities near the southern entrance of the Solomon Sea (*Hristova et al.*, 2014).

3.4 Conclusions

The Pandora and MoorSPICE cruises explored the Solomon Sea during two contrasted trade wind seasons: July-August 2012 (austral winter) and March 2014 (austral summer), respectively. Both cruises coincided with neutral ENSO conditions, and weak active phases of MJO over the Solomon Sea region. This suggests, that at least during the time of the cruises, intraseasonal wind forcing did not likely play a strong role in upper ocean variability or circulation, although atmospheric conditions appeared to be less variable during July-August 2012 than during March 2014. The observed differences in sea surface properties between the two cruises are likely driven by seasonal variability. During Pandora, cooler surface waters are observed within the Solomon Sea, associated with much stronger monsoonal winds compared with MoorSPICE, when sea surface temperature was largely above 29°C (coinciding with the onset of the aborted El Niño) and regional winds were extremely weak.

The surface circulation and cyclonic eddy activity are also largely influenced by seasonal variability. Despite strong limitations along the coastlines and between small Islands, our reconstructed geostrophic velocity field (annual mean from GDP drifter minus AVISO-DUACS surface current anomalies) and associated MEKE distributions are generally in good agreement with previous altimetric observations (*Melet et al.*, 2010b), historical S-ADCP measurements (*Cravatte et al.*, 2011) and drifters (*Hristova and Kessler*, 2012) during both austral winter and summer.

The July-August 2012 cruise is characterized by a strong and well defined equatorward NGCC that exits through Vitiaz Strait, associated with high surface EKE along the northern branch of the SEC, which is typical of the strong trade season (*Melet et al.*, 2010b; *Hristova and Kessler*, 2012). Conversely, during the March 2014 cruise, the NGCC is much weaker along its pathway within the sea and reverses at Vitiaz Strait, in addition to an intensified surface inflow through Solomon Strait. We observed different mean EKE distributions than those of July-August 2012, with high values within the Solomon Sea and along the SECC pathway. Similar patterns were typically found during the weak trade season (*Melet et al.*, 2010b; *Cravatte et al.*, 2011; *Hristova and Kessler*, 2012).

Moreover, some phase transitions between "small-scale" and "large-scale" eddies were also identified at seasonal time scales (*Hristova et al.*, 2014). Small mesoscale eddies (<80 km), mostly cyclonic, are numerous in late austral winter and larger but fewer in December-March. Consistent results are found in March 2014, where large mesoscale eddies (>150 km) propagate from the southern entrance to the interior Solomon Sea. The contribution of the small mesoscale eddies depicted in late austral winter is not represented in this analysis, as those scales are not well resolved by altimetry.

Chapter 4

Thermocline and Intermediate Circulation of the Solomon Sea

Contents

4.1 Introduction

In the first chapter, I introduced the Solomon Sea as a key element of the South Pacific circulation in connecting the subtropics to the equator through low-latitude western boundary currents, with potential effects on the western equatorial WWV and the EUC. Several studies based on limited observations (*Cravatte et al.*, 2011; *Hristova and Kessler*, 2012) and numerical simulations (*Melet et al.*, 2010a; *Djath et al.*, 2014) describe the circulation and associated current pathways from the surface down to the thermocline whereas the deeper circulation remains relatively unknown, and only based on scattered measurements from the pioneering WEPOCS cruises (*Lindstrom et al.*, 1987; *Butt and Lindstrom*, 1994) in the mid-1980s. Water properties in the Solomon Sea are also of major interest, as similar properties were found near the core of the EUC at σ_θ $\sim$25 (*Tsuchiya et al.*, 1989; *Fine et al.*, 1994), suggesting that waters emanating upstream from the Solomon Sea are the main source of the EUC. Consistent results were found in Lagrangian numerical studies (*Blanke and Raynaud*, 1997; *Grenier et al.*, 2011), and identified those waters as a major source of the EUC.

A model study tracing water masses across the Solomon Sea (*Melet et al.*, 2011) found significant transformations caused by intense vertical mixing along the LLWBC pathways, particularly at the thermocline level. Vertical gradients in salinity and temperature were eroded between the southern entrance and the northern exits of the Solomon Sea. However, only scarce in situ measurements were available before Pandora and MoorSPICE cruises to investigate the evolution of the water properties within the Solomon Sea.

4.2 Data and Methods

Our article provides a detailed study of the water mass circulation and associated properties across the Solomon Sea from the surface to 1000 m, during two contrasted seasons. As indicated in Chapter 2, we used an inverse box model to estimate a mean circulation at the cruise scale (roughly a month) and associated volume transports with uncertainties.

For this, a specific configuration of an inverse box model based on S-ADCP velocities has been set up rather than using geostrophic flow, as it is classically done. The reason is that strong internal wave activity is suspected within the Solomon Sea (*Melet et al.*, 2011; *Alberty et al.*, 2016), generating possible isopycnal displacements, and so biased geostrophic velocities. Furthermore, the circulation in the narrow straits of the Solomon Sea is probably dominated by ageostrophic currents that will not be taken into account through geostrophic calculation, but potentially captured via the along-track S-ADCP velocity profiles.

4.3 What is our article about?

Supplemental information related to this article is available in Appendix B.

Pathways and Water Mass Properties of the Thermocline and Intermediate Waters in the Solomon Sea

CYRIL GERMINEAUD AND ALEXANDRE GANACHAUD

Laboratoire d'Etudes en Géophysique et Océanographie Spatiales, Université de Toulouse, CNES, CNRS, IRD, UPS, Toulouse, France

JANET SPRINTALL

Scripps Institution of Oceanography, University of California, San Diego, La Jolla, California

SOPHIE CRAVATTE AND GÉRARD ELDIN

Laboratoire d'Etudes en Géophysique et Océanographie Spatiales, Université de Toulouse, CNES, CNRS, IRD, UPS, Toulouse, France

MARION S. ALBERTY

Scripps Institution of Oceanography, University of California, San Diego, La Jolla, California

EMILIEN PRIVAT

Laboratoire d'Etudes en Géophysique et Océanographie Spatiales, Université de Toulouse, CNES, CNRS, IRD, UPS, Toulouse, France

(Manuscript received 9 May 2016, in final form 15 July 2016)

ABSTRACT

The semienclosed Solomon Sea is the final passage in the equatorward transit of the South Pacific western boundary currents (WBCs) that play a key role in heat and mass budgets of the equatorial Pacific. The Solomon WBCs and their associated water properties are examined using data from two oceanographic cruises undertaken during the contrasting trade wind seasons: July 2012 and March 2014. The mean circulation and associated transports with uncertainties is determined from the cruise data using a unique configuration of an inverse box model formulated based on measured shipboard acoustic Doppler current profiler velocities. An intense inflow of 36 Sv is found entering the Solomon Sea in July–August 2012 that falls by 70% to 11 Sv in March 2014. Large differences are also found in the total transport partitioning through each of the major exit passages during each season. Different water masses are found in the WBC stream northeast of the Solomon Islands that are likely related to a northern stream of the South Equatorial Current. Within the Solomon Sea, isopycnal salinity gradients are gradually stronger than within the subtropical Pacific, likely induced by stronger diapycnal mixing processes. WBC pathways exhibit distinct water mass signatures in salinity, oxygen, and nutrients that can be traced across the Solomon Sea, associated with significant water mass modifications at the northern exit straits and south of the Woodlark Island.

Denotes Open Access content.

Supplemental information related to this paper is available at the Journals Online website: http://dx.doi.org/10.1175/JPO-D-16-0107.s1.

Corresponding author address: Cyril Germineaud, Laboratoire d'Etudes en Géophysique et Océanographie Spatiales, Université de Toulouse, 14 Avenue E. Belin, 31400 Toulouse, France.
E-mail: cyril.germineaud@legos.obs-mip.fr

DOI: 10.1175/JPO-D-16-0107.1

1. Introduction

The low-latitude western boundary currents (LLWBCs) of the southwest Pacific establish a major connection between the subtropics and the equator (McCreary and Lu 1994; Fine et al. 1994; Johnson and McPhaden 1999; Grenier et al. 2014). They cross the semienclosed Solomon Sea east of Papua New Guinea (PNG; Fig. 1a) before redistributing waters to the equatorial band, where LLWBCs are considered to be an important component of the equatorial Pacific water mass budget (Kleeman et al. 1999; Lee and Fukumori 2003). Any changes in mass transports or water mass properties from these LLWBCs could strongly affect the western Pacific with potential downstream effects on the eastern Pacific.

Within the CLIVAR Southwest Pacific Ocean Circulation and Climate Experiment (SPICE) program (Ganachaud et al. 2014), substantial efforts were carried out to understand the southwest Pacific ocean circulation and its influence on regional climate. The Solomon Sea was the focus of many studies, as it is the main pathway for the LLWBCs to reach the equator through a double system of currents (Melet et al. 2010a). At the northern exits of the sea, one stream flows through Vitiaz Strait (Fig. 1) to ultimately feed the Equatorial Undercurrent (EUC) or the equatorial current system, or the Indonesian Throughflow (ITF). Another stream exits the Solomon Strait (Fig. 1), providing a more direct connection with the equatorial region. Before SPICE, our knowledge of the circulation in the Solomon Sea was based on scattered in situ measurements from isolated ship transits. Recent modeling efforts (Melet et al. 2010a; Djath et al. 2014) and a 20-yr shipboard ADCP (S-ADCP) velocity climatology (Cravatte et al. 2011) provided a first description of the mean thermocline circulation and its seasonal variability across the Solomon Sea (Ganachaud et al. 2014).

To improve our understanding of the circulation in the Solomon Sea, two exploratory oceanographic cruises were undertaken during contrasted seasons through a France–U.S. collaboration as part of SPICE (Ganachaud et al. 2016, manuscript submitted to *Elementa*). The first cruise, named Pandora (27 June to 6 August 2012, R/V *L'Atalante*), combined physics, geochemistry, and biogeochemistry to explore the region (Fig. 1a). The second cruise, named MoorSPICE (28 February to 31 March 2014, R/V *Thomas G. Thompson*), focused on physics and biogeochemistry, partly repeated the July–August hydrographic sections and also carried out measurements in the Bismarck Sea, northwest of the Solomon Sea (Fig. 1b). The July–August 2012 cruise corresponded to the strong trade season whereas the March 2014 cruise was during weak trade season (Fig. 1c). Both cruises were related with neutral phases of ENSO, as suggested by the near-zero Southern Oscillation index (SOI) values (red line, Fig. 1c).

In this study, we examine water mass pathways and properties in the Solomon Sea from hydrographic data collected during these two cruises. We use an inverse box model set up with S-ADCP velocities to infer a mean circulation during each cruise and to provide realistic transport estimates with a near-closed mass budget. The main questions addressed in this paper are 1) how do observed currents and associated water masses evolve within the Solomon Sea during the opposing strong and weak trades, 2) how typical were the currents with respect to climatology during July–August 2012 and March 2014, and 3) what are the transport partitions between the entrance and the exits of the Solomon Sea during both cruises?

To place this study into context, section 2 provides a detailed background on the current pathways and water properties feeding the Solomon Sea. The cruise data and climatological datasets are presented in section 3 along with the inverse box model description. Monthly climatologies show water masses around the Solomon Sea in section 4a, while water mass properties inside the Solomon Sea are described from the cruise data in section 4b. Current pathways and associated volume transports are shown for both cruises in section 5, and changes in water properties within the Solomon Sea are described in section 6. A summary and a discussion of our results are presented in section 7, followed by some perspectives.

2. Background: Currents and water masses feeding the Solomon Sea

Many studies describe the mean circulation in the Coral Sea (Sokolov and Rintoul 2000; Qu and Lindstrom 2002; Kessler and Cravatte 2013b) and Solomon Sea (Melet et al. 2010a; Cravatte et al. 2011). At thermocline level, the southwest Pacific LLWBCs (Fig. 1a) are fed by the westward zonal South Equatorial Current (SEC). One stream of the SEC bifurcates at the Australian coast into the northward-flowing Gulf of Papua Current (GPC) to feed the New Guinea Coastal Undercurrent (NGCU), with a maximum velocity core at $\sigma_\theta \sim 26.5$. Another stream of the SEC feeds directly into the North Vanuatu Jet (NVJ) and the NGCU as it flows equatorward inside the Solomon Sea. South of Woodlark Island (Fig. 1a), the NGCU splits into two branches that then remerge north of the archipelago, to then bifurcate again into two branches south of New Britain (Fig. 1a). The westward branch flows equatorward through the Vitiaz Strait while the eastward branch

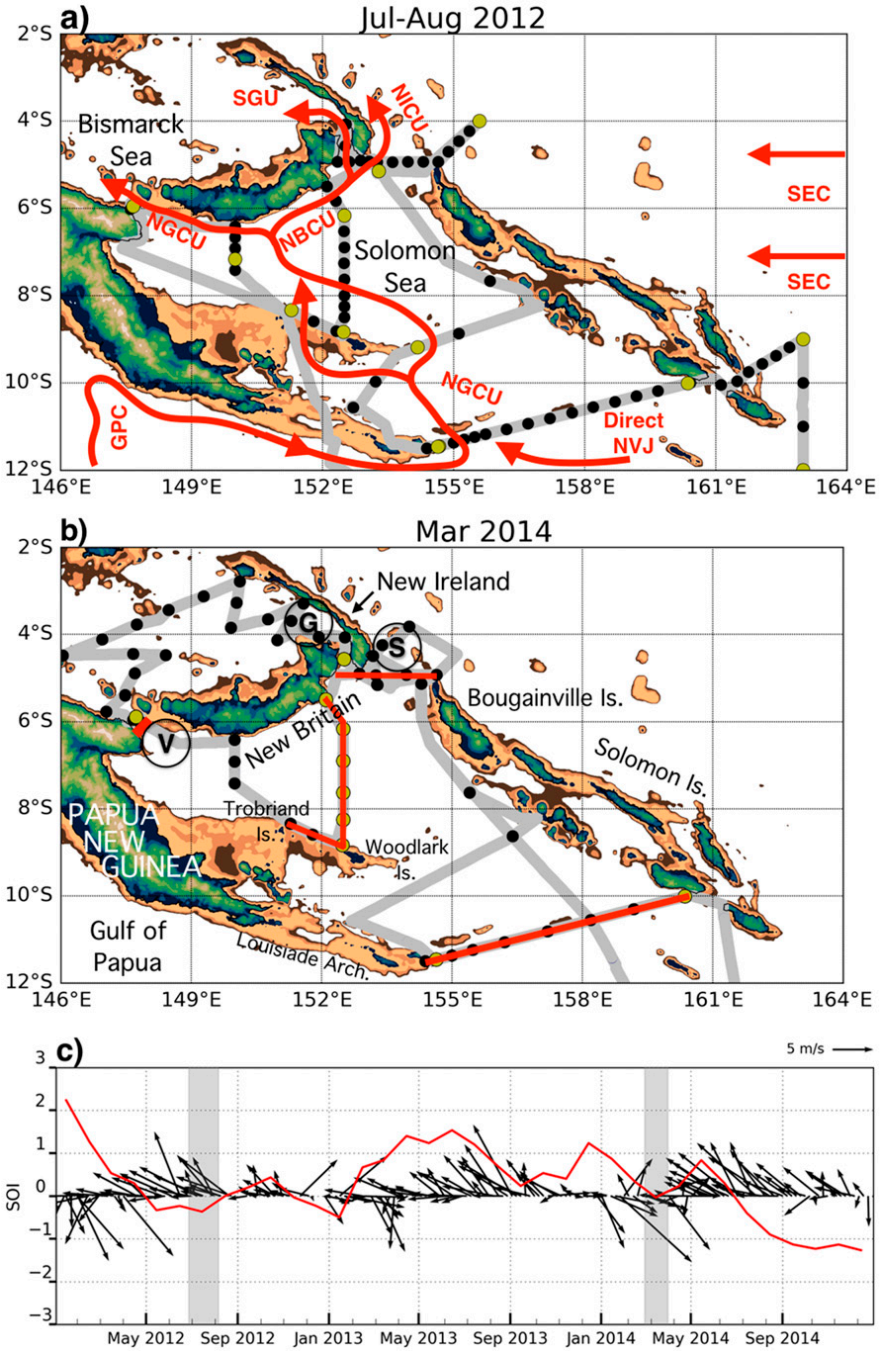

FIG. 1. Shallow bathymetry at 100, 500, and 1000 m (brown shading); station positions (black dots); and repeat stations (yellow dots) along cruise tracks (gray background) during (a) the Pandora cruise (July–August 2012) and (b) the MoorSPICE cruise (March 2014). Red arrows in (a) denote the main thermocline currents in and around the Solomon Sea. In (b), the transects defining the boundaries of the inverse model are overlaid in red. The circled "V" and "S" represent Vitiaz and Solomon Straits, respectively, while "G" represents St Georges Channel. (c) ASCAT winds ($m\,s^{-1}$) averaged over the Solomon Sea basin from 2012 to 2014 (black arrows), overlaid by a 3-month moving average of the SOI (red line). Note the background shading during Pandora and MoorSPICE cruises.

forms the New Britain Coastal Undercurrent (NBCU). The NBCU splits to flow northward through St Georges Channel to form the St Georges Undercurrent (SGU) in the Bismarck Sea, and eastward through the Solomon Strait to form the New Ireland Coastal Undercurrent (NICU) east of New Ireland. Seasonal variations in the Solomon Sea are evident through strong wind stress anomalies, induced by the trade reversal (Hristova and Kessler 2012; Cravatte et al. 2011; Melet et al. 2010b). Sea surface temperature (SST) and sea surface salinity (SSS) variations are also associated with the seasonal cycle, with coldest and saltiest waters found in austral winter (Delcroix et al. 2014), inducing potential water mass modifications at the surface and deeper levels. Circulation and mass transports are expected to be modified at seasonal time scales; however, the scarcity of data so far has prevented the determination of the extent of these modifications.

A few studies have estimated net transports into the Solomon Sea. A net inflow was estimated at 30 Sv ($1\,\mathrm{Sv} \equiv 10^6\,\mathrm{m^3\,s^{-1}}$) over 0–2000 m from an August 2007 hydrographic cruise (Gasparin et al. 2012). The mean transport from repeated glider transects that transited across the Solomon Sea southern entrance was estimated at 15 Sv from the surface down to 700 m over 2007–11 (Davis et al. 2012). An Argo-based study from 2004 to 2011, which included data until 170°E because there are so few Argo floats into Solomon Sea, found a similar estimate of 19 Sv over 0–1000 m (Zilberman et al. 2013). From S-ADCP measurements (20–300-m depth range) and a single mooring with three current meters (at 354, 467, and 556 m) collected during the Western Equatorial Pacific Ocean Climate Studies (WEPOCS), Lindstrom et al. (1987, 1990) estimated transports through Vitiaz Strait at 8–14 Sv with a maximum velocity core around 200 m. This study suggested that the transport through Vitiaz Strait is a main source of the EUC, which was subsequently confirmed by the water properties analysis of Tsuchiya et al. (1989). Murray et al. (1995) estimated transports through Vitiaz Strait for the 50–800-m depth range, at 14.9–19 Sv from March 1992 to March 1993, with strong flows during June–August and weaker flows during September–March.

Water properties in the southwest Pacific exhibit strong signatures in salinity and oxygen that can be tracked along the LLWBCs from the Coral Sea to the equator through four main water masses. The South Pacific Tropical Water (SPTW), also referred to as the upper salinity maximum water in Qu and Lindstrom (2002), flows at the upper thermocline level ($\sigma_\theta \sim 24.5$) and originates in the southeast Pacific gyre (e.g., Kessler 1999; Hasson et al. 2013; Qu et al. 2013). Below the SPTW, two mode waters are identified with no vertical extrema in temperature or salinity; rather, they are characterized by the thermostad typical of mode waters (Tomczak and Hao 1989; Grenier et al. 2014). The Subtropical Mode Water (STMW; $\sim\sigma_\theta$ = 25.5–26; Roemmich and Cornuelle 1992; Qu et al. 2008) emanates from north of the Tasman Sea (Donguy and Henin 1977) and partly northeast of New Zealand (Tsuchiya 1981; Qu et al. 2008), and the Subantarctic Mode Water (SAMW; $\sim\sigma_\theta$ = 26.5–27; McCartney 1977; Grenier et al. 2013) with quite high oxygen originates from the Southern Ocean by subduction north of the Antarctic Circumpolar Current (Hanawa and Talley 2001). A salinity minimum and an oxygen maximum identify the Antarctic Intermediate Water (AAIW) near $\sigma_\theta \sim 27.2$, with origins between 50° and 60°S (Qu and Lindstrom 2004).

3. Data and inverse model

a. *Hydrographic cruise data*

Both cruises and associated data processing are described in Ganachaud et al. (2016, manuscript submitted to *Elementa*); here we summarize the main features. During the July–August 2012 cruise (Pandora), hydrographic sections, including some repeat 28–36-h time series stations, were carried out. On stations, CTD O_2 sensors were used to measure temperature, salinity, and oxygen. Niskin bottles were used to collect water samples at specific depths to measure salinity, oxygen, and nutrients (nitrite, nitrate, phosphate, and silica). Overall, 83 stations were sampled, most to 2000 m depth (Fig. 1a). Currents were recorded during most profiles with a pair of lowered acoustic Doppler current profilers (L-ADCPs; RDI Instruments) attached to the CTD rosette (150 and 300 kHz, down- and up-looking with a vertical resolution of 16 and 10 m, respectively). Currents were also recorded along the ship track with two S-ADCPs (models RDI 0S-38 and 0S-150), with typical vertical ranges of 1300–1350 m and 300–350 m, respectively.

During the March 2014 cruise (MoorSPICE), 57 stations were surveyed, including some repeat 28–36-h time series, along CTD hydrographic sections that measured temperature, salinity, and oxygen (Fig. 1b), most to 2000 m or to 1000 m at the southern entrance. As in July–August 2012, discrete samples were carried out on station with Niskin bottles to measure salinity, oxygen, and nutrients. Currents were recorded at each station using a pair of down- and up-looking 300-kHz RDI L-ADCPs with vertical resolution of 8 m and a 0S-75 S-ADCP working in both broadband and narrowband modes that reached around 700 and 900 m, respectively.

In both cruises, the repeat stations (Figs. 1a,b) are used to estimate uncertainties in S-ADCP velocity data near

TABLE 1. Water masses and associated volume transports (Sv) during July–August 2012 [Pandora (P)] and March 2014 [MoorSPICE (M)]. Positive values are northward or eastward, negative values are southward or westward, and uncertainties are one standard deviation. Transport estimates do not entirely sum up, which is likely induced by diapycnal fluxes to deeper layers than 1000 m and residual noise.

Upper (σ_θ, kg m^{-3})	Lower (σ_θ, kg m^{-3})	Water mass	Southern entrance	St Georges–Solomon	Vitiaz	Woodlark–New Britain	Trobriand–Woodlark
Surface	24	TSW	P: 3.3 ± 0.4	2.4 ± 0.3	4.5 ± 0.1	2.2 ± 0.2	2.1 ± 0.2
			M: −5 ± 0.3	−6.7 ± 0.4	2.2 ± 0.1	1.5 ± 0.3	−0.7 ± 0.2
24	26	SLW	P: 11.4 ± 0.3	6.3 ± 0.3	3.4 ± 0.1	1.8 ± 0.2	3.1 ± 0.2
			M: 2.7 ± 0.4	3.5 ± 0.3	4.2 ± 0.1	1.6 ± 0.2	1 ± 0.2
26	26.9	SAMW	P: 12.2 ± 0.5	6.2 ± 0.5	6.9 ± 0.1	1.8 ± 0.3	4.1 ± 0.2
			M: 8.7 ± 0.6	3.8 ± 0.5	3.1 ± 0.1	5.6 ± 0.3	1.4 ± 0.5
26.9	27.4	AAIW	P: 9.3 ± 1.4	3.8 ± 1.2	4.6 ± 0.2	5.8 ± 0.9	−1.4 ± 0.8
			M: 4.3 ± 1.4	1.7 ± 1.2	1.4 ± 0.2	0.2 ± 1	0 ± 0.8
Surface	27.4		P: 36.2 ± 2.6	18.8 ± 2.3	19.4 ± 0.4	11.6 ± 1.7	7.9 ± 1.7
			M: 10.7 ± 2.6	2.2 ± 2.3	10.9 ± 0.4	8.8 ± 1.7	1.7 ± 1.7

1000 m, associated with high-frequency natural variability (e.g., barotropic and baroclinic tides). Velocity uncertainties are lower than ±5 cm s^{-1} at most repeat stations during both cruises, except in July–August 2012 at Vitiaz Strait (repeat station 77), where observed velocity variability reached ±10 cm s^{-1}, likely induced by the strong tides.

Temperature, salinity, and oxygen profiles are filtered using a 5-m median to remove spikes. Velocity data from the narrowband 38-kHz S-ADCP during July–August 2012 and the narrowband 75-kHz S-ADCP in March 2014 are averaged every 10 min. Because S-ADCP profiles start at 50 m, they are extrapolated as a constant to the surface. To highlight the water property changes within the Solomon Sea (see section 6), hydrographic and S-ADCP data were averaged over potential density ranges (Table 1) encompassing the main water masses, defined in section 2.

b. *Meteorological products*

The Advanced Scatterometer (ASCAT) winds on a lateral resolution of 0.25° were spatially averaged over the Solomon Sea basin (6°–10°S, 148°–160°E) from January 2012 to December 2014. Monthly CPC Merged Analysis of Precipitation (CMAP) products at 2.5° lateral resolution were averaged over the Solomon Sea region (2°–14°S, 146°–164°E) during both cruises. A 3-month moving average of the SOI was used from January 2012 to December 2014.

c. *Ocean climatology*

The Monthly Isopycnal/Mixed-Layer Ocean Climatology (MIMOC) provides monthly mean salinity data at 0.5° lateral resolution over 81 standard pressure levels from the surface (0 dbar) to 1950 dbar (Schmidtko et al. 2013). Maps are mostly based on Argo and shipboard data from 2007 to 2011, but they can relax back to historical CTD measurements when no recent data are available. MIMOC uses a mapping scheme based on a fast marching algorithm, which improves property fields near the coasts and around the Solomon Islands.

d. *Inverse box model*

Inversion methods are used to infer synoptic current pathways and associated quantitative transports within an ocean volume (i.e., a box divided in layers along the z axis and bounded by hydrographic transects). The usual procedure (Wunsch 1996; Macdonald and Wunsch 1996; Ganachaud and Wunsch 2000) uses as an initial guess of geostrophic currents calculated between pairs of stations from a deep reference level. Then the inverse model is used to determine an adjusted flow with associated uncertainties, so that the flow conserves mass, salt, or heat to avoid large mass imbalances. This results in velocities and property transports with uncertainty estimates obtained directly from the hydrographic surveys.

MODEL CONFIGURATION

Our inverse box model uses the Gauss–Markov method (Wunsch 1996; Ganachaud and Wunsch 2000) along bounding hydrographic transects to adjust the flow and estimate errors of our diagnostics over 12 evenly spaced isopycnal layers from the surface to 1000 m (Table A1). Potential density surfaces that encompass main water masses found in the southwest Pacific (see section 2; Qu and Lindstrom 2002; Grenier et al. 2013; Gasparin et al. 2014) are grouped to calculate corresponding volume transport (Table 1). SPTW and STMW are grouped in a single layer, identified by Wyrtki (1962) as the Subtropical Lower Water (SLW; $24 < \sigma_\theta < 26$). The model is set up to enforce mass, salt, heat, and silica conservations.

Calculation of geostrophic velocities is subject to biases from temporary displacements of isopycnals

due to internal waves. This noise is exacerbated in the Solomon Sea because of the high internal wave activity from tides (e.g., Melet et al. 2011; M. S. Alberty et al. 2016, unpublished manuscript) coupled with the low latitude. In addition, strong ageostrophic currents are expected in the narrow straits. To overcome this difficulty, we chose to use the gridded S-ADCP velocity profiles as our first guess and to allow a barotropic adjustment referenced to 1000 m depth through the inverse model; though necessarily the simplest, this barotropic adjustment is a realistic hypothesis. Locally, the required adjustment is relatively small, but nevertheless, its integral effect on coast-to-coast transport is important.

The inverse box model is bounded by three hydrographic transects enclosing the Solomon Sea and two transects crossing the midbasin, common to both cruises (Fig. 1b). A transect crosses the southern entrance of the Solomon Sea, with S-ADCP velocities rotated 346 degrees True (hereinafter °T) to be perpendicular to the transect. A second transect joins the St Georges Channel and Solomon Strait outflow passages (velocities rotated 359.9°T). At Vitiaz Strait, another transect crosses the outflow with S-ADCP velocities rotated 344°T. In the midbasin, a transect joins the Woodlark Island and New Britain with S-ADCP velocities first rotated 270°T (from 9° to 6°S) and then 242°T (from 6° to 5.5°S). A last transect joins the flow from Trobriand to Woodlark Islands, where S-ADCP velocities are rotated 203°T. During the March 2014 cruise, S-ADCP velocities do not reach 1000 m, so we used a merged velocity field based on S-ADCP in the upper ocean and L-ADCP at depths where S-ADCP velocities were not available, typically below 900 m. L-ADCP velocity profiles were compared with corresponding S-ADCP profiles at overlapping depths, and minor differences were found (0–1 $\mathrm{cm\,s^{-1}}$). L-ADCP velocities were interpolated on the S-ADCP velocity grid using a Gaussian weighting function.

Freshwater transports are in the local mass balance: CMAP precipitation products provide estimates of 6 and 10 $\mathrm{mm\,day^{-1}}$ over the area of the Solomon Sea, which correspond to mass fluxes of 0.01 and 0.016 Sv during the 2012 and 2014 cruises, that is, much smaller than uncertainties (Table 1). The Ekman component in the surface layer is partially included in the absolute S-ADCP currents, although an adjustment to the integral Ekman transport is allowed through the inversion. ASCAT winds during each cruise period were used to estimate a range for this Ekman adjustment (±3 Sv).

A solution to the S-ADCP velocity adjustments, the reference velocities, and the advective and diffusive vertical transfers between the different box layers must be determined so that budgets in mass, salt, heat, and silica are balanced in the upper 1000 m. Silica is conserved from the surface to 1000 m (layers 1–12) but not within individual layers. A priori uncertainties on mass were specified following Ganachaud et al. (2008), who used an inverse model to determine circulation in the Coral Sea. For both cruises, these uncertainties are detailed for each layer in Table A1. We set near the surface (i.e., layers 1–3) larger mass uncertainties (±2 Sv), as higher residual mass variability is expected (Ganachaud 2003). Heat and salt are not conserved in these upper layers because of potential exchanges with the atmosphere. In the deepest layer 12 (>800 m), an allowance of ±2 Sv permits possible exchanges with the deeper ocean. No conservation is applied to heat and salt in this last layer to allow exchange with the deeper ocean. To enforce heat and salt conservations, anomaly equations are used (Ganachaud and Wunsch 2000; Ganachaud 2003) associated with scaling factors (Table A1), which are determined experimentally to minimize the mass residuals between the initial and adjusted velocity fields.

Cross isopycnal transfers (w) are allowed with a priori values of $\pm 1 \times 10^{-3}\,\mathrm{cm\,s^{-1}}$ between layers 1 and 2 and $\pm 1 \times 10^{-4}\,\mathrm{cm\,s^{-1}}$ between the deeper layers, since larger vertical exchanges are expected near the surface than in deeper layers. A priori vertical diffusion coefficients (κ_z) are believed to be strong in the Solomon Sea (Melet et al. 2011; Olbers and Eden 2013), as it is strongly influenced by the South Pacific LLWBCs and rough topography. Thus, a κ_z range of adjustment was set to $\pm 10\,\mathrm{cm^2\,s^{-1}}$.

The range of adjustment for S-ADCP velocities is determined from repeat stations (yellow dots in Figs. 1a,b), except at Vitiaz Strait in July–August 2012, where variability is strongly impacted by tides (see section 3a). Thus, the velocity range is set to be the conservative value of $\pm 5\,\mathrm{cm\,s^{-1}}$ for all transects during both cruises.

4. Water mass properties

a. *MIMOC climatology*

Monthly mean salinity over the southwest Pacific is shown for July and March (Fig. 2) to provide a climatological view of water masses entering and exiting the Solomon Sea at thermocline and intermediate levels. We overlay the corresponding salinity values from the cruise data (colored dots, Fig. 2).

In March and July, the SLW (Figs. 2a,b; $\sigma_\theta \sim$ 24–26), exhibits high salinity (>35.7) carried westward by the SEC from the high evaporation region (20°S, 120°W). These salty waters are spread out from the eastern Pacific to the Solomon Strait in July but are confined east of the Solomon Islands in March. In both seasons,

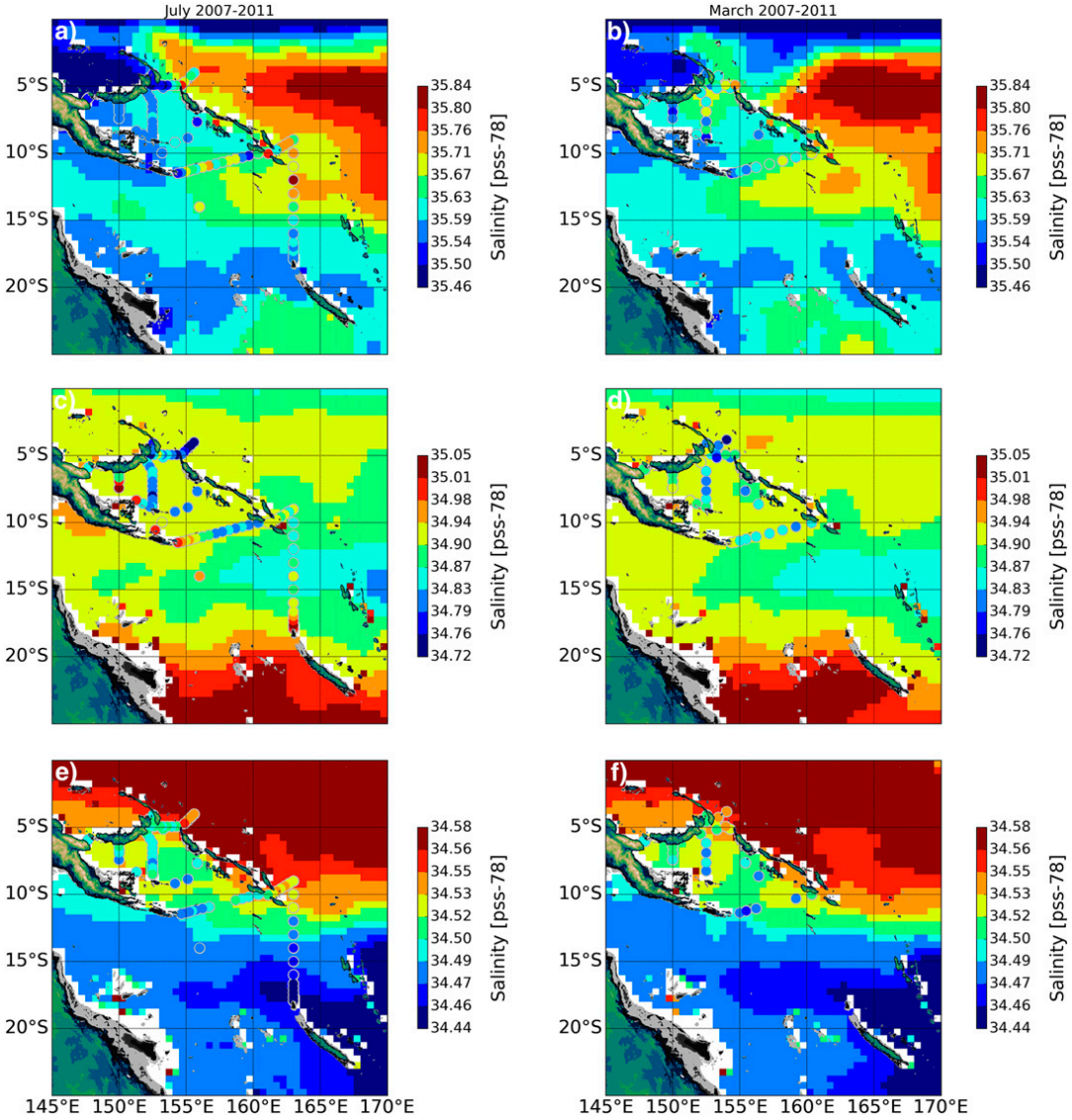

FIG. 2. Mean salinity climatology during (left) July and (right) March for (a),(b) SLW ($\sigma_\theta \sim 24$–26); (c),(d) SAMW ($\sigma_\theta \sim 26$–26.9); and (e),(f) AAIW ($\sigma_\theta \sim 26.9$–27.4) levels. Colored dots correspond to measured salinity during each July–August 2012 and March 2014 cruise. Note the choice in salinity scale used for each potential density range.

the direct NVJ pathway carrying more salty waters (Kessler and Cravatte 2013b) is not distinguishable once in the Solomon Sea. Fresher waters coming from the eastern Pacific are tracked across the Coral Sea (south of 15°S) to the GPC before entering into the Solomon Sea. Downstream, the NGCU and the SGU carry fresh waters into the Bismarck Sea with lower salinity in July than March.

At the SAMW level (Figs. 2c,d; $\sigma_\theta \sim 26$–26.9), both seasons show salty waters (>34.9) carried by the GPC to feed the NGCU and ultimately the Solomon Sea. These salty waters originating from north of New Zealand are also carried westward by the northern stream of the SEC and are found in the Bismarck Sea. Fresh waters enter the Coral Sea (~13°–15°S), emanating from the eastern Pacific. MIMOC climatological fields appear to be too smooth to allow inference of detailed pathways, but the salty NGCU is clearly visible in the July–August 2012 cruise data.

At the intermediate level (Figs. 2e,f $\sigma_\theta \sim 26.9$–27.4), fresh waters related to the AAIW salinity minimum are observed within the Coral Sea. They are not traceable inside the Coral Sea, and their signature vanishes as they flow equatorward. Conversely, AAIW is traced inside the Solomon Sea with both July–August 2012 and March 2014 cruise data. Salty waters (>34.53) are observed

northeast of the Solomon Islands and in the Bismarck Sea during both seasons.

Thus, in the MIMOC climatology major differences are found between both seasons at the SLW near Solomon Strait, where northeastern salty waters seem to enter the Solomon Sea during March and not in July. In contrast, there is not much difference at SAMW and AAIW levels in the MIMOC climatology. As expected, MIMOC does not agree well with the cruise data within the Solomon Sea, since only a few scattered profiles were available in the region before the two SPICE cruises.

b. *July–August 2012 and March 2014 cruises*

During both cruises, the SPTW identified as a salinity maximum (Figs. 3c,d) is found at $\sigma_\theta \sim 24.5$ within the Solomon Sea. During both cruises, salty waters are observed at the eastern entrance of the Solomon Sea, carried by the direct NVJ, and also northeast of Bougainville Island. The western Solomon Sea has less saltier waters during both cruises at the southern entrance where the NGCU flows into the Solomon Sea (dark red, Figs. 3c,d). These less salty waters, which exhibit a deeper salinity maximum (below $\sigma_\theta = 24.5$), are found in Vitiaz Strait and St Georges Channel, as we will discuss further in section 6. Nutrients (see Fig. S1 in the supplemental material) exhibit common features between both cruises. Nitrate (Figs. S1a,b) and phosphate (Figs. S1c,d) concentrations range from 10 to 15 and 0.4 to 0.8 μmol kg^{-1}, respectively, and silica (Figs. S1e,f) is $<10\,\mu$mol kg^{-1}. Below the SPTW, the STMW ($\sigma_\theta \sim 25.5$–26) is observed (Figs. 3c,d) with similar temperature, salinity, and nutrient characteristics between both cruises. Below $\sigma_\theta = 26$, waters with temperatures from 8° to 10°C (Figs. 3c,d) and with high oxygen ($>160\,\mu$mol kg^{-1}; Figs. 3e,f) are identified as the SAMW during both cruises with similar nutrient concentrations.

Near $\sigma_\theta = 27.2$, a salinity minimum (<34.6, Figs. 3c,d) and an oxygen maximum (~150–200 μmol kg^{-1}; Figs. 3e,f) identify the AAIW during both cruises, except northeast of Bougainville Island, where saltier waters associated with low oxygen, high phosphate, and high nitrate are found. These waters emanate from the equatorial region, where Bostock et al. (2010) identified the Equatorial Pacific Intermediate Water (EqPIW) with higher salinity, phosphate, and nitrate and lower oxygen compared with other intermediate waters. Northeast of Bougainville Island, similar silica concentrations to those found by Bostock et al. (2010) (20–100 μmol kg^{-1}) were measured during both cruises. Tracer signatures indicate that the EqPIW is older than both AAIW and the North Pacific Intermediate Water (NPIW), suggesting a formation of the EqPIW by diapycnal mixing with older upwelled waters as the Pacific Deep Water (Bostock et al. 2010). Both Θ–S and Θ–O_2 diagrams (Fig. 3) reveal strong erosion of the extrema as the water masses flow across the Solomon Sea with significant differences between both cruises, as investigated below in section 6.

5. Pathways and integrated transports

In this section, the main currents and their associated volume transports are detailed across the Solomon Sea during the two SPICE cruises. Reference velocity adjustments through the inversion at 1000 m are presented (Fig. 4, top panels), and are much smaller than the a priori velocity uncertainties of ± 5 cm s^{-1} (see section 3d).

a. *Southern entrance of Solomon Sea in austral winter 2012*

The estimated July–August 2012 velocity field reveals strong currents across the southern entrance section to the Solomon Sea (Fig. 4a), associated with a surface-to-1000-m volume transport of 36 Sv (Table 1), which is in the upper range of previous estimates (Kessler and Cravatte 2013a). Waters between $24 < \sigma_\theta < 26.9$ (SLW and SAMW) and below $\sigma_\theta = 26.9$ (AAIW) represent 65% (~24 Sv) and 26% (~9 Sv), respectively, of this transport estimate (Table 1). The striking feature is a strong NGCU confined against PNG (~18 Sv; Table A2), with a main core located at 500 m (Fig. 4a). East of the NGCU, the direct NVJ flows into the Solomon Sea (~8 Sv; Table A2), centered on $\sigma_\theta = 25.5$ (~200 m), before merging with the NGCU south of Woodlark Island (Figs. 1a,b). On the eastern part, a southward current (5–10 cm s^{-1}; Fig. 4a) is observed at 159°–160°E between 400 and 1000 m, which suggests waters flowing out of the Solomon Sea along the Solomon Islands.

b. *Interior pathways in austral winter 2012*

A surface-to-1000-m volume transport is estimated at 12 Sv (Table 1) between Woodlark and New Britain Islands, largely as a result of the westward current across the section except along the New Britain coast, where an eastward flow is observed (Fig. 4e). Below the surface, the most striking feature is the sharp and intense eastward flowing NBCU (~28 Sv; Table A2) confined along the New Britain coast (north of 6°S; Fig. 4e). A strong westward flowing NGCU is identified (7.5°–8.4°S; Fig. 4e) with a high-velocity core located at 500 m (16 Sv; Table A2), a similar magnitude and depth to the NGCU as it enters across the southern entrance (northward flow south of 155°E in Fig. 4a). A recirculation is also identified through an eastward flow sandwiched between Woodlark and the NGCU. Farther north, a westward flow is observed centered on $\sigma_\theta = 27$ (~6.5°S), likely

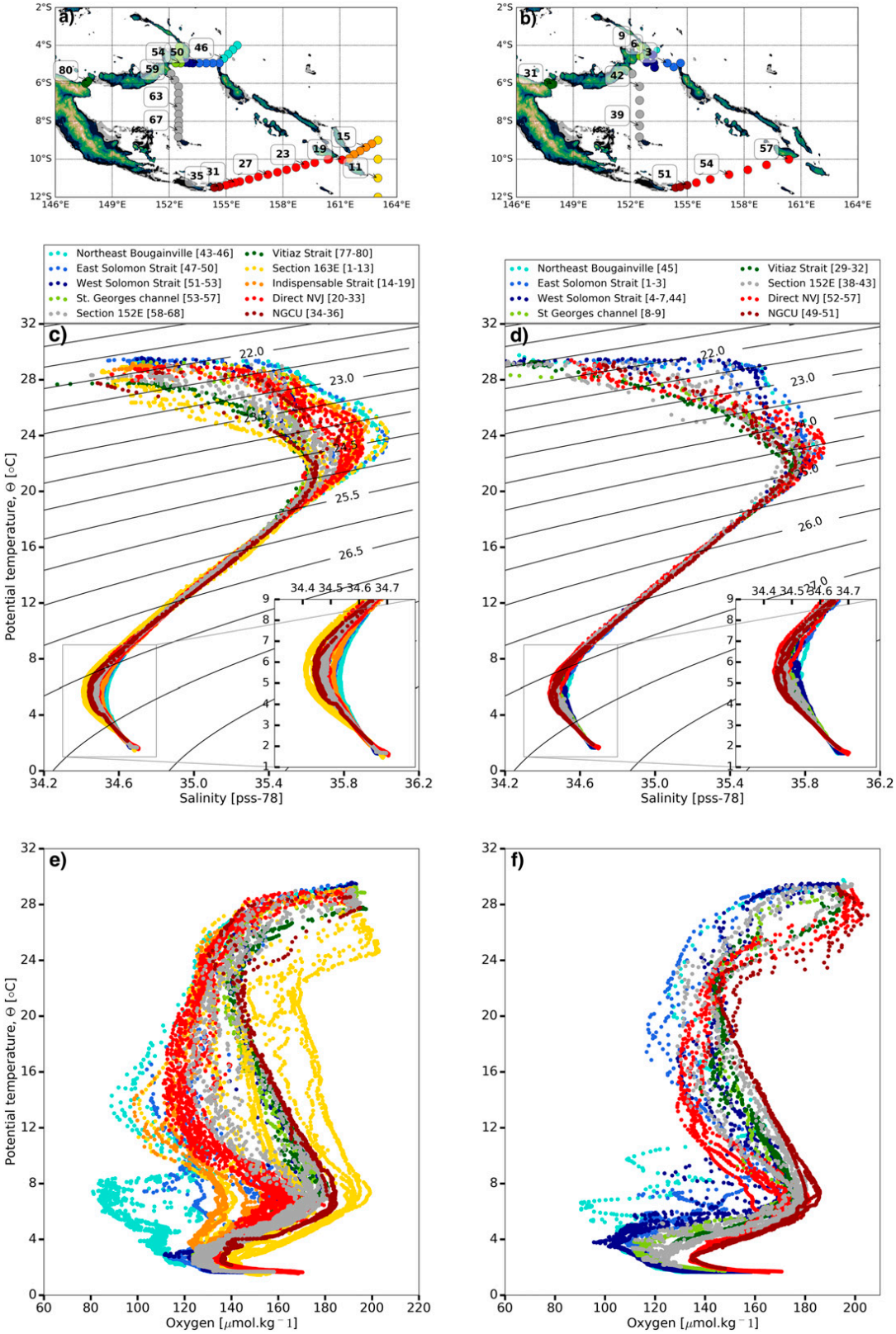

FIG. 3. Hydrographic stations during (a) Pandora and (b) MoorSPICE. Shown are the Θ–*S* diagrams during (c) Pandora and (d) MoorSPICE and Θ–O_2 diagrams during (e) Pandora and (f) MoorSPICE, respectively. Note expanded inset for Θ–*S* diagrams. Color corresponds to locations as indicated in legends and maps in (a) and (b).

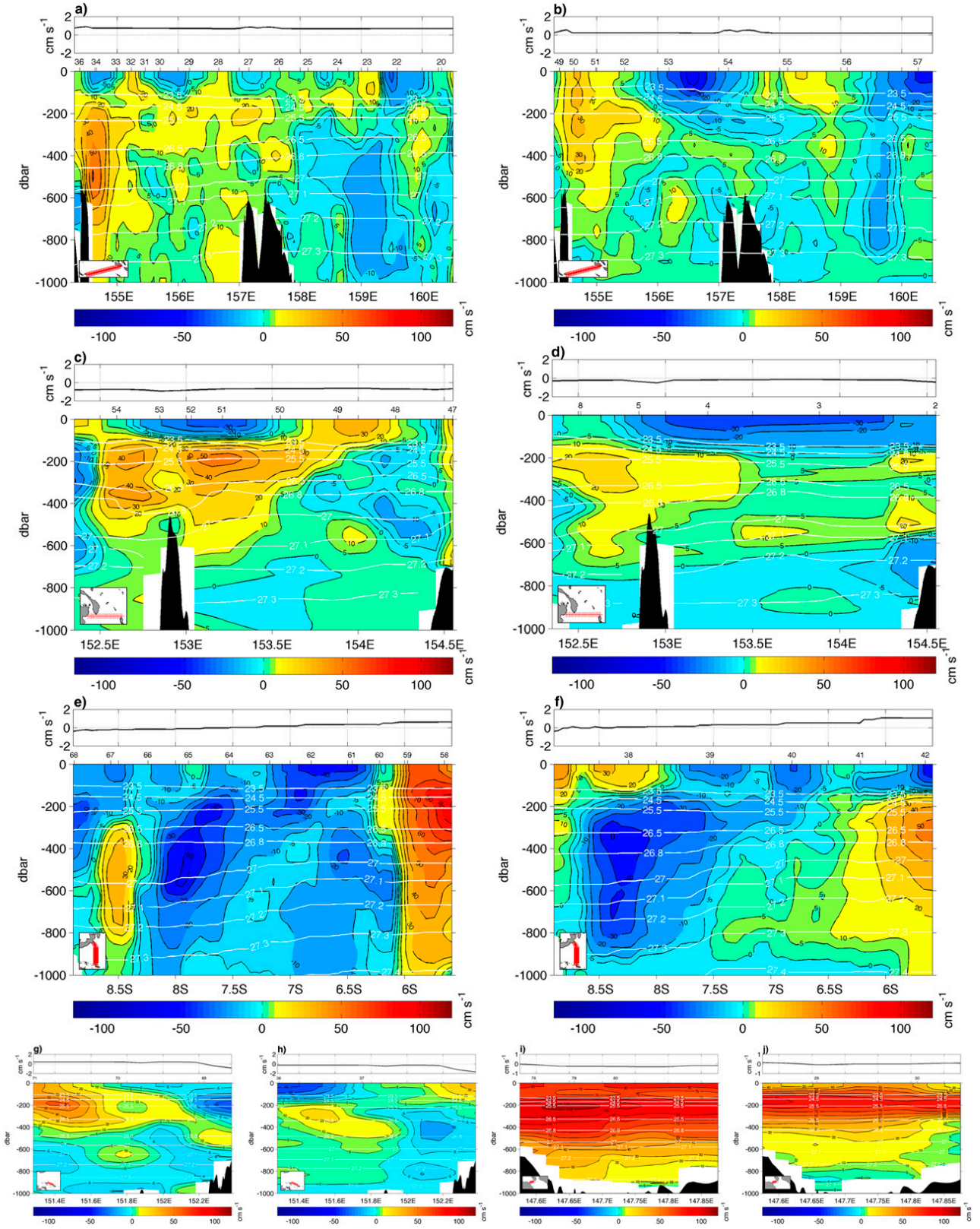

FIG. 4. The top part of each panel shows the difference between estimated and initial reference velocities at 1000 m (solid line). (left) July–August 2012 and (right) March 2014 estimated zonal cross-section S-ADCP velocities (a),(b) at the southern entrance of the Solomon Sea; (c),(d) between St Georges Channel and Solomon Strait; (e),(f) between New Britain and Woodlark Islands; (g),(h) between Trobriand and Woodlark Islands; and (i),(j) at Vitiaz Strait. Positive values indicate northward and eastward directions, and overlaid white lines indicate potential density anomaly (kg m^{-3}).

resulting from another recirculation confined to the northern part of the basin. Between Trobriand and Woodlark Islands (Fig. 4g), we estimated a northward flow of 8 Sv (Table 1), with a strong current along the Trobriand coast. A southward flow centered on $\sigma_\theta = 25.5$ is observed near Woodlark Island.

c. *Northern outflow pathways in austral winter 2012*

Across the St Georges–Solomon transect (Fig. 4c), the estimated volume transport reaches 19 Sv (Table 1), with ~8 Sv flowing through St Georges Channel and ~11 Sv across Solomon Strait (Fig. S2c). Near 67% (12.5 Sv) of the total integrated transport is found between $24 < \sigma_\theta < 26.9$, while 20% (~4 Sv) is attributed to the AAIW (Table 1). Above 150 m, transports are estimated to be 2 Sv and are associated with a persistent anticyclonic eddy, observed by altimetry as present during the whole austral winter 2012 cruise in Solomon Strait (Ganachaud et al. 2016, manuscript submitted to *Elementa*). At St Georges Channel, the northward SGU (Fig. 4c, west of 153°E) transports ~6 Sv between $24 < \sigma_\theta < 26.9$ (Table A2), with two velocity cores of ~40 cm s^{-1}. At Solomon Strait (Fig. 4c, east of 153°E), a strong NICU is found at this density range, transporting equatorward ~6 Sv (Table A2). The eastern part of Solomon Strait shows a southward current centered on $\sigma_\theta = 27$ (153.5°–154.5°E) entering the Solomon Sea. This current potentially feeds westward into the interior Solomon Sea, or perhaps contributes to the southward current found at the southern entrance (Fig. 4a). Below $\sigma_\theta = 27$, a core of weak velocities (0–10 cm s^{-1}) exits Solomon Strait at 154°E. These transport estimates and current structures are consistent with previous studies (Melet et al. 2010a; Cravatte et al. 2011).

At Vitiaz Strait, a high-velocity core of 90–110 cm s^{-1} is found at 200 m (Fig. 4i), consistent with previous studies (Lindstrom et al. 1990; Murray et al. 1995; Cravatte et al. 2011). Near 53% (~10 Sv) of the total volume transport (Table 1), is found between $24 < \sigma_\theta < 26.9$. Above 150 m and at the AAIW density range, we found a similar contribution of almost 25% (4.5 Sv; Table 1) to the total volume transport, leading to a total estimate of 19 Sv across the strait, which is also consistent with previous estimates (Lindstrom et al. 1990; Murray et al. 1995; Cravatte et al. 2011). Thus, the circulation during July–August 2012 is slightly stronger, but close to the mean conditions.

d. *Southern entrance of Solomon Sea in austral summer 2014*

During March 2014, the volume transport fell by 70% to 11 Sv across the southern entrance, compared to the austral winter 2012 cruise (Table 1), although there were quite similar contributions from waters encompassing the SLW and SAMW (near 70%) and the AAIW (25%). The NGCU is less intense and extended to the surface (Fig. 4b, west of 155°E), with a transport almost halved (~10 Sv; Table A2) in comparison with austral winter 2012.

The direct NVJ appears to be impacted by surface eddies (Fig. 4b, east of 156°E) and fell to 4 Sv (Table A2), as it flows deeper than in austral winter into the Solomon Sea ($\sigma_\theta \sim 26.5$). Above 150 m, the estimated transport is −5 Sv, implying a southward outflow likely induced by persistent cyclonic eddies (Fig. 4b, 156°–157.5°E; east of 159°E), which have been also identified through satellite altimetry (Ganachaud et al. 2016, manuscript submitted to *Elementa*). Farther east near 160°E, a southward current (0–10 cm s^{-1}) is observed as during winter 2012, suggesting a downstream inflow along the Solomon Islands.

e. *Interior pathways in austral summer 2014*

In March 2014, a weaker total volume transport is estimated at 9 Sv (Table 1) between Woodlark and New Britain Islands. The westward NGCU core is slightly less intense but extends down to 800 m depth (Fig. 4f) and is associated with a similar transport (~16 Sv; Table A2) to that during July–August 2012. The eastward NBCU is weaker and appears to be less confined against New Britain, and its transport is 14 Sv, half that found in the austral winter cruise (Table A2), with a high-velocity core centered on $\sigma_\theta = 26.5$. Moreover, opposite surface currents are observed along New Britain in March 2014 compared with July–August 2012. Across the transect between Trobriand and Woodlark Islands, we also observe opposite surface currents compared with July–August 2012 (Fig. 4h), associated with a negligible northward transport (Table 1).

f. *Northern outflow pathways in austral summer 2014*

At St Georges Channel, volume transports are almost halved (~4 Sv; Fig. S2d) compared to that found in austral winter, with minor contributions of the surface and AAIW layers. Most of the northward outflow is carried by the SGU (~4 Sv; Table A2) between the SLW and SAMW. Across Solomon Strait, a strong surface inflow is found above 150 m, estimated at −6 Sv (Fig. S2d). Volume transports fell to −2 Sv (Fig. S2d) across the Solomon Strait, where the NICU transports northward ~3 Sv (Table A2) and ~1 Sv is associated with the AAIW (Fig. S2d).

As during July–August 2012, Vitiaz Strait exhibits high velocities (90 cm s^{-1}) at 200 m (Fig. 4j), but the total volume transport was almost halved to 10.9 Sv (Table 1). Near 70% (~7 Sv) of this estimate is found

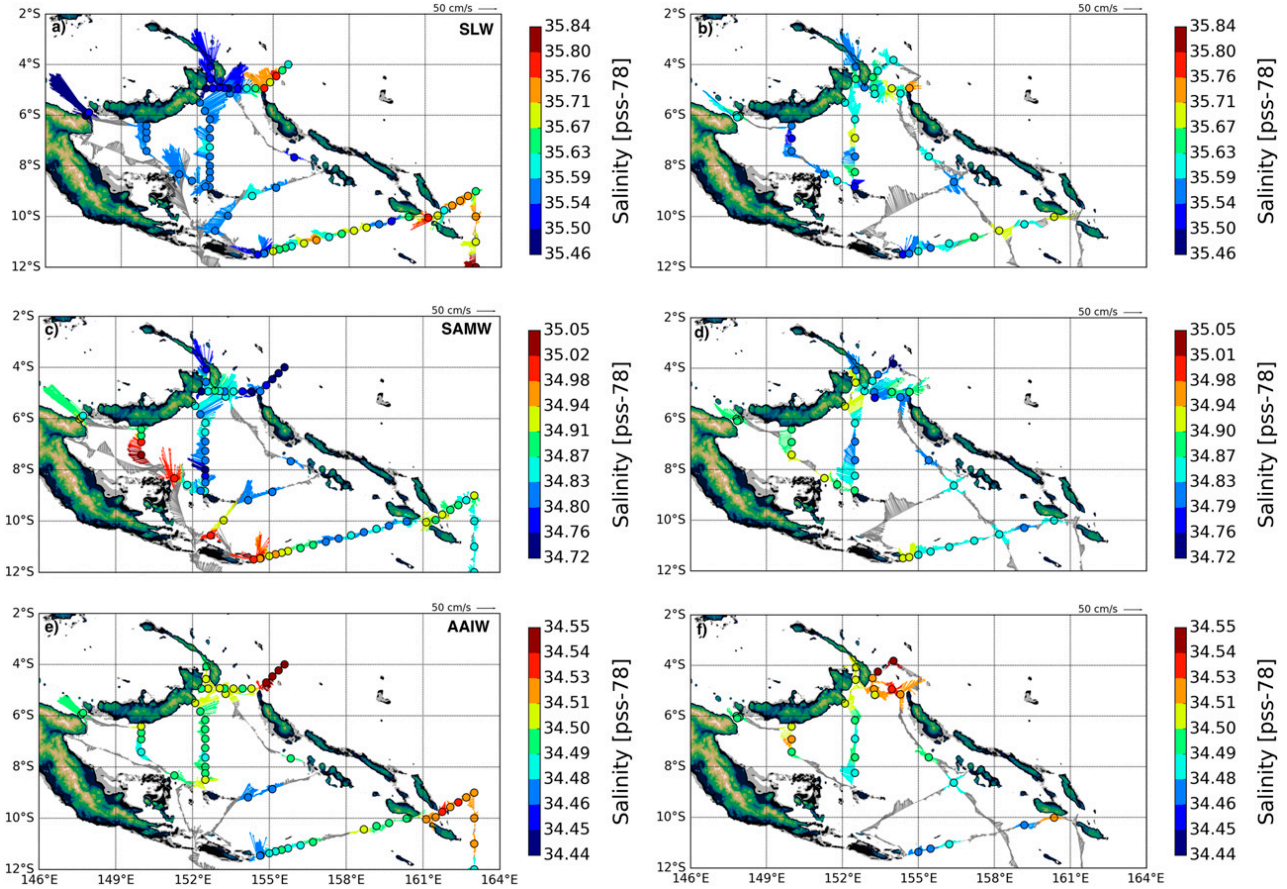

FIG. 5. Mean currents from nonadjusted S-ADCP velocities (arrows) colored by salinity during (left) July–August 2012 and (right) March 2014 for (a),(b) SLW ($\sigma_\theta \sim 24$–26); (c),(d) SAMW ($\sigma_\theta \sim 26$–26.9); and (e),(f) AAIW ($\sigma_\theta \sim 26.9$–27.4) levels.

between the SLW and SAMW, while unlike during austral winter, surface waters and the AAIW have only minor contributions (20% and 13%, respectively).

6. Water mass modifications across Solomon Sea

In this section we focus on salinity, silica, and nitrate distributions vertically averaged within density ranges encompassing the SLW ($24 < \sigma_\theta < 26$), the SAMW ($26 < \sigma_\theta < 26.9$), and the AAIW ($26.9 < \sigma_\theta < 27.4$). Oxygen patterns are similar to salinity with anticorrelated values during both cruises, except for the SAMW (see supplemental materials, Fig. S3). Phosphate distributions are similar to nitrate and so are not shown.

a. The SLW ($24 < \sigma_\theta < 26$)

In July–August 2012, fresh (Fig. 5a), oxygenated (Fig. S3a) waters are associated with the upper NGCU confined along the PNG coast and its streams (SGU and NICU) across and out of the Solomon Sea. Low silica (Fig. S4a) is also associated with the NGCU from its southern entrance and along its pathway toward Vitiaz Strait, while higher silica is found along the SGU and NICU streams and northeast of Bougainville Island. Saltier waters with lower oxygen and higher silica are carried into the Solomon Sea by the direct NVJ and merge with the NGCU south of the Woodlark Island. These salty waters are significantly eroded by lateral and vertical mixing along their equatorward pathways, with the lowest salinities (<35.5) found at Vitiaz Strait. Northeast of Bougainville, salty and poorly oxygenated waters are carried by the westward-flowing SEC, but do not seem to intrude into the Solomon Sea. Similarly in March 2014, fresh (Fig. 5b) and oxygenated (Fig. S3b) waters are associated with the upper NGCU, but with higher salinity and oxygen values than those of July–August 2012. The NGCU salinity gradually increases (~0.05) as it flows equatorward, likely induced by isopycnal mixing with salty waters coming from Solomon Strait or the southern entrance at ~158°E. Silica (Fig. S4b) exhibits similar distributions to that during July–August 2012 along the NGCU and the direct NVJ pathways.

b. The SAMW ($26 < \sigma_\theta < 26.9$)

During both cruises, the NGCU can be tracked within the Solomon Sea through salty and oxygenated waters with low silica and nitrate (Figs. S4c,d and Figs. S5c,d, respectively), confined along the PNG coast. Salinity decreases as the SAMW flows northward during both cruises, in particular south of Woodlark Island, where strong mixing might occur. Northeast of Bougainville Island, fresh and poorly oxygenated waters associated with high silica and nitrate are also found, suggesting a distinct water mass likely emanating from the equatorial region and carried by the SEC.

c. The AAIW ($26.9 < \sigma_\theta < 27.4$)

At the intermediate level and during both cruises, the lower NGCU carries the AAIW salinity minimum (Figs. 5e,f) with high oxygen (Figs. S3e,f), low silica and nitrate signatures (Figs. S4e,f and Figs. S5e,f, respectively) from its southern entrance to its separation south of Woodlark Island. Further north in the mid-basin, where the two NGCU streams rejoin, salinity and silica increase as the AAIW flows toward Vitiaz Strait. After the bifurcation of the NGCU south of New Britain, relatively high salinity is found at St Georges Channel and Solomon Strait. The striking feature is the strong contrast between the interior of the Solomon Sea and waters outside of Solomon Strait, northeast of Bougainville Island. AAIW is exiting through Vitiaz, but cannot be detected through Solomon Strait. Salty and poorly oxygenated waters are observed, with high silica ($>50\,\mu mol\,kg^{-1}$; Fig. S4e,f) and nitrate ($>30\,\mu mol\,kg^{-1}$; Fig. S5e,f). As suggested in section 4b, these distinct water properties are clearly related with the EqPIW emanating from the northern branch of the SEC in the eastern Pacific.

7. Discussion

a. Overview of our results

This paper provides a first snapshot of the South Pacific LLWBCs over the upper 1000 m during two contrasted seasons through a key region connecting the subtropics and the equator: the Solomon Sea. From two cruises, we depict the main pathways, associated transports, and water mass properties of the LLWBCs through the Solomon Sea. The July–August 2012 cruise sampled during the strong phase of the trade season, while the March 2014 cruise coincided with the opposite weak trade season. We implemented a new inverse box model configuration using measured S-ADCP velocities and basic conservation requirements to estimate at the cruise scale, velocities, transports, and related uncertainties.

In July–August 2012, we estimate a surface-to-1000-m transport of 36 Sv across the southern entrance with a major contribution from the NGCU, confined along the PNG coast and ~50 km wide. At the northern exits, we estimate 19 Sv through Vitiaz Strait, 8 Sv through St Georges Channel, and 11 Sv across Solomon Strait. At the thermocline level, salty waters from the SLW are found, with the freshest waters and low nutrients (nitrate, phosphate, and silica) observed within the equatorward NGCU pathways, confined along the PNG coast. Vitiaz Strait had lower salinity than at the southern entrance of the NGCU (~0.05), suggesting an erosion of the salinity maximum as the NGCU flows across the Solomon Sea. Below, the SAMW carries the intense NGCU core associated with salty and oxygenated waters along the PNG coast. At the intermediate level, the AAIW is a prominent feature characterized by a salinity minimum and relatively high oxygen. The water properties in the AAIW are eroded as it flows equatorward along the PNG coast within a narrower NGCU (width ~25 km).

In March 2014, the surface-to-1000-m estimated transport is 11 Sv across the southern inflow, again with a major contribution of the NGCU. Transports are 11 Sv across Vitiaz Strait, while ~4 Sv exits St Georges Channel. A strong surface inflow is found at Solomon Strait, leading to a total transport estimated to −2 Sv across the strait. These transport estimates do not sum up exactly with small volume imbalances at the southern entrance and across the St Georges–Solomon transect that are lower than transport uncertainties (see Table 1). At the thermocline level, both cruises exhibit freshest SLW at the southern entrance, where the NGCU enters into the Solomon Sea. The SAMW shows similar water properties to that during July–August 2012, but associated with a weaker NGCU. At the intermediate level, lower velocities are found in comparison with July–August 2012, especially at the southern entrance of the NGCU and at Vitiaz Strait. Salinity and nutrient distributions within the Solomon Sea appear to be similar to those found during July–August 2012, where an erosion of the salinity minimum (~0.05) is detected along the NGCU equatorward pathways.

Transports from the inversion technique provide realistic mean estimates during the two SPICE cruises, but it is worth comparing with plain geostrophy and adjusted and nonadjusted S-ADCP (Table A3). Across the southern entrance, the surface-1000 m cumulative geostrophic transport referenced to 1700 m is 30 Sv in July–August 2012. Nonadjusted S-ADCP transport is 31 Sv, partly including the negligible Ekman transport, with a difference compared to the adjusted S-ADCP transport of 5 Sv. In March 2014, the surface-to-1000-m geostrophic transport is also referenced to 1700 m (no data at deeper

depths) but reaches only 3 Sv, which represents ~30% of both S-ADCP estimates. Nonadjusted S-ADCP transport is 9 Sv, again with negligible Ekman and a difference of 2 Sv in adjusted transport. The gap between geostrophy and S-ADCP transports is the result of unaccounted transports of 7 Sv between the PNG coast and the first station, where the narrow NGCU carries most of the inflow.

b. How representative are the observed currents during both cruises with respect to climatology?

A strong transport variability was revealed between the two SPICE cruises that occurred during opposite seasons, especially at the surface and thermocline levels. This current seasonality inside the Solomon Sea has been discussed by Melet et al. (2010a,b), Cravatte et al. (2011), and Hristova and Kessler (2012), and our results are quite consistent with their findings. The seasonality results from a combination of basinwide forcings with different phasings, including equatorial dynamics, remotely forced Rossby waves, and monsoon winds. At the exit of Solomon Strait, the current variability is driven both by the annual cycle of the EUC and by remotely forced Rossby waves arriving east of the Solomon Islands. At the entrance of the Solomon Sea, the equatorward inflow seasonal variability is driven by the SEC transport variability south of 10°S, driven by a spinup and spindown of the subtropical gyre at annual time scales (Kessler and Gourdeau 2007). In March, the subtropical gyre spins down, leading to a decreased NVJ transport and a weaker flow entering into the Solomon Sea, consistent with what is observed during the MoorSPICE cruise. In contrast, the SEC arriving at the latitude east of the Solomon Strait is stronger, implying a weaker NICU, weaker currents exiting the Solomon Strait, and a weaker NBCU. A weaker Vitiaz transport is also expected, in part due to the monsoon winds and in part due to mass balance. The opposite situation is observed in July–August 2012 during the Pandora cruise, with a stronger inflow through the southern entrance and a stronger NGCU, NBCU, and NICU.

At the thermocline level (100–300 m), our results are also in good agreement with Cravatte et al. (2011), who observed a strengthening of the NGCU and its branches within the Solomon Sea during JJA and a weakening in DJF from observations. A modeling study (Melet et al. 2010a) has shown quite similar results, but with smaller seasonal variations and larger transport estimations in the straits.

At interannual time scales, a 2007–11 glider time series (Davis et al. 2012) and numerical simulations (Melet et al. 2013) indicated large LLWBC transport variations, as strong as the mean. In the model and the repeated glider transects, ENSO is identified as the main driving factor of the interior flow (direct NVJ) associated with increasing transports during El Niño and decreasing transports during La Niña. Previous studies (Melet et al. 2010b, 2013) suggest a correlation factor of −0.8 between peak ENSO phase and peak transports with a 3-month lag through the Solomon Sea at the surface and the upper thermocline. Neutral phases of ENSO even existed 3 months prior to both cruises (Fig. 1c), suggesting little ENSO influence on our transport estimates. Moreover, a modeling study (Melet et al. 2010a) inferred that transports through Vitiaz Strait are hydrodynamically constrained by bathymetry, especially during El Niño conditions (Melet et al. 2013); thus, enhanced transports were mainly found at the Solomon Strait exit, although this may have been dominated by the transient eddy phenomena during the cruises. Our results might suggest a less effective hydrodynamic constraint, as Vitiaz transports change by 100% between the cruises.

At higher frequency, large transport variations were observed at the southern entrance of the Solomon Sea from the 2007–11 glider time series over 0–700 m (see Fig. 2 of Davis et al. 2012) and a high-resolution model (see Fig. 7h of Djath et al. 2014) over 0–300 m. Within the Coral Sea, Kessler and Cravatte (2013a) highlighted the influence of mesoscale eddies in generating large current fluctuations and potential aliasing in cross-section transport estimates. A modeling study (see Fig. 12 of Hristova et al. 2014) identified small and intense surface eddies during JJA while larger and much weaker ones were found during DJF, such as the large and persistent cyclonic eddies found in March 2014 at the southern entrance, which strongly impact our transport estimate (>50% of the total 0–1000-m transport).

Thus, our transport estimates through an inversion model during both SPICE cruises appear to be mostly representative at seasonal time scales rather than at interannual time scales. The July–August 2012 cruise is related with JJA conditions whereas the March 2014 cruise is associated with DJF conditions.

c. How water mass properties within the LLWBCs evolve across the southwest Pacific?

Water masses entering the Solomon Sea from the Coral Sea exhibit different characteristics at different depth levels. They undergo significant transformations as shown in section 6, through mixing processes during their transit across the Solomon Sea. A modeling study (Melet et al. 2011) attributed these water mass transformations mostly to diapycnal mixing (~60%) rather than isopycnal mixing. In our model, vertical diffusivity estimates (κ_z) are not statistically significant to be realistic, and our results are mostly descriptive. A study based on CTD/L-ADCP data

from the two SPICE cruises (M. S. Alberty et al. 2016, unpublished manuscript) investigates the strength of diapycnal mixing and its causes in the Solomon Sea.

1) EQUATORWARD PATHWAYS OF THERMOCLINE WATERS

At the upper thermocline ($\sigma_\theta \sim 24.5$), two branches of SPTW can be traced across the Coral Sea from the subtropics (Gasparin et al. 2012, 2014; Grenier et al. 2013; Kessler and Cravatte 2013b) with a salinity gradient $\sim 7 \times 10^{-5}\,\mathrm{km}^{-1}$ (170°E–100°W; Johnson and McPhaden 1999). A SPTW branch with high salinity and relatively high oxygen originates from the subtropical central South Pacific around 20°S (Grenier et al. 2013). It enters into the Coral Sea north of Vanuatu, then flows within the direct NVJ to ultimately reach the Solomon Sea. A fresher SPTW branch with higher oxygen is formed by subduction in the subtropics around 30°S (Qu and Lindstrom 2002). It flows westward within the North Caledonian Jet (NCJ) into the Coral Sea (Gasparin et al. 2011) before feeding the GPC and ultimately the NGCU south of the Louisiade Archipelago. In our results, the two SPTW branches with their distinct signatures appear to merge south of Woodlark Island, inducing significant water mass modifications. During July–August 2012, the fresher and highly oxygenated SLW is carried along the NGCU pathways to the exiting straits with water property modifications (see section 6a) and is associated with a similar salinity gradient ($\sim 1 \times 10^{-4}\,\mathrm{km}^{-1}$) to that found across the subtropics. The salty waters carried by the direct NVJ are associated with a marginally stronger salinity gradient ($\sim 2 \times 10^{-4}\,\mathrm{km}^{-1}$) between the southern entrance and the Solomon Sea exits (Vitiaz, St Georges, and Solomon Straits). In March 2014, fresh NGCU waters exhibit a lower salinity gradient ($\sim 4 \times 10^{-5}\,\mathrm{km}^{-1}$) than during July–August 2012, suggesting weaker mixing processes associated with the NGCU at the thermocline level. The salty direct NVJ also exhibits lower salinity gradients ($\sim 5 \times 10^{-5}\,\mathrm{km}^{-1}$) between the southern entrance and the Solomon Sea exits, likely induced by mixing with surface waters caused by surface transient eddies (see section 5d).

2) EQUATORWARD PATHWAYS OF MODE WATERS

Below the thermocline, the SAMW is carried equatorward within the LLWBCs from the southeastern Pacific near $\sigma_\theta = 27.07$ with low salinity and high oxygen signatures (Grenier et al. 2013). Kessler and Cravatte (2013b) observed these water mass signatures entering the Coral Sea at $\sigma_\theta = 26.5$, corresponding to the 13°C waters, emanating northeast of New Zealand (Tsuchiya 1981; Qu et al. 2009). Across the subtropics, these 13°C waters are strongly related with the SAMW and the Eastern Subtropical Mode Water (ESTMW) through diapycnal mixing (Qu et al. 2009) and a salinity gradient $\sim 2 \times 10^{-5}\,\mathrm{km}^{-1}$ (Johnson and McPhaden 1999). They exhibit higher salinity and higher oxygen as they flow equatorward within the LLWBCs across the Coral Sea to the southern entrance of the Solomon Sea. Our results exhibit significant water mass transformations (see section 6b) as the 13°C waters flow across the Solomon Sea. In July–August 2012, the salty NGCU gets fresher along its equatorward pathways, with a stronger salinity gradient than across the subtropics from the southern entrance and Vitiaz Strait ($\sim 1 \times 10^{-4}\,\mathrm{km}^{-1}$). The salinity gradient from the entrance and northeast Solomon Sea exits (St Georges Channel and Solomon Strait) is 10 times higher than across the subtropics ($\sim 2 \times 10^{-4}\,\mathrm{km}^{-1}$), which is likely caused by strong diapycnal mixing south of Woodlark Island. In March 2014, the NGCU gets also fresher as it flows equatorward, but with lower salinity gradients that fall by 70% from the southern entrance and Vitiaz Strait and by 50% between the southern entrance and northeast exits. Hence, the weak NGCU that flows into the Solomon Sea in March 2014 is associated with less water mass transformation along its pathways across the Solomon Sea.

3) EQUATORWARD PATHWAYS OF INTERMEDIATE WATERS

At the intermediate level, the AAIW identified as a salinity minimum with high oxygen can be tracked along $\sigma_\theta = 27.2$ from the subtropical gyre to the Coral Sea before reaching the LLWBCs (Qu and Lindstrom 2002; Gasparin et al. 2012; Grenier et al. 2013; Kessler and Cravatte 2013b), with a salinity gradient $\sim 1 \times 10^{-5}\,\mathrm{km}^{-1}$ (Johnson and McPhaden 1999). Previous studies based on scattered observations (Tsuchiya 1991; Qu and Lindstrom 2004) tracked this salinity minimum (<34.5) within the Solomon Sea and beyond the equator without strong modifications. In our results, the AAIW undergoes significant transformations (see section 6c) through the erosion of its extrema in salinity and oxygen. During both cruises, the AAIW carried equatorward by the NGCU exhibits higher salinity gradients than across the subtropics ($\sim 3 \times 10^{-5}\,\mathrm{km}^{-1}$) from the southern entrance to Vitiaz Strait. However, the salinity gradient between the southern entrance and the northeast exits increased by 70% in March 2014, potentially induced by a salty inflow from the EqPIW. Furthermore, the AAIW layer shows significant mass transports across the Solomon Sea with significant variations between the July–August 2012 and the March 2014 cruises. Downstream in the Bismarck Sea, Zenk et al. (2005) found a mean AAIW velocity core ($\sim \sigma_\theta = 27.2$) near $20\,\mathrm{cm\,s}^{-1}$ from float observations over 1996–98.

TABLE A1. Potential density layers used to construct the inverse box model, which constraints on mass and silica budgets and dimensionless scaling factor applied to the heat and salt anomaly equations (see text for details; NC = not constrained) during July–August 2012 and March 2014 cruises. P and M abbreviate Pandora and MoorSPICE.

Layer	Upper (σ_θ, kg m^{-3})	Lower (σ_θ, kg m^{-3})	Mass (Sv rms)	Heat scaling	Salt scaling	Silica (kmolSi s^{-1})
1	Surface	22.5	2	NC	NC	NC
2	22.5	24	2	NC	NC	NC
3	24	25.5	2	0.4	0.05	NC
4	25.5	26	1	0.4	0.05	NC
5	26	26.5	1	0.4	0.05	NC
6	26.5	26.7	1	0.4	0.05	NC
7	26.7	26.9	1	0.4	0.05	NC
8	26.9	27	1	0.4	0.05	NC
9	27	27.1	1	0.4	0.05	NC
10	27.1	27.2	1	0.4	0.05	NC
11	27.2	27.3	1	0.4	0.05	NC
12	27.3	27.4	2	NC	NC	NC
Top to 1000 m	Surface	27.4	3	NC	NC	P: ± 147 M: ± 171

They estimated corresponding transports across hydrographic sections (October–November 1996) at 5 Sv into the western Bismarck Sea (near 146°E) and 2 Sv into the eastern Bismarck Sea (near 148°E). These estimates are consistent with our upstream results during July–August 2012, as shown in section 5. From a ~1.5-yr mooring time series (near 2.5°S, 142°E; from October–November 1996 to March 1998) and model results, Zenk et al. (2005) also found the NGCU vertically extended to the AAIW depth level and was associated with significant seasonal variations. Another mooring study (Kawabe et al. 2008) in the same area from 1998 to 2002 confirmed the NGCU seasonality at the AAIW depth level with high velocities during austral winter and weak velocities during austral summer. This is consistent with our results that suggest a reduced NGCU transport of almost 50% at the southern entrance of the Solomon Sea in March 2014.

Thus, our results show significant water mass transformations within the Solomon Sea, as they flow equatorward in the southwest Pacific LLWBC system. Salinity gradients within the Solomon Sea appear to be higher than across the whole subtropics from the Coral Sea to the eastern Pacific (170°E–100°W). These water mass transformations, mostly found south of Woodlark Island and likely induced by diapycnal mixing, impact downstream water masses through the NGCU, which is a main source to equatorial waters (Tsuchiya et al. 1989; Fine et al. 1994; Grenier et al. 2011).

4) WATER MASSES NORTHEAST OF BOUGAINVILLE ISLAND

One of the striking results from both cruises is the strong differences between water masses exiting Solomon Strait near New Ireland and those carried along the Bougainville eastern coast, as shown by tracers (see section 6). In July–August 2012, geochemical tracers such as aluminum, manganese, and iron also suggest these differences (Ganachaud et al. 2016, manuscript submitted to *Elementa*). During the two SPICE cruises, waters east of Bougainville are likely emanating from the equatorial Pacific, carried by the westward SEC or perhaps by an as-yet-unobserved northwestward Solomon Islands Coastal Undercurrent (SICU) found in a model study (Melet et al. 2010a). In March 2014, these equatorial Pacific waters are flowing into the Solomon Sea at the surface and intermediate level (see S-ADCP velocities, Fig. 4d). In July–August 2012, they do not seem to intrude into the Solomon Strait [see S-ADCP velocities in Fig. 4c and water properties in Fig. S9 in Ganachaud et al. (2016, manuscript submitted to *Elementa*)]. Waters exiting through Solomon Strait are likely flowing directly northwestward, without influencing waters farther east.

d. *Relation with the WWV*

Warm waters ($T > 20$°C) are found above 150 m depth ($\sigma_\theta = 24$) within the Solomon Sea, corresponding to the Tropical Surface Water (TSW; Table 1). As described in section 5, the two SPICE cruises depict a strong transport variability associated with these warm waters carried equatorward by the LLWBCs. This study highlights the crucial contribution of these LLWBCs for the warm water volume (WWV) recharge/discharge (e.g., Melet et al. 2013; Hu et al. 2015) with potential impacts on eastern equatorial heat fluxes.

e. *Limitations and perspectives*

Our analysis based on two oceanographic cruises is limited in many ways, giving a mean representation of

TABLE A2. Main currents across the Solomon Sea and associated volume transports (Sv) during July–August 2012 (Pandora) and March 2014 (MoorSPICE). Positive values are northward or eastward, and negative values are southward or westward. P and M abbreviate Pandora and MoorSPICE.

Main currents	Spatial extent	Upper (σ_θ, kg m^{-3})	Lower (σ_θ, kg m^{-3})	Transport estimates (Sv)
At the southern entrance:				
New Guinea Coastal	154°–155°E	24	27.4	P: 18
Undercurrent (NGCU)	154°–155°E	Surface	26.9	M: 12
North Vanuatu Jet (NVJ)	155°–159°E	24	26	P: 8
	155°–156°E	24	26	M: 4
Across Woodlark and New Britain Islands:				
New Guinea Coastal	7.5°–8.4°S	24	27.4	P: 16
Undercurrent (NGCU)	7.5°–8.4°S	24	27.4	M: 16
New Britain Coastal	5.4°–6.1°S	Surface	27.4	P: 28
Undercurrent (NBCU)	5.4°–6.1°S	24	27.4	M: 14
Across St Georges Channel and Solomon Strait:				
St Georges	152.35°–153°E	24	26.9	P: 6
Undercurrent (SGU)	152.35°–153°E	24	26.9	M: 4
North Ireland Coastal	153°–153.75°E	24	26.9	P: 6
Undercurrent (NICU)	153°–153.75°E	24	26.9	M: 3
Across Vitiaz Strait:				
New Guinea Coastal	147.58°–147.88°E	Surface	27.4	P: 19
Undercurrent (NGCU)	147.58°–147.88°E	Surface	27.4	M: 11

the ocean circulation whereas currents, such as the NGCU, are heavily influenced by transient eddies. To address this, and more generally the time variability, nine subsurface moorings were deployed in St Georges Channel and Vitiaz and Solomon Straits in July–August 2012, then recovered and redeployed during the March 2014 cruise before a final recovery in August 2015. These moored data will be used to assess the current variability and heat and salt fluxes through the exit straits of the Solomon Sea in a future study.

Acknowledgments. The Pandora and MoorSPICE cruises are contributions to the CLIVAR/SPICE and GEOTRACES International programs. The Pandora cruise has been cofunded by ANR (project ANR-09-BLAN-0233-01), INSU/LEFE, IRD, LEGOS, and NSF Grant OCE1029487. The MoorSPICE cruise has been cofunded by NSF Grant OCE1029487, ANR-09-BLAN-0233-01, and INSU/LEFE project Solwara. MoorSPICE data can be found through Cruise DOI:10.7284/903044. We are grateful to the crews of the R/V *Atalante* and *Thompson*. We are also grateful to the engineers, especially from the IRD US-IMAGO team and DT-INSU, and scientists who carefully sampled, recorded, and treated the data. This work benefited from stimulating and helpful comments from William S. Kessler and two anonymous reviewers to improve the manuscript. Meteorological data were freely downloaded from different databases: ASCAT (online at http://www.remss.com/missions/ascat), CMAP (online at http://www.esrl.noaa.gov/psd/data/gridded/data.cmap.html), and the SOI index (online at http://www.cpc.ncep.noaa.gov/data/indices/soi).

APPENDIX

Constraints and Volume

Constraints used to configure the inverse model are summarized in Table A1. Transport estimates by major

TABLE A3. Volume transport estimates (Sv) across the southern entrance transect from three methods—geostrophy, direct ADCP, and adjusted ADCP through inversion—during July–August 2012 (Pandora) and March 2014 (MoorSPICE). Positive values are northward and P and M abbreviate Pandora and MoorSPICE.

	Geostrophy (reference level at 1000 m)	Geostrophy (reference level at 1700 m)	Geostrophy (reference level at 1800 m)	Nonadjusted ADCP (before inversion)	Adjusted ADCP (after inversion)
P	17	30	31	31	36 ± 2.6
M	4	3	—	9	11 ± 2.6

currents within the Solomon Sea are provided in Table A2. Integrated transports from geostrophy, from direct ADCP, and after inversion across the southern entrance are provided in Table A3.

REFERENCES

Bostock, H. C., B. N. Opdyke, and M. J. Williams, 2010: Characterising the intermediate depth waters of the Pacific Ocean using δ^{13}C and other geochemical tracers. *Deep-Sea Res. I*, **57**, 847–859, doi:10.1016/j.dsr.2010.04.005.

Cravatte, S., A. Ganachaud, Q.-P. Duong, W. S. Kessler, G. Eldin, and P. Dutrieux, 2011: Observed circulation in the Solomon Sea from SADCP data. *Prog. Oceanogr.*, **88**, 116–130, doi:10.1016/j.pocean.2010.12.015.

Davis, R. E., W. S. Kessler, and J. T. Sherman, 2012: Gliders measure western boundary current transport from the South Pacific to the equator. *J. Phys. Oceanogr.*, **42**, 2001–2013, doi:10.1175/JPO-D-12-022.1.

Delcroix, T., M.-H. Radenac, S. Cravatte, G. Alory, L. Gourdeau, F. Léger, A. Singh, and D. Varillon, 2014: Sea surface temperature and salinity seasonal changes in the western Solomon and Bismarck Seas. *J. Geophys. Res. Oceans*, **119**, 2642–2657, doi:10.1002/2013JC009733.

Djath, B., J. Verron, A. Melet, L. Gourdeau, B. Barnier, and J.-M. Molines, 2014: Multiscale dynamical analysis of a high-resolution numerical model simulation of the Solomon Sea circulation. *J. Geophys. Res. Oceans*, **119**, 6286–6304, doi:10.1002/2013JC009695.

Donguy, J., and C. Henin, 1977: Origin of the surface tropical water in the Coral and Tasman Seas. *Mar. Freshwater Res.*, **28**, 321–332, doi:10.1071/MF9770321.

Fine, R. A., R. Lukas, F. M. Bingham, M. J. Warner, and R. H. Gammon, 1994: The western equatorial pacific: A water mass crossroads. *J. Geophys. Res.*, **99**, 25 063–25 080, doi:10.1029/94JC02277.

Ganachaud, A., 2003: Error budget of inverse box models: The North Atlantic. *J. Atmos. Oceanic Technol.*, **20**, 1641–1655, doi:10.1175/1520-0426(2003)020<1641:EBOIBM>2.0.CO;2.

——, and C. Wunsch, 2000: Improved estimates of global ocean circulation, heat transport and mixing from hydrographic data. *Nature*, **408**, 453–457, doi:10.1038/35044048.

——, L. Gourdeau, and W. Kessler, 2008: Bifurcation of the subtropical south equatorial current against New Caledonia in December 2004 from a hydrographic inverse box model. *J. Phys. Oceanogr.*, **38**, 2072–2084, doi:10.1175/2008JPO3901.1.

——, and Coauthors, 2014: The Southwest Pacific Ocean Circulation and Climate Experiment (SPICE). *J. Geophys. Res. Oceans*, **119**, 7660–7686, doi:10.1002/2013JC009678.

Gasparin, F., A. Ganachaud, and C. Maes, 2011: A western boundary current east of New Caledonia: Observed characteristics. *Deep-Sea Res. I*, **58**, 956–969, doi:10.1016/j.dsr.2011.05.007.

——, ——, ——, F. Marin, and G. Eldin, 2012: Oceanic transports through the Solomon Sea: The bend of the New Guinea Coastal Undercurrent. *Geophys. Res. Lett.*, **39**, L15608, doi:10.1029/2012GL052575.

——, C. Maes, J. Sudre, V. Garcon, and A. Ganachaud, 2014: Water mass analysis of the Coral Sea through an Optimum Multiparameter method. *J. Geophys. Res. Oceans*, **119**, 7229–7244, doi:10.1002/2014JC010246.

Grenier, M., S. Cravatte, B. Blanke, C. Menkes, A. Koch-Larrouy, F. Durand, A. Melet, and C. Jeandel, 2011: From the western boundary currents to the Pacific Equatorial Undercurrent: Modeled pathways and water mass evolutions. *J. Geophys. Res.*, **116**, C12044, doi:10.1029/2011JC007477.

——, C. Jeandel, F. Lacan, D. Vance, C. Venchiarutti, A. Cros, and S. Cravatte, 2013: From the subtropics to the central equatorial Pacific Ocean: Neodymium isotopic composition and rare earth element concentration variations. *J. Geophys. Res. Oceans*, **118**, 592–618, doi:10.1029/2012JC008239.

——, ——, and S. Cravatte, 2014: From the subtropics to the equator in the southwest Pacific: Continental material fluxes quantified using neodymium data along modeled thermocline water pathways. *J. Geophys. Res. Oceans*, **119**, 3948–3966, doi:10.1002/2013JC009670.

Hanawa, K., and L. D. Talley, 2001: Mode waters. *Ocean Circulation and Climate—Observing and Modelling the Global Ocean*, G. Siedler, J. Church, and J. Gould, Eds., International Geophysics Series, Vol. 77, Academic Press, 373–386, doi:10.1016/S0074-6142(01)80129-7.

Hasson, A., T. Delcroix, and J. Boutin, 2013: Formation and variability of the South Pacific Sea surface salinity maximum in recent decades. *J. Geophys. Res. Oceans*, **118**, 5109–5116, doi:10.1002/jgrc.20367.

Hristova, H. G., and W. S. Kessler, 2012: Surface circulation in the Solomon Sea derived from Lagrangian drifter observations. *J. Phys. Oceanogr.*, **42**, 448–458, doi:10.1175/JPO-D-11-099.1.

——, ——, J. C. McWilliams, and M. J. Molemaker, 2014: Mesoscale variability and its seasonality in the Solomon and Coral Seas. *J. Geophys. Res. Oceans*, **119**, 4669–4687, doi:10.1002/2013JC009741.

Hu, D., and Coauthors, 2015: Pacific western boundary currents and their roles in climate. *Nature*, **522**, 299–308, doi:10.1038/nature14504.

Johnson, G. C., and M. J. McPhaden, 1999: Interior pycnocline flow from the subtropical to the equatorial Pacific Ocean. *J. Phys. Oceanogr.*, **29**, 3073–3089, doi:10.1175/1520-0485(1999)029<3073:IPFFTS>2.0.CO;2.

Kawabe, M., Y. Kashino, and Y. Kuroda, 2008: Variability and linkages of New Guinea coastal undercurrent and lower equatorial intermediate current. *J. Phys. Oceanogr.*, **38**, 1780–1793, doi:10.1175/2008JPO3916.1.

Kessler, W. S., and L. Gourdeau, 2007: The annual cycle of circulation of the southwest subtropical Pacific, analyzed in an ocean GCM. *J. Phys. Oceanogr.*, **37**, 1610–1627, doi:10.1175/JPO3046.1.

——, 1999: Interannual variability of the subsurface high salinity tongue south of the equator at 165°E. *J. Phys. Oceanogr.*, **29**, 2038–2049, doi:10.1175/1520-0485(1999)029<2038:IVOTSH>2.0.CO;2.

——, and S. Cravatte, 2013a: ENSO and short-term variability of the south equatorial current entering the Coral Sea. *J. Phys. Oceanogr.*, **43**, 956–969, doi:10.1175/JPO-D-12-0113.1.

——, and ——, 2013b: Mean circulation of the Coral Sea. *J. Geophys. Res. Oceans*, **118**, 6385–6410, doi:10.1002/2013JC009117.

Kleeman, R., J. P. McCreary, and B. A. Klinger, 1999: A mechanism for generating ENSO decadal variability. *Geophys. Res. Lett.*, **26**, 1743–1746, doi:10.1029/1999GL900352.

Lee, T., and I. Fukumori, 2003: Interannual-to-decadal variations of tropical-subtropical exchange in the Pacific Ocean: Boundary versus interior pycnocline transports. *J. Climate*, **16**, 4022–4042, doi:10.1175/1520-0442(2003)016<4022:IVOTEI>2.0.CO;2.

Lindstrom, E., R. Lukas, R. A. Fine, J. S. Godfrey, G. Meyers, and M. Tsuchiya, 1987: The Western Equatorial Pacific Ocean Circulation Study. *Nature*, **330**, 533–537, doi:10.1038/330533a0.

——, J. Butt, R. Lukas, and S. Godfrey, 1990: The flow through Vitiaz Strait and St. George's Channel, Papua New Guinea. *The Physical Oceanography of Sea Straits*, L. J. Pratt, Ed., NATO ASI Series, Vol. 318, Springer, 171–189, doi:10.1007/978-94-009-0677-8_7.

Macdonald, A. M., and C. Wunsch, 1996: An estimate of global ocean circulation and heat fluxes. *Nature*, **382**, 436–439, doi:10.1038/382436a0.

McCartney, M., 1977: Subantarctic mode water. *A Voyage of Discovery: George Deacon 70th Anniversary Volume*, M. Angel, Ed., Pergamon Press, 103–119.

McCreary, J. P., and P. Lu, 1994: Interaction between the subtropical and equatorial ocean circulations: The subtropical cell. *J. Phys. Oceanogr.*, **24**, 466–497, doi:10.1175/1520-0485(1994)024<0466:IBTSAE>2.0.CO;2.

Melet, A., L. Gourdeau, W. S. Kessler, J. Verron, and J.-M. Molines, 2010a: Thermocline circulation in the Solomon Sea: A modeling study. *J. Phys. Oceanogr.*, **40**, 1302–1319, doi:10.1175/2009JPO4264.1.

——, ——, and J. Verron, 2010b: Variability in Solomon Sea circulation derived from altimeter sea level data. *Ocean Dyn.*, **60**, 883–900, doi:10.1007/s10236-010-0302-6.

——, J. Verron, L. Gourdeau, and A. Koch-Larrouy, 2011: Equatorward pathways of Solomon sea water masses and their modifications. *J. Phys. Oceanogr.*, **41**, 810–826, doi:10.1175/2010JPO4559.1.

——, L. Gourdeau, J. Verron, and B. Djath, 2013: Solomon Sea circulation and water mass modifications: Response at ENSO timescales. *Ocean Dyn.*, **63**, 1–19, doi:10.1007/s10236-012-0582-0.

Murray, S., E. Lindstrom, J. Kindle, and E. Weeks, 1995: Transport through the Vitiaz Strait. *WOCE Notes*, Vol. 7, No. 1, 21–23.

Olbers, D., and C. Eden, 2013: A global model for the diapycnal diffusivity induced by internal gravity waves. *J. Phys. Oceanogr.*, **43**, 1759–1779, doi:10.1175/JPO-D-12-0207.1.

Qu, T., and E. J. Lindstrom, 2002: A climatological interpretation of the circulation in the western South Pacific. *J. Phys. Oceanogr.*, **32**, 2492–2508, doi:10.1175/1520-0485-32.9.2492.

——, and ——, 2004: Northward intrusion of Antarctic Intermediate Water in the western Pacific. *J. Phys. Oceanogr.*, **34**, 2104–2118, doi:10.1175/1520-0485(2004)034<2104:NIOAIW>2.0.CO;2.

——, S. Gao, I. Fukumori, R. A. Fine, and E. J. Lindstrom, 2008: Subduction of South Pacific waters. *Geophys. Res. Lett.*, **35**, L02610, doi:10.1029/2007GL032605.

——, ——, ——, ——, and ——, 2009: Origin and pathway of equatorial 13°C water in the Pacific identified by a simulated passive tracer and its adjoint. *J. Phys. Oceanogr.*, **39**, 1836–1853, doi:10.1175/2009JPO4045.1.

——, ——, and R. A. Fine, 2013: Subduction of South Pacific tropical water and its equatorward pathways as shown by a simulated passive tracer. *J. Phys. Oceanogr.*, **43**, 1551–1565, doi:10.1175/JPO-D-12-0180.1.

Roemmich, D., and B. Cornuelle, 1992: The subtropical mode waters of the South Pacific Ocean. *J. Phys. Oceanogr.*, **22**, 1178–1187, doi:10.1175/1520-0485(1992)022<1178:TSMWOT>2.0.CO;2.

Schmidtko, S., G. C. Johnson, and J. M. Lyman, 2013: MIMOC: A global monthly isopycnal upper-ocean climatology with mixed layers. *J. Geophys. Res. Oceans*, **118**, 1658–1672, doi:10.1002/jgrc.20122.

Sokolov, S., and S. Rintoul, 2000: Circulation and water masses of the southwest Pacific: WOCE section P11, Papua New Guinea to Tasmania. *J. Mar. Res.*, **58**, 223–268, doi:10.1357/002224000321511151.

Tomczak, M., and D. Hao, 1989: Water masses in the thermocline of the Coral Sea. *Deep-Sea Res.*, **36A**, 1503–1514, doi:10.1016/0198-0149(89)90054-X.

Tsuchiya, M., 1981: The origin of the pacific equatorial 13°C water. *J. Phys. Oceanogr.*, **11**, 794–812, doi:10.1175/1520-0485(1981)011<0794:TOOTPE>2.0.CO;2.

——, 1991: Flow path of the Antarctic Intermediate Water in the western equatorial South Pacific Ocean. *Deep-Sea Res.*, **38A**, S273–S279, doi:10.1016/S0198-0149(12)80013-6.

——, R. Lukas, R. A. Fine, E. Firing, and E. Lindstrom, 1989: Source waters of the Pacific Equatorial Undercurrent. *Prog. Oceanogr.*, **23**, 101–147, doi:10.1016/0079-6611(89)90012-8.

Wunsch, C., 1996: *The Ocean Circulation Inverse Problem.* Cambridge University Press, 442 pp.

Wyrtki, K., 1962: The subsurface water masses in the western South Pacific Ocean. *Mar. Freshwater Res.*, **13**, 18–47, doi:10.1071/MF9620018.

Zenk, W., G. Siedler, A. Ishida, J. Holfort, Y. Kashino, Y. Kuroda, T. Miyama, and T. J. Müller, 2005: Pathways and variability of the Antarctic Intermediate Water in the western equatorial Pacific Ocean. *Prog. Oceanogr.*, **67**, 245–281, doi:10.1016/j.pocean.2005.05.003.

Zilberman, N., D. Roemmich, and S. Gille, 2013: The mean and the time variability of the shallow meridional overturning circulation in the tropical South Pacific Ocean. *J. Climate*, **26**, 4069–4087, doi:10.1175/JCLI-D-12-00120.1.

4.4 Conclusions and unresolved issues

Mean thermocline and intermediate pathways across the Solomon Sea were examined during July-August 2012 (Pandora) and March 2014 (MoorSPICE) from a new inverse model configuration that was never tested so far to our knowledge. We used measured S-ADCP currents as a first guess, rather than geostrophic currents derived from direct T-S measurements through the thermal wind equation. We also examined the strait transport partitions at the northern exits of the sea, as well as the water properties and their transformations of the LLWBC pathways. The major results of this study are:

- The mean circulations during July-August 2012 and March 2014 are strongly related with the seasonal cycle rather than interannual time scales, with enhanced LLWBC transports in austral winter
- At the southern entrance, surface to 1000 m transport is 36 Sv in July-August 2012, and fell down by 70% to 11 Sv in March 2014
- The seasonal transport variability is smaller at Vitiaz Strait but still 40% (19 to 11 Sv), while most of the NGCU seasonal fluctuations are associated with the NBCU, especially at Solomon Strait
- Distinct water mass signatures can be traced along the WBC pathways across the Solomon Sea, and undergo significant transformations through evident erosion of salinity ($\sim$0.05) and oxygen extrema at both the thermocline and intermediate levels
- Within the Solomon Sea, isopycnal salinity gradients are gradually stronger than within the subtropical Pacific, likely induced by enhanced vertical mixing

Important unresolved issues remain from this study, especially regarding the large mixing processes that cause the observed water mass transformations across the Solomon Sea. Numerical simulations suggested a large contribution from diapycnal mixing, and partly from tidal mixing that both need to be verified and clearly quantified from in situ observations, although direct measurements, such as those from microstructure profilers, are not available. A dedicated study (*Alberty et al.*, 2016) aims to examine spatial mixing patterns in the Solomon Sea based on observations from the Pandora and MoorSPICE cruises and the Argo database. Two indirect methods (the Thorpe scale and finescale parameterization) are used to estimate turbulent dissipation rates (ϵ). The results indicate much higher dissipation in the Solomon Sea than elsewhere in the equatorial Pacific, with enhanced patterns of ϵ during July-August 2012 (the strong trade season).

In addition, the large western boundary current variability at different time scales across the Solomon Sea is also a major unresolved issue, and thus stimulated the deployment of nine subsurface moorings at the northern exit passages to better understand the intraseasonal and seasonal cycles of these currents (Chapter 6).

Chapter 5

The Deep circulation in the Solomon Sea

Contents

5.1 Introduction

The water masses of the deep Pacific ocean have long been known to originate from the Southern Ocean. They do not derived directly from abyssal Antarctic waters but from the shallower Circumpolar Deep Water (CDW), identified as a mixture of Antarctic waters with salty, oxygen-rich and nutrient-poor deep waters carried from the North Atlantic (*Mantyla and Reid*, 1983). First sketchy pictures of the CDW pathways and associated water properties were presented in several studies since the mid-1960s (e.g. *Wyrtki*, 1961; *Reid and Lynn*, 1971; *Mantyla and Reid*, 1983). The CDW appeared to be modified by mixing with less salty overlying waters, as it extended northward across the Pacific Ocean.

A few studies have estimated northward transport of the CDW through the Southwest Pacific. *Reid* (1986) and *Taft et al.* (1991) suggested 8 to 12 Sv below 2500 m from waters coming along the Tonga-Kermadec Ridge (Figure 5.1). Further north, the CDW crosses the Samoan Passage before reaching the western equatorial Pacific as a deep western boundary current (DWBC), and ultimately the North Pacific (Figure 5.1). *Taft et al.* (1991) estimated an inflow into the Samoan Passage of 6 Sv for waters deeper than 3500 m, assuming that only flow above 4800 m can exit the northern Samoa Basin because of bathymetric constraints.

Major advancements were then made from the World Ocean Circulation Experiment (WOCE) conducted in the 1990s, including refined descriptions of near bottom pathways of the CDW (e.g. *Roemmich et al.*, 1996; *Reid*, 1997; *Tsimplis et al.*, 1998; *Wijffels et al.*, 2001; *Ganachaud*, 2003b). Salinity and oxygen characteristics are found to be higher in the South Pacific, associated with lower nutrient concentrations. These distinct water properties gave more insights about the CDW pathways across the western equatorial region and then in the North Pacific, where a return flow was identified at intermediate depths as part of the extended cyclonic gyre (*Reid*, 1997). The WOCE observations also provided refined northward transports (e.g. *Roemmich et al.*, 1996; *Rudnick*, 1997; *Tsimplis et al.*, 1998) through the Southwest Pacific basin ($\sim$12 Sv), and first transport estimates of the global Pacific deep circulation (e.g. *Wijffels et al.*, 2001; *Ganachaud*, 2003b), that were in the range of 16 to 20 Sv.

Despite significant efforts since the WOCE program, the deep circulation in the Southwest Pacific remains poorly understood, especially in areas with complex bathymetry, such as the Coral Sea and Solomon Sea basins. These areas are tightly related with the meridional overturning circulation, associated with small-scale turbulent mixing supported by the breaking of internal waves (e.g. *Nikurashin and Ferrari*, 2009; *Olbers and Eden*, 2013), and where upwellings might occur. It is therefore important to depict a more accurate picture of the deep pathways in the Solomon Sea region, as they may contribute to the deep western boundary current system, and so to the overall circulation in the Pacific Ocean.

The present chapter takes advantages of the measurements collected during the July-August 2012 and March 2014 cruises to describe the deep circulation and associated water properties in the Solomon Sea, using an inverse model to provide quantitative transport estimates with uncertainties.

5.2 The Pacific Ocean deep pathways: an overview

The Circumpolar Deep Water is typically divided in two layers, the Upper Circumpolar Deep Water (UCDW) and the Lower Circumpolar Deep Water (LCDW) emanating from the Antarctic Circumpolar Current (ACC), southeast of New Zealand. The UCDW is typically detected between 1000 and 2000 m within the ACC through an increase in salinity, relatively low oxygen and high nutrient concentrations (*Callahan*, 1972). The transition to the LCDW corresponds to an increase in salinity and a decrease in silica around 2000 m in the Southern Ocean (*Warren*, 1973; *Orsi et al.*, 1999). Both water mass routes are still only approximately understood.

From previous observations (e.g. *Reid*, 1997; *Tsimplis et al.*, 1998; *Kawabe and Fujio*, 2010), the UCDW is conveyed by the anticyclonic flow in the Southwest Pacific, taking a detour around the subtropical gyre and reaching the equatorial western Pacific (Figure 5.1). UCDW enters the North Pacific east of the Solomon Rise and flows westward by the East and West Caroline basins and partly via the East Mariana Basin, before reaching the Philippine Sea Basin. Then, UCDW flows east-southeastward towards the Hawaiian Ridge, while the North Pacific Deep Water (NPDW; see Section 5.5) turns in the same direction further north, near 30°N. Both waters mix around the Hawaiian Ridge to form a modified NPDW that proceeds southeastward in the eastern Pacific before encountering the South American coast, and flowing back into the ACC via the drake Passage (*Talley et al.*, 2007).

The LCDW (referred to as the deeper CDW in past studies) is characterized by a salinity maximum, a silica minimum (*Warren*, 1973; *Orsi et al.*, 1999) and relatively high oxygen content (*Johnson and Toole*, 1993; *Siedler et al.*, 2004), and mostly encompasses Antarctic Bottom Water (AABW) according to *Johnson* (2008). This lower deep layer is typically found in the South Pacific (north of the mid-latitudes) at depths greater than approximately 3500 m (*Kawabe et al.*, 2003). It flows northward via complex pathways to the east of the Tonga-Kermadec Ridge, then to the Central Pacific Basin through the Samoan Passage (e.g. *Roemmich et al.*, 1996; *Rudnick*, 1997). The flow of LCDW splits into the western ($\sim$4 Sv) and the eastern branches ($\sim$8 Sv), as it proceeds northward within the Central Pacific Basin. Both branches ultimately join the Northeast Pacific Basin via intricate pathways, mostly constrained by bathymetry (Figure 2c of *Kawabe and Fujio*, 2010 for detailed pathways). On its northern route, the LCDW accumulates silica from bottom sediments (*Toole et al.*, 1994; *Roemmich et al.*, 1996), associated with a decrease in oxygen before being upwelled in the upper deep layers and transformed into NPDW in the northeastern Pacific (*Reid*, 1997; *Talley et al.*, 2007).

5.3 Topographic constraints of the South Pacific Ocean

The bathymetry of the South Pacific region is quite complex with a large number of deep basins (Figure 5.1), which are either close to the north or to the south, and provide constraints to the flow of deep waters. The Tasman Basin, located between the Australian east coast extends to about 55°S, and is closed to the north at depths greater than 3000 m (Figure 5.1). The two deep waters (UCDW and LCDW) enter the Tasman Basin, thought the LCDW is blocked around 20°S into the Tasman Abyssal Plain (*Reid*, 1997; *Tsimplis et al.*, 1998). Further north, the Coral Sea Basin (Figure 5.2) has an abyssal plain with depths greater than 4000 m, and is connected with the New Hebrides Basin, north of New Caledonia (Figure 5.2) through a narrow channel (the Pocklington Trough) extending to the northeast with a depth of more than 3500 m.

The Solomon Sea Basin is closed to the north below 3000 m, and it is divided into two basins by a ridge with a sill depth of ∼3500 m (Figure 5.2). South, the basin is connected with the New Hebrides Basin by the South Solomon Trench that runs along the Solomon Islands. However, the Solomon Sea Basin is closed to the east at depths of about 3500 m, and so it is no longer connected with the Central Pacific Basin (Figure 5.1). South of 20°S, the New Caledonian Trough and the South Fiji Basin are closed to the south below 3000 m, while the Southwest Pacific Basin is constrained below 4000 m to the west mostly by the Kermadec-Tonga Ridge, and to the east by the East Pacific Rise (Figure 5.1).

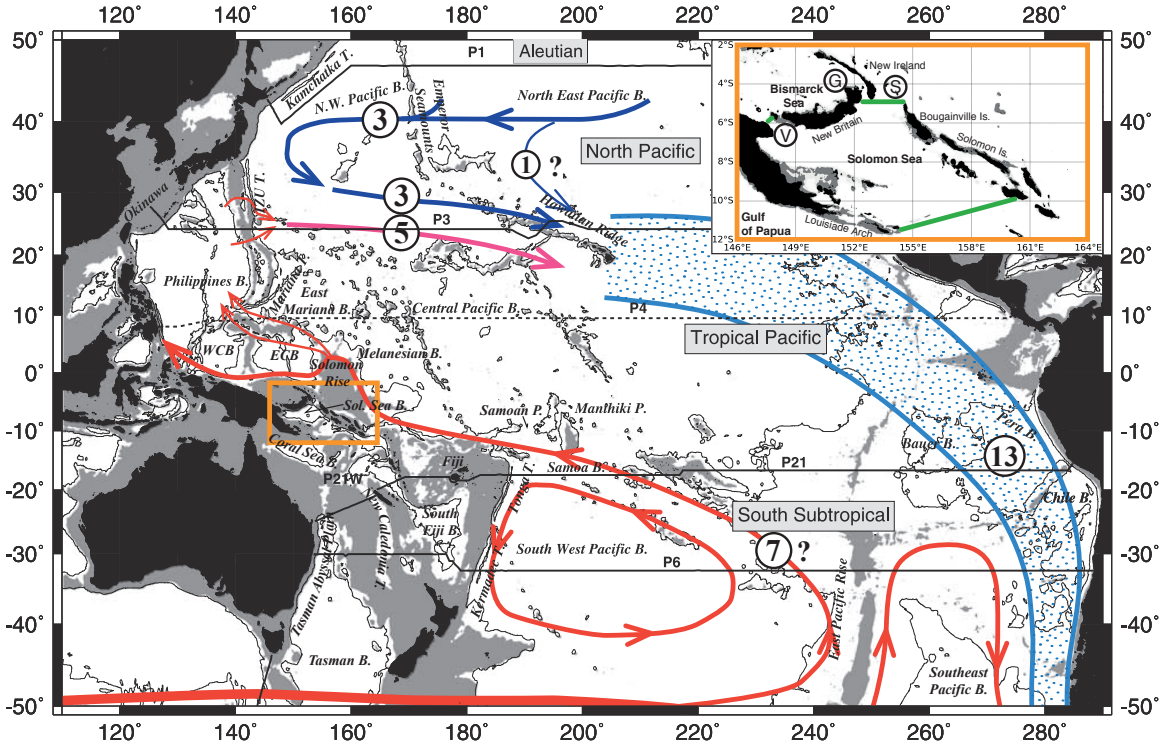

Figure 5.1 – Map of the Pacific Ocean (adapted from *Ganachaud*, 2003b) showing the Solomon area enclosed as an orange square. Areas shallower than 3000 m are shaded and the 4000 m isobath is contoured. The pre-WOCE sections P1, P3 and P4 and the WOCE sections P21 (April-June 1994) and P6 (May-July 1992) are indicated. WCB=West Carolina Basin; ECB=East Carolina Basin. The inset shows the transects defining the boundaries (green lines) of the "deep" inverse model; the circled "V", "S" and "G" represent Vitiaz and Solomon Straits, and St Georges Channel, respectively. Arrows indicate schematic pathways of the Upper Circumpolar Deep Water (UCDW) in red, the North Pacific Deep Water (NPDW) in blue, while the large blue dotted line indicate the modified return flow of NPDW (based on Figure 2b of *Kawabe and Fujio*, 2010). Circled numbers show upwelling volume transports in Sv (10^6 $m^3.s^{-1}$) at depths of 2000 to 3500 m (from *Kawabe and Fujio*, 2010).

5.4 Data an Model

5.4.1 Hydrographic data

The deep water mass properties are investigated using the CTD-O_2 and bottle measurements collected during the two SPICE cruises (see Chapter 2) along with historical data from the world Ocean Database 2013 (WOD13).

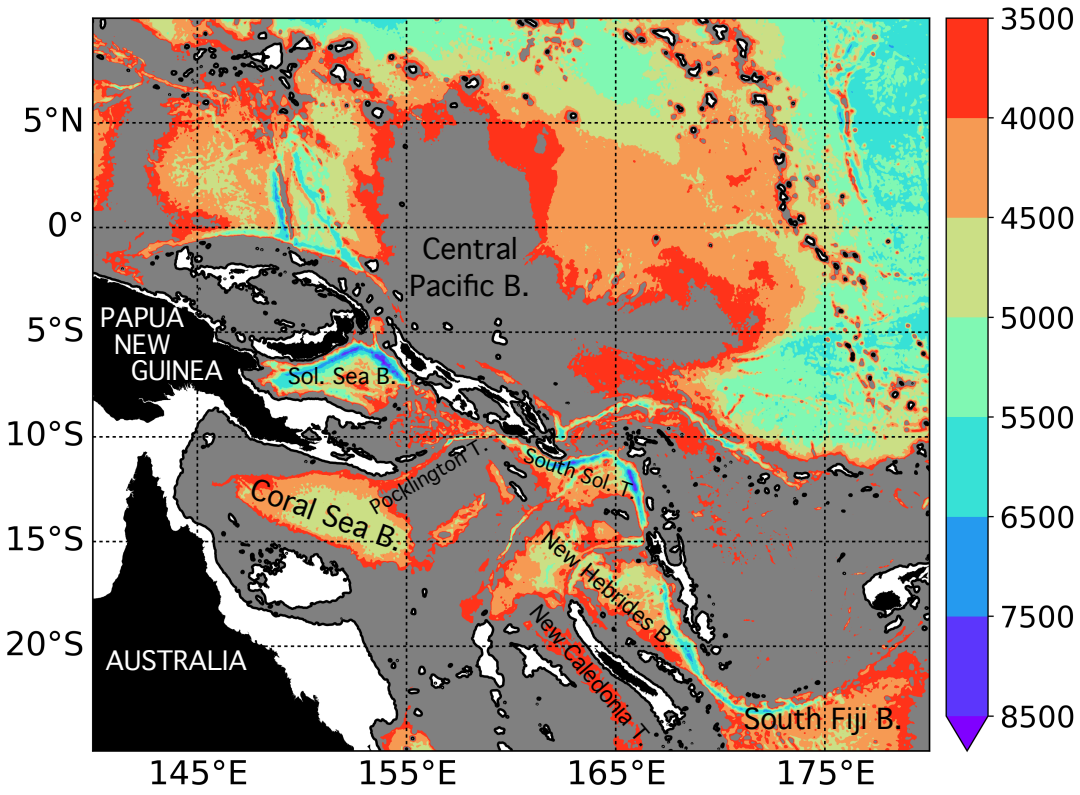

Figure 5.2 – Southwest Pacific bathymetry at depths greater than 3500 m (color scale, meters). The 1000 m contour (black line) is shown. Areas shallower than 1000 m are in white. Grey shading shows areas deeper than 1000 m and shallower than 3500 m.

The data set provides measurements of salinity, temperature, oxygen and nutrients collected during oceanographic cruises. Data were quality controlled, including individual flag values over 137 standard depth levels, from the surface to 5500 m depth.

5.4.2 The "deep" inverse model

This model configuration is designed to estimate deep reference-level velocities and associated transports along three hydrographic transects enclosing the Solomon Sea (see inset, Figure 5.1). From the surface to 1000 m, the gridded S-ADCP velocity field is used as a first guess, with similar isopycnal layers than those from the "shallow" configuration.

At the southern entrance at depths where S-ADCP is not available, we used geostrophic currents calculated between station pairs, and then interpolated on the S-ADCP grid using a Gaussian weighting function. A vertical smoothing was performed using a moving average filter to avoid large discontinuities at the transition between between S-ADCP and geostrophy (∼1000 m). The S-ADCP part was rotated to be perpendicular to the transect, then combined with the geostrophic velocity field. For the geostrophic part, the initial reference velocities were taken at 0 ± 5 $cm.s^{-1}$, with a 1700 m reference level (i.e. deepest common depth) during both cruises. Potential density surfaces used to constrain the inverse model encompass the UCDW that was split into two distinct water masses, the $UCDW_{upper}$ and $UCDW_{lower}$ (Table 5.1). The St Georges Channel and Solomon Strait are expected to be influenced by strong internal wave activity from tides.

Therefore, I decided to use below 1000 m, the L-ADCP velocity measurements recorded along the St Georges-Solomon transect rather than geostrophy to avoid again, temporal displacements of ispopycnals. Besides, no spurious L-ADCP deep currents such as those found at the southern entrance were detected (see Chapter 2). L-ADCP velocities were interpolated on the S-ADCP grid, using again a Gaussian weighting function after rotating the S-ADCP part. Initial velocity uncertainties are also set to $\pm 5\ cm.s^{-1}$ for the St Georges-Solomon transect.

Freshwater and Ekman transport estimates are set based on the "shallow" inverse configuration (see Chapter 4), as well as a priori values of cross isopycnal transfers and vertical diffusion coefficients (i.e. w and κ_z, respectively). Silica is conserved from the surface down to the deepest layers (1-25 during Pandora, and 1-21 during MoorSPICE) but not within individual layers, as silica content is expected to be nearly conservative within a top to bottom oceanic volume enclosed by hydrographic transects (*Ganachaud and Wunsch*, 2002). A priori uncertainties on mass were set following the "shallow" configuration, with larger uncertainties ($\pm 2\ Sv$) near the surface (layers 1-3) and in the deepest layer, allowing exchanges with the abyssal ocean. Heat and salt were also not conserved in the upper and last layers, using anomaly equations and associated scaling factors.

Table 5.1 – Water masses and associated volume transports (Sv) during July-August 2012 and March 2014. Positive values are northward, negative values are southward and uncertainties are one standard deviation. Transport estimates between the lower and upper parts of the UCDW do not entirely sum up, induced by diapycnal fluxes to surrounding layers and residual noise.

Upper[1]	*Lower*[1]	Water mass	Southern entrance	St Georges-Solomon
27.4	27.65	Upper Circumpolar Deep Water	$\mathbf{P}^2$: 5.5 ± 1.6	6.1 ± 1.4
(∼*1000 m*)	(∼*2000 m*)	(*upper extent*)	$\mathbf{M}^3$: 2.7 ± 1.3	-0.2 ± 1
27.65	27.76	Upper Circumpolar Deep Water	$\mathbf{P}^2$: 3 ± 2	2 ± 1.9
(∼*2000 m*)	(∼*3200 m*)	(*lower extent*)	$\mathbf{M}^3$: 1.6 ± 0.7	3.3 ± 1.1

[1] $\sigma_\theta, kg.m^{-3}$

[2] Pandora

[3] MoorSPICE

5.5 Deep water mass properties

In order to place both SPICE cruises into context, historical measurements of salinity (Figure 5.4), dissolved oxygen (Figure 5.5), silica (Figure 5.6) and nitrate (Figure 5.7) are shown over the Southwest Pacific region from the WOD13 climatology (colored dots), overlaid by the corresponding tracers measured during each cruise (colored stars) at depths that encompass the UCDW. The different tracers are firstly displayed along σ_θ=27.4 (∼1000 m north of 12°S), which corresponds to the lower limit of the intermediate layer characterized by the AAIW.

Below, we chose to display water property distributions at 2000 and 3000 m depth levels rather than along potential density (i.e. σ_2 and σ_3) or neutral density surfaces to compare those properties with past studies; though this is less accurate, the depth of both σ_2 and σ_3 isopycnals along the WOCE section P11[1] exhibit small variations (<100 m) between 50°-12°S.

[1] see WOCE Atlas Volume 2: Pacific Ocean, online at https://doi.org/10.21976/C6WC77

Phosphate concentrations (Appendix C1) are not discussed here, as they are found to be well correlated with nitrate, and so provide little additional information. Temperature distributions (Appendix C2) are generally in good agreement with salinity and oxygen distributions.

5.5.1 The upper deep layers

The isopycnal σ_θ=27.4 level marks the transition from the AAIW to the upper deep waters, as salinity and nutrient concentrations increase in the Solomon Sea region (Figure 5.3). Salinity signatures (Figure 5.4a,b) exhibit relatively high salinity (>34.5) carried by the westward stream of the South Equatorial Current (SEC), that has been previously detected as deep as 1000 m near 15°S (*Gourdeau et al.*, 2008) across the Coral Sea. At 2000 m, saltier waters (Figure 5.4c,d) are traced either from the Coral Sea Basin, or eastward from the New Caledonia Trough and the New Hebrides and South Fiji basins (Figure 5.2) before entering into the Solomon Sea. The Vitiaz Strait is closed at this depth, interbasin exchanges are possible through Solomon Strait, where fresher waters are observed during both cruises (Figure 5.4c,d).

Similarly, oxygen (Figure 5.5a,b) and potential temperature (Appendix C2a,b) patterns associated with SEC origins are observed at σ_θ=27.4 within the Solomon Sea, though WOD13 exhibit slightly higher values at the southern entrance than those from the two cruise data. At 2000 m, high oxygen (Figure 5.5c,d) can also be traced from the New Caledonia Trough and the New Hebrides and South Fiji basins. At Solomon Strait and within the mid-basin, lower oxygen concentrations ($\sim$130 μmol.kg^{-1}) suggest water mass modifications, potentially explained by either by isopycnal or diapycnal mixing with equatorial waters from the West and East and Carolina basins.

Silica (Figure 5.6a,b) and nitrate (Figure 5.7a,b) exhibit common features at σ_θ=27.4 between both cruises and historical data. Lowest nitrate concentrations are found within the Solomon Sea, possibly carried by the SEC, which is associated with similar nitrate values as it enters into the Coral Sea $\sim$15°S. At 2000 m, both silica (Figure 5.6c,d) and nitrate (Figure 5.7c,d) exhibit different distributions between both cruises, with lower concentrations within the mid-basin and at the southern entrance during July-August 2012 than during March 2014.

These different property distributions suggest that waters flowing around 2000 m into the Solomon Sea are likely emanating from the eastern Coral Sea region. In the equatorial western Pacific, distinct water properties are observed with low salinity, low oxygen and high nutrient concentrations. Previous studies found similar characteristics (*Johnson and Toole*, 1993; *Reid*, 1997; *Siedler et al.*, 2004), indicating the influence of the North Pacific Deep Water (NPDW) in the Mariana and Caroline basins (Figure 5.1). The NPDW is formed through mixing as LCDW upwells in the Northeast Pacific, with the imprint of strong silica (>130 μmol.kg^{-1}) from the seabed (*Talley and Joyce*, 1992). It then flows westward through the Hawaiian Ridge before feeding both West and East Mariana Basins (*Wijffels et al.*, 1996).

Thus, deep waters flowing around 2000 m in the Solomon Sea region are possibly related with a mixture between UCDW and NPDW, at least during the March 2014 cruise where high silica concentrations are measured.

Furthermore, the Bismarck Sea is closed to the surrounding basins below 2000 m, and so exchanges with surrounding waters might only occur through vertical mixing. Measurements from the March 2104 cruise display distinct water property distributions within the basin, such as lower salinity (34.61-34.62), lower oxygen (<113 μmol.kg^{-1}), higher potential temperature (>2.4°C) and lower silica (<130 μmol.kg^{-1}).

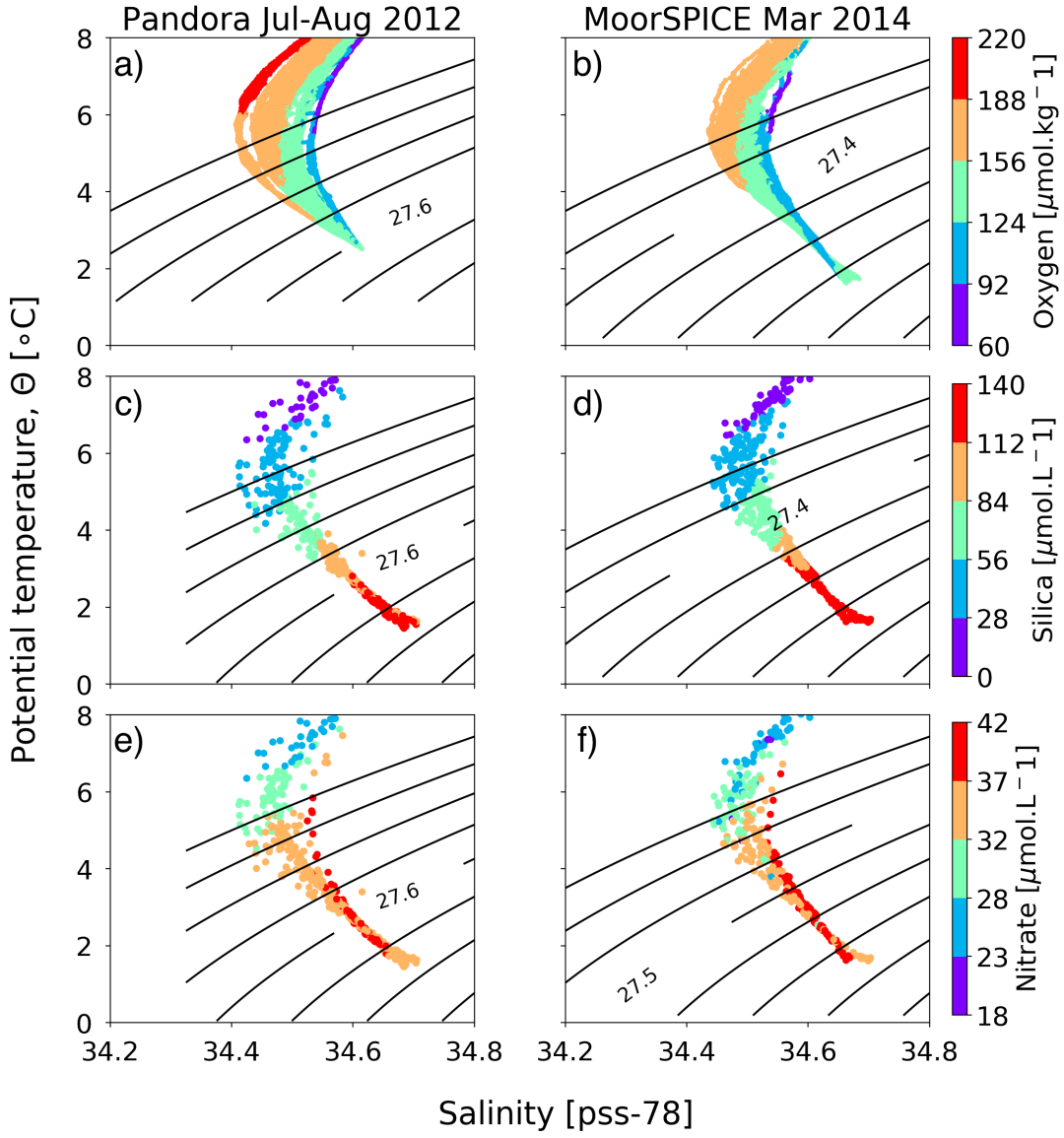

Figure 5.3 – Θ-S diagrams during (left) July-August 2012; (right) Mars 2014, color-coded by (a),(b) oxygen; (c),(d) silica and (e),(f) nitrate concentrations.

5.5.2 The lower deep layers

During both cruises, only few measurements were collected within the Solomon Sea to detect the possible transition from the Upper to the Lower CDW (i.e. at depths greater than 3000 m). Those measurements have been carried out south of New Ireland, at the Solomon Strait and at stations 47 and 48 (∼8°S-156°E) during the MoorSPICE cruise (Figure A1a,b). Water property distributions at 3000 m down to 3500 m, are found to be consistent with the LCDW characteristics (see Section 5.2).

At 3000 m depth, salinity (Figure 5.4e,f) increases with values ranging from 34.68 to 34.70 (up to 0.08 saltier than at 2000 m) within the Solomon Sea. Similar salinity distributions are found in the New Caledonia Trough and the Coral Sea Basin, while lower salinity (<34.68) are found in the South Fiji Basin. Deep waters are even saltier (>34.71) in the Tasman Basin, however, they are not directly connected to the Southwest Pacific Basin at those depths (see Section 5.3), but upwelling in the upper deep layers in the Coral Sea Basin might occur. During the July-August 2012 cruise, silica distributions (Figure 5.6e,f) exhibit low concentrations (<110 μmol.kg^{-1}) at the southern entrance, likely coming from the Coral Sea via the Pocklington Trough (Figure 5.2).

In contrast, silica concentrations are greater than 140 μmol.kg^{-1} in March 2014, which suggest a possible deep water inflow coming from the Central Pacific Basin, or diapycnal mixing with upper silica-rich layers. Lindstrom and Hayes (1989)[2] found consistent silica content in the Coral Sea Basin (<110 μmol.kg^{-1}) and the South Solomon Through (∼135 μmol.kg^{-1}) at depths greater than 3500 m, as part of the Transports of Equatorial Waters (TEW) program[3].

The distribution of oxygen (Figure 5.5e,f) exhibits relatively high concentrations (>150 μmol.kg^{-1}) at the southeast entrance of the Solomon Sea, likely originating from the New Caledonia Trough or the South Fiji Basin, where similar oxygen signatures are observed. Potential temperature distributions (Appendix C2e,f) ranging from 1.62° to 1.7°C also support this view.

At depths of 3200 and 3500 m (not shown), the measurements from both cruises and the WOD13 data display consistent tracer signatures than those at 3000 m depth, which may indicate the upper limit of the LCDW with southern origins from the New Caledonia Trough and the South Fiji Basin; though bathymetric constraints warrant further investigation to infer more precisely the LCDW pathway across the Southwest Pacific (see Section 5.7).

[2]contribution to the Klaus Wyrtki Symposium on ocean circulation and air-sea interactions, unpublished manuscript

[3]NOAA research program conducted in 1987

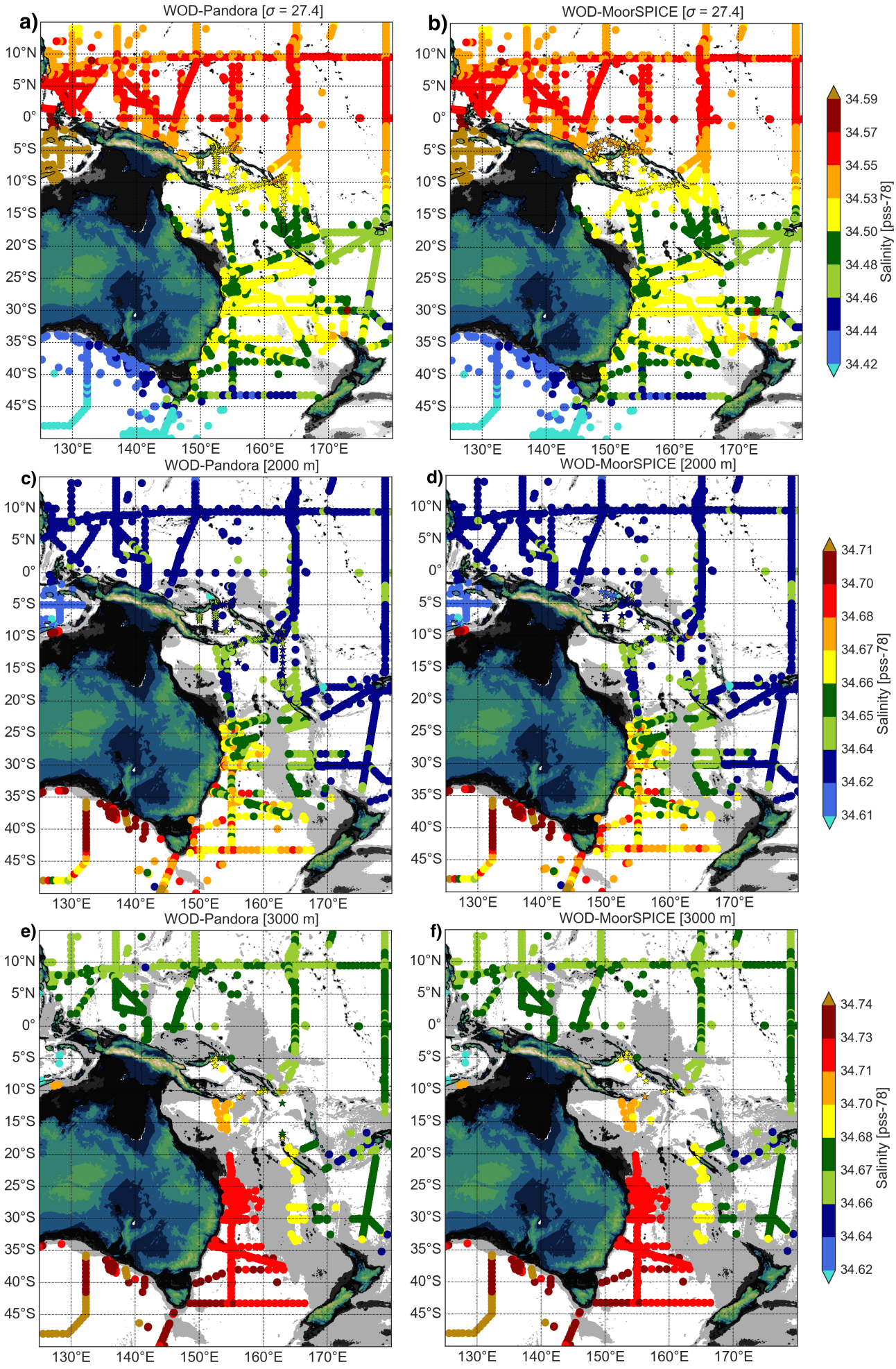

Figure 5.4 – Historical salinity climatology at (a),(b) σ_θ=27.4 isopycnal level; (c),(d) 2000 m depth level and (e),(f) 3000 m depth level. Colored stars indicate measured salinity during July-August 2012 (left) and March 2014 (right). Note the color scale and that areas deeper than each vertical level are shaded.

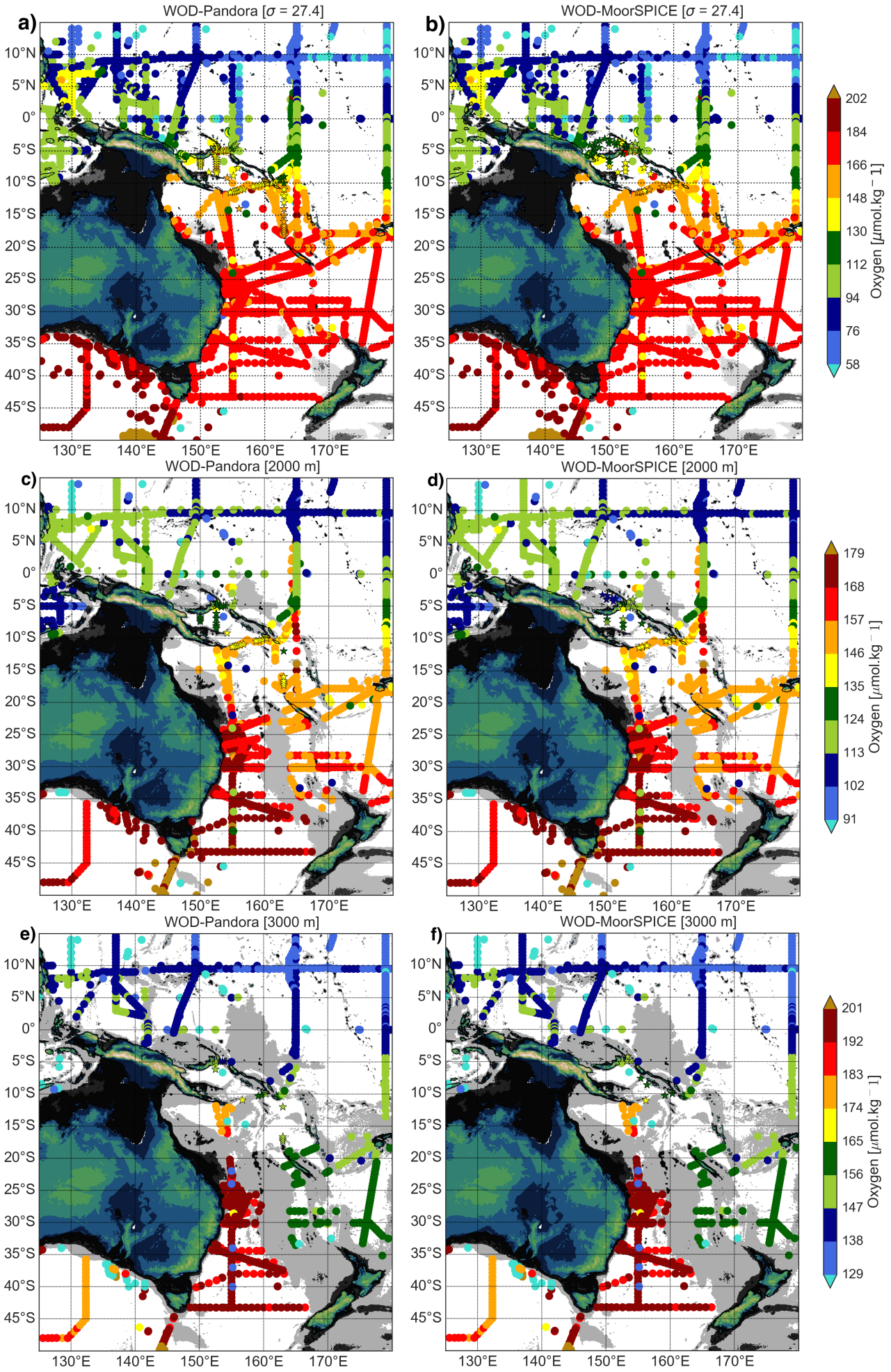

Figure 5.5 – Historical oxygen climatology at (a),(b) σ_θ=27.4 isopycnal level; (c),(d) 2000 m depth level and (e),(f) 3000 m depth level. Colored stars indicate measured oxygen concentrations during July-August 2012 (left) and March 2014 (right). Note the color scale and that areas deeper than each vertical level are shaded.

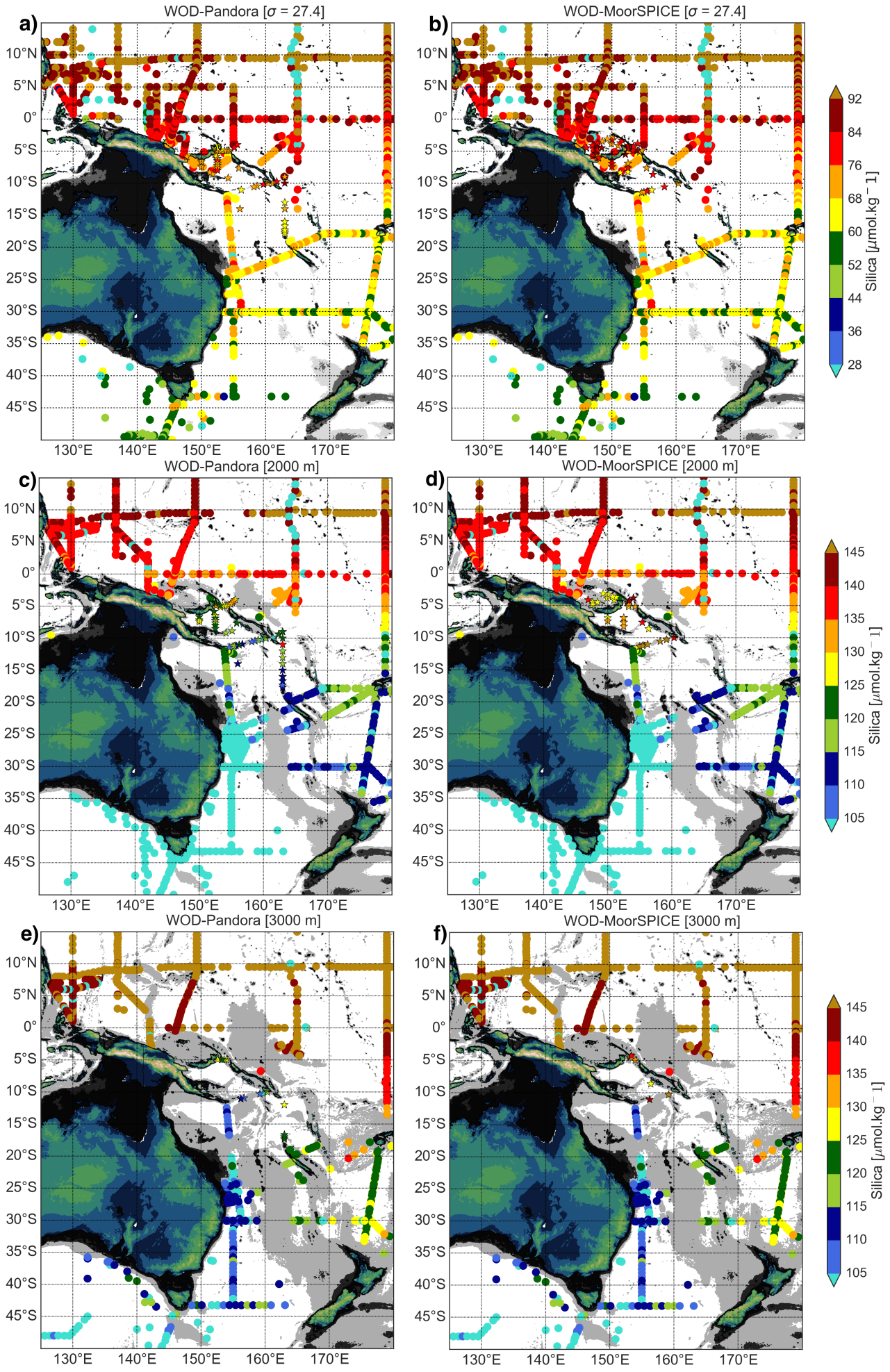

Figure 5.6 – Historical silica climatology at (a),(b) σ_θ=27.4 isopycnal level; (c),(d) 2000 m depth level and (e),(f) 3000 m depth level. Colored stars indicate measured silica concentrations during July-August 2012 (left) and March 2014 (right). Note the color scale and that areas deeper than each vertical level are shaded.

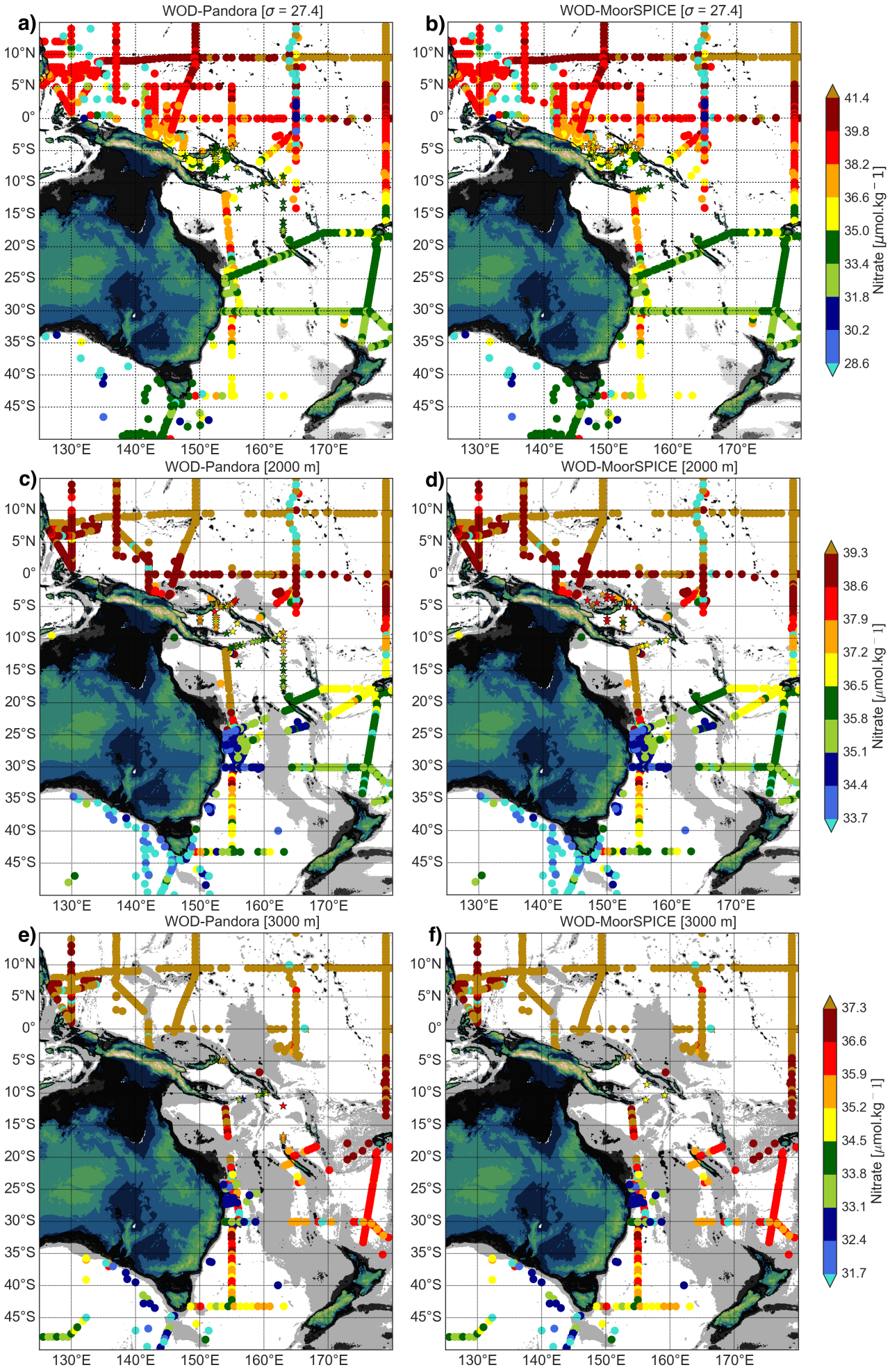

Figure 5.7 – Historical nitrate climatology during July-August 2012 (left) and March 2014 (right) at (a),(b) σ_θ=27.4 isopycnal level; (c),(d) 2000 m depth level and (e),(f) 3000 m depth level. Colored stars indicate measured nitrate concentrations during July-August 2012 (left) and March 2014 (right). Note the color scale that areas deeper than each vertical level are shaded.

5.6 Deep flow across the Solomon Sea

In this section, the major deep pathways through the Solomon Sea and their volume transports are described during the two SPICE cruises. The estimated velocities adjusted to the deep reference level are indicated in Figure 5.8 (black line, top panels), and are smaller than the initial velocity uncertainties set to $\pm 5\ cm.s^{-1}$, as the "shallow" inverse model. Note that the structure of corrections at the reference level is sometimes a bit step like; this might be an interpolation artifact of the geostrophic and L-ADCP currents at the southern entrance and along the St Georges-Solomon transect, respectively. In addition, the transport estimates do not sum up exactly, although the small imbalances are lower than associated uncertainties (Table 5.1), and could be related with vertical exchanges through upwelling or downwelling of nearly 1 Sv to the surrounding deep layers.

5.6.1 Southern entrance of Solomon Sea in July-August 2012

The estimated velocity field below 1000 m (Figure 5.8a) shows currents of 5-10 $cm.s^{-1}$ down to near 1300 m in the western part of the transect (west of 157°E), particularly near Papua New Guinea, as a lower extent of the NGCU. On the eastern part, velocities are mostly ranging from 0-5 $cm.s^{-1}$, where the southward flow identified at 159°-160°E is confined in the upper 1000 m. Between $27.4 < \sigma_\theta < 27.65$ ($UCDW_{upper}$) and below $\sigma_\theta = 27.65$ ($UCDW_{lower}$), the northward volume transport estimates are $6 \pm 2\ Sv$ and $3 \pm 2\ Sv$, respectively (Table 5.1).

5.6.2 Solomon Strait and St Georges Channel flow in July-August 2012

Below 1000 m, the deep flow exits the Solomon Sea either through the St Georges Channel or the Solomon Strait. We found a northward volume transport of $6 \pm 1\ Sv$ between $27.4 < \sigma_\theta < 27.65$ ($UCDW_{upper}$), while $2 \pm 2\ Sv$ are attributed to the $UCDW_{lower}$ across the St Georges-Solomon transect, though most of the northward transport occurs at Solomon Strait (east of 153°E). A striking feature is the presence of two opposite currents (Figure 5.8c), one flowing southward centered on $\sigma_\theta = 27.4$ (153.5°E) with two velocity cores of $\sim 10\ cm.s^{-1}$, and the other flowing northward near 1500 m (154°-154.5°E) with stronger velocities of 10-20 $cm.s^{-1}$. Two northward velocity cores ($\sim 10\ cm.s^{-1}$) exit St Georges Channel (west of 153°E) at depths of 1000-1500 m, while a southward flow (0-5 $cm.s^{-1}$) confined along the western sidewall of the channel enters into the Solomon Sea. Below 2000 m, weak velocities of 0-5 $cm.s^{-1}$ are found down to ~3000 m.

5.6.3 Southern entrance of Solomon Sea in March 2014

The northward flow observed west of 157°E (Figure 5.8b) appears to be weaker in March 2014 than during the austral winter 2012, with velocities of 0-5 $cm.s^{-1}$. As for the southward flow previously found at 159°-160°E, it seems to be also confined above 1000 m depth. Overall, the northward volume transport estimates are halved over both $UCDW_{upper}$ and $UCDW_{lower}$ (i.e. $3 \pm 1\ Sv$ and $1.6 \pm 1\ Sv$, respectively) compared to those found in July-August 2012 (Table 5.1), this is possibly due to unaccounted volume transports across the southern entrance (especially east of 159°E), as most of the measurements along the transect are shallower than those collected during July-August 2012.

5.6.4 Solomon Strait and St Georges Channel flow in March 2014

As during July-August 2012, most of the volume transports occur at Solomon Strait (east of 153°E), but we found negligible $UCDW_{upper}$ contributions of 0 ± 1 Sv to the total volume transport, whereas 3 ± 1 Sv are associated with the $UCDW_{lower}$ below $\sigma_\theta = 27.65$ (Table 5.1). The two opposite flows located at mid-transect are also found in March 2014, however both currents exhibit weak velocities of 5-10 $cm.s^{-1}$ without distinct cores unlike those observed in July-August 2012. At St Georges Channel, the flow is now southward and enters into the Solomon Sea around 1500 m with velocities of 5-10 $cm.s^{-1}$. This reversal could be explained by seasonal variations between both cruises, although it is quite unlikely at those depths. Further investigation is required to determine the mechanisms that could explain such a large current variability so deep, possibly through a dedicated analysis of the 1.5 year mooring data set presented in the next chapter.

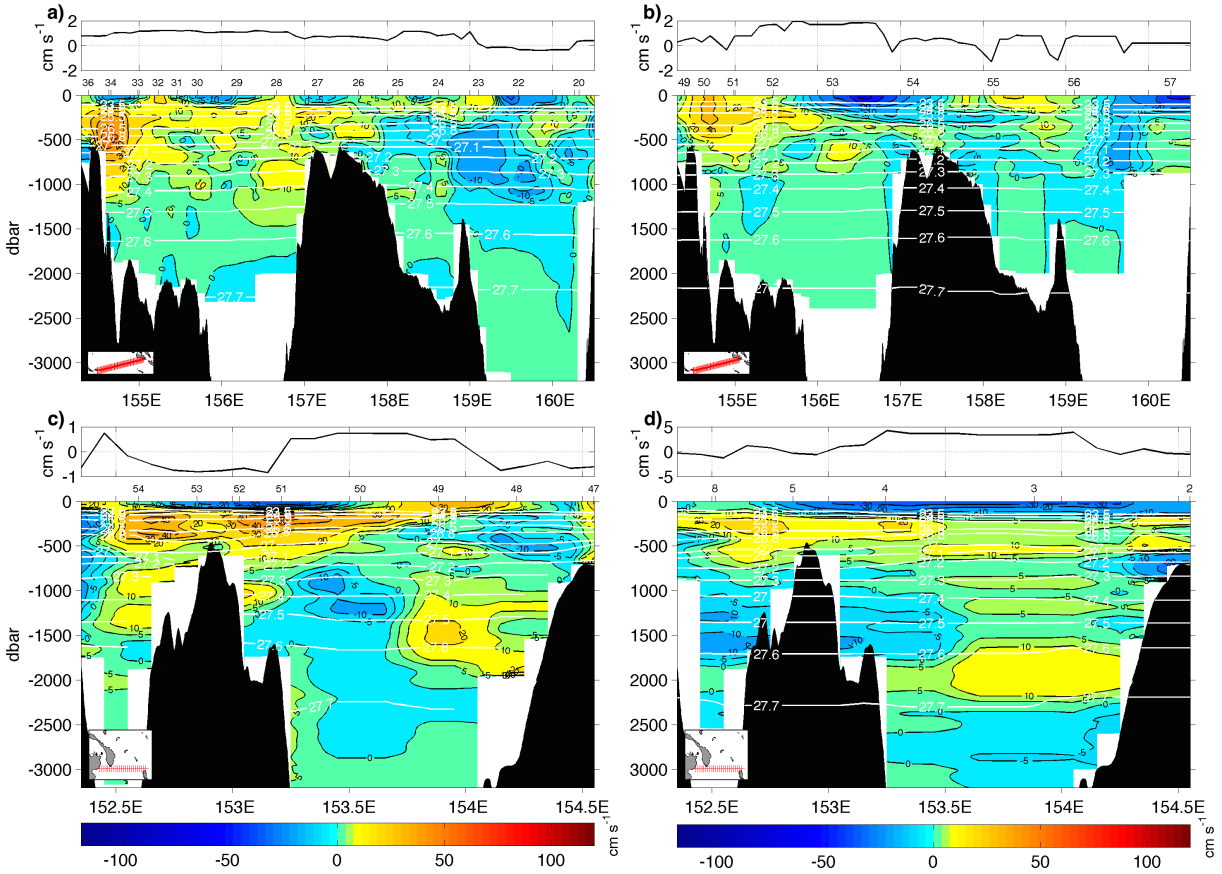

Figure 5.8 – (top panels) Difference between estimated and initial reference velocities at deep reference level (solid line). (left panels) July-August 2012 and (right panels) March 2014 estimated zonal cross-section velocities. (a, b) at the southern entrance of the Solomon Sea and (c, d) between St Georges Channel and Solomon Strait. Positive values indicate northward direction, and overlaid white lines indicate potential density anomaly ($kg.m^{-3}$).

5.7 How is the deep flow in the Solomon Sea connected to the Pacific deep layers?

The upper deep layer, characterized by the inflow of the UCDW (see Section 5.2), exhibits a quite low oxygen signature from the ACC to around 25°S (*Reid*, 1986; *Wijffels et al.*, 2001; *Talley et al.*, 2007); though on an isopycnal layer, UCDW is associated with higher dissolved oxygen concentrations than in the surrounding waters (*Reid*, 1986, 1997). As the UCDW flows northwestward across the Southwest Pacific Basin, from the Samoan Passage to Papua New Guinea, oxygen decreases north of 15°S and part of the UCDW seems to return southward via the subtropical gyre (*Reid*, 1997). The total net transport of the UCDW across the South Pacific has been estimated to 7 Sv (identified as the $UCDW_{lower}$ in our study) at depths of 2000-3500 m (*Kawabe and Fujio*, 2010).

In the North Pacific, the 7 Sv of UCDW flows into the Philippine Basin as a deep western boundary current. According to (*Kawabe and Fujio*, 2010), $\sim$5 Sv of UCDW flows out the Philippine Sea before flowing eastward towards the Hawaiian Ridge to ultimately form modified NPDW after mixing with the NPDW, while the remaining 2 Sv are suggested to be upwelled to the layer shallower than 2000 m within the Philippine Sea.

Nevertheless, the presence of the UCDW within the Coral and Solomon seas is poorly documented. As part of the WOCE program, *Sokolov and Rintoul* (2000) proposed a circulation scheme of the UCDW (referred to as CDW in their study) from CTD measurements collected along the section P11S. At depths above 3000 m, they have estimated a UCDW inflow of 3 Sv into the Coral Sea from the Tasman Basin. Upper deep waters from the Central Pacific Basin were suggested to enter to the east from the South Solomon Trench and to proceed southward into the basins and trenches of the eastern Coral Sea (their Figure 16f *Sokolov and Rintoul*, 2000). Our present results based on water property distributions from the two SPICE cruises and historical data suggest (see Section 5.5.1), in contrast, less widespread Central Pacific Basin waters, which are mostly confined in the New Hebrides Basin and the South Solomon Trench.

Indeed, part of the estimated $UCDW_{lower}$ inflow of 2-3 $\pm$ 2 Sv into the Solomon Sea derives from the New Caledonia Trough and the South Fiji Basin, based on distinct water properties (i.e. high salinity, quite high oxygen in its lateral distribution and high nutrient concentrations, as defined by *Callahan* (1972) and *Reid* (1997)). Further north, transport estimates suggest a northward outflow from the Solomon Sea during both cruises, rather than a NPDW inflow from the northwestern Pacific. However, episodic flow incursions coming from the East Carolina Basin might occur at depths shallower than 3000 m (below, the Solomon Sea Basin is closed to the north), bringing fresher, oxygen-poor and silica-rich waters into the sea.

The lower deep layer in the Pacific Ocean carries northward the LCDW (see Section 5.2), which is typically detected by an increase in salinity and a decrease in silica below the UCDW. The first description of the deep layer pathways in the South Pacific has been proposed by *Wyrtki* (1961). This pioneer study suggested that deep waters from the Coral Sea and the Solomon Sea basins emanated from the Tasman Basin, whereas waters in the Caledonian Through and the Fiji Basin came from the Central Pacific Basin, located further northeast.

The study from Lindstrom and Hayes (1989) was in good agreement with *Wyrtki* (1961), suggesting the presence of the Central Pacific Basin deep waters into the South Solomon Trench, with possible impacts on the deep water properties of the New Hebrides and South Fiji basins; though it was pointed out that more observations were required to infer the pathway and associated characteristics of those deep waters within the Coral Sea.

More recent studies (e.g. *Tsimplis et al.*, 1998; *Wijffels et al.*, 2001; *Kawabe et al.*, 2003; *Kawabe and Fujio*, 2010) have refined the description of the LCDW pathways across the Southwest Pacific, and it has been shown that the LCDW coming from the Tasman Sea is too dense to flow into the Coral Sea. Nevertheless, its occurrence and fate within the Coral and Solomon seas remain poorly known. The deep measurements collected during the two SPICE cruises suggest a LCDW inflow into the Solomon Sea at depths below 3000 to ∼3500 m (see Section 5.5.2), though only few observations are available. Below 3500 m, the Coral and Solomon seas are closed to the north and the south, and are no longer connected with the Central Pacific Basin. Therefore, the densest LCDW is prevented from spreading to the Southwest Pacific by topography.

5.8 Conclusions

The deep measurements collected during the two SPICE cruises are used to document the deep pathways and associated water masses in the Solomon Sea region. The circulation is inferred from an inverse box model that provides quantitative transport estimates with uncertainties, while property distributions provide indications for the water mass characteristics.

During the July-August 2012 cruise, the northward flow across the southern entrance transports 6 $\pm$ 1 Sv between 1000 and 2000 m and carries SEC water origins within the Solomon Sea, characterized by low salinity, low silica and high oxygen compared with deeper layers. This transport is halved in March 2014, while the encountered water properties are similar than those of July-August 2012. Below 2000 to around 3000 m, the northern inflow of UCDW is mostly connected to the south, via the New Caledonia Trough and the South Fiji and New Hebrides basins, though upper deep waters also emanate from the Tasman Sea. This northward deep flow transports 2-3 $\pm$ 2 Sv into the Solomon Sea, associated with high salinity, low oxygen and high nutrient characteristics.

The UCDW proceeds northward into the Solomon sea and possibly undergo significant water mass transformations due to mixing with the NPDW found to the north of the sea, before flowing out through Solomon Strait with a volume transport of 2-3 $\pm$ 2 Sv. It then probably reaches the western equatorial Pacific via the deep western boundary current, passing through the Solomon Sea Rise and the East and West Carolina basins, from 2000 to at least 2500 m. At depths greater than 3000 m, the northern outflow appears to be confined near Solomon Strait, as the basin is closed further north. As a result, weak southward inflows (0-5 $cm.s^{-1}$) into the Solomon Sea can occur at those depths.

Schematics of the UCDW pathway in the Southwest Pacific provided in previous studies (e.g. *Reid*, 1997; *Kawabe and Fujio*, 2010) do not show the branch current flowing through the Coral and Solomon seas, leading to underestimated transports of the UCDW towards the North Pacific. Our present results permit to infer an additional UCDW transport of 2-3 $\pm$ 2 Sv, passing mostly across the New Caledonia Trough and the South Fiji and New Hebrides basins, and then through the Solomon Sea to ultimately join the UCDW branch north of the Solomon Rise (Figure 5.9). This refined picture of the upper deep layers permits the conclusion of an equatorward western boundary current that transports 9-10 Sv towards the North Pacific along complex bathymetric features.

In addition, the distributions of water properties from both cruises and the WOD13 data set, indicate an inflow of the LCDW at depths ranging below 3000 to 3500 m into the Coral and Solomon seas. However, more observations are required to thoroughly determine the LCDW pathway across the Southwest Pacific.

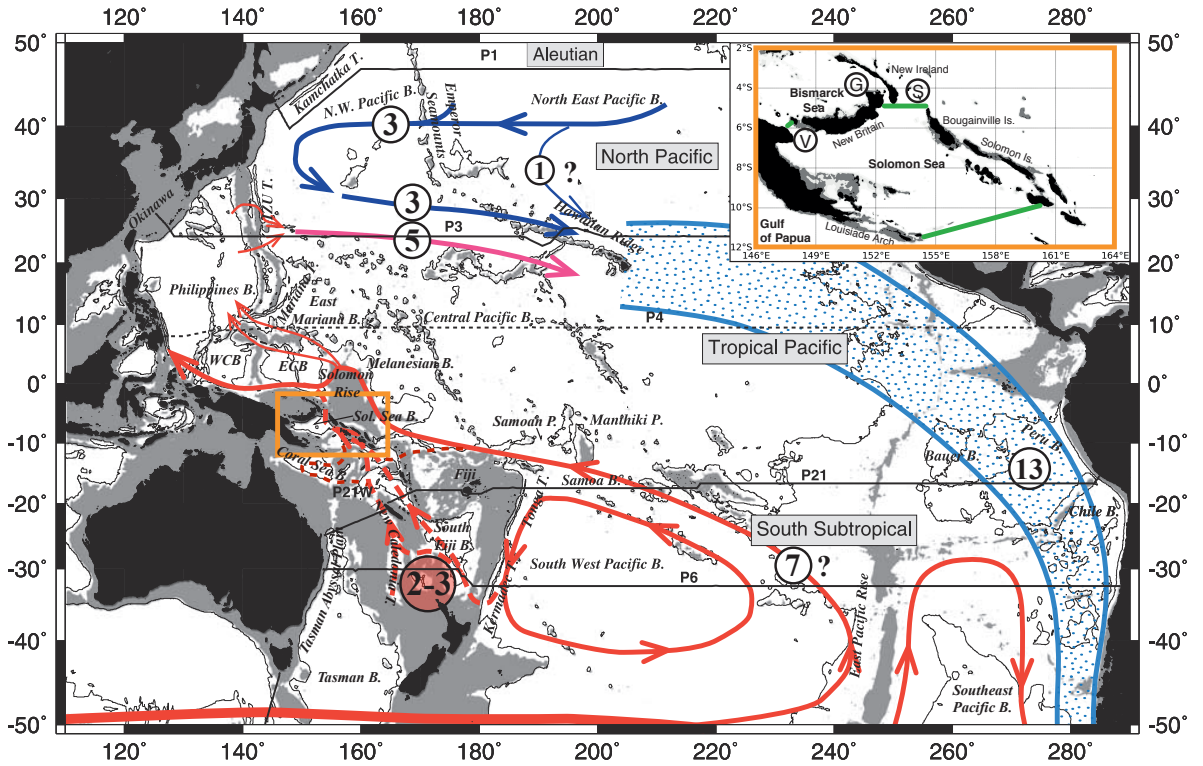

Figure 5.9 – Same as Figure 5.1 but including the conjectured branch of the UCDW (red dashed arrows) that possibly flows equatorward through the Coral Sea and Solomon Sea basins. Note the red circled numbers that indicate UCDW transport estimates through the Solomon Sea from the "deep" inverse model.

Chapter 6

Variability in the Solomon Sea: A Mooring Analysis

Contents

6.1 Introduction

Mooring array measurements can be used to construct in situ timeseries of mass transports, especially in remote regions where it is challenging to work in, as the Solomon Sea. As briefly introduced in Chapter 1, the France-U.S. MoorSPICE program consists in a 1.5-year deployment of mooring instruments, including pairs of up-and down-looking ADCPs near the surface, T-S sensors, flotation buoys and additional current meters in the northern exit passages of the Solomon Sea. Overall, nine subsurface moorings (Figure 6.1) were deployed in Vitiaz Strait (U.S), St Georges Channel (U.S) and Solomon Strait (France) to resolve the distinct cross-passage flow variability of the complex western boundary currents that feed the equatorial current system.

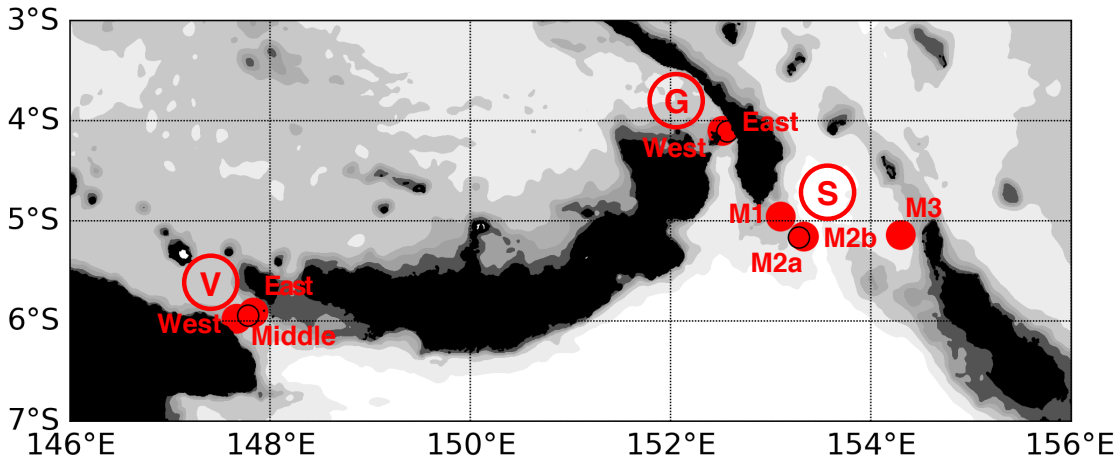

Figure 6.1 – Bathymetry map at 100, 500, 1000, 2000 and 4000 m (grey shading). The mooring locations of the first 1.5-year deployment are shown as red dots at Vitiaz Strait (V), St Georges Channel (G) and Solomon Strait (S).

As part of the pioneering WEPOCS I and II expeditions (June-August 1985 and January-February 1986, respectively), early measurements depicted a first picture of the mean and seasonal variability of the NGCU outflow through Vitiaz Strait. Using WEPOCS data, a 6-month deployment of one mooring equipped with three current meters (at depths 350, 450 and 550 m) and S-ADCP repeated transects, *Lindstrom et al.* (1987, 1990) estimated a mean transport of 8 Sv in the 200-700 m depth range across Vitiaz Strait, associated with a steady northwestward flow. A similar mooring was also deployed at St Georges Channel, however two of the current meters stopped recording and data were not discussed in *Lindstrom et al.* (1990).

Few years later, during the WOCE program, five moorings were deployed in Vitiaz Strait from March 1992 to March 1993 to extend the spatial and temporal resolution of the pioneering WEPOCS measurements (*Murray et al.*, 1995). In this study, they found a similar steady northwestward NGCU through Vitiaz Strait, and estimated a mean top-to-bottom transport of 15.8 Sv. They also found that NGCU transport estimates fluctuated over time from 14.9 to 19 Sv, with maximum estimates during austral winter. Nevertheless, this work on moorings has never been published in peer-review journal because of technical problems.

The present experiment complements these existing western boundary current monitoring efforts through Vitiaz Strait, and depicts an unprecedented quantitative picture of the outflow variability across the two other exit passages of the Solomon Sea, the St Georges Channel and Solomon Strait. The next section provides details about the mooring data and their associated quality control, followed by preliminary results and on going analyses. Then, some elements of conclusion will be given, as well as work perspectives regarding this promising data set.

6.2 The MoorSPICE mooring data

The mooring array measurements required to be carefully designed, with quite similar configurations to those of the INSTANT[1] program (*Cowley et al.*, 2008), associated with preliminary studies on the bathymetry in the straits. Deployment operations were conducted aboard the French vessel R/V L'Atalante in July 2012 and lasted approximately three to four hours for each buoy, depending on bottom depth at the different sites.

The location and depth of each deployment are given in Table 6.1. The first site is Solomon Strait, the widest exit passage of the Solomon Sea (∼170 km) where four moorings were deployed, including Solomon M1 and two paired moorings (Solomon M2a and M2b) on the western side of the strait, and a last mooring (Solomon M3) on the other side, northeast of Bougainville Island. The next site is the narrow St Georges channel (∼15 km), where two moorings (St Georges West and St Georges East) were deployed northeast at the entrance of the Bismarck Sea. Finally, three moorings were deployed at the shallow Vitiaz Strait (Vitiaz East, Vitiaz West and Vitiaz Middle), that is ∼1000 m deep and 42 km wide at its larger extent.

All nine moorings were recovered, and four of them were renewed before being redeployed in Vitiaz and Solomon Straits (Vitiaz-a, Vitiaz-b, Solomon M2 and M3) from the U.S. vessel R/V Thomas G. Thompson. A final recovery of these four moorings occurred in August 2014 during the Cassiopée cruise on the R/V L'Atalante. In this thesis, our work is only focused on the first 1.5 year deployment period.

Table 6.1 – Location, depth and deployment periods of each mooring are given for the first 1.5 year deployment period (July 2012-March 2014).

Strait	Mooring	Location	Depth (m)	Deployment Period
Vitiaz Strait	West	147°39.96'E 5°58.69'S	980	28 July 2012 - 14 March 2014
	East	147°50.05'E 5°54.98'S	900	28 July 2012 - 13 March 2014
	Middle	147°46.68'E 5°56.64'S	1130	28 July 2012 - 15 March 2014
St Georges Channel	West	152°31.116'E 4°6.82'S	1243	20 July 2012 - 07 March 2014
	East	152°33.86'E 4°6.17'S	1433	20 July 2012 - 08 March 2014
Solomon Strait	M1 (Northwest)	153°16.024'E 4°57.48'S	2050	21 July 2012 - 06 March 2014
	M2a (Southwest)	153°16.864'E 5°09.853'S	2560	16 July 2012 - 06 March 2014
	M2b (Southwest)	153°19.937'E 5°09.448'S	2710	15 July 2012 - 06 March 2014
	M3 (East)	154°17.975'E 5°08.283'S	2627	18 July 2012 - 04 March 2014

[1]International Nusantara STratification ANd Transport (INSTANT) project conducted in the Indonesian Seas to measure the Indonesian throughflow from 2003-2006

6.2.1 Mooring array design and instrumentation

They are some differences in the array design between the U.S. and French moorings, although both configurations include temperature, salinity and pressure sensors, along with current meters. The MoorSPICE array consisted of 160 instruments distributed over the full-depth mooring line, ending with twin acoustic releases and a least at each mooring site. At Solomon Strait, 78 instruments were deployed over an approximately 80-3000 m depth range. At St Georges Channel and Vitiaz Strait, the array consisted of 29 (51 m down to 1200-1400 m) and 53 instruments (51 m down to 900-970 m), respectively. Temperature, temperature-pressure and temperature-salinity-pressure sensors (e.g. SBE instruments, SIO-T loggers) were deployed at discrete depths along the mooring line. Up-and-downward looking ADCPs allowed to profile the water column from the surface down to ∼700 m. Single point current meters (Aquadopps[2] and RCMs[3]) are generally used to record deeper flows, with the deepest at 1700 m.

The detailed design diagram for moorings Solomon M2a and M3 are shown in Figure 6.2 as an example. All subsurface ADCPs and Aquadopps measured pressure and temperature in addition with velocity (speed and direction). Sampling rates were set to capture the tides and subinertial frequencies, and varied between 10 minutes through two hours for the deepest RCMs. On both Vitiaz West and East moorings, the top instruments were lost above 250 m and 400 m as the mooring line broke in July-August 2013 and September 2012, respectively. On St Georges West and East, the top most temperature and pressure sensors were missing due to broken lines, while on Solomon moorings, all the different instruments were fortuitously recovered. Pressure timeseries from the ADCPs revealed significant vertical displacements (variations of 100-500 dbar) at Vitiaz Strait and St Georges Channel, where strong tidal and/or frictional forcing is expected. At Solomon Strait, pressure variability is generally lower than 100 dbar for the most eastern moorings (i.e. M2a, M2b and M3), while pressure variations can reach 400 dbar at Solomon M1.

Detailed information of all mooring array measurements, deployment depths, data temporal coverage, and the required quality control for each instrument can be found in a dedicated data report[4]. As part of a 3-month internship performed by Alexis Calandry[5] and supervised by Alex Ganachaud, Marion Alberty[6] and myself, complete details about the first 1.5-year deployment were gathered and raw data were roughly visually inspected to address obvious problems.

The data required adjustments, as time and sensor drift corrections, and a step by step quality control procedure that was led through a joint-collaboration between the Scripps Institution of Oceanography and LEGOS with Marion Alberty and myself, under the supervision of Janet Sprintall.

[2]Aquadopps are acoustic Doppler current meters that were combined with MicroCAT sensors to include conductivity measurements

[3]Rotor current meters (RCMs) record flow velocity with a propeller and a vane to detect the direction of the flow

[4]SPICE Mooring Data Report in preparation

[5]2-year student in metrology at the University Technical Institute of Toulouse

[6]Ph.D candidate at Scripps, working on spatial mixing patterns in marginal seas

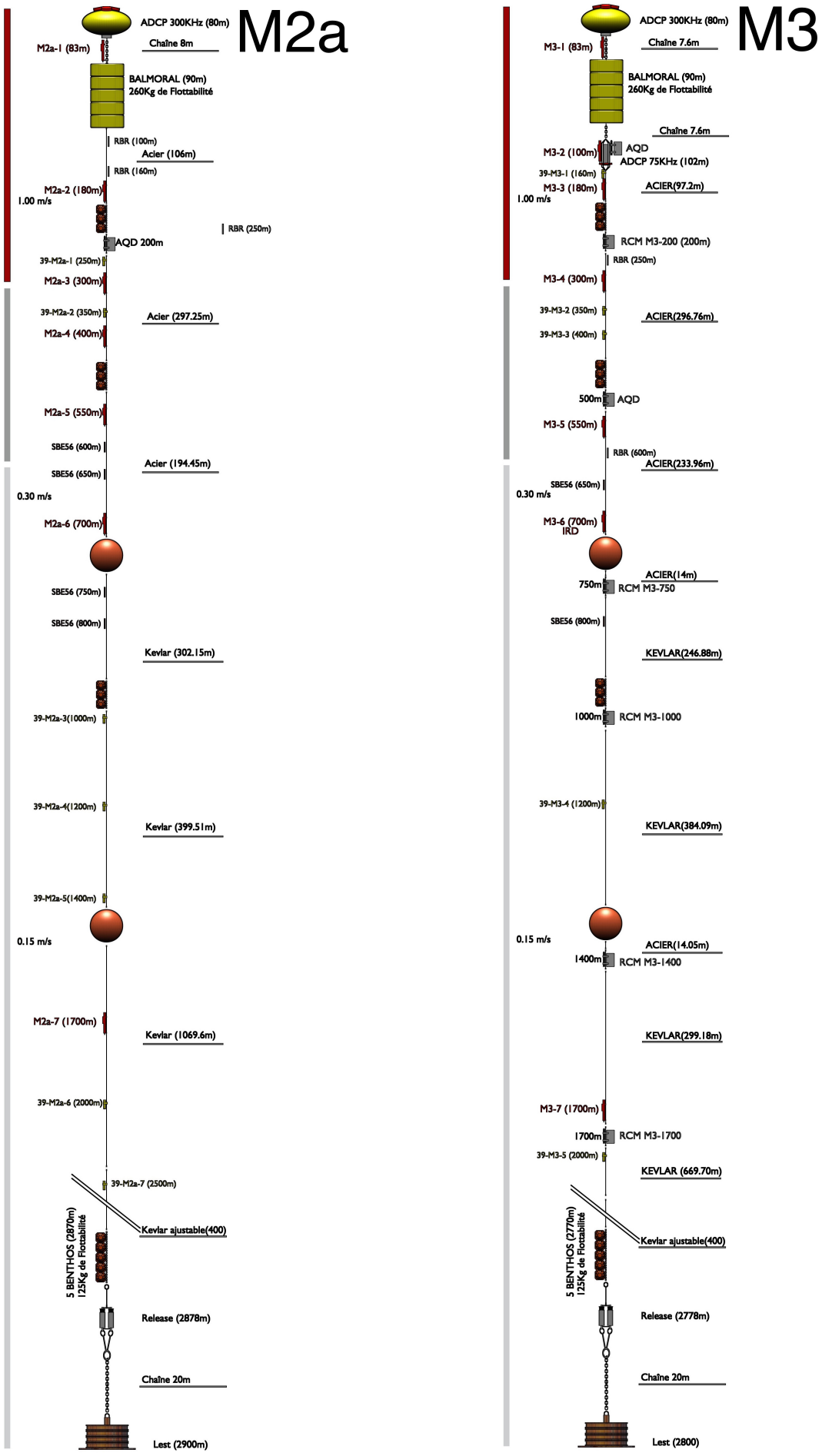

Figure 6.2 – Design diagrams for Mooring (left) Solomon M2a and (right) Solomon M3, showing the distribution of instrumentation and flotation at discrete depths along the mooring line (courtesy O. Desprez de Gesincourt, DT-INSU).

6.2.2 Mooring data quality control

All the 160 instrument records were first quality controlled for treatment of sensor and time drifts. Marion worked on temperature, salinity and single point current meters, while I focused on ADCP data. We then both trimmed the data to remove any out of water values. Instrument time bases were checked using the noted "start" and "stop" times on deployment and retrieval of each mooring. Various plots of temperature, pressure, salinity and velocity timeseries were done to visually inspect the data again, where any missing data point was flagged as "bad data". Then, I compiled each mooring by stacking the data fields to put them on the same start time-base (i.e. that of the ADCP). To get some insight on the time variability of each instrument record, I plotted mean vertical profiles as a function of pressure of both zonal (u) and meridional (v) velocity components, and temperature within a two standard deviation uncertainty (see Appendix D).

The ADCP instruments required additional quality control, especially for the upward looking ADCPs where the upper bins[7] (see Figure 6.3) are contaminated by surface reflection. Based on the determination of thresholds for six different parameters (presented below), a specific quality control procedure was developed by Janet Sprintall as part of the INSTANT program (*Cowley et al.*, 2008), and applied to the MoorSPICE moorings (see Section 6.2.3). Complete details about the method of determining the thresholds for each moored ADCP are given in Appendix E. As an example, a description of this method applied to the upward looking ADCP moored at Solomon M3 is provided in Section 6.2.4. Finally, the magnetic declination (angle between true north and the horizontal trace of the local magnetic field) was corrected on all ADCP velocity fields.

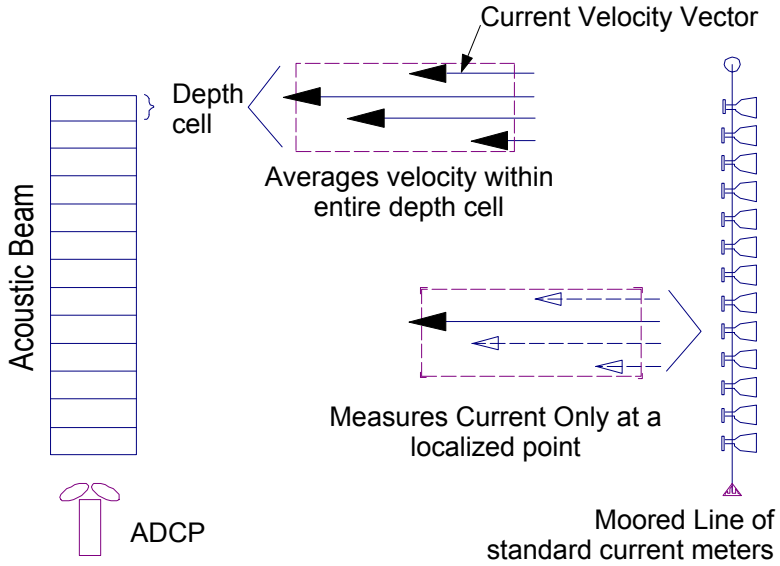

Figure 6.3 – Schematic of the ADCP bins (depth cells) compared with discrete current meters on a mooring. From *Gordon and Instruments* (1996).

[7]Bin (or Depth Cell): A measurement within an ADCP velocity profile, which is generally equivalent to a single-point current meter on a mooring line

6.2.2.1 Echo intensity

For an ADCP instrument, the echo intensity (hereinafter referred as echo amplitude[8]) is a measure of the signal strength intensity that is returned to the transducer. High echo amplitude possibly indicates a boundary, an obstruction or fish in the water column, while low echo amplitude correspond to insufficient scatterers or that the range profiling limits of the sensor are exceeded.

6.2.2.2 Correlation magnitude

The correlation magnitude is a measure of the pulse[9]-to-pulse correlation in a ping[10] for each depth cell. The correlation magnitude should remain relatively constant throughout the velocity profile, and it ensures the highest quality data as part of the quality control procedure.

6.2.2.3 Percent good

The Percent good is the ratio of good pings (that passed data rejection criteria) per total pings. Causes of low values are related with low correlation magnitude, large error velocity and fish detection. The percent good is a key parameter for the quality control procedure, as it ensures a small standard deviation uncertainty in the data.

6.2.2.4 Vertical velocity

The recorded vertical velocity for each bin is the average between the two vertical velocity components that are calculated using the four acoustic beams of an ADCP. It measures the vertical tilt of the transducer, where high vertical velocities can indicate turbulence in the water column and non-homogeneous horizontal currents, however it does not correspond to a vertical ocean velocity. The vertical velocity test is realized by comparing the vertical velocity in each depth cell to a threshold value (see next section).

6.2.2.5 Horizontal velocity

The horizontal velocity within each bin is determined from the two horizontal components (east and west after transformation to earth coordinates) for each beam. The horizontal velocity test can be seen as as a gross error check, where horizontal currents are not expected to exceed a defined threshold value (see next section).

6.2.2.6 Error velocity

The error velocity is the difference of the two vertical velocity measurements for each pair of opposite beams, and is used as a measure of consistency. A high error velocity possibly indicates the four beams are not measuring the same body of water, or an inhomogeneous flow.

[8] for consistency with INSTANT quality control procedure
[9] sound wave emitted by an ADCP transducer
[10] the full sound emitted by an ADCP transducer for a single measurement

6.2.3 The ADCP quality control procedure

Relevant ADCP raw data (i.e. pitch, roll, pressure and temperature) were primary checked to identify strong horizontal or vertical displacements over time. Each measurement within a velocity profile (the depth cell, or bin) moves up or down as a result of the pitch and roll (angles in degrees relative to true north measured by a vertical gyrocompass and inclinometers, respectively), and so the depth cells used to determine the velocities might correspond to different water depths (Figure 6.4). A depth cell mapping algorithm was applied in post-processing to align the depths cells, although strong ADCP tilts (typically greater than 20-25°) might cause severe damages to the ADCP records. Thus, a particular attention was given to pitch and roll motions in this quality control procedure.

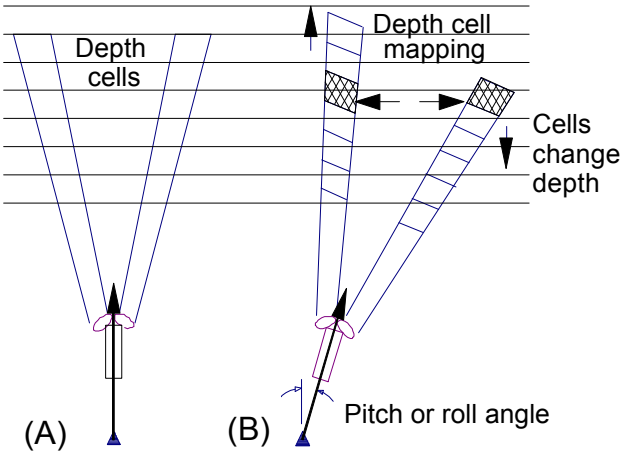

Figure 6.4 – Schematic of the ADCP tilt induced by pitch and roll variations. The hatched cells in (B) indicate different depth cells than those in (A). From *Gordon and Instruments* (1996).

The procedure consists of six tests (for each parameter previously defined), where data in each bin can be flagged as fail, suspect or pass depending on defined threshold values (Table 6.2). As the INSTANT data quality control, we chose a conservative approach, where suspected data are designated as failed. For tests 1 to 5, the tests are carried out for each cell with the binary condition: 0=pass; 1=fail. The results are summed, and if the sum is larger than 2 (i.e. the cell has failed 2 out of 5 tests) the cell is removed. Test 6 (the echo amplitude) is a surface detection test to remove surface data from each cell. Thus, rejection of cells can occur for one or two reasons: (1) two out of the five tests that comprise the sum of tests 1 to 5 fail (OTfails) and (2) failure of the echo amplitude test 6 (EAfail).

Table 6.2 – Tests and associated thresholds used to quality control the upward looking moored ADCP velocity fields.

Tests:	Error Velocity ($m.s^{-1}$)	Percent Good	Correlation Magnitude	Vertical Velocity ($m.s^{-1}$)	Horizontal Velocity ($m.s^{-1}$)	Echo Amplitude (counts)
	0.15	>80%	>110	<0.2	<2	30

6.2.4 An upward ADCP quality control example: Solomon M3

The upward looking ADCP on the mooring site Solomon M3 was a 300 kHz Teledyne-RD Instrument, with 40 bins for 14331 time realizations. Pitch and roll variations (Figure 6.5a,b) were lower than 5 degrees over time, and some punctual vertical variations in pressure (<50 dbar, Figure 6.5c) and temperature (<5°C, Figure 6.5d) are observed. The average, standard deviation, and range values for the different parameters used in each quality control test (Figure 6.6) are preliminarily considered to choose corresponding thresholds.

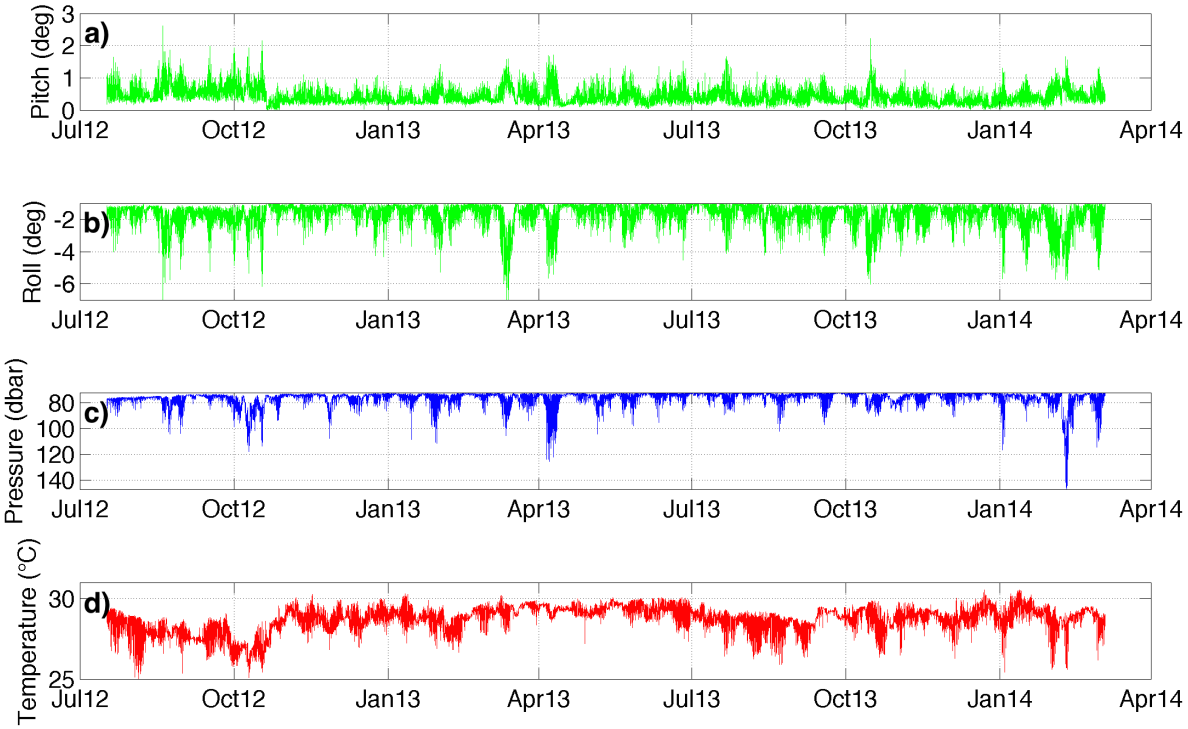

Figure 6.5 – Solomon M3 upward ADCP raw data timeseries of (a) pitch; (b) roll; (c) pressure and (d) temperature.

The echo amplitude test results in 10-15% failure in bins 21-40 to total fails for each threshold value (20, 25, 30 and 35 counts) and no EAfail below bin 21. In addition, the strong discontinuity on the mean profile (Figure 6.6f) suggests that the surface is likely detected near bins 20-21. A threshold of 30 counts was found appropriate for the upward ADCP, following INSTANT recommendations for similar instruments.

The percent good (i.e. fraction of data that already passed a variety of criteria) test contributes 100% to OTfails for each threshold value in upper bins 25-40. It means that percent good is at least one out of the two parameters that lead to OTfails. I found a quite similar contribution with the correlation magnitude (i.e. a measure of data quality) test. In addition, both tests contribute to ∼90% of the total fail in most upper bins. I suggest to use a 80 percent good and a 110 correlation magnitude, following first estimates from mean profiles near bins 20-21 (Figure 6.6b,c) and based on previous estimates for a similar instrument during INSTANT.

The error velocity test exhibits rejected cells mostly in bins 18-28 for each threshold value in OTfails. The vertical and horizontal velocity tests rejects cells mostly around bin 25 for the different thresholds in OTfails. Due to this threshold insensitivity, I decided to follow INSTANT choices of 0.15, 0.2 and 2 m.s^{-1}.

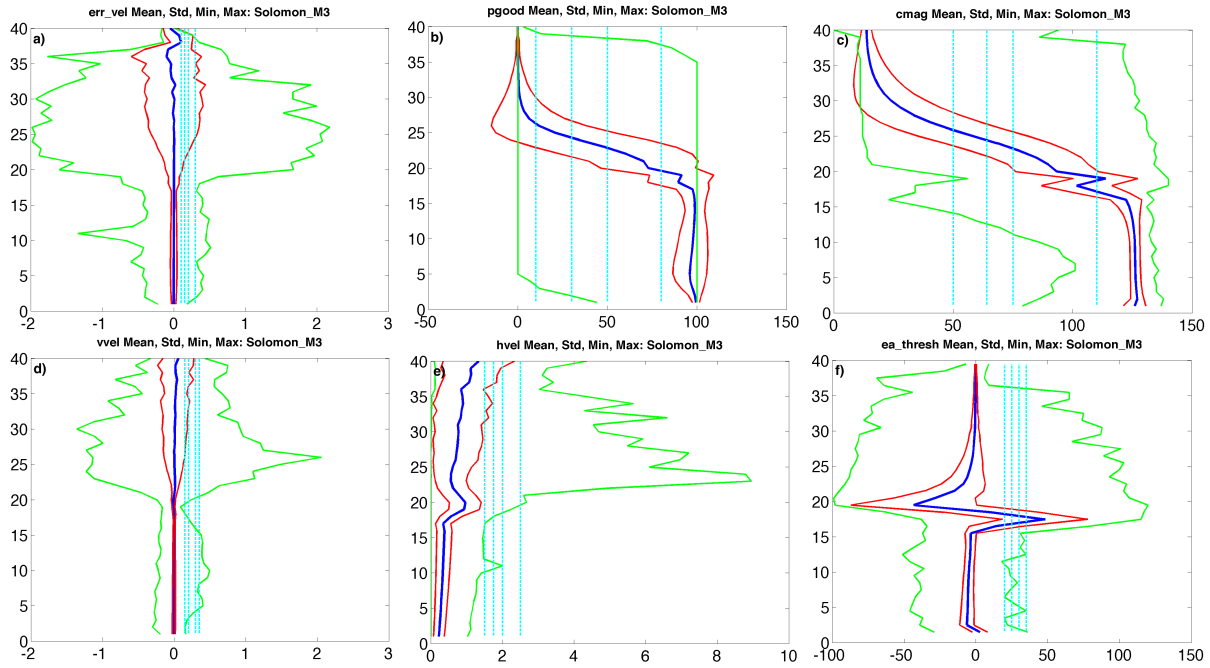

Figure 6.6 – Mean (thick blue line), standard deviation (red lines) and minimum and maximum (green lines) of the (a) error velocity ($m.s^{-1}$); (b) percent good; (c) correlation magnitude; (d) vertical velocity ($m.s^{-1}$); (e) horizontal velocity ($m.s^{-1}$) and (f) echo amplitude (counts) for the Solomon M3 upward ADCP versus bin. The four threshold values used in each quality control test are marked by cyan lines in panels (a) to (f).

The zonal velocities are shown before and after quality control (Figure 6.7a,b), as well as the meridional velocities (Figure 6.7c,d). The differences occur mostly above bin 18, where the revised thresholds eliminate most of the cells near the sea surface.

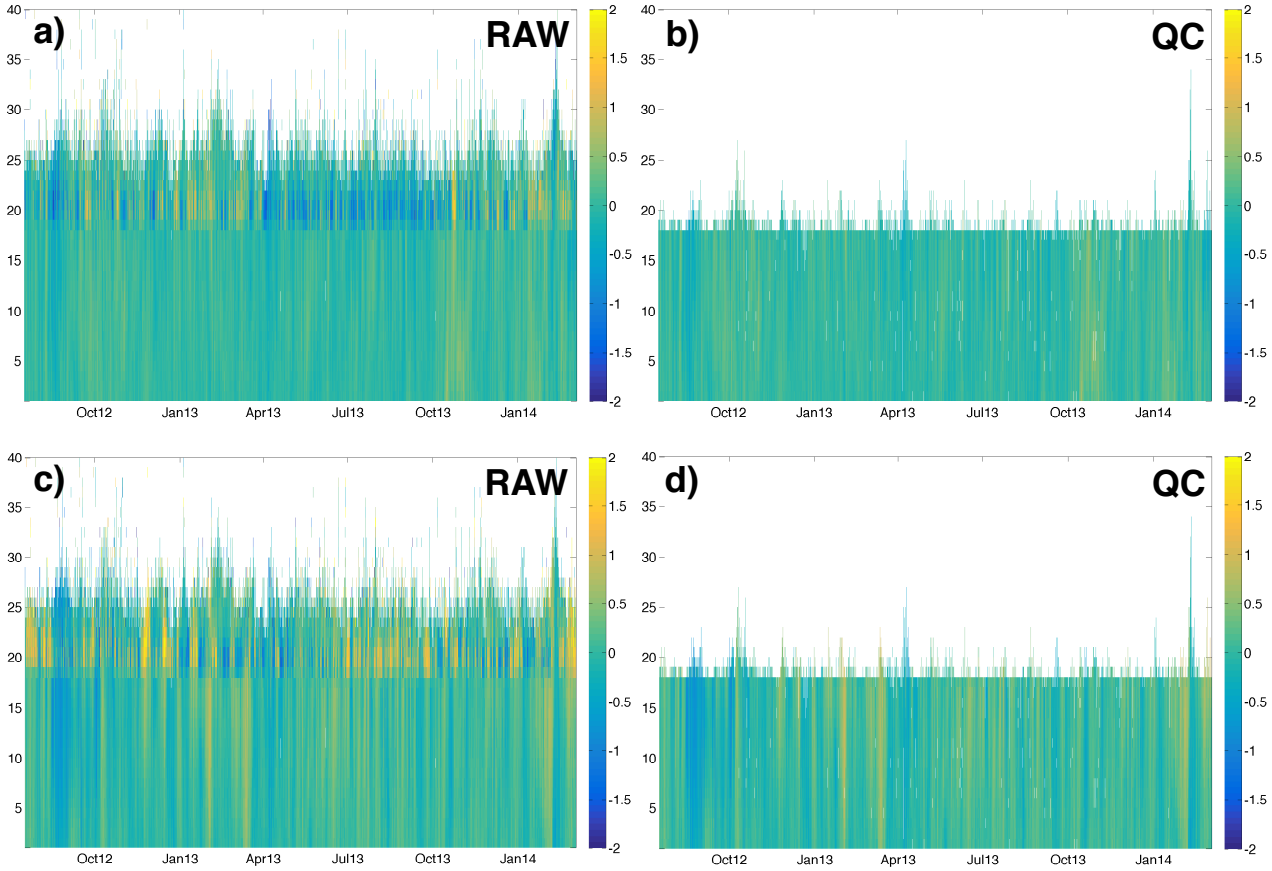

Figure 6.7 – Comparisons of (a),(c) raw and (b),(d) quality controlled ADCP velocities ($m.s^{-1}$) for the (a),(b) zonal and (b),(d) meridional components.

6.2.5 Mooring data processing

After a quality control of all the instrumental records, a data product was built for each mooring, where data were interpolated to a common time step of 1 hour. The temperature, salinity, and velocity data were then linearly interpolated into vertical profiles of 20 m depth for each time step. The gridded velocity data timeseries were low-pass filtered using a 4-day Hamming window (to remove the sub-inertial and tidal frequencies), and subsampled to daily values in a separate data set. As the top instruments were missing at both Vitiaz East and West moorings, velocity data only correspond to one single point current meter for each mooring (near 700 m and 800 m, respectively), and so are not shown. Furthermore, the upward-looking ADCP data at Solomon M2a could not be exploited for technical reasons, and so velocity data were only available through a single point current meter moored at 200 m depth (see M2a design in Figure 6.2). Thus, only six out the nine subsurface moorings (without Vitiaz East and West, and Solomon M2a) were further processed and analyzed.

Finally, the u and v velocity components were rotated (degrees True, hereinafter °T) in order to be parallel and perpendicular, respectively to the mean direction of the flow at different depth levels. For this purpose, the velocity field was first averaged over the 1.5 year deployment period, at the surface (0-100 m), the thermocline (100-300 m) and the intermediate level (500-1000 m), for each subsurface mooring (Figure 6.8a,b). At St Georges and Solomon moorings, the surface time-averaged velocities indicate, as expected, an inflow into the Solomon Sea, while the thermocline and intermediate flows are mostly oriented in the opposite direction. At Vitiaz Middle, the time-averaged flow is oriented northwestward over the whole water column. In addition, we can observe relatively consistent time-averaged flow directions between the thermocline and intermediate levels, I thus decided to rotate the u and v components respectively along and across the same mean direction for both depth layers (Table 6.3).

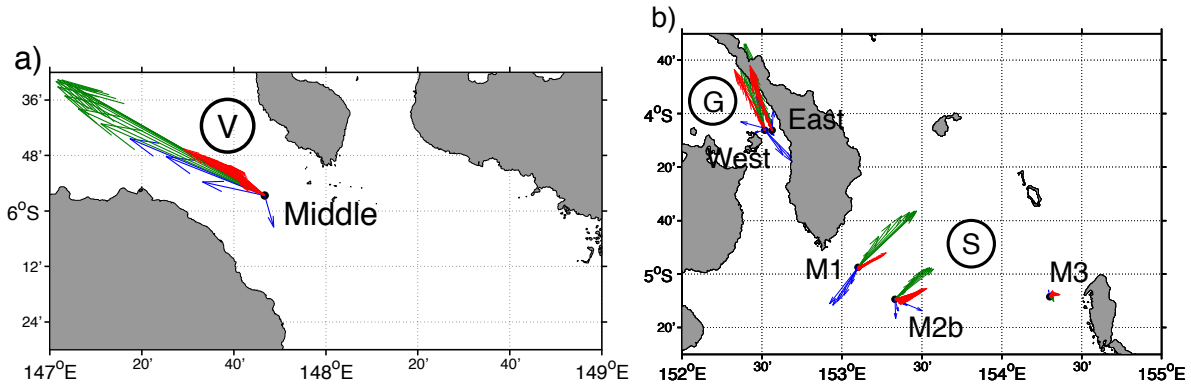

Figure 6.8 – Time-averaged flows over the first 1.5 year deployment period at the surface (0-100 m, blue arrows), the thermocline (100-300 m, green arrows) and the intermediate level (500-1000 m, red arrows) at (a) Vitiaz Middle and (b) St Georges West and East and Solomon M1, M2b and M3. Circled "V" and "S" abbreviate Vitiaz and Solomon straits, while "G" abbreviates St Georges Channel.

Table 6.3 – MoorSPICE mooring u and v velocity components are rotated to be oriented respectively along and across the time-averaged outflow direction at the thermocline and intermediate levels.

Mooring name	angle of rotation (°T)
Vitiaz Middle	300
St Georges East	335
St Georges West	330
Solomon M1	330
Solomon M2b	355
Solomon M3	0

6.3 Preliminary analyses

The next section provides basic spectral characteristics of the northern outflow at the six mooring locations and averaged over the thermocline and intermediate levels. The power spectra were estimated for the 1.5-year period for both flows, by averaging the periodograms of segments to reduce noise-induced variations in the power amplitudes. The associated degrees of freedom (DOF) is calculated (see *Emery and Thomson*, 2001), knowing the length of the timeseries and the number of independent measurements that is, as a simple hypothesis, the number of averaged periodograms to result in 5 DOF.

6.3.1 Thermocline and Intermediate flow variability: a spectral overview

Power spectra of the thermocline flow at each mooring location (Figure 6.9a) exhibit, as expected, more power at time scales larger than 50 days, except for Solomon M3 where power is quite stable beyond that period. At time scales ranging from 1 to 30 days, we cannot detect any narrow band variability and only a relatively constant power. At higher frequency, a mixed tidal cycle is distributed in two bands (as expected in the Solomon Sea region), the diurnal and semidiurnal tidal constituents with typical periods of 24hrs 50mins (M1 tide) and 12hrs 25mins (M2 tide). High power is also observed at periods of about 6hrs, likely corresponding to second tidal harmonics (also called overtides), which are usually formed in continental shelf areas by nonlinear processes (*Le Provost*, 1991).

At the intermediate level (Figure 6.9b), quite similar spectral distributions are found over the different mooring sites, associated with high power at periods larger than 50 days, a broad band component from 1-30 days, and tidal harmonics that peak in diurnal, semidiurnal and fourth-diurnal bands. Nevertheless, different power patterns than those observed over the thermocline are found at time scales larger than 100 days. Power is decreasing at both St Georges moorings, and to a lesser extent at Solomon M2b, whereas power is increasing at Vitiaz Middle and Solomon M3.

In a following section, the low-pass filtered and daily subsampled velocity data is shown to document the velocity vertical structure, as well as time variations of averaged flow over the thermocline and intermediate levels. Due to instrument loss in the upper layers at both Vitiaz West and East, velocity timeseries consist only in a single record at 800 and 700 m, respectively and so are not shown.

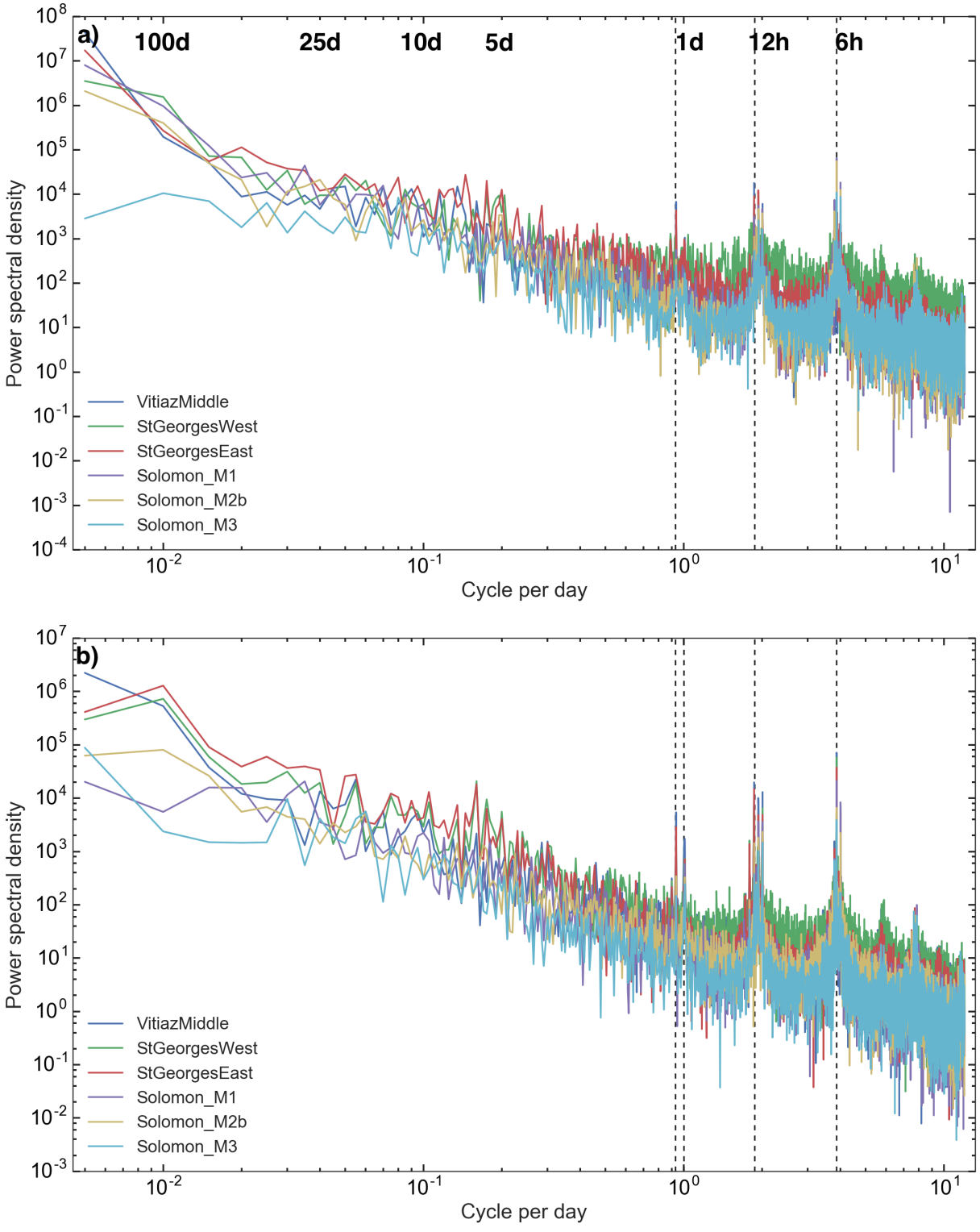

Figure 6.9 – Power spectral density computed for each MoorSPICE mooring where colors correspond to locations as indicated in legends (lower left) for (a) thermocline and (b) intermediate layers. The dashed lines indicate the highest power contributions of the tidal spectrum in both depth layers.

6.3.2 Velocity structure and intraseasonal to seasonal variability

Along Solomon M1, located southeast of New Ireland (Figure 6.1), most of the NICU is confined near 200 m all year long (Figure 6.10a). The current is enhanced in July-October (strong trade winds) with a velocity core of $\sim$0.7 m.s^{-1}, while we observe a weaker NICU in January-May 2013 (weak trade winds), associated with a strong southward current stretched down to 200 m. Velocities averaged over the thermocline (100-300 m) oscillate near 0.5 m.s^{-1}, while at intermediate depths (500-1000 m) the mean flow is weaker ($<$0.2 m.s^{-1}), with near zero velocities below 1000 m (lower panel, Figure 6.10a).

At Solomon M2b (further southeast), the NICU is also confined near the thermocline Figure 6.10b) with once again, maximum velocities in July-October (0.3-0.6 m.s^{-1}) and minimum ones in January-May ($<$0.3 m.s^{-1}). The surface inflow is also intensified and deeper during the weak trade season, while the NICU seems to vanish in April. At intermediate depths, currents are weak with similar velocities than those found at Solomon M1.

Further East, northwest of Bougainville Island, Solomon M3 (Figure 6.10c) is associated with low velocities ($<$0.2 m.s^{-1}), from the thermocline down to 1600 m, and over the whole 1.5-year timeseries. Above 100 m, we detect high velocity cores ($>$0.6 m.s^{-1}), likely related with transient surface eddies in July-August 2012 (also detected during Pandora cruise), and in February-March 2013 and 2014, when large surface cyclonic eddies are typically found in this region.

At St Georges Channel, a strong and highly variable SGU is observed (Figure 6.10d,e) at both thermocline and intermediate levels. We observe a strong northward flow in austral winter 2012 and April-September 2013, whereas the SGU reverse in late September-March to flow southward into the Solomon Sea. Maximum velocities can reach 0.8-1 m.s^{-1} at 200 m, while velocities range from 0.3 to 0.5 m.s^{-1} below 300 m at both St Georges moorings. However, the thermocline outflow is generally less intense, associated with a stronger seasonal variability and a lower vertical extent at St Georges East than at St Georges West. This marked and unexpected seasonality of the SGU has never been documented yet, and diverges from a 20-year S-ADCP climatology (*Cravatte et al.*, 2011) that identified a non seasonal variability, especially in austral summer.

At Vitiaz Middle, the striking feature is the all year long intense NGCU ($>$0.8 ms^{-1}) centered on 200 m (Figure 6.10f), previously documented as part of WEPOCS (*Lindstrom et al.*, 1987, 1990) and WOCE (*Murray et al.*, 1995) experiments. However, the vertical extent of the NGCU fluctuates seasonally, as it appears to be much thinner in austral summer 2013 ($\sim$100-300 m) than during austral winter ($\sim$100-450 m), which is consistent with S-ADCP surveys from the SPICE cruises, carried out during these two contrasted seasons. In addition, a seasonal reversal appears to occur below 600 m, with a southward flow during austral summer.

We thus found consistent results with our previous power spectra at both thermocline and intermediate levels, as most of the variability seems to occur at seasonal time scales.

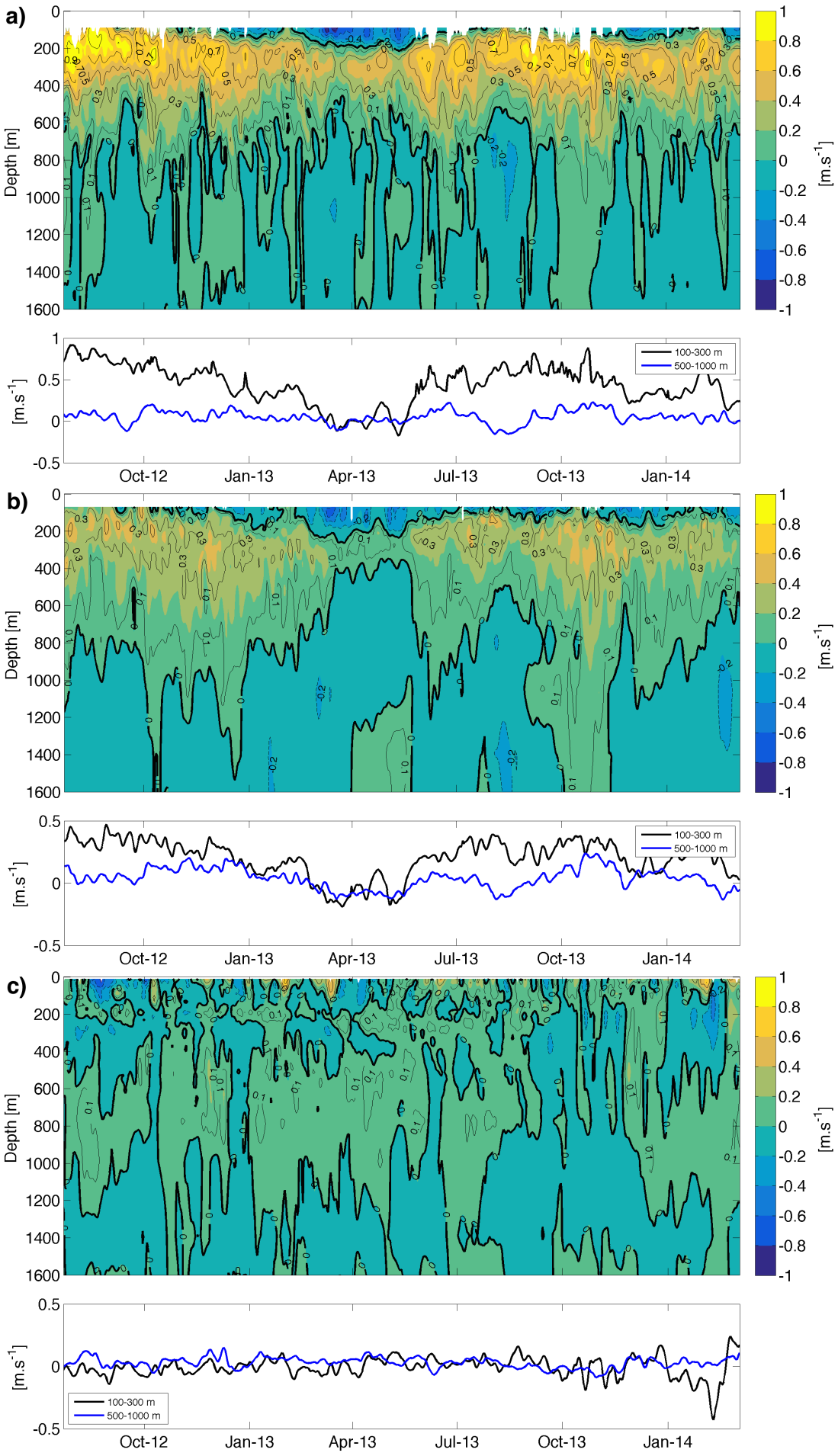

Figure 6.10 – Timeseries of the gridded velocity field (color scale) rotated along the mean flow direction, after a low-pass filter with a 4-day Hamming window near the surface to 1600 m (top panel) and averaged over the thermocline (100-300 m, black line) and intermediate (500-1000 m, blue line) layers (bottom panels) at (a) Solomon M1, (b) Solomon M2b and (c) Solomon M3.

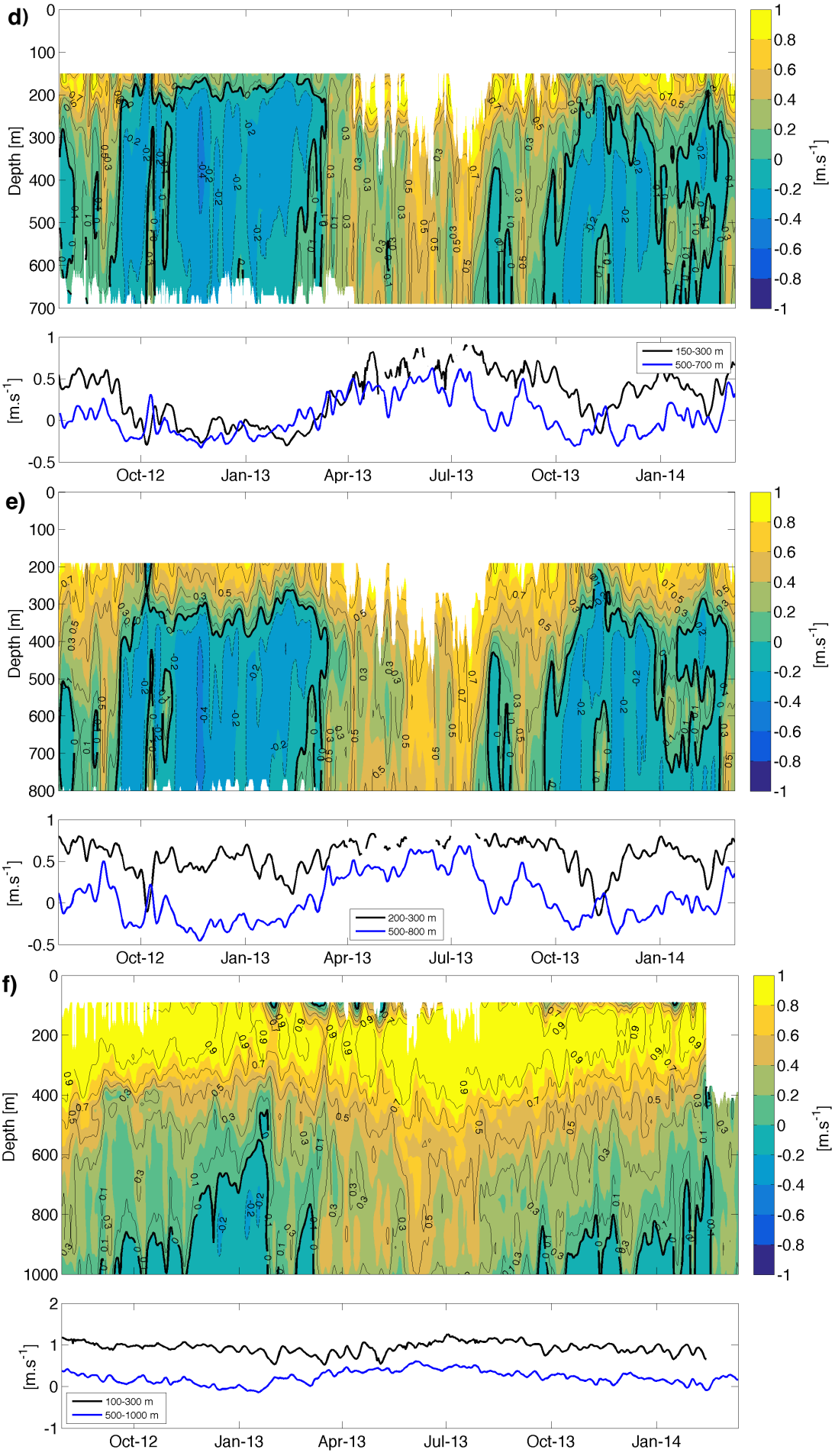

Figure 6.11 – Timeseries of the gridded velocity field (color scale) rotated along the mean flow direction, after a low-pass filter with a 4-day Hamming window between 200 and 700-800 m (top panel) and averaged over the thermocline (100-300 m, black line) and intermediate (500-800 m, blue line) layers (bottom panels) at (d) St Georges West and (e) St Georges East. In (f), similar velocity timeseries are shown at Vitiaz Middle for depths ranging from 100 to 1000 m (top panel) and averaged over 100-300 m for the thermocline and 500-1000 m for the intermediate level (bottom panel).

6.3.3 Variability between the northern exit passages: a coherence study

The coherence-squared is a statistic that is commonly used to examine the relation between two timeseries $x_1(t)$ and $x_2(t)$, defined for frequencies $f_k, k = 0, 1, ..., N-1$, as

$$\Upsilon_{12}^2(f_k) = \frac{|G_{12}(f_k)|^2}{G_{12}(f_k)G_{22}(f_k)} \tag{6.1}$$

where $G_{11}(f_k)$ is the one-sided spectrum (confined to $f_k \geq 0$) and $G_{12}(f_k)$ is the one-sided cross spectrum. Here

$$0 \leq \Upsilon_{12}^2(f_k) \leq 1 \tag{6.2}$$

and

$$\Upsilon_{12}(f_k) = \left|\Upsilon_{12}^2(f_k)\right|^{\frac{1}{2}} e^{-i\phi_{12}f_k} \tag{6.3}$$

where $\left|\Upsilon_{12}^2(f_k)\right|^{\frac{1}{2}}$ is the modulus of the coherence function and $\phi_{12}(f_k)$ the phase lag between the two signal at frequency f_k. Two signals of frequency f_k are considered highly coherent and in phase if $\left|\Upsilon_{12}^2(f_k)\right| \approx 1$ and $\phi_{12}(f_k) \approx 0$, respectively. Note that phase estimates generally become unreliable where the coherence-squared amplitudes fall below the 90-95% confidence levels for a given frequency. One can also determine the one standard deviation random errors associated with the coherence-squared estimates, described in *Bendat and Piersol* (2011) as

$$\epsilon[\Upsilon_{12}^2(f_k)] = (1 - \Upsilon_{12}^2(f_k))\sqrt{\frac{2\Upsilon_{12}^2(f_k)}{n_d}} \tag{6.4}$$

where n_d is the number of spectra averages, and it is assumed that $n_d \geq 1$. Note that $\epsilon[\Upsilon_{12}^2(f_k)]$ approaches zero as either $n_d \to \infty$ or $\Upsilon_{12}^2(f_k) \to 1$.

The one standard deviation errors for the coherence phase can also be determined (*Bendat and Piersol*, 2011):

$$\epsilon[\phi_{12}(f_k)] = \frac{\sqrt{\frac{1-\Upsilon_{12}^2(f_k)}{2\Upsilon_{12}^2(f_k)n_d}}}{2\pi f_k} \tag{6.5}$$

In order to determine if the flow variability is coherent and in phase between the moorings, the coherence-squared function (hereinafter coherence) and the phase lag with associated errors are computed for the thermocline (Figure 6.12a) and intermediate (Figure 6.12b) levels. The 95% confidence level for the coherence is calculated following *Emery and Thomson* (2001), $\gamma^2_{95\%} = 1 - (0.05)^{[2/(DOF-2)]}$ and is equal to 0.86.

Vitiaz Middle is used as a reference to compare the outflow passages, as well as Solomon M1 for direct comparisons between St Georges Channel and Solomon Strait (lower right panels). At the thermocline, periods where we observe energy in a broad band pattern (<50 days) are associated with low coherence features with large uncertainties. In the period of 50 days, the pairs of moorings are generally coherent (higher than the 95% level, with moderate uncertainties), although the Vitiaz-Solomon M3 case shows lower values, with quite low statistical significance. Maximum energy together with maximum coherence is found around 100-day periods (seasonal forcing), again except for the Vitiaz-Solomon M3 case, where much lower coherence suggests that the intraseasonal to seasonal variability might be driven by other physical processes or to contain additional components, potentially hiding the underlying coherence. We will then focus on coherent cases to examine the phase estimates and associated errors.

At periods of 50 days, the phase information (Figure 6.13a) suggests a lead (8-10 days) of the thermocline flow between both St Georges West and East with respect to Vitiaz, while a 5-day lag is observed between Vitiaz and the two Solomon sites (M1 and M2b). We thus observe opposite phases between both St Georges moorings with respect to Solomon M1 and M2b, associated with significant coherence estimates. Periods of 100 days exhibit no lead/lag in the flow between the different mooring locations, suggesting an uniformly phased thermocline circulation within the Solomon Sea, forced at seasonal scales by the annual march of the trade winds.

At the intermediate level, coherence is mostly significant for shorter periods around 50 days (0.02- cycle.d^-1) than those at the thermocline. Nevertheless, distinct features occur between each pair of moorings. The Vitiaz-St Georges East and Vitiaz-St Georges West cases appear to be also coherent (although near the 95% confidence level) at monthly time scales (0.03 cycle.d^-1), while Vitiaz-Solomon M1 and Vitiaz-Solomon M3 exhibit significant coherence for longer 100-day periods. Thus, the intermediate flow is related with different other modes of variability than the seasonal cycle, as the flow appears to be dynamically coherent at monthly to intraseasonal time scales between Vitiaz and St Georges.

Regarding the phase, we observed a lead of 1-2 days at monthly scales, and a lag of similar days at periods of ∼50 days between Vitiaz and both St Georges West and East. No lag is associated with Vitiaz-Solomon M1 and Vitiaz-Solomon M3 (unlike at the thermocline) at periods of 100 days. In addition, Vitiaz and Solomon M2b appears to be almost in opposing phase, as we detect a 20-day lead for the coherent periods of 50 days.

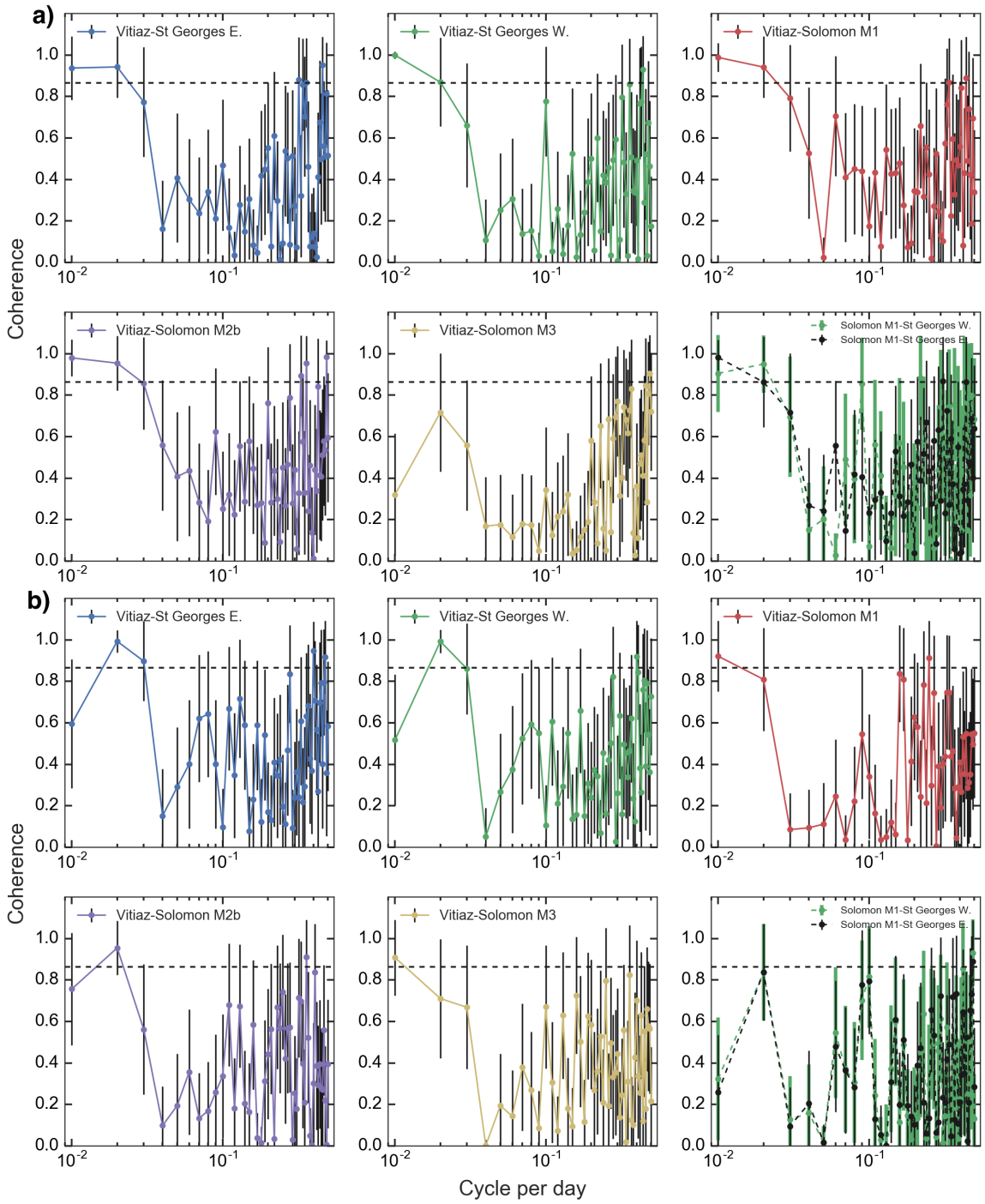

Figure 6.12 – Spectral coherence computed for each MoorSPICE mooring at (a) the thermocline and (b) intermediate levels. Line colors indicate the selected pair of moorings as shown in legends. Error bars (black lines) are one standard deviation. The 95% confidence interval is indicated (dash lines) following *Emery and Thomson* (2001) (see text).

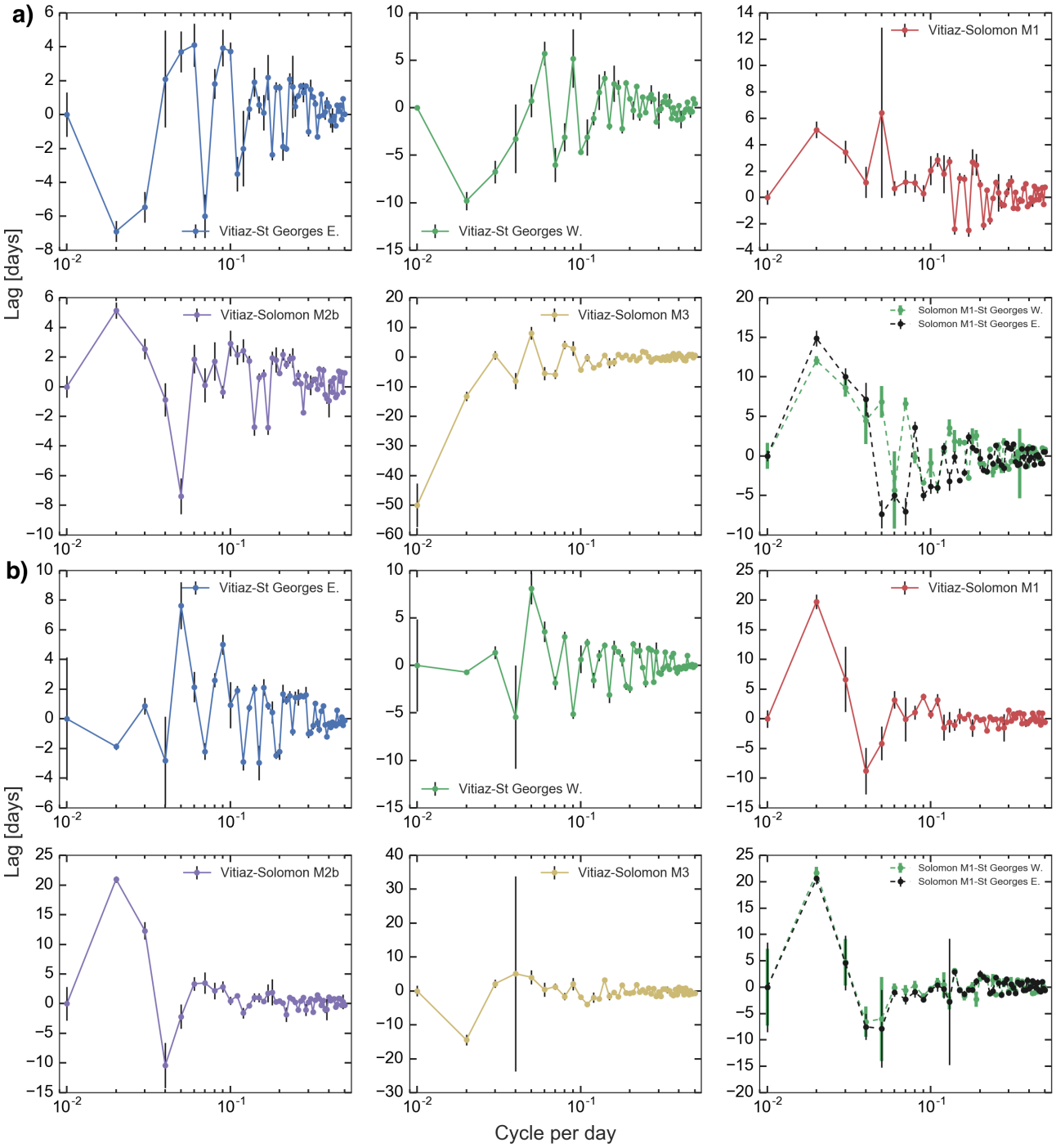

Figure 6.13 – Phases (expressed as lags in days) computed for each MoorSPICE mooring at the (a) thermocline and (b) intermediate levels. Line colors indicate the selected pair of moorings as shown in legends. Error bars (black lines) are one standard deviation.

6.4 Conclusions and perspectives

The MoorSPICE program, consisting of a 1.5-year deployment of nine moorings in the northern exit passages of the Solomon Sea, provides an unprecedented dataset to assess intraseasonal to seasonal variability of the equatorward LLWBC pathways. For the first time, a quasi simultaneous picture of the outflow through Vitiaz Strait, St Georges and Solomon Strait is available based on moored in situ velocity measurements.

The focus of this chapter was to briefly present the mooring instrumentation and associated data quality control, and give some insights into the thermocline and intermediate outflow variability through the three exit passages. High power contributions are found at tidal frequencies over diurnal, semidiurnal and fourth-diurnal bands for both thermocline and intermediate layers. At lower frequency, both outflows suggest that high power is present at seasonal time scales, for periods larger than 50 days.

Regarding the vertical structure of the velocity field over time, the striking feature is a strong thermocline outflow all year long at the different mooring sites, except for Solomon M3 where currents stronger than 20 cm.s^{-1} are occasional and confined near the surface and likely related with transient eddies. Despite this strong steady outflow, variations in intensity and vertical extent occur at seasonal time scale, coinciding with the trade season fluctuations. Indeed, strong northward currents extending down to intermediate layers are generally observed from July to late September during the height of the southeast trade season, which is consistent with previous studies based on model (*Melet et al.*, 2010a) and a 20-year S-ADCP climatology (*Cravatte et al.*, 2011).

In October-March, when the weak southeasterly trades prevail, the thermocline flow is weaker at Vitiaz Strait and St Georges Channel whereas at Solomon Strait, weaker currents are observed in January-May, suggesting a 2-month lag associated with the NICU. This difference might be explained by the southward shift of the SEC (near 8°S) during November-January, when *Melet et al.* (2010a) identifies a stronger SICU than the mean to compensate the water removal by the SEC east of the Solomon Sea. Moreover, we observed a strong and unexpected seasonal variability of the SGU at intermediate depths with a reversed southward flow during austral summer, while a similar reversal is noticed at Vitiaz Strait below 600 m. Causes of seasonal variability at intermediate depths require further investigations, however this is beyond the scope of this thesis work.

Regarding the outflow variability between the MoorSPICE moorings, thermocline pathways appear to vary coherently and in phase at intraseasonal to seasonal time scales, except in the case of Solomon M3 which is likely forced by other physical processes, such as subsurface mesoscale variability. It thus means that the whole LLWBC system within the Solomon Sea moves seasonally together at the thermocline level.

The intermediate flow is coherent at both monthly and intraseasonal time scales between Vitiaz and St Georges moorings with a lead and a lag of 1-2 days, respectively. At periods of 100 days, the pairs Vitiaz-Solomon M1 and Vitiaz-Solomon-M3 are coherent and in phase, while Vitiaz-Solomon M2b seems to vary in opposing phase at periods of 50 days.

A next step could be to investigate the temperature and salinity timeseries to infer the intraseasonal to seasonal variability of the water properties at both thermocline and intermediate levels. Another step could be to analyze the tides more thoroughly to assess potential modulation in time of the amplitude, as well as investigating the respective contributions of barotropic tides and internal waves.

The velocity fields might also be laterally interpolated between the moorings at Vitiaz Strait and St Georges Channel, and extrapolated to the strait sidewalls to estimate volume transports through both passages. The choices in interpolation and extrapolation methods could be guided by earlier available mooring analysis (*Lindstrom et al.*, 1987; *Murray et al.*, 1995) and an historical S-ADCP climatology (*Cravatte et al.*, 2011) in Vitiaz Strait, while the S-ADCP and L-ADCP measurements conducted during Pandora and MoorSPICE cruises could be used in St Georges Channel. As for Solomon Strait, velocities could be laterally interpolated between Solomon M1 and M2b, while geostrophic transports might be estimated between Solomon M2a and M3. In addition, corresponding heat and salt transport variability could be determined through the three passages. These transport timeseries would allow a full description of seasonal changes in mass and water properties in the narrow exit passages of the Solomon Sea, and provide more insights into whether the subtropical spiciness anomalies carried equatorward from the South Pacific subtropical gyre (*Kolodziejczyk and Gaillard*, 2012; *Qu et al.*, 2013) are damped within the Solomon Sea, which could reduce their impact on the equatorial Pacific water mass budget.

In addition, these seasonal timeseries of volume transports could be compared with a recent high-resolution numerical simulation *Djath et al.* (2014) developed specifically in the region, to better understand the mechanisms of the variability.

Finally, the analysis of the second 1.5-year mooring deployment (March 2014-August 2015) combined with this present data set will provide a refined description of the seasonal forcing on the western boundary current system, and potentially some insights into the interannual variability.

Conclusions and Perspectives

The Pacific western boundary currents (WBCs) transport mass and heat from the subtropical gyre to the equator, and represent a major source of the Equatorial Undercurrent (EUC) and the Indonesian Throughflow (ITF). They largely influence the western Pacific Warm Water Volume (WWV), with potential effects on the low frequency modulation of the equatorial climate, including the El *Niño* Southern Oscillation (ENSO) and Pacific decadal variability. Despite their widely accepted importance in the Pacific climate, the WBCs remain poorly documented. They are indeed narrow and swift currents flowing through intricate bathymetric features, making it difficult to develop and maintain suitable surveys. As such, the Pacific WBC region has motivated recent research efforts, including intensive observational focus together with targeted modeling studies. In particular, two international programs are underway: the Northwestern Pacific Ocean Circulation and Climate Experiment (NPOCE) and the Southwest Pacific Ocean Circulation and Climate Experiment (SPICE).

Within SPICE, significant advancements were made, including a better description of the WBC route across the South Pacific. The equatorward branches of the WBCs transit through the numerous islands of the Solomon Sea and exit through three narrow passages before reaching the equator. Each pathway possibly means different water mass combinations, and implies a different time scale for water to reach the equator. The ratio of transport through each of the passages may also vary with time. However, our understanding of the Solomon Sea WBCs is currently based on numerical studies, a S-ADCP climatology and sporadic ship-based measurements collected since the pioneering WEPOCS program, especially below the thermocline.

Thus, as part of SPICE, two oceanographic cruises were undertaken during two contrasted seasons: July-August 2012 and March 2014, including hydrographic transects and the deployment of nine moorings over the exit passages.

This thesis firstly aimed to assess the climate context and the near surface conditions during the July-August 2012 and March 2014 cruises. A second objective was to determine a refined picture of the low-latitude Solomon Sea WBC pathways during both seasons and associated transport partitions across each exit passage, as well as characterize the associated water mass properties and their modifications along those pathways. A last objective was to take a first step to examine the flow variability at the northern passages over both thermocline and intermediate levels from intraseasonal to seasonal time scales.

The climatic context during the July-August 2012 and March 2014 seasons shows distinct surface circulations and sea surface conditions, largely attributed to the southeast trade variations. Changes in eddy properties were identified due to a typical seasonal transition from "small scale" to "large scale" regimes. Both OLR and the Wheeler and Hendon Index suggest a relatively week MJO during each season, while at interannual time scales, both cruises were related with neutral phases of ENSO.

An intense inflow of 36 ± 3 Sv was found entering the Solomon Sea in July-August 2012 that fell by 70% in March 2014 to 11 ± 3 Sv. Large differences were also found in the total transport partitioning through each of the major exit straits during each season. The LLWBC pathways exhibit distinct water mass signatures in salinity, oxygen and nutrients that can be traced across the Solomon Sea, associated with significant water mass modifications. Salinity extrema at the thermocline and intermediate levels are both eroded, as waters transit through the sea. Salinity gradients within the subtropical Pacific are generally increased within the Solomon Sea, likely induced by stronger diapycnal mixing processes.

At depths greater than 2000 m, the deep flow within the Solomon Sea is related with the Upper Circumpolar Deep Water (UCDW) that emanates from the New Caledonia Trench and the South Fiji Basin. The UCDW transports 2-3 $Sv \pm 2$ Sv into the sea through the southern entrance, associated with high salinity, low oxygen and high nutrients characteristics. A northward flow carries 2-3 $Sv \pm 2$ Sv through the Solomon Strait, and probably reaches the western equatorial Pacific via the deep western boundary current (DWBC) between 2000 down to at least 2500 m. This previously unknown branch of the UCDW permits to better understand the upper deep layer pathways in the South Pacific, and to infer an equatorward transport of 9-10 Sv towards the North Pacific.

Seasonal variations in both intensity and vertical extent of the low-latitude WBCs occur at the MoorSPICE mooring sites, following the annual march of the trade winds. At the thermocline down to 1000 m, high velocity currents flow northward during the strong phase of the trades, while in October-March (weak trade season), the thermocline outflow decreases at Vitiaz Strait and St Georges Channel. At Solomon Strait, a decreased NICU is observed in January-May, when the eastward flowing SEC is expected to be enhanced east of the Solomon Sea. A striking feature is the well marked seasonal flow variability at St Georges Channel below the thermocline, with strong northward currents through March to September 2013 and a reversed inflow during austral winter.

Thermocline pathways vary coherently and in phase at intraseasonal to seasonal time scales, which means that the system of WBCs in the Solomon Sea moves seasonally together. The intermediate flow at Vitiaz and St Georges moorings is mostly coherent from monthly to intraseasonal time scales.

These new results provide a refined description of the oceanic circulation within the Solomon Sea, leading to an improved understanding of the low-latitude WBCs in the region during two contrasted seasons, as well as some insights into their variability between July-August 2012 and March 2014. Nevertheless, in spite of these new observations, two questions remain in the Solomon Sea regarding the mixing processes that cause the water mass transformations: (1) Is there a large contribution from diapycnal mixing as suggested in numerical simulations? (2) What is the part of mixing due to tidal forcing in the northern exit straits?

In our two inverse model configurations, the degree of mixing could have been examined through the vertical diffusivity estimates (κ_z) between the different layers, though they were not statistically significant to be realistic. The inverse model technique does not appear to be a suitable tool to investigate mixing in the Solomon Sea. Hence, other options need to be explored, such as indirect methods that provide estimates of turbulent dissipation rates (ϵ) to assess the mixing patterns in the Solomon Sea, as well as their potential sources, strength and their vertical and horizontal structures (*Alberty et al.*, 2016).

Another approach could be based on that of *Ffield and Gordon* (1992) who applied a simple advection-diffusion model to CTD profiles within the ITF to determine κ_z estimates and residence times. The solution is achieved based on "similarity" of model T-S profiles with the profiles of those within the Indonesian Seas, although it is a ad hoc model that requires various experiments on how to achieve this "similarity" and how to properly initialize the model with known conditions of T-S profiles.

Moreover, early results have shown the richness of the 1.5-year mooring data set, while next steps might include a time variability analysis of the water properties or a dedicated study to examine the tides more thoroughly. The barotropic contribution of the tides might be then compared to a tidal model specifically developed in the Solomon Sea region.

In order to estimate volume transports through Vitiaz Strait and St Georges Channel, the mooring velocity fields could be laterally interpolated and extrapolated to the sidewalls. At Solomon Strait, the velocities could also be interpolated between Solomon M1 and M2b, and then combined to velocities calculated between Solomon M2a an M3 from temperature and salinity measurements through geostrophic balance.

As a next step, heat and salt fluxes could be determined through the three northern straits. The timeseries of transport and property fluxes would be then examined in addition to their variability from intraseasonal to seasonal time scales. The analysis of the second 1.5-year mooring deployment (March 2014-August 2015) will provide an extended overview of the seasonal forcing on the Solomon Sea WBCs, and potentially some insights into the interannual variability. Comparisons with transport timeseries derived from CPIES[11] and "Spray" glider surveys near the southern entrance of the Solomon Sea would also provide valuable additional information. To better understand the mechanisms of the variability, the SPICE mooring timeseries could be compared with a recent numerical simulation dedicated to the region (*Djath et al.*, 2014).

Another work perspective concerns the coupling between ocean dynamics and biogeochemistry, in particular the distributions of diazotrophic (or N_2 fixing) organisms, such as *Trichodesmium*, that act as "natural fertilizers" and so contribute to sustain primary productivity in the global ocean (*Bonnet et al.*, 2015). During the July-August 2012 cruise, extremely high rates of N_2 fixation were measured in Vitiaz Strait, St Georges Channel and at the southern entrance of the Solomon Sea. This indicates that the buoyant *Trichodesmium* accumulated in the northern straits are probably transported via the strong low-latitude WBCs, and so its distribution might depend on the surface and subsurface circulation.

[11] Current and Pressure-recording Inverted Echo Sounders

As part of this study, we examined the salinity gradients in the Solomon Sea (Figure 6.14), as they could be the signature of local convergence in surface waters. However, only a weak correlation between salinity gradient and *Trichodesmium* was found, requiring to explore other indicators of possible water convergence, especially in the northern straits of the Solomon Sea, where the use of altimetric observations is strongly limited.

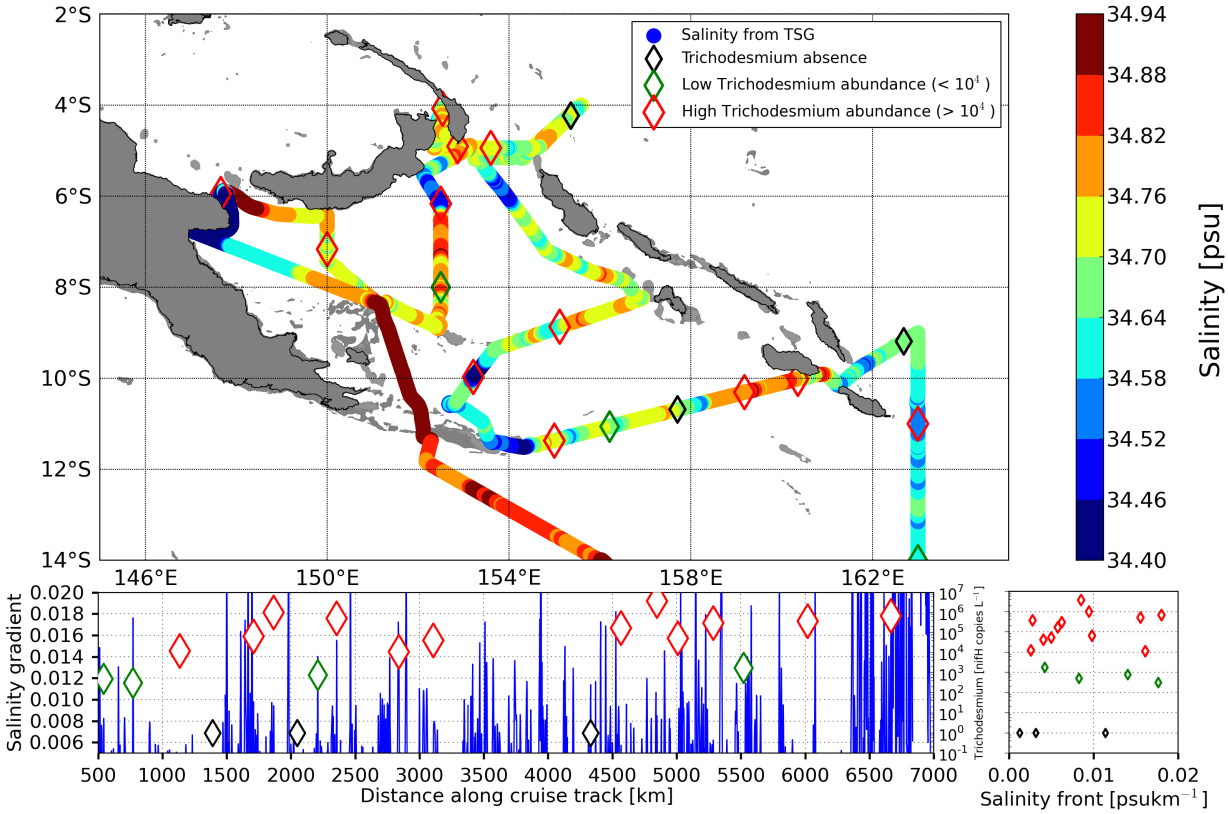

Figure 6.14 – Surface (0-30 m) *Trichodesmium* distributions and observed along-track sea surface salinity from the Thermosalinograph (TSG). Colored diamonds indicate different *Trichodesmium* abundance as indicated in the legend. (bottom left) salinity gradient (blue lines) along the cruise track and *Trichodesmium* abundance (see legend, diamonds) for the 0-30 m upper layer. (bottom right), same figure as (bottom left) but as *Trichodesmium* abundance versus salinity front.

Finally, the water mass enrichment in micro-nutrients such as iron, that feed the equatorial Pacific is tightly linked with the WBC dynamics in the Solomon Sea. The transport variability of the NGCU and the NICU at different time scales might modulate the equatorward supply of iron, as suggested by numerical tracer studies (*Grenier et al.*, 2013; *Qin et al.*, 2016), and so influence the primary productivity in the equatorial band.

The analysis of the traced elements collected during the two SPICE cruises together with the refined description of the WBC pathways and associated water properties depicted in this thesis will provide valuable information to better understand the iron supply variability into the equatorial Pacific.

Conclusions et perspectives

Ce travail de thèse porte sur la circulation océanique en mer des Salomon, identifiée comme un passage clé pour l'étude des courants de bord ouest dans le Pacifique Sud-ouest. Des études numériques ont suggéré des variations de transport saisonnières et interannuelles très fortes en mer des Salomon, ainsi que des transformations de masses d'eau induites par un fort mélange diapycnal. Néanmoins, seules quelques observations collectées pendant les programmes WEPOCS et WOCE étaient disponibles pour vérifier ces simulations numériques, ou tout au moins les comparer.

Dans le cadre du programme SPICE, deux campagnes en mer ont été réalisées en Juillet-Août 2012 (Pandora) et Mars 2014 (MoorSPICE), deux saisons contrastées de la mousson dans le Pacifique tropical, pour palier ce manque d'observations. Lors de ces deux campagnes, des mesures hydrologiques, courantométriques mais aussi géochimiques et biogéochimiques ont été collectées. En outre, des mouillages ont été déployés au niveau des détroits entre les deux campagnes (un an et demi environ), afin d'estimer la variabilité temporelle de cette circulation aux échelles intra-saisonnières et saisonnières.

Les objectifs de cette thèse étaient de caractériser la circulation en mer des Salomon pendant les deux campagnes, de déterminer les propriétés des masses d'eau passant par la mer des Salomon ainsi que leurs transformations, avant de rejoindre l'équateur. Pour cela, une approche par modèle inverse a été utilisée à partir des données hydrologiques, incluant deux configurations distinctes permettant d'estimer une circulation quasi-synoptique (i.e. à l'échelle des deux campagnes) de la surface jusqu'à en moyenne 3000 m de profondeur. Le traitement des données de mouillages fut aussi un objectif majeur de ce travail de thèse, suivi d'une première analyse pour estimer la variabilité des eaux de thermocline et des eaux intermédiaires au niveau des détroits situés au nord de la mer des Salomon.

La circulation en mer des Salomon pendant les deux campagnes, est étroitement liée au cycle saisonnier avec des transports associés aux courants de bord ouest plus intenses pendant l'hiver austral 2012. A l'entrée Sud de la mer des Salomon, le transport des 1000 premiers mètres atteint 36 ± 3 Sv en Juillet-Août 2012 alors qu'il n'est que de 11 ± 3 Sv en Mars 2014. La variabilité des transports entre les deux campagnes est surtout induite par des variations du NBCU et du NICU mais aussi de la circulation de surface au niveau du détroit des Salomon, où l'on observe un flot sortant de 2 Sv pendant l'hiver austral 2012 et un flot entrant d'environ 6 Sv en Mars 2014.

Par ailleurs, des masses d'eau avec des propriétés distinctes sont associées aux courants de bord ouest au cours de leur transit en mer des Salomon. Des transformations de masse d'eau ont été mises en évidence, notamment via l'érosion d'extrema de salinité et d'oxygène et des gradients de sel généralement plus importants en mer des Salomon que sur l'ensemble du Pacifique subtropical. Les gradients associés au transit du NGCU en mer des Salomon sont toutefois plus forts en Juillet-Août 2012 qu'en Mars 2014 au niveau de la thermocline et vice versa au niveau des eaux intermédiaires, attestant de la présence d'une variabilité saisonnière des transformations de masses d'eau en mer des Salomon.

La circulation profonde en mer des Salomon est caractérisée par le passage de l'UCDW entre 2000 jusqu'à environ 3000 m, associée à une forte salinité, un faible niveau d'oxygène et de fortes concentrations en sels nutritifs. L'UCDW peut être tracée depuis le bassin de Fidji et la fosse de la Nouvelle-Calédonie jusqu'à la mer des Salomon, où 2 à 3 $\pm$ 2 Sv traversent le détroit des Salomon avant de rejoindre le courant de bord ouest profond (DWBC) qui alimente le Pacifique équatorial ouest.

La série temporelle des mouillages nous a permis d'identifier d'importantes variations de l'intensité et de la structure verticale des courants de bord ouest en relation avec les fluctuations saisonnières des alizés. Concernant la variabilité entre les différents mouillages, les eaux de la thermocline varient de manière cohérente et en phase à l'échelle intra-saisonnière et saisonnière sauf à l'est du détroit des Salomon où d'autres processus physiques semblent affecter la variabilité de la circulation. Les eaux intermédiaires sont quant à elles cohérentes à l'échelle mensuelle et intra-saisonnière entre Vitiaz et les deux mouillages du chenal St Georges. Pour des périodes proches de 100 jours, les paires de mouillages Vitiaz-Salomon M1 et Vitiaz-Salomon M3 sont corrélées et en phase, alors que la paire Vitiaz-Solomon M2b semble varier en opposition de phase à l'échelle intra-saisonnière.

Les résultats obtenus dans le cadre cette thèse ont permis de mieux comprendre la circulation associée au courants de bord ouest en mer des Salomon. Toutefois, des questions restent encore sans réponses, notamment concernant les processus de mélange à l'origine des transformations de masses d'eau observées. Une étude numérique ciblée sur la région (*Melet et al.*, 2011) a identifié les ondes de marée interne comme étant une cause majeure de ce mélange, mais cette hypothèse a toujours besoin d'être vérifiée et potentiellement quantifiée par des observations in situ. Pour ce faire, l'utilisation d'instruments récents capables de mesurer les microstructures dans l'océan pourrait être envisagée (e.g. "Microstructure Turbulence Profilers", ou encore des "Ocean Microstructure gliders").

Une des perspective majeure de cette thèse est d'estimer la variabilité des transports de masse et de chaleur à travers les passages clés de la mer des Salomon, ainsi que la variabilité des propriétés des masses d'eaux. De plus, la campagne Cassiopée menée en Août 2015 a permis de récupérer les mouillages déployés dans les différents détroits en Mars 2014, mettant à disposition une nouvelle série temporelle d'un an et demi. L'analyse de ces nouvelles données permettra une vision plus détaillée du cycle saisonnier associé aux courants de bord ouest, et probablement un aperçu du cycle interannuel dans un contexte particulier concernant ENSO, comme le suggère l'El Niño avorté de 2014 et l'arrivée d'un fort El Niño en 2015.

D'autres perspectives d'études peuvent être envisagées concernant le couplage entre dynamique physique et biogéochimique, notamment la fixation d'azote faite par des cyanobactéries diazotrophiques qui agissent comme des "fertilisateurs naturels" et contribuent donc à soutenir la production primaire (*Bonnet et al.*, 2015). Durant l'hiver austral de 2012, une forte concentration en diazotrophes a été mesurée en mer des Salomon, dont la distribution spatiale est fortement dépendante de la circulation de surface et de subsurface.

Dans le cadre de cette étude, nous avons examiné les zones de gradients de salinité comme un indicateur potentiel de convergence des eaux de surface, et donc des diazotrophes (Figure 6.14) étant donné que la région est difficilement accessible par altimétrie à cause des passages étroits et des nombreuses îles de la mer des Salomon. Seule une faible corrélation a été établie entre forts gradients et forte abondance de diazotrophes, nécessitant d'explorer d'autres indicateurs de convergence possibles.

Enfin, l'enrichissement des masses d'eau qui alimentent le Pacifique équatorial en éléments micro-nutritifs, tels que le fer, est étroitement lié à la dynamique des courants de bord ouest en mer des Salomon. La variabilité des transports du NGCU et du NICU à différentes échelles de temps peuvent moduler l'apport en fer, comme suggéré par des simulations numériques lagrangiennes (*Grenier et al.*, 2013; *Qin et al.*, 2016) et donc impacter la production primaire du Pacifique équatorial.

Il apparaît donc essentiel d'examiner les concentrations en éléments traces collectés pendant les deux campagnes de Juillet-Août 2012 et Mars 2014 en mer des Salomon, à la lumière de la circulation et des propriétés des masses d'eau apportés par ce travail de thèse.

References

Alberty, M. S., Sprintall, J., MacKinnon, J., Ganachaud, A., Cravatte, S., Eldin, G., and Germineaud, C. (2016). Spatial patterns of mixing in the solomon sea. *Journal of Geophysical Research*. Manuscript in preparation.

Alexander, M. A., Bladé, I., Newman, M., Lanzante, J. R., Lau, N.-C., and Scott, J. D. (2002). The atmospheric bridge: The influence of enso teleconnections on air–sea interaction over the global oceans. *Journal of Climate*, 15(16):2205–2231.

Anderson, L. A. and Sarmiento, J. L. (1994). Redfield ratios of remineralization determined by nutrient data analysis. *Global biogeochemical cycles*, 8(1):65–80.

Ashok, K., Behera, S. K., Rao, S. A., Weng, H., and Yamagata, T. (2007). El niño modoki and its possible teleconnection. *Journal of Geophysical Research: Oceans*, 112(C11). C11007.

Battisti, D. S. and Hirst, A. C. (1988). Interannual variability in a tropical atmosphere–ocean model: Influence of the basic state, ocean geometry and nonlinearity. *Journal of the Atmospheric Sciences*, 46(12):1687–1712.

Bendat, J. S. and Piersol, A. G. (2011). *Random data: analysis and measurement procedures*, volume 729. John Wiley & Sons.

Bjerknes, J. (1969). Atmospheric teleconnections from the equatorial pacific. *Monthly Weather Review*, 97:l63–l72.

Blanke, B. and Raynaud, S. (1997). Kinematics of the pacific equatorial undercurrent: An eulerian and lagrangian approach from gcm results. *Journal of Physical Oceanography*, 27(6):1038–1053.

Bonnet, S., Rodier, M., Turk-Kubo, K. A., Germineaud, C., Menkes, C., Ganachaud, A., Cravatte, S., Raimbault, P., Campbell, E., Queroue, F., Sarthou, G., Desnues, A., Maes, C., and Eldin, G. (2015). Contrasted geographical distribution of N2 fixation rates and nif H phylotypes in the Coral and Solomon Seas (southwestern Pacific) during austral winter conditions. *Global Biogeochemical Cycles*, pages n/a–n/a.

Broecker, W. S. (1974). "no", a conservative water-mass tracer. *Earth and Planetary Science Letters*, 23(1):100–107.

Butt, J. and Lindstrom, E. (1994). Currents off the east coast of New Ireland, Papua New Guinea, and their relevance to regional undercurrents in the western equatorial Pacific Ocean. *Journal of Geophysical Research*, 99(C6):12503.

Cai, W., Borlace, S., Lengaigne, M., van Rensch, P., Collins, M., Vecchi, G., Timmermann, A., Santoso, A., McPhaden, M. J., Wu, L., England, M. H., Wang, G., Guilyardi, E., and Jin, F.-F. (2014). Increasing frequency of extreme el nino events due to greenhouse warming. *Nature Clim. Change*, 4(2):111–116.

Cai, W., Lengaigne, M., Borlace, S., Collins, M., Cowan, T., McPhaden, M. J., Timmermann, A., Power, S., Brown, J., Menkes, C., Ngari, A., Vincent, E. M., and Widlansky, M. J. (2012). More extreme swings of the south pacific convergence zone due to greenhouse warming. *Nature*, 488(7411):365–369.

Callahan, J. E. (1972). The structure and circulation of deep water in the antarctic. *Deep Sea Research and Oceanographic Abstracts*, 19(8):563–575.

Cheng, W., McPhaden, M. J., Zhang, D., and Metzger, E. J. (2007). Recent changes in the pacific subtropical cells inferred from an eddy-resolving ocean circulation model. *Journal of Physical Oceanography*, 37(5):1340–1356.

Collins, M., An, S.-I., Cai, W., Ganachaud, A., Guilyardi, E., Jin, F.-F., Jochum, M., Lengaigne, M., Power, S., Timmermann, A., et al. (2010). The impact of global warming on the tropical pacific ocean and el niño. *Nature Geoscience*, 3(6):391–397.

Cowley, R., Heaney, B., Wijffels, S., Pender, L., Sprintall, J., Kawamoto, S., and Molcard, R. (2008). Instant sunda data report: Description and quality control.

Cravatte, S., Ganachaud, A., Duong, Q.-P., Kessler, W. S., Eldin, G., and Dutrieux, P. (2011). Observed circulation in the Solomon Sea from SADCP data. *Progress In Oceanography*, 88(1-4):116–130.

Davis, R. E., Kessler, W. S., and Sherman, J. T. (2012). Gliders Measure Western Boundary Current Transport from the South Pacific to the Equator. *Journal of Physical Oceanography*, 42(11):2001–2013.

Delcroix, T., Radenac, M.-H., Cravatte, S., Alory, G., Gourdeau, L., Léger, F., Singh, A., and Varillon, D. (2014). Sea surface temperature and salinity seasonal changes in the western solomon and bismarck seas. *Journal of Geophysical Research: Oceans*, 119(4):2642–2657.

Deser, C., Alexander, M. A., and Timlin, M. S. (1996). Upper-ocean thermal variations in the north pacific during 1970–1991. *Journal of Climate*, 9(8):1840–1855.

Djath, B., Melet, A., Verron, J., Molines, J.-M., Barnier, B., Gourdeau, L., and Debreu, L. (2014). A 1/36 model of the Solomon Sea embedded into a global ocean model: On the setting up of an interactive open boundary nested model system. *Journal of Operational Oceanography*, 7(1):34–46.

Donguy, J. and Henin, C. (1977). Origin of the surface tropical water in the Coral and Tasman Seas. *Mar. Freshwater Res.*, 28(3):321–332.

Donlon, C. J., Martin, M., Stark, J., Roberts-Jones, J., Fiedler, E., and Wimmer, W. (2012). The operational sea surface temperature and sea ice analysis (ostia) system. *Remote Sensing of Environment*, 116:140–158.

Ducet, N., Le Traon, P.-Y., and Reverdin, G. (2000). Global high-resolution mapping of ocean circulation from topex/poseidon and ers-1 and-2. *Journal of Geophysical Research: Oceans*, 105(C8):19477–19498.

Emery, W. J. and Thomson, R. E. (2001). *Data analysis in physical oceanography*. Elsevier.

Ffield, A. and Gordon, A. L. (1992). Vertical mixing in the indonesian thermocline. *Journal of Physical Oceanography*, 22(2):184–195.

Fieux, M., Molcard, R., and Ilahude, A. G. (1996). Geostrophic transport of the pacific-indian oceans throughflow. *Journal of Geophysical Research: Oceans*, 101(C5):12421–12432.

Fine, R. A., Lukas, R., Bingham, F. M., Warner, M. J., and Gammon, R. H. (1994). The western equatorial pacific: A water mass crossroads. *Journal of Geophysical Research: Oceans*, 99(C12):25063–25080.

Folland, C. K., Renwick, J. A., Salinger, M. J., and Mullan, A. B. (2002). Relative influences of the interdecadal pacific oscillation and enso on the south pacific convergence zone. *Geophysical Research Letters*, 29(13):21–1–21–4.

Frankignoul, C. and Sennéchael, N. (2007). Observed influence of north pacific sst anomalies on the atmospheric circulation. *Journal of Climate*, 20(3):592–606.

Fukumori, I., Lee, T., Cheng, B., and Menemenlis, D. (2004). The origin, pathway, and destination of niño-3 water estimated by a simulated passive tracer and its adjoint. *Journal of Physical Oceanography*, 34(3):582–604.

Ganachaud, A. (2003a). Error budget of inverse box models: The north atlantic. *Journal of Atmospheric and Oceanic Technology*, 20(11):1641–1655.

Ganachaud, A. (2003b). Large-scale mass transports, water mass formation, and diffusivities estimated from world ocean circulation experiment (woce) hydrographic data. *Journal of Geophysical Research: Oceans*, 108(C7).

Ganachaud, A., Cravatte, S., Melet, A., Schiller, A., Holbrook, N. J., Sloyan, B. M., Widlansky, M. J., Bowen, M., Verron, J., Wiles, P., Ridgway, K., Sutton, P., Sprintall, J., Steinberg, C., Brassington, G., Cai, W., Davis, R., Gasparin, F., Gourdeau, L., Hasegawa, T., Kessler, W., Maes, C., Takahashi, K., Richards, K. J., and Send, U. (2014). The Southwest Pacific Ocean circulation and climate experiment (SPICE). *Journal of Geophysical Research: Oceans*, 119(11):7660–7686.

Ganachaud, A., Cravatte, S., Sprintall, J., Germineaud, C., Alberty, M. S., Jeandel, C., Eldin, G., Benavides, M., Bonnet, S., Heimburger, L.-E., Lefevre, J., Metzl, N., Michael, S., Resing, J., Queroue, F., Sarthou, G., Rodier, M., Berthelot, H., Baurand, F., Grelet, J., Hasegawa, T., Kessler, W., Kilepak, M., Lacan, F., Privat, E., Send, U., Van Beek, P., and Souhaut, M. (2016). Two oceanographic cruises explore the Solomon Sea circulation, chemistry, geochemistry and biology. *Elementa*. Manuscript submitted for publication.

Ganachaud, A., Gourdeau, L., and Kessler, W. (2008). Bifurcation of the subtropical south equatorial current against new caledonia in december 2004 from a hydrographic inverse box model*. *Journal of Physical Oceanography*, 38(9):2072–2084.

Ganachaud, A. and Wunsch, C. (2002). Oceanic nutrient and oxygen transports and bounds on export production during the world ocean circulation experiment. *Global Biogeochemical Cycles*, 16(4).

Ganachaud, A., Wunsch, C., Marotzke, J., and Toole, J. (2000). Meridional overturning and large-scale circulation of the indian ocean. *Journal of Geophysical Research: Oceans*, 105(C11):26117–26134.

Gasparin, F., Ganachaud, A., Maes, C., Marin, F., and Eldin, G. (2012). Oceanic transports through the Solomon Sea: The bend of the New Guinea Coastal Undercurrent. *Geophysical Research Letters*, 39(15).

Gordon, A. L. and Fine, R. A. (1996). Pathways of water between the pacific and indian oceans in the indonesian seas. *Nature*, 379(6561):146–149.

Gordon, A. L. and McClean, J. L. (1999). Thermohaline stratification of the indonesian seas: Model and observations. *Journal of Physical Oceanography*, 29(2):198–216.

Gordon, R. L. and Instruments, R. (1996). Principles of operation a practical primer. *RD Instruments, San Diego*.

Gourdeau, L., Kessler, W. S., Davis, R. E., Sherman, J., Maes, C., and Kestenare, E. (2008). Zonal jets entering the coral sea. *Journal of Physical Oceanography*, 38(3):715–725.

Gourdeau, L., Verron, J., Melet, A., Kessler, W., Marin, F., and Djath, B. (2014). Exploring the mesoscale activity in the Solomon Sea: A complementary approach with a numerical model and altimetric data. *Journal of Geophysical Research: Oceans*, 119(4):2290–2311.

Grenier, M., Cravatte, S., Blanke, B., Menkes, C., Koch-Larrouy, A., Durand, F., Melet, A., and Jeandel, C. (2011). From the western boundary currents to the Pacific Equatorial Undercurrent: Modeled pathways and water mass evolutions. *Journal of Geophysical Research*, 116(C12):C12044.

Grenier, M., Jeandel, C., Lacan, F., Vance, D., Venchiarutti, C., Cros, A., and Cravatte, S. (2013). From the subtropics to the central equatorial Pacific Ocean: Neodymium isotopic composition and rare earth element concentration variations. *Journal of Geophysical Research*.

Gu, D. and Philander, S. G. H. (1997). Interdecadal climate fluctuations that depend on exchanges between the tropics and extratropics. *Science*, 275(5301):805–807.

Haffke, C. and Magnusdottir, G. (2013). The south pacific convergence zone in three decades of satellite images. *Journal of Geophysical Research: Atmospheres*, 118(19):10,839–10,849. 2013JD019929.

Hanawa, K. and Talley, L. D. (2001). Mode waters. *International Geophysics Series*, 77:373–386.

Harper, S. (2000). Thermocline ventilation and pathways of tropical–subtropical water mass exchange. *Tellus A*, 52(3):330–345.

Hasson, A., Delcroix, T., and Boutin, J. (2013). Formation and variability of the South Pacific Sea surface salinity maximum in recent decades. *Journal of Geophysical Research: Oceans*.

Hazeleger, W., Visbeck, M., Cane, M., Karspeck, A., and Naik, N. (2001). Decadal upper ocean temperature variability in the tropical pacific. *Journal of Geophysical Research: Oceans*, 106(C5):8971–8988.

Hristova, H. G. and Kessler, W. S. (2012). Surface Circulation in the Solomon Sea Derived from Lagrangian Drifter Observations. *Journal of Physical Oceanography*, 42(3):448–458.

Hristova, H. G., Kessler, W. S., McWilliams, J. C., and Molemaker, M. J. (2014). Mesoscale variability and its seasonality in the Solomon and Coral Seas. *Journal of Geophysical Research: Oceans*.

Hu, D., Wu, L., Cai, W., Gupta, A. S., Ganachaud, A., Qiu, B., Gordon, A. L., Lin, X., Chen, Z., Hu, S., Wang, G., Wang, Q., Sprintall, J., Qu, T., Kashino, Y., Wang, F., and Kessler, W. S. (2015). Pacific western boundary currents and their roles in climate. *Nature*, 522(7556):299–308.

Hummon, J. M. and Firing, E. (2003). A direct comparison of two rdi shipboard adcps: A 75-khz ocean surveyor and a 150-khz narrow band. *Journal of Atmospheric and Oceanic Technology*, 20(6):872–888.

Ishida, A., Kashino, Y., Hosoda, S., and Ando, K. (2008). North-south asymmetry of warm water volume transport related with el niño variability. *Geophysical Research Letters*, 35(18).

Izumo, T. (2005). The equatorial undercurrent, meridional overturning circulation, and their roles in mass and heat exchanges during el niño events in the tropical pacific ocean. *Ocean Dynamics*, 55(2):110–123.

Izumo, T., Picaut, J., and Blanke, B. (2002). Tropical pathways, equatorial undercurrent variability and the 1998 la niña. *Geophysical Research Letters*, 29(22):37–1–37–4. 2080.

Jin, F.-F. (1997). An equatorial ocean recharge paradigm for enso. part I: Conceptual model. *Journal of the Atmospheric Sciences*, 54(7):811–829.

Johnson, G. C. (2008). Quantifying antarctic bottom water and north atlantic deep water volumes. *Journal of Geophysical Research: Oceans*, 113(C5):n/a–n/a. C05027.

Johnson, G. C. and McPhaden, M. J. (1999). Interior pycnocline flow from the subtropical to the equatorial pacific ocean. *Journal of Physical Oceanography*, 29(12):3073–3089.

Johnson, G. C., McPhaden, M. J., Rowe, G. D., and McTaggart, K. E. (2000). Upper equatorial pacific ocean current and salinity variability during the 1996–1998 el niño–la niña cycle. *Journal of Geophysical Research: Oceans*, 105(C1):1037–1053.

Johnson, G. C. and Toole, J. M. (1993). Flow of deep and bottom waters in the Pacific at 10%N. *Deep Sea Res. Part I*, 40:371–394.

Kawabe, M. and Fujio, S. (2010). Pacific ocean circulation based on observation. *Journal of Oceanography*, 66(3):389–403.

Kawabe, M., Fujio, S., and Yanagimoto, D. (2003). Deep-water circulation at low latitudes in the western north pacific. *Deep Sea Research Part I: Oceanographic Research Papers*, 50(5):631–656.

Kawabe, M., Yanagimoto, D., and Kitagawa, S. (2006). Variations of deep western boundary currents in the melanesian basin in the western north pacific. *Deep Sea Research Part I: Oceanographic Research Papers*, 53(6):942–959.

Kessler, W. S. (1999). Interannual variability of the subsurface high salinity tongue south of the equator at 165 °e. *Journal of Physical Oceanography*, 29(8):2038–2049.

Kessler, W. S. and Cravatte, S. (2013a). ENSO and Short-Term Variability of the South Equatorial Current Entering the Coral Sea. *Journal of Physical Oceanography*, 43(5):956–969.

Kessler, W. S. and Cravatte, S. (2013b). Mean circulation of the Coral Sea. *Journal of Geophysical Research: Oceans*, 118(12):6385–6410.

Kessler, W. S. and Gourdeau, L. (2007). The annual cycle of circulation of the southwest subtropical pacific, analyzed in an ocean gcm. *Journal of Physical Oceanography*, 37(6):1610–1627.

Kessler, W. S. and McPhaden, M. J. (1995). The 1991–1993 el niño in the central pacific. *Deep Sea Research Part II: Topical Studies in Oceanography*, 42(2):295–333.

Kleeman, R., McCreary, J. P., and Klinger, B. A. (1999). A mechanism for generating enso decadal variability. *Geophysical Research Letters*, 26(12):1743–1746.

Kolodziejczyk, N. and Gaillard, F. (2012). Observation of spiciness interannual variability in the pacific pycnocline. *Journal of Geophysical Research: Oceans*, 117(C12):n/a–n/a. C12018.

Kug, J.-S., Jin, F.-F., and An, S.-I. (2009). Two types of el niño events: Cold tongue el niño and warm pool el niño. *Journal of Climate*, 22(6):1499–1515.

Larkin, N. K. and Harrison, D. E. (2005a). Global seasonal temperature and precipitation anomalies during el niño autumn and winter. *Geophysical Research Letters*, 32(16). L16705.

Larkin, N. K. and Harrison, D. E. (2005b). On the definition of el niño and associated seasonal average u.s. weather anomalies. *Geophysical Research Letters*, 32(13). L13705.

Latif, M. (1998). Dynamics of interdecadal variability in coupled ocean–atmosphere models. *Journal of Climate*, 11(4):602–624.

Le Provost, C. (1991). *Generation of overtides and compound tides, review.* John Wiley & Sons, Inc., New York, New York.

Lee, H. (2014). Climate algorithm theoretical basis document (c-atbd): Outgoing longwave radiation (olr)—daily. noaa's climate data record (cdr) program. Technical report, CDRP-ATBD-0526.

Lee, T. and Fukumori, I. (2003). Interannual-to-decadal variations of tropical-subtropical exchange in the pacific ocean: Boundary versus interior pycnocline transports. *Journal of Climate*, 16(24):4022–4042.

Lengaigne, M., Hausmann, U., Madec, G., Menkes, C., Vialard, J., and Molines, J. M. (2012). Mechanisms controlling warm water volume interannual variations in the equatorial pacific: diabatic versus adiabatic processes. *Climate Dynamics*, 38(5):1031–1046.

Levitus, S., Antonov, J. I., Boyer, T. P., Baranova, O. K., Garcia, H. E., Locarnini, R. A., Mishonov, A. V., Reagan, J. R., Seidov, D., Yarosh, E. S., and Zweng, M. M. (2012). World ocean heat content and thermosteric sea level change (0–2000 m), 1955–2010. *Geophysical Research Letters*, 39(10):n/a–n/a. L10603.

Liebmann, B. (1996). Description of a complete (interpolated) outgoing longwave radiation dataset. *Bull. Amer. Meteor. Soc.*, 77:1275–1277.

Lindstrom, E., Butt, J., Lukas, R., and Godfrey, S. (1990). The flow through vitiaz strait and st. george's channel, papua new guinea. In *The Physical Oceanography of Sea Straits*, pages 171–189. Springer.

Lindstrom, E., Lukas, R., Fine, R. A., Godfrey, J. S., Meyers, G., and Tsuchiya, M. (1987). The Western Equatorial Pacific Ocean Circulation Study. *Nature*, 330:533–537.

Liu, Z., Wu, L., and Bayler, E. (1999). Rossby wave–coastal kelvin wave interaction in the extratropics. part i: Low-frequency adjustment in a closed basin. *Journal of Physical Oceanography*, 29(9):2382–2404.

Lu, P. and McCreary, J. P. (1995). Influence of the itcz on the flow of thermocline water from the subtropical to the equatorial pacific ocean. *Journal of Physical Oceanography*, 25(12):3076–3088.

Lumpkin, R. and Johnson, G. C. (2013). Global ocean surface velocities from drifters: Mean, variance, el niño–southern oscillation response, and seasonal cycle. *Journal of Geophysical Research: Oceans*, 118(6):2992–3006.

Luo, Y., Rothstein, L. M., Zhang, R.-H., and Busalacchi, A. J. (2005). On the connection between south pacific subtropical spiciness anomalies and decadal equatorial variability in an ocean general circulation model. *Journal of Geophysical Research: Oceans*, 110(C10).

Lysne, J., Chang, P., and Giese, B. (1997). Impact of the extratropical pacific on equatorial variability. *Geophysical Research Letters*, 24(21):2589–2592.

Macdonald, A. M., Mecking, S., Robbins, P., Toole, J., Johnson, G. C., Talley, L., Cook, M., and Wijffels, S. (2009). The woce-era 3-d pacific ocean circulation and heat budget. *Progress in Oceanography*, 82(4):281–325.

Madden, R. A. and Julian, P. R. (1972). Description of global-scale circulation cells in the tropics with a 40–50 day period. *Journal of the Atmospheric Sciences*, 29(6):1109–1123.

Mantua, N. J., Hare, S. R., Zhang, Y., Wallace, J. M., and Francis, R. C. (1997). A pacific interdecadal climate oscillation with impacts on salmon production. *Bulletin of the American Meteorological Society*, 78(6):1069–1079.

Mantyla, A. W. and Reid, J. L. (1983). Abyssal characteristics of the world ocean waters. *Deep Sea Research Part A. Oceanographic Research Papers*, 30(8):805–833.

Matthews, A. J. (2012). A multiscale framework for the origin and variability of the south pacific convergence zone. *Quarterly Journal of the Royal Meteorological Society*, 138(666):1165–1178.

McCartney, M. (1977). Subantarctic mode water. *A Voyage of Discovery: George Deacon 70th Anniversary Volume*, pages 103–119.

McCreary, J. P. and Lu, P. (1994). Interaction between the subtropical and equatorial ocean circulations: The subtropical cell. *Journal of Physical Oceanography*, 24(2):466–497.

McPhaden, M. J. (2015). Playing hide and seek with el nino. *Nature Clim. Change*, 5(9):791–795.

McPhaden, M. J., Busalacchi, A. J., Cheney, R., Donguy, J.-R., Gage, K. S., Halpern, D., Ji, M., Julian, P., Meyers, G., Mitchum, G. T., et al. (1998). The tropical ocean-global atmosphere observing system: A decade of progress. *Journal of Geophysical Research: Oceans*, 103(C7):14169–14240.

McPhaden, M. J., Zebiak, S. E., and Glantz, M. H. (2006). Enso as an integrating concept in earth science. *Science*, 314(5806):1740–1745.

McPhaden, M. J. and Zhang, D. (2002). Slowdown of the meridional overturning circulation in the upper pacific ocean. *Nature*, 415(6872):603–608.

McPhaden, M. J. and Zhang, D. (2004). Pacific ocean circulation rebounds. *Geophysical Research Letters*, 31(18):n/a–n/a. L18301.

Meinen, C. S. and McPhaden, M. J. (2000). Observations of warm water volume changes in the equatorial pacific and their relationship to el niño and la niña. *Journal of Climate*, 13(20):3551–3559.

Meinen, C. S. and McPhaden, M. J. (2001). Interannual variability in warm water volume transports in the equatorial pacific during 1993–99. *Journal of Physical Oceanography*, 31(5):1324–1345.

Melet, A., Gourdeau, L., Kessler, W. S., Verron, J., and Molines, J.-M. (2010a). Thermocline circulation in the solomon sea: A modeling study*. *Journal of Physical Oceanography*, 40(6):1302–1319.

Melet, A., Gourdeau, L., and Verron, J. (2010b). Variability in solomon sea circulation derived from altimeter sea level data. *Ocean Dynamics*, 60(4):883–900.

Melet, A., Gourdeau, L., Verron, J., and Djath, B. (2013). Solomon Sea circulation and water mass modifications: response at ENSO timescales. *Ocean Dynamics*, 63(1):1–19.

Melet, A., Verron, J., Gourdeau, L., and Koch-Larrouy, A. (2011). Equatorward Pathways of Solomon Sea Water Masses and Their Modifications. *Journal of Physical Oceanography*, 41:810–826.

Murray, S., Lindstrom, E., Kindle, J., and Weeks, E. (1995). Transport through the vitiaz strait. *Woce notes*, pages 21–23.

Newman, M., Compo, G. P., and Alexander, M. A. (2003). Enso-forced variability of the pacific decadal oscillation. *Journal of Climate*, 16(23):3853–3857.

Nikurashin, M. and Ferrari, R. (2009). Radiation and dissipation of internal waves generated by geostrophic motions impinging on small-scale topography: Theory. *Journal of Physical Oceanography*, 40(5):1055–1074.

Nonaka, M., Xie, S.-P., and McCreary, J. P. (2002). Decadal variations in the subtropical cells and equatorial pacific sst. *Geophysical Research Letters*, 29(7):20–1–20–4.

Olbers, D. and Eden, C. (2013). A global model for the diapycnal diffusivity induced by internal gravity waves. *Journal of Physical Oceanography*, 43(8):1759–1779.

Orsi, A. H., Johnson, G. C., and Bullister, J. L. (1999). Circulation, mixing, and production of antarctic bottom water. *Progress in Oceanography*, 43(1):55–109.

Orsi, A. H., Whitworth, T., and Nowlin, W. D. (1995). On the meridional extent and fronts of the antarctic circumpolar current. *Deep Sea Research Part I: Oceanographic Research Papers*, 42(5):641–673.

Picaut, J., Masia, F., and du Penhoat, Y. (1997). An advective-reflective conceptual model for the oscillatory nature of the enso. *Science*, 277(5326):663–666.

Power, S., Casey, T., Folland, C., Colman, A., and Mehta, V. (1999). Inter-decadal modulation of the impact of enso on australia. *Climate Dynamics*, 15(5):319–324.

Qin, X., Menviel, L., Sen Gupta, A., and van Sebille, E. (2016). Iron sources and pathways into the pacific equatorial undercurrent. *Geophysical Research Letters*, 43(18):9843–9851. 2016GL070501.

Qiu, B. and Chen, S. (2004). Seasonal modulations in the eddy field of the south pacific ocean. *Journal of Physical Oceanography*, 34(7):1515–1527.

Qiu, B. and Chen, S. (2011). Multidecadal sea level and gyre circulation variability in the northwestern tropical pacific ocean. *Journal of Physical Oceanography*, 42(1):193–206.

Qiu, B. and Lukas, R. (1996). Seasonal and interannual variability of the north equatorial current, the mindanao current, and the kuroshio along the pacific western boundary. *Journal of Geophysical Research: Oceans*, 101(C5):12315–12330.

Qu, T., Gao, S., and Fine, R. A. (2013). Subduction of south pacific tropical water and its equatorward pathways as shown by a simulated passive tracer. *Journal of Physical Oceanography*, 43(8):1551–1565.

Qu, T., Gao, S., Fukumori, I., Fine, R. A., and Lindstrom, E. J. (2008). Subduction of south pacific waters. *Geophysical Research Letters*, 35(2):n/a–n/a. L02610.

Qu, T. and Lindstrom, E. J. (2002). A Climatological Interpretation of the Circulation in the Western South Pacific. *Journal of Physical Oceanography*, 32(9):2492–2508.

Qu, T. and Lindstrom, E. J. (2004). Northward Intrusion of Antarctic Intermediate Water in the Western Pacific. *Journal of Physical Oceanography*, 34(9):2104–2118.

Qu, T. and Lukas, R. (2003). The bifurcation of the north equatorial current in the pacific. *Journal of Physical Oceanography*, 33(1):5–18.

Reid, J. L. (1986). On the total geostrophic circulation of the south pacific ocean: Flow patterns, tracers and transports. *Progress in Oceanography*, 16(1):1–61.

Reid, J. L. (1997). On the total geostrophic circulation of the pacific ocean: flow patterns, tracers, and transports. *Progress in Oceanography*, 39(4):263–352.

Reid, J. L. and Lynn, R. J. (1971). On the influence of the norwegian-greenland and weddell seas upon the bottom waters of the indian and pacific oceans. *Deep Sea Research and Oceanographic Abstracts*, 18(11):1063 – 1088.

Rodgers, K. B., Friederichs, P., and Latif, M. (2004). Tropical pacific decadal variability and its relation to decadal modulations of enso. *Journal of Climate*, 17(19):3761–3774.

Roemmich, D., Hautala, S., and Rudnick, D. (1996). Northward abyssal transport through the samoan passage and adjacent regions. *Journal of Geophysical Research: Oceans*, 101(C6):14039–14055.

Rudnick, D. L. (1997). Direct velocity measurements in the samoan passage. *Journal of Geophysical Research: Oceans*, 102(C2):3293–3302.

Rudnick, D. L. and Davis, R. E. (2003). Red noise and regime shifts. *Deep Sea Research Part I: Oceanographic Research Papers*, 50(6):691–699.

Salinger, M., Renwick, J., and Mullan, A. (2001). Interdecadal pacific oscillation and south pacific climate. *International Journal of Climatology*, 21(14):1705–1721.

Schneider, N., Miller, A. J., Alexander, M. A., and Deser, C. (1999). Subduction of decadal north pacific temperature anomalies: Observations and dynamics. *Journal of Physical Oceanography*, 29(5):1056–1070.

Schott, F. A., Wang, W., and Stammer, D. (2007). Variability of pacific subtropical cells in the 50-year ecco assimilation. *Geophysical Research Letters*, 34(5). L05604.

Shi, G., Ribbe, J., Cai, W., and Cowan, T. (2008). An interpretation of australian rainfall projections. *Geophysical Research Letters*, 35(2). L02702.

Siedler, G., Holfort, J., Zenk, W., Müller, T. J., and Csernok, T. (2004). Deep-Water Flow in the Mariana and Caroline Basins. *Journal of Physical Oceanography*, 34(3):566–581.

Sokolov, S. and Rintoul, S. (2000). Circulation and water masses of the southwest Pacific: WOCE section P11, Papua New Guinea to Tasmania. *Journal of marine research*, 58(2):223–268.

Sprintall, J., Roemmich, D., and Bailey, R. (1995). Regional climate variability and ocean heat transport in the. *Journal of geophysical research*, 100(C8):15–865.

Stocker, T., Qin, D., Plattner, G.-K., Alexander, L., Allen, S., Bindoff, N., Bréon, F.-M., Church, J., Cubasch, U., Emori, S., Forster, P., Friedlingstein, P., Gillett, N., Gregory, J., Hartmann, D., Jansen, E., Kirtman, B., Knutti, R., Krishna Kumar, K., Lemke, P., Marotzke, J., Masson-Delmotte, V., Meehl, G., Mokhov, I., Piao, S., Ramaswamy, V., Randall, D., Rhein, M., Rojas, M., Sabine, C., Shindell, D., Talley, L., Vaughan, D., and Xie, S.-P. (2013). *Climate Change 2013: The Physical Science Basis. Contribution of Working Group I to the Fifth Assessment Report of the Intergovernmental Panel on Climate Change*, book section TS, pages 33–115. Cambridge University Press, Cambridge, United Kingdom and New York, NY, USA.

Suarez, M. J. and Schopf, P. S. (1988). A delayed action oscillator for enso. *Journal of the Atmospheric Sciences*, 45(21):3283–3287.

Sudre, J., Maes, C., and Garçon, V. (2013). On the global estimates of geostrophic and ekman surface currents. *Limnology and Oceanography: Fluids and Environments*, 3(1):1–20.

Sverdrup, H. U. and Munk, W. H. (1947). Wind, sea, and swell: theory of relations for forecasting. Technical Report 601, U. S. Hydrographic Office.

Taft, B. A., Hayes, S. P., Friederich, G. E., and Codispoti, L. A. (1991). Flow of abyssal water into the samoa passage. *Deep Sea Research Part A. Oceanographic Research Papers*, 38:S103–S128.

Taguchi, B., Nakamura, H., Nonaka, M., and Xie, S.-P. (2009). Influences of the kuroshio/oyashio extensions on air–sea heat exchanges and storm-track activity as revealed in regional atmospheric model simulations for the 2003/04 cold season. *Journal of Climate*, 22(24):6536–6560.

Takahashi, K. and Battisti, D. S. (2007). Processes controlling the mean tropical pacific precipitation pattern. part II: The spcz and the southeast pacific dry zone. *Journal of Climate*, 20(23):5696–5706.

Talley, L. D. and Joyce, T. M. (1992). The double silica maximum in the north pacific. *Journal of Geophysical Research: Oceans*, 97(C4):5465–5480.

Talley, L. D., Sparrow, M. D., Chapman, P., and Gould, J. (2007). *Hydrographic atlas of the World Ocean Circulation Experiment (WOCE): Volume 2: Pacific Ocean*. WOCE International Project Office.

Thompson, C. J. and Battisti, D. S. (2001). A linear stochastic dynamical model of enso. part II: Analysis. *Journal of Climate*, 14(4):445–466.

Timmermann, A., Jin, F.-F., and Abshagen, J. (2003). A nonlinear theory for el niño bursting. *Journal of the Atmospheric Sciences*, 60(1):152–165.

Toole, J. M., Schmitt, R. W., and Polzin, K. L. (1994). Estimates of diapycnal mixing in the abyssal ocean. *Science*, 264(5162):1120.

Tsimplis, M. N., Bacon, S., and Bryden, H. L. (1998). The circulation of the subtropical south pacific derived from hydrographic data. *Journal of Geophysical Research: Oceans*, 103(C10):21443–21468.

Tsuchiya, M. (1981). The origin of the pacific equatorial 13 °c water. *Journal of Physical Oceanography*, 11(6):794–812.

Tsuchiya, M. (1991). Flow path of the antarctic intermediate water in the western equatorial south pacific ocean. *Deep Sea Research Part A. Oceanographic Research Papers*, 38, Supplement 1:S273–S279.

Tsuchiya, M., Lukas, R., Fine, R. A., Firing, E., and Lindstrom, E. (1989). Source waters of the Pacific Equatorial Undercurrent. *Progress In Oceanography*, 23(2):101–147.

van Sebille, E., Sprintall, J., Schwarzkopf, F. U., Sen Gupta, A., Santoso, A., England, M. H., Biastoch, A., and Böning, C. W. (2014). Pacific-to-indian ocean connectivity: Tasman leakage, indonesian throughflow, and the role of enso. *Journal of Geophysical Research: Oceans*, 119(2):1365–1382.

Vimont, D. J. (2002). *The seasonal footprinting mechanism in the CSIRO coupled general circulation models and in observations*. PhD thesis, University of Washington.

Vimont, D. J., Battisti, D. S., and Hirst, A. C. (2003a). The seasonal footprinting mechanism in the csiro general circulation models. *Journal of Climate*, 16(16):2653–2667.

Vimont, D. J., Wallace, J. M., and Battisti, D. S. (2003b). The seasonal footprinting mechanism in the pacific: Implications for enso. *Journal of Climate*, 16(16):2668–2675.

Vincent, D. G. (1994). The south pacific convergence zone (spcz): A review. *Monthly Weather Review*, 122(9):1949–1970.

Vincent, E. M., Lengaigne, M., Menkes, C. E., Jourdain, N. C., Marchesiello, P., and Madec, G. (2011). Interannual variability of the south pacific convergence zone and implications for tropical cyclone genesis. *Climate Dynamics*, 36(9):1881–1896.

Visbeck, M. (2002). Deep velocity profiling using Acoustic Doppler Current Profilers : Bottom tracks and inverse solutions. *J. Atm. Oc. Tech.*, 19:794–807.

Wang, C. (2001). A unified oscillator model for the el niño–southern oscillation. *Journal of Climate*, 14(1):98–115.

Wang, C. and Picaut, J. (2004). Understanding enso physics: A review. *Geophysical monograph*, 147:21–48.

Wang, C., Weisberg, R. H., and Virmani, J. I. (1999a). Western pacific interannual variability associated with the el niño-southern oscillation. *Journal of Geophysical Research: Oceans*, 104(C3):5131–5149.

Wang, C., Weisberg, R. H., and Yang, H. (1999b). Effects of the wind speed–evaporation–sst feedback on the el niño–southern oscillation. *Journal of the Atmospheric Sciences*, 56(10):1391–1403.

Wang, X., Jin, F.-F., and Wang, Y. (2003a). A tropical ocean recharge mechanism for climate variability. part i: Equatorial heat content changes induced by the off-equatorial wind. *Journal of Climate*, 16(22):3585–3598.

Wang, X., Jin, F.-F., and Wang, Y. (2003b). A tropical ocean recharge mechanism for climate variability. part ii: A unified theory for decadal and enso modes. *Journal of Climate*, 16(22):3599–3616.

Warren, B. A. (1973). Transpacific hydrographic sections at lats. 43 °s and 28 °s: the scorpio expedition—ii. deep water. *Deep Sea Research and Oceanographic Abstracts*, 20(1):9 – 38.

Weisberg, R. H. and Wang, C. (1997). A western pacific oscillator paradigm for the el niño-southern oscillation. *Geophysical Research Letters*, 24(7):779–782.

Wheeler, M. C. and Hendon, H. H. (2004). An all-season real-time multivariate mjo index: Development of an index for monitoring and prediction. *Monthly Weather Review*, 132(8):1917–1932.

Wijffels, S. E., Toole, J. M., Bryden, H. L., Fine, R. A., Jenkins, W. J., and Bullister, J. L. (1996). The water masses and circulation at 10 °n in the pacific. *Deep Sea Research Part I: Oceanographic Research Papers*, 43(4):501–544.

Wijffels, S. E., Toole, J. M., and Davis, R. (2001). Revisiting the south pacific subtropical circulation: A synthesis of world ocean circulation experiment observations along 32 °s. *Journal of Geophysical Research: Oceans*, 106(C9):19481–19513.

Wunsch, C. (1978). The north atlantic general circulation west of 50 °w determined by inverse methods. *Reviews of Geophysics*, 16(4):583–620.

Wunsch, C. (1996). *The ocean circulation inverse problem*. Cambridge University Press.

Wunsch, C., Hu, D., and Grant, B. (1983). Mass, heat, salt and nutrient fluxes in the south pacific ocean. *Journal of Physical Oceanography*, 13(5):725–753.

Wyrtki, K. (1961). The flow of water into the deep sea basins of the western south pacific ocean. *Marine and Freshwater Research*, 12(1):1–16.

Wyrtki, K. (1981). An estimate of equatorial upwelling in the pacific. *Journal of Physical Oceanography*, 11(9):1205–1214.

Zhang, D. and McPhaden, M. J. (2006). Decadal variability of the shallow pacific meridional overturning circulation: Relation to tropical sea surface temperatures in observations and climate change models. *Ocean Modelling*, 15(3–4):250–273.

Zhang, R.-H., Rothstein, L. M., and Busalacchi, A. J. (1998). Origin of upper-ocean warming and el nino change on decadal scales in the tropical pacific ocean. *Nature*, 391(6670):879–883.

Zhang, R. H., Rothstein, M. L., and Busalacchi, J. A. (1999). Interannual and decadal variability of the subsurface thermal structure in the pacific ocean: 1961–90. *Climate Dynamics*, 15(10):703–717.

Zilberman, N., Roemmich, D., and Gille, S. (2013). The mean and the time variability of the shallow meridional overturning circulation in the tropical south pacific ocean. *Journal of Climate*, 26(12):4069–4087.

Appendix A

Hydrographic sections during the Pandora and MoorSPICE cruises

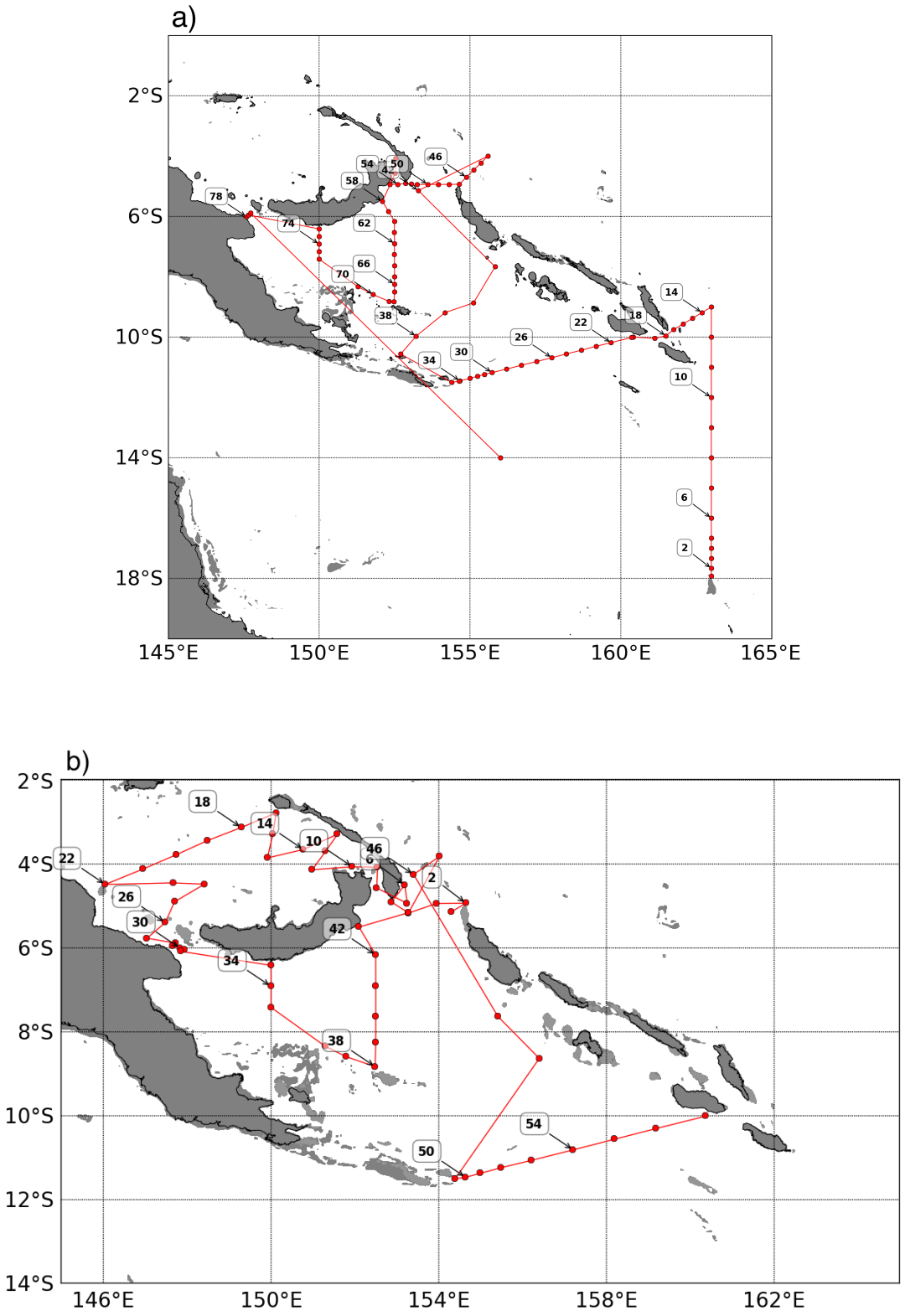

Figure A1 – Cruise tracks (red line) during (a) the Pandora cruise, June- August 2012, R/V L'Atalante and (b) the MoorSPICE cruise, February-March 2014, R/V Thomas G. Thompson. Both cruises departed and arrived from Nouméa, New Caledonia. Station numbers (red dots) are indicated every 4th station.

Appendix B

Supplementary materials: Pathways and Water Properties of The Thermocline and Intermediate Waters in the Solomon Sea

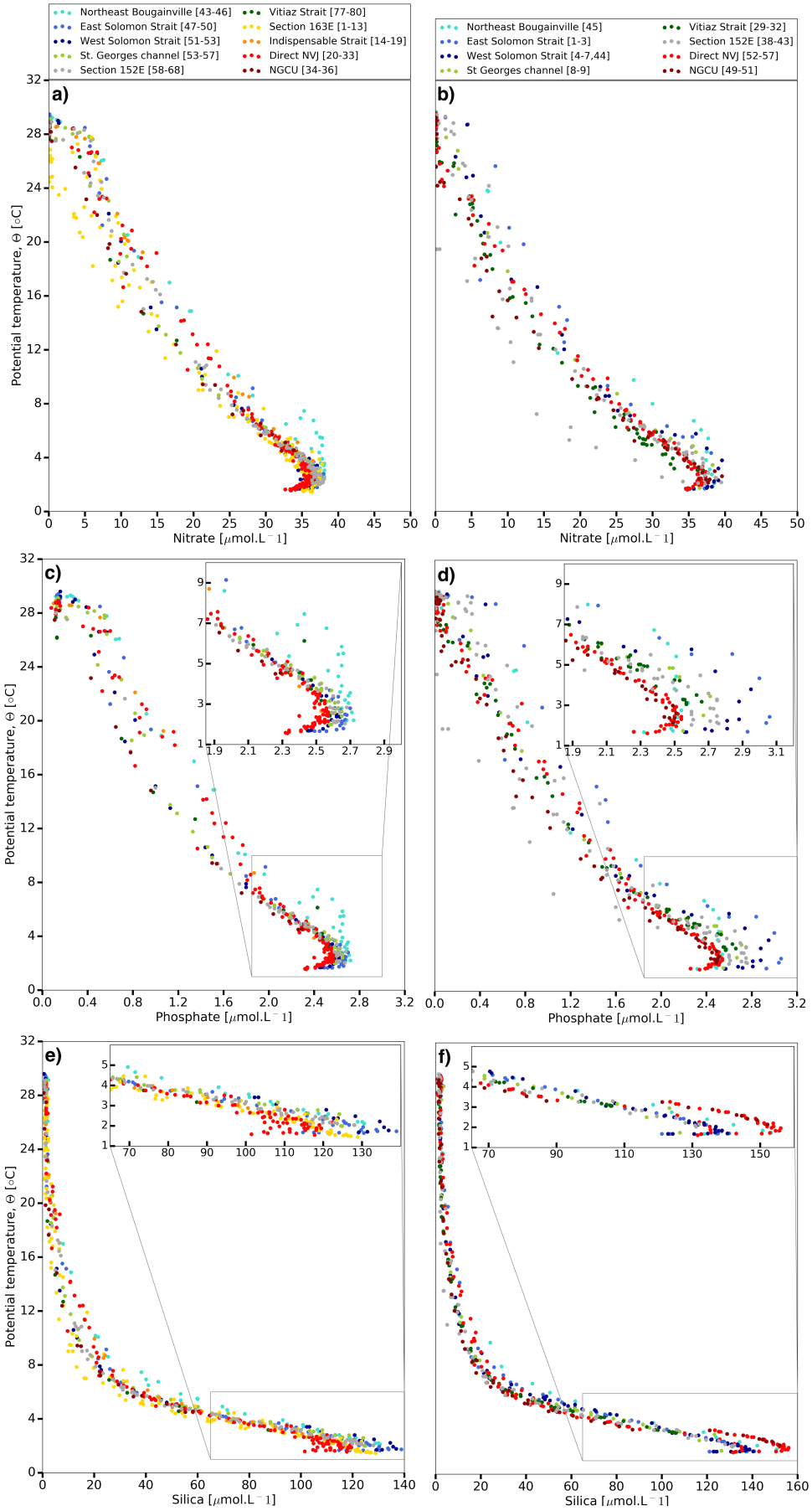

Figure B1 – Θ-Nitrate during Pandora (a) and (b) MoorSPICE, Θ-Phosphate during (c) Pandora and (e) MoorSPICE and Θ-Silica during (d) Pandora and (f) MoorSPICE, respectively. Note expanded inset for Θ-Phosphate and Θ-Silica diagrams. Color corresponds to locations as indicated in legends and maps in Fig. 3.

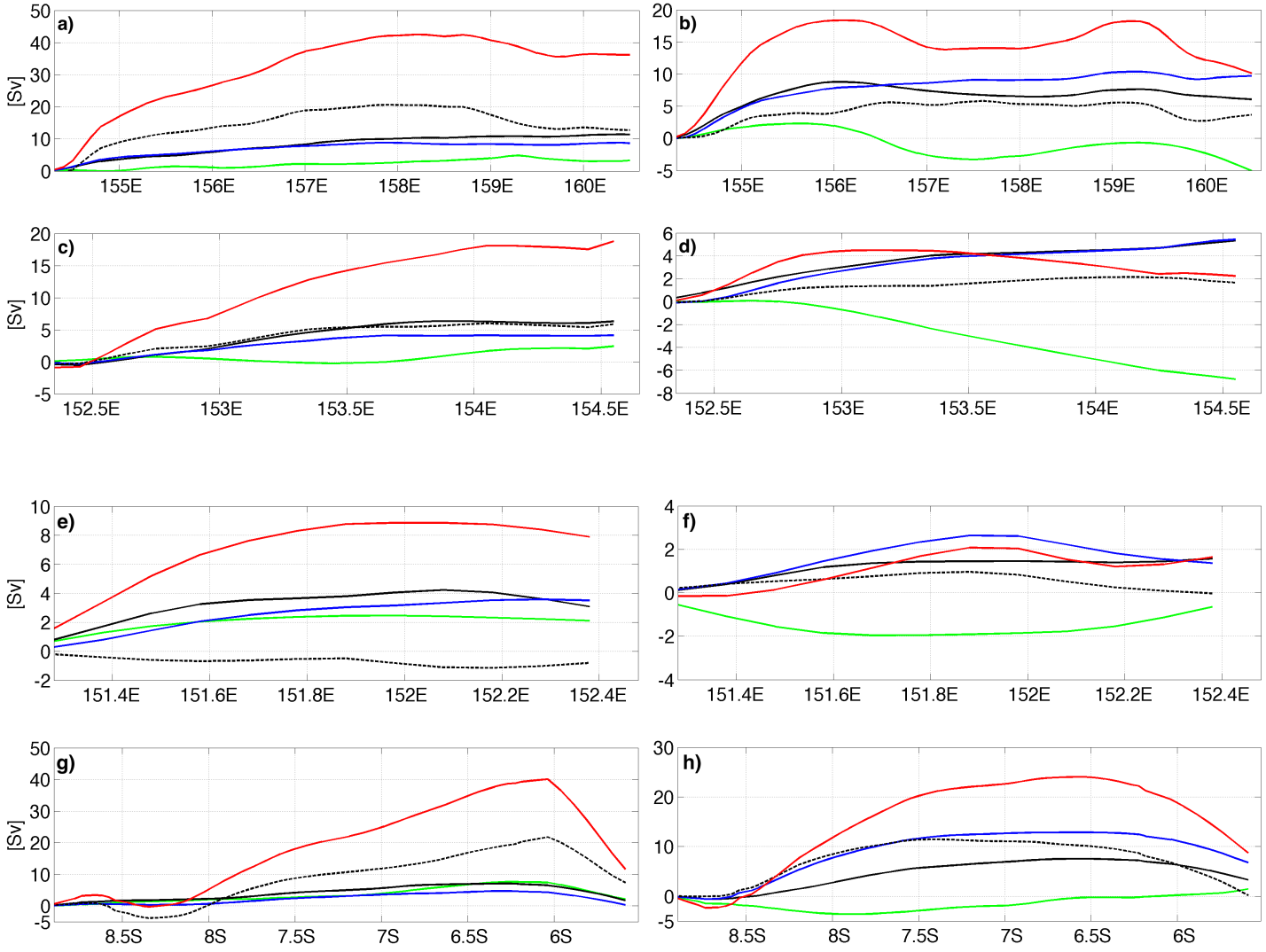

Figure B2 – (left panels) July-August 2012 and March (right panels) cumulative transports (Sv) from the surface to σ_θ=24 (green line), σ_θ=24 to 26 (black solid line), σ_θ=26 to 26.9 (blue line), σ_θ=26.9 to 27.4 (black dash line) and the surface to 27.4 (red line) at (a, b) the southern entrance (c, d) St Georges and Solomon Strait, (e, f) between Trobriand and Woodlark Islands and (g, h) between Woodlark and New Britain Islands. Cumulative transports linearly increase at Vitiaz Strait and so are not shown.

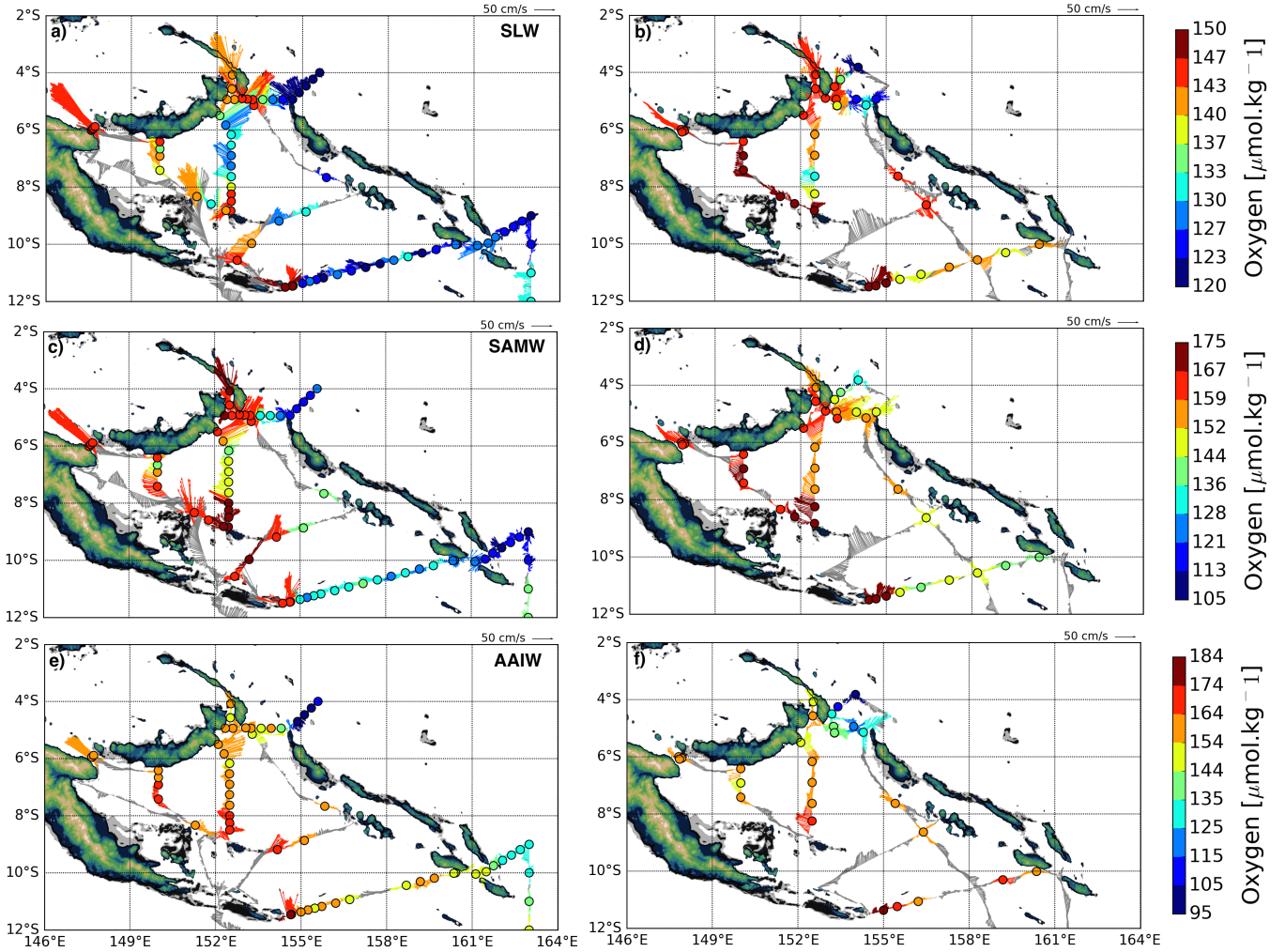

Figure B3 – Mean currents from non adjusted S-ADCP data (arrows) colored by oxygen during (a,c) July-August 2012 (left panels) and March 2014 (right panels) for (a,b) SLW (σ_θ ~24 to 26); (c,d) SAMW (σ_θ ~26 to 26.9) and (e,f) AAIW (σ_θ ~26.9 to 27.4) levels.

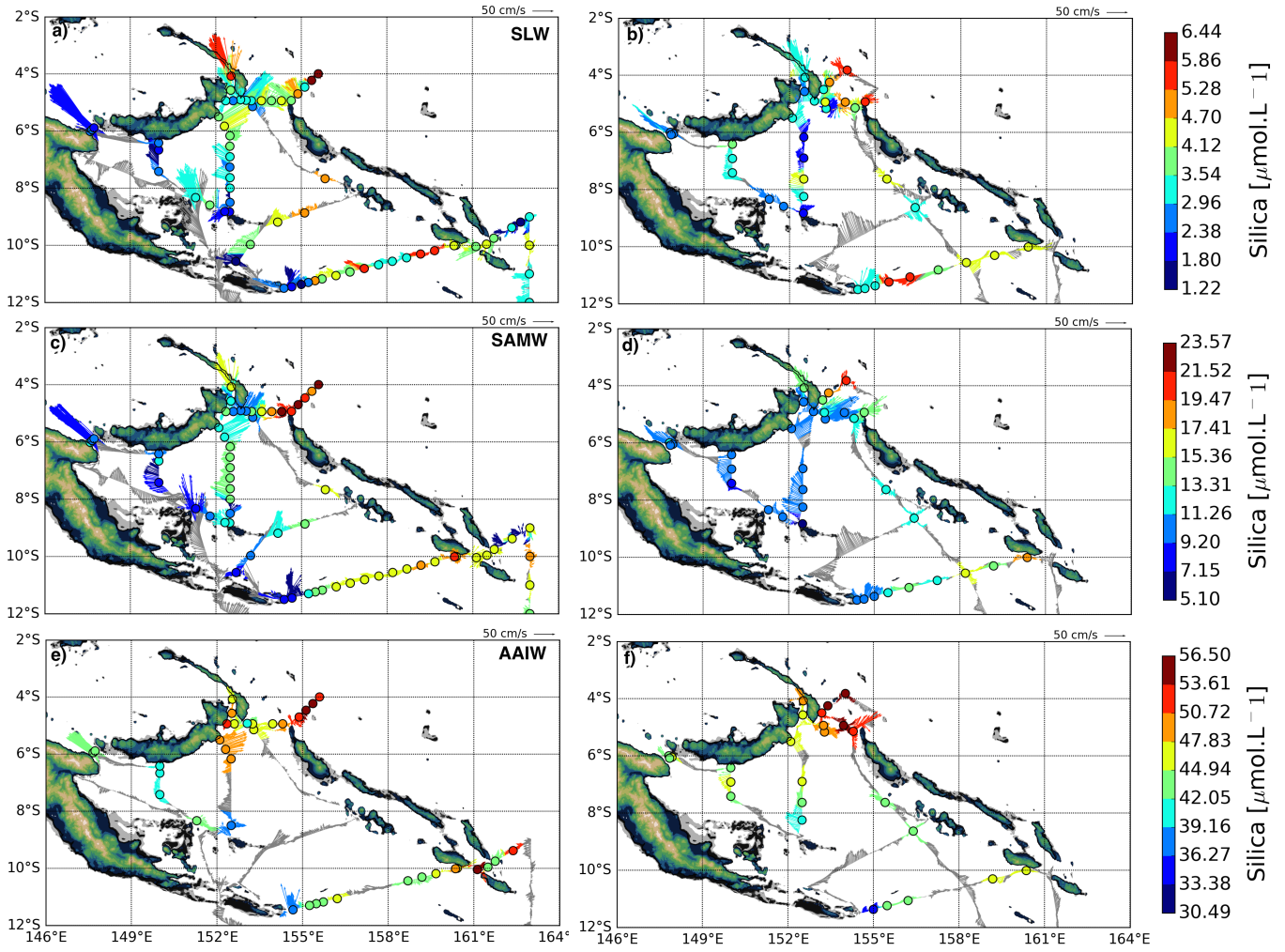

Figure B4 – Mean currents from non adjusted S-ADCP data (arrows) colored by silica during (a,c) July-August 2012 (left panels) and March 2014 (right panels) for (a,b) SLW (σ_θ ~24 to 26); (c,d) SAMW (σ_θ ~26 to 26.9) and (e,f) AAIW (σ_θ ~26.9 to 27.4) levels.

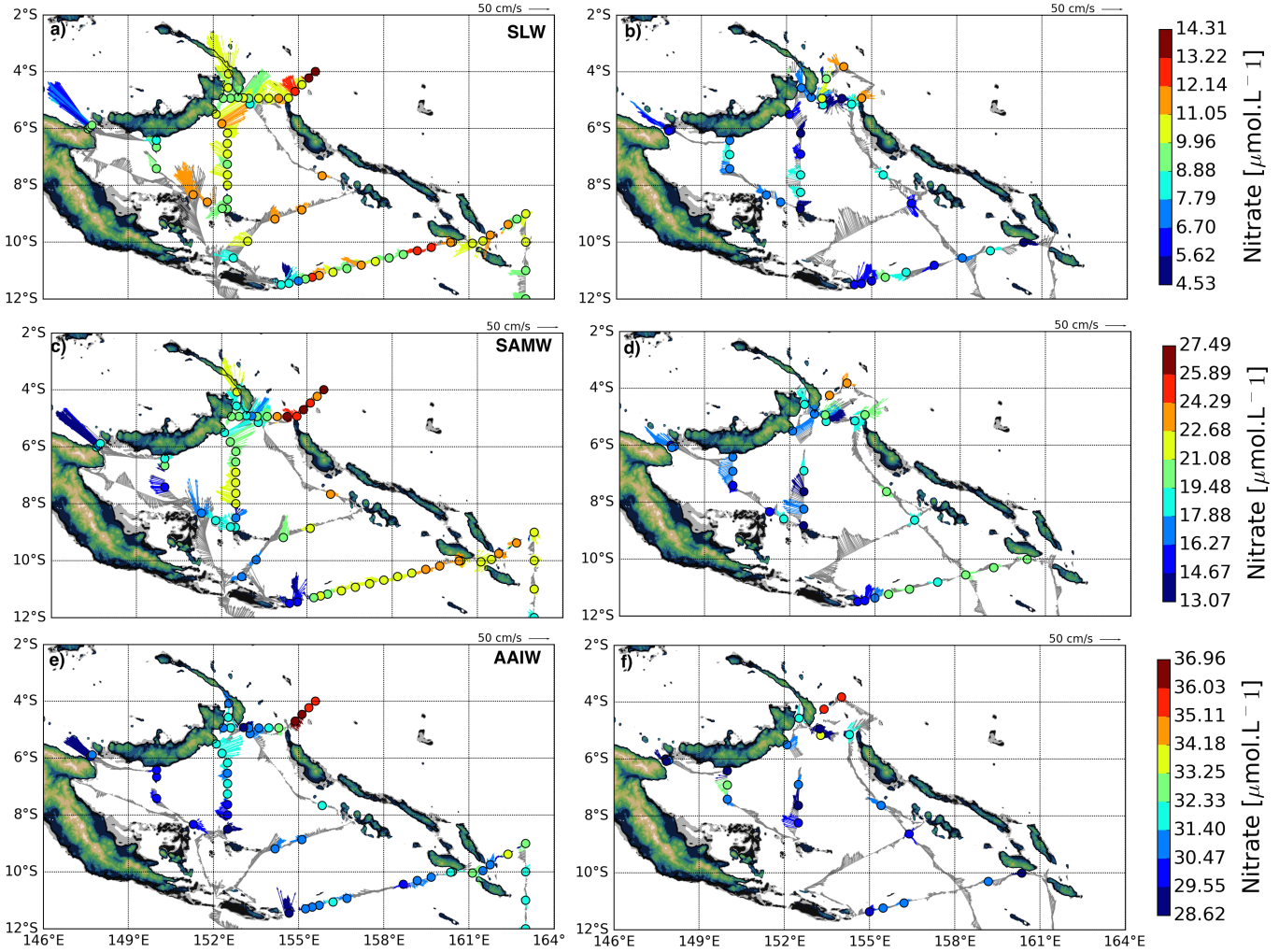

Figure B5 – Mean currents from non adjusted S-ADCP data (arrows) colored by nitrate during (a,c) July-August 2012 (left panels) and March 2014 (right panels) for (a,b) SLW (σ_θ ∼24 to 26); (c,d) SAMW (σ_θ ∼26 to 26.9) and (e,f) AAIW (σ_θ ∼26.9 to 27.4) levels.

Appendix C

Phosphate and potential temperature distributions from the World Ocean Database 2013 and the two SPICE cruises

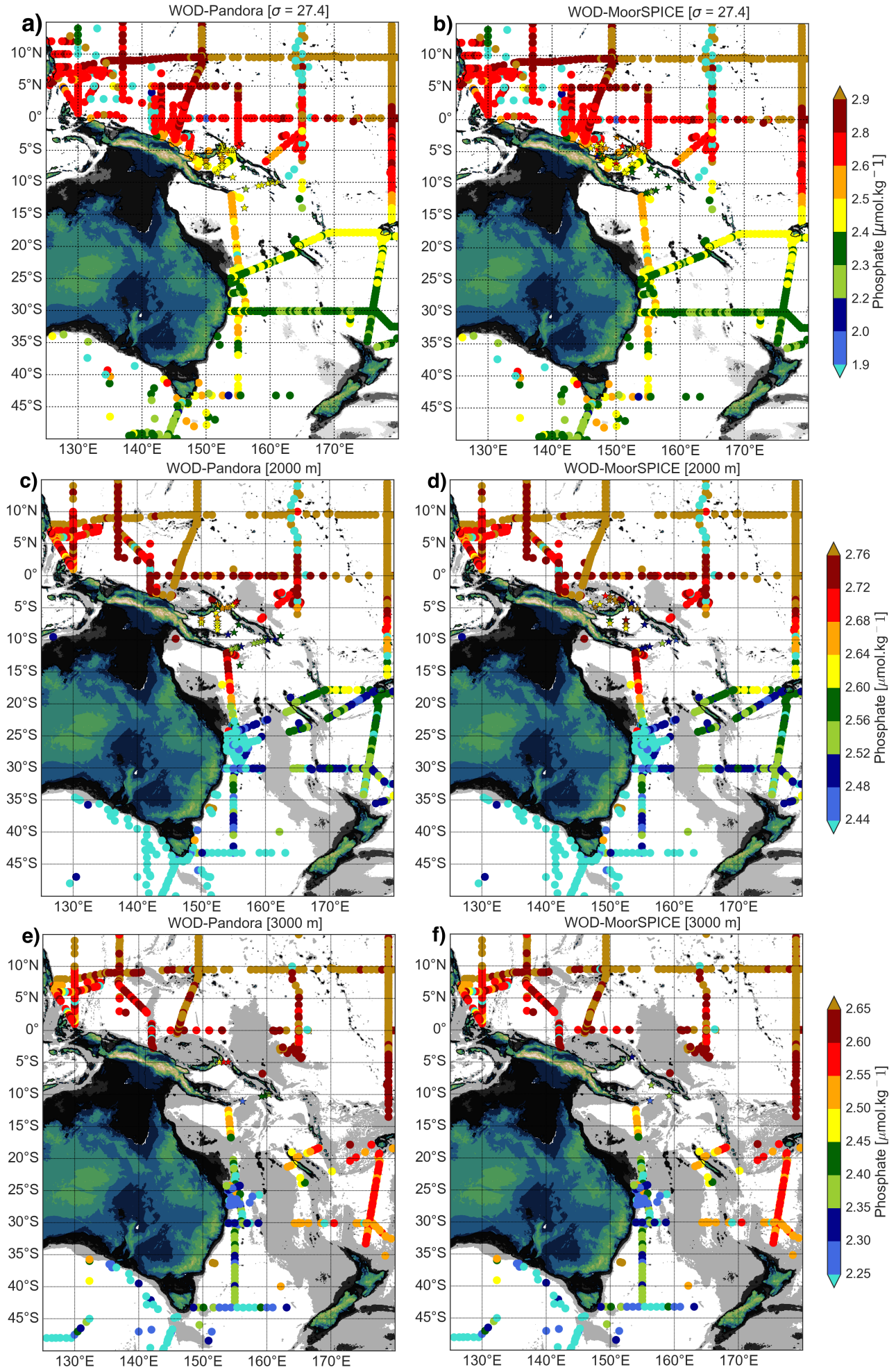

Figure C1 – Historical phosphate climatology at (a),(b) σ_θ=27.4 isopycnal level; (c),(d) 2000 m depth level and (e),(f) 3000 m depth level. Colored stars indicate measured phosphate during July-August 2012 (left) and March 2014 (right). Note the color scale and that areas deeper than each vertical level are shaded.

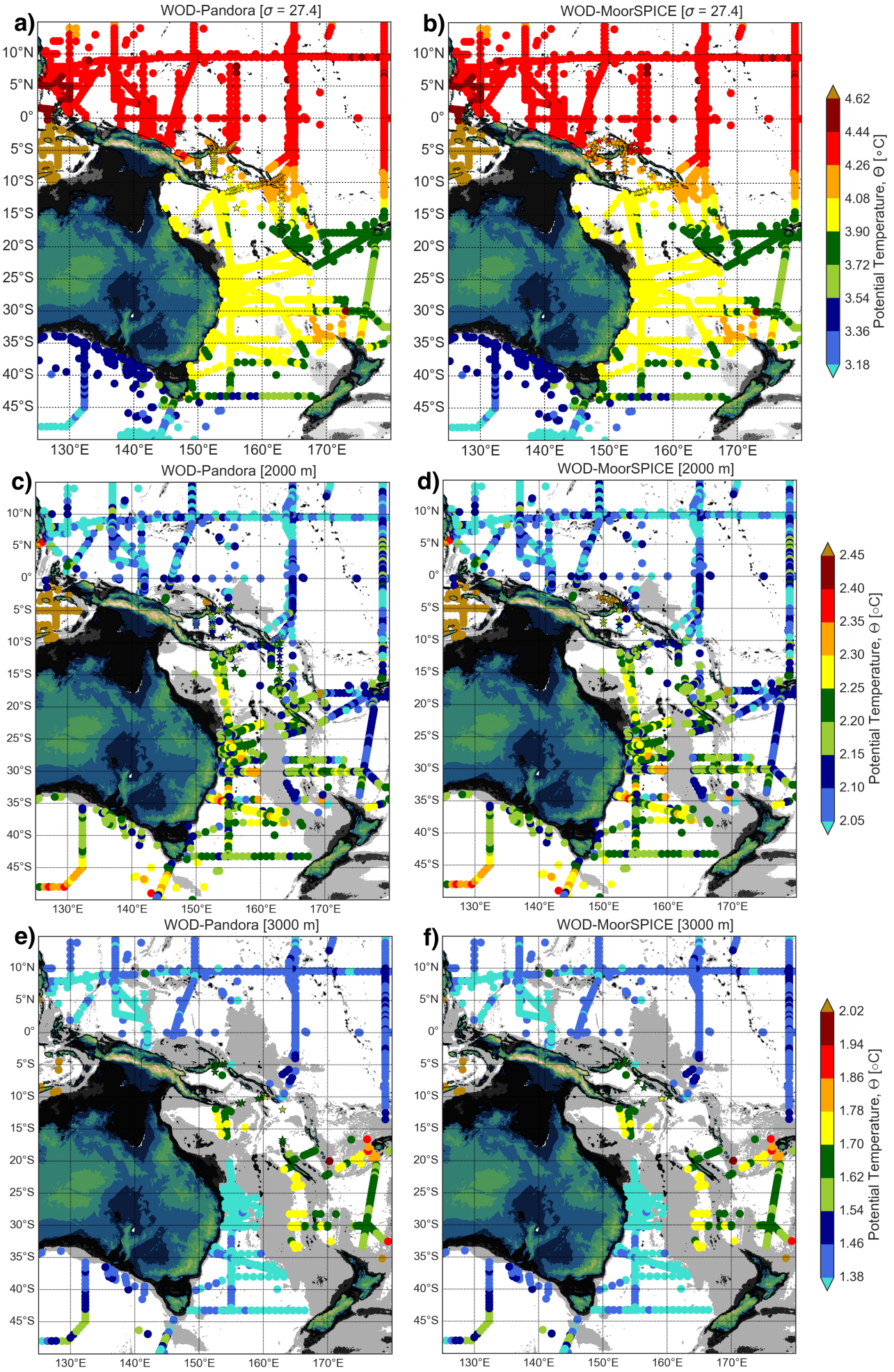

Figure C2 – Historical potential temperature climatology at (a),(b) σ_θ=27.4 isopycnal level; (c),(d) 2000 m depth level and (e),(f) 3000 m depth level. Colored stars indicate measured phosphate during July-August 2012 (left) and March 2014 (right). Note the color scale and that areas deeper than each vertical level are shaded.

Appendix D

The MoorSPICE mooring array: time variability of velocity and temperature records

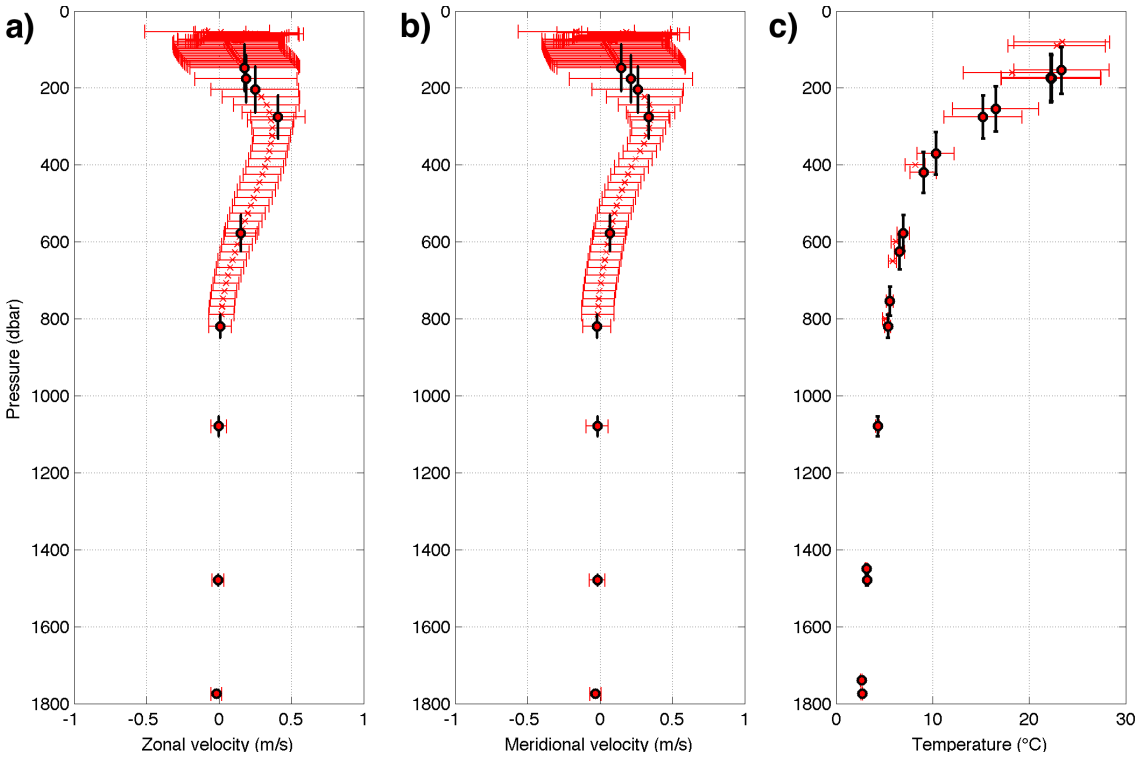

Figure D1 – Solomon M1 vertical profiles averaged over time (red dots) within a two standard deviation uncertainty (red lines) of (a) zonal velocity; (b) meridional velocity and (c) temperature as a function of pressure. Note the two standard deviation uncertainty for pressure (black lines).

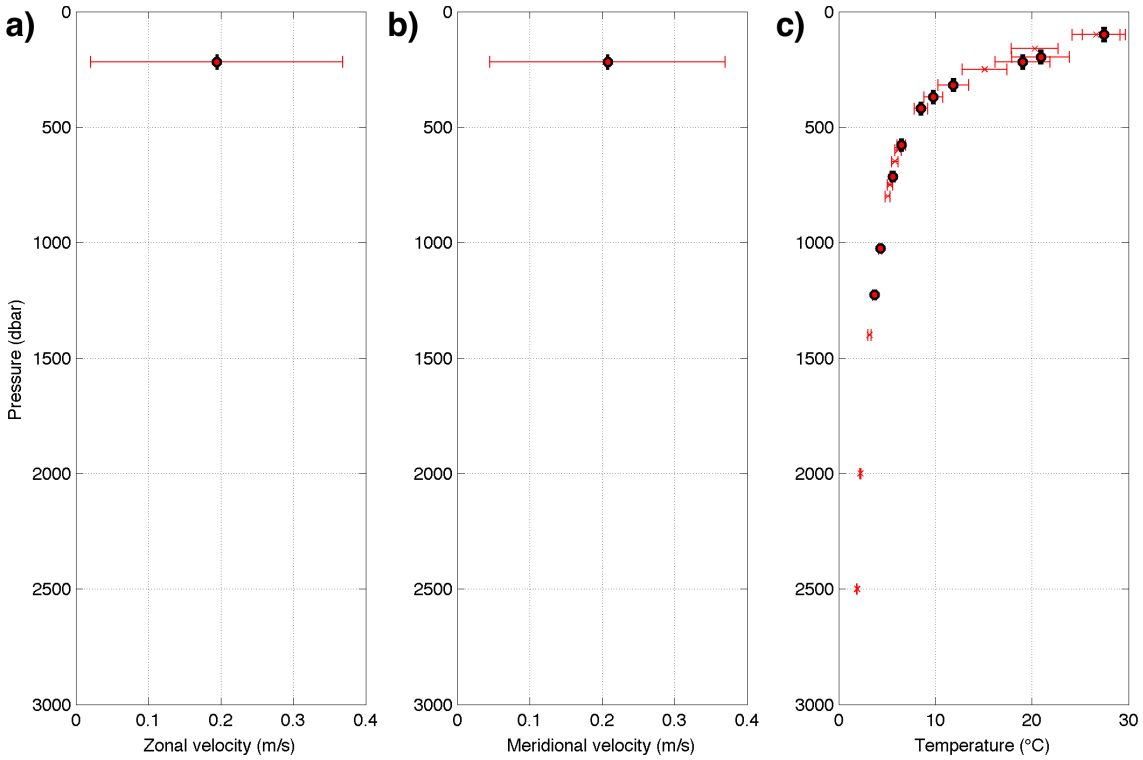

Figure D2 – Solomon M2a vertical profiles averaged over time (red dots) within a two standard deviation uncertainty (red lines) of (a) zonal velocity; (b) meridional velocity and (c) temperature as a function of pressure. Note the two standard deviation uncertainty for pressure (black lines).

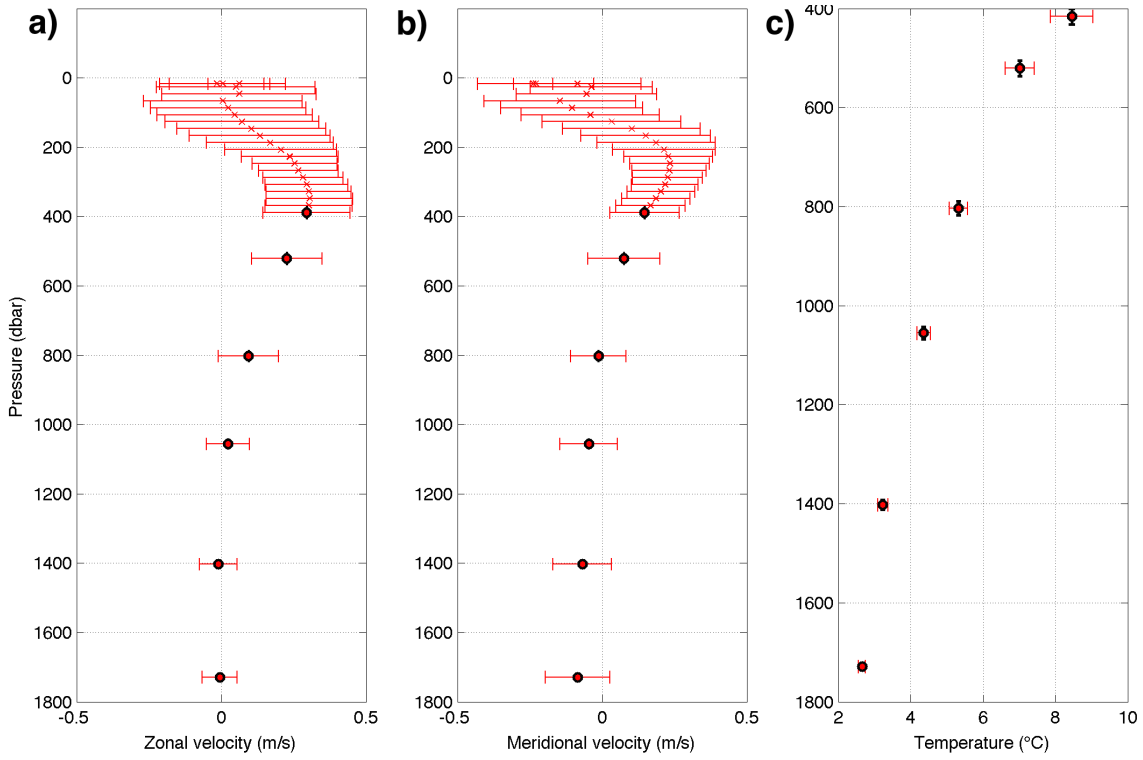

Figure D3 – Solomon M2b vertical profiles averaged over time (red dots) within a two standard deviation uncertainty (red lines) of (a) zonal velocity; (b) meridional velocity and (c) temperature as a function of pressure. Note the two standard deviation uncertainty for pressure (black lines).

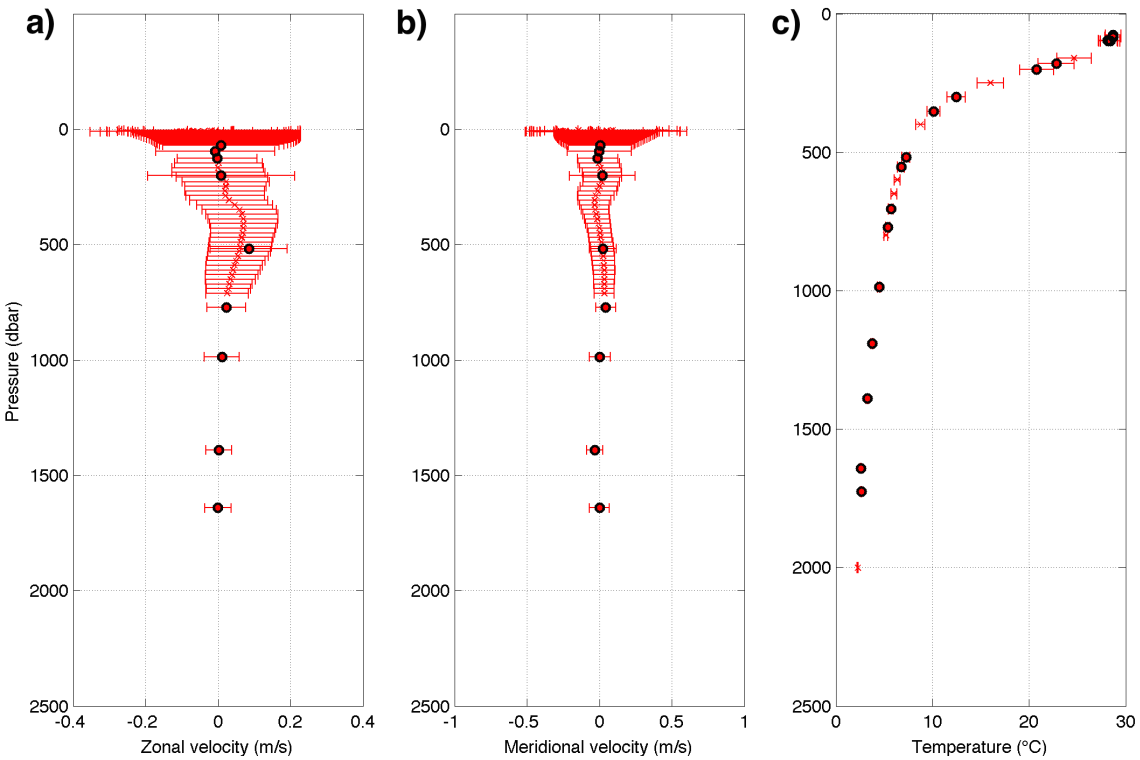

Figure D4 – Solomon M3 vertical profiles averaged over time (red dots) within a two standard deviation uncertainty (red lines) of (a) zonal velocity; (b) meridional velocity and (c) temperature as a function of pressure. Note the two standard deviation uncertainty for pressure (black lines).

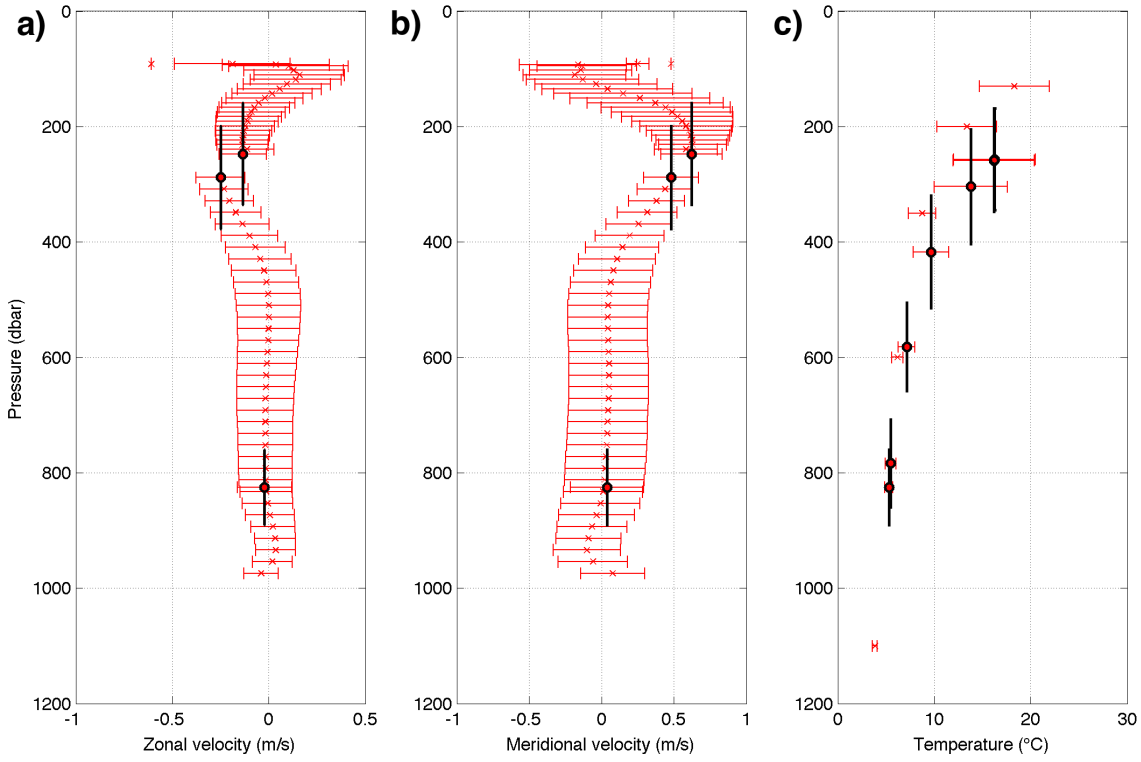

Figure D5 – St Georges East vertical profiles averaged over time (red dots) within a two standard deviation uncertainty (red lines) of (a) zonal velocity; (b) meridional velocity and (c) temperature as a function of pressure. Note the two standard deviation uncertainty for pressure (black lines).

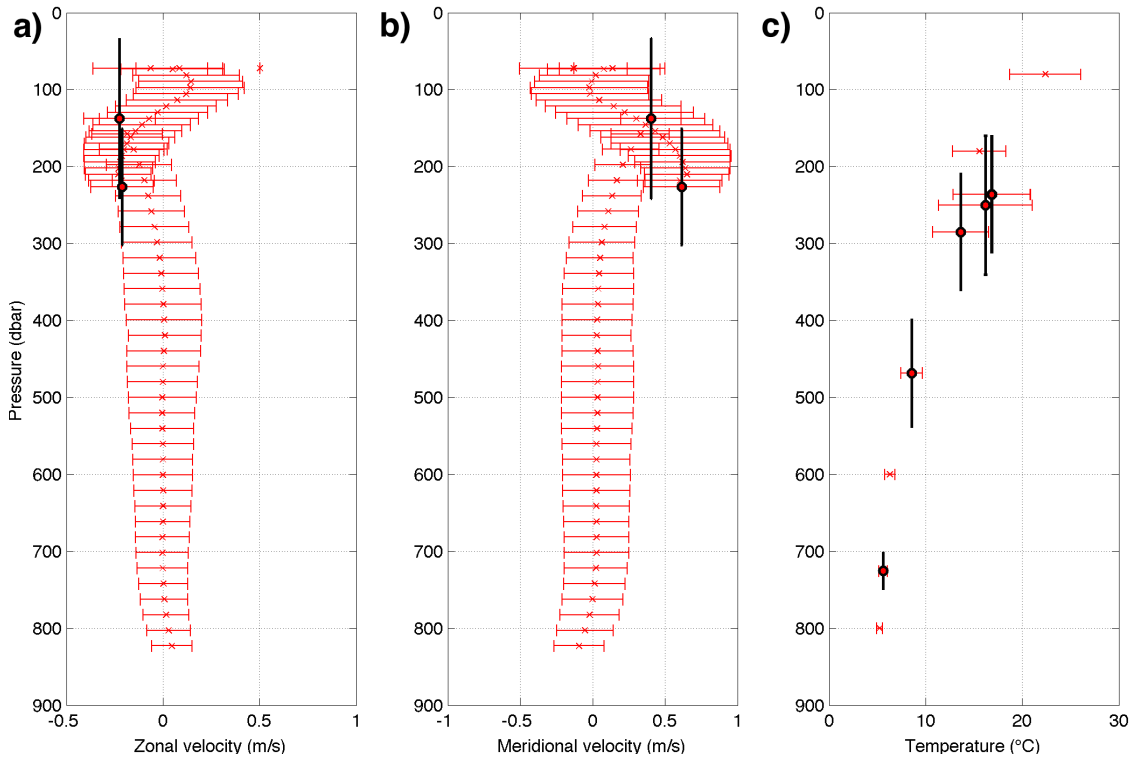

Figure D6 – St Georges West vertical profiles averaged over time (red dots) within a two standard deviation uncertainty (red lines) of (a) zonal velocity; (b) meridional velocity and (c) temperature as a function of pressure. Note the two standard deviation uncertainty for pressure (black lines).

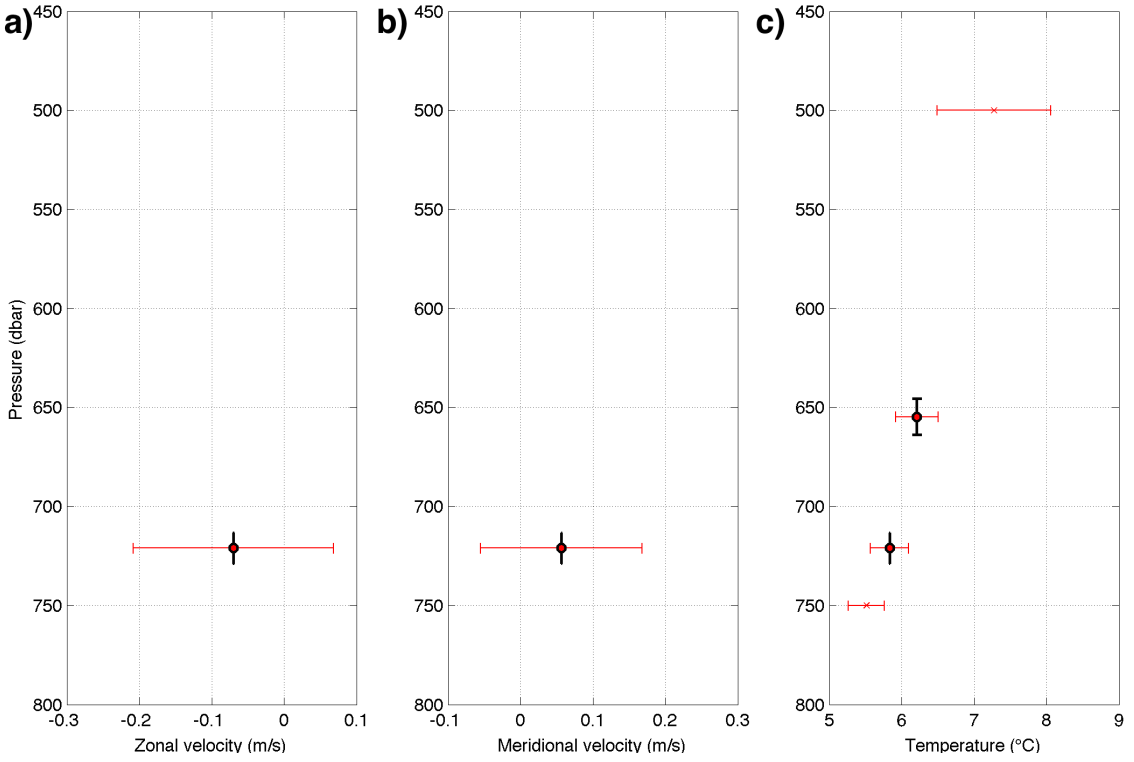

Figure D7 – Vitiaz East vertical profiles averaged over time (red dots) within a two standard deviation uncertainty (red lines) of (a) zonal velocity; (b) meridional velocity and (c) temperature as a function of pressure. Note the two standard deviation uncertainty for pressure (black lines).

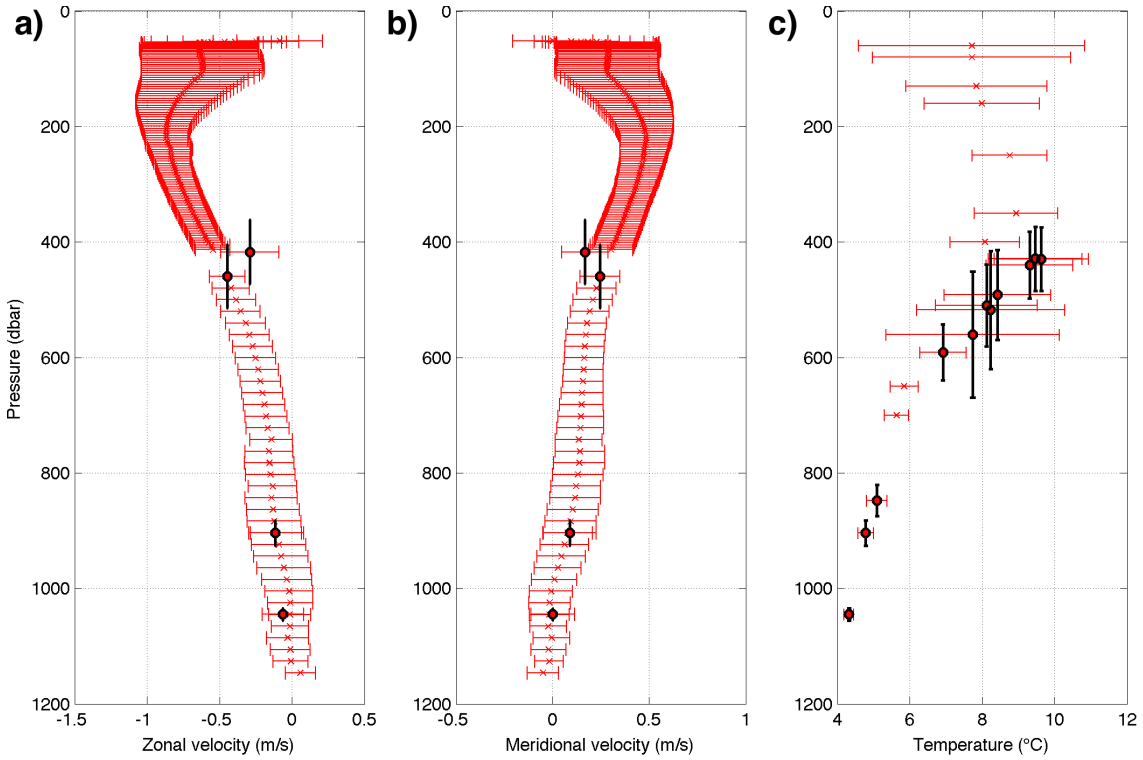

Figure D8 – Vitiaz Middle vertical profiles averaged over time (red dots) within a two standard deviation uncertainty (red lines) of (a) zonal velocity; (b) meridional velocity and (c) temperature as a function of pressure. Note the two standard deviation uncertainty for pressure (black lines).

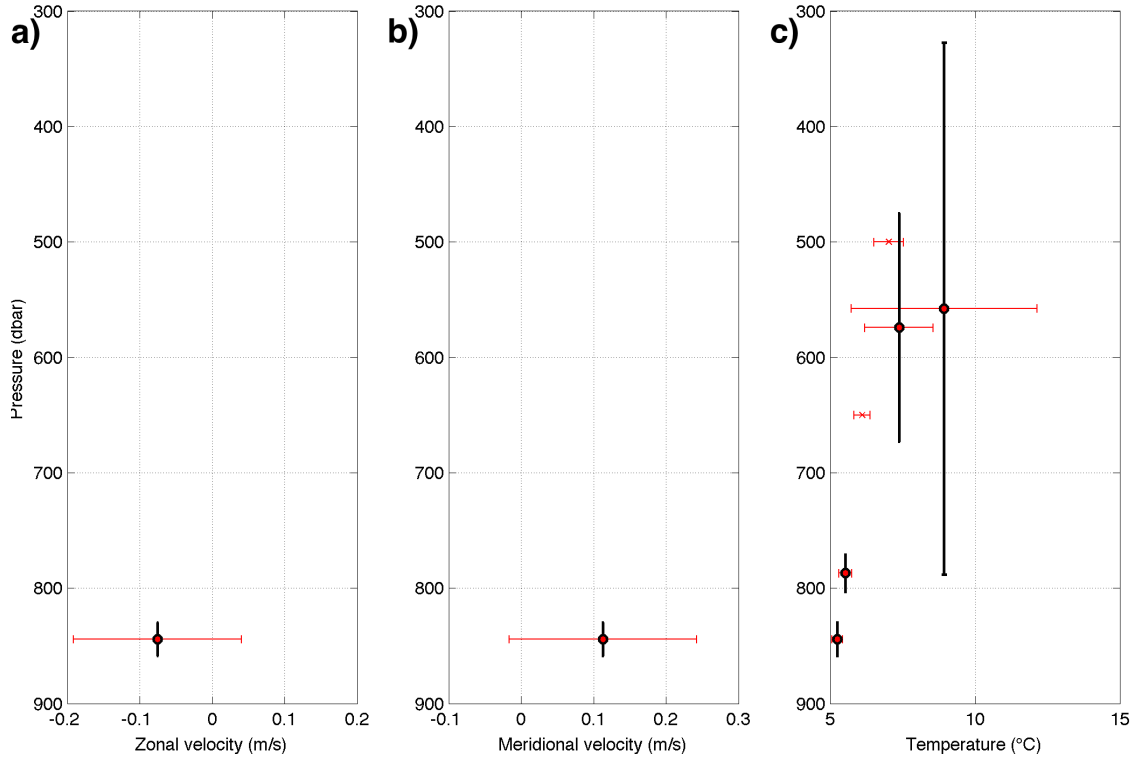

Figure D9 – Vitiaz West vertical profiles averaged over time (red dots) within a two standard deviation uncertainty (red lines) of (a) zonal velocity; (b) meridional velocity and (c) temperature as a function of pressure. Note the two standard deviation uncertainty for pressure (black lines).

Appendix E

Determination of ADCP Thresholds: Quality Control of the Moor-SPICE ADCP Velocity

1 Introduction

The traditional quality control (QC) of the Acoustic Doppler Current Profilers (ADCPs) is mainly focused on the Percent Good (i.e. ratio of good pings per total pings) threshold. During the International Nusantara STratification ANd Transport (INSTANT) program (*Cowley et al.*, 2008), it was determined that additional quality control was required for moored ADCPs, especially for the upward-looking ADCPs, where upper bins are contaminated by the surface reflection and need to be removed without retaining near surface "good" data. A new QC procedure was firstly implemented by *Crout et al.* (2006) by the National Data Data Boy Center (NDBC) based on Ocean Observer 38 kHz and Workhorse 75 kHz ADCPs for deployments in the Gulf on Mexico. During INSTANT, Workhorse Longranger 75 kHz and 300 kHz were deployed in the narrow straits of the Indonesian Seas. A revised QC procedure was recommended with different thresholds (see Appendix 2, *Cowley et al.*, 2008), especially for the Percent Good test.

In the frame of the Southwest Pacific Ocean and Climate Circulation Experiment (SPICE) program (*Ganachaud et al.*, 2014), moored subsurface upward and downward looking ADCPs were deployed in the northern passages of the Solomon Sea (i.e. Vitiaz and Solomon Straits, and St Georges Channel) between July 2012 and March 2014. These ADCPs were also Workhorse Longranger 75 kHz and 300 kHz, and were deployed in narrow straits influenced by strong tidal currents. Thus, an additional QC is implemented for the SPICE moored ADCPs, following the INSTANT procedure. Beforehand, ADCP data were converted into depth bins to determine where the surface is, and data above the surface were removed.

2 QC procedure description

The QC procedure consists of six tests, where data in each bin can be flagged as fail, suspect or pass depending on defined threshold values (Table 1). As the INSTANT data QC, we chose a conservative approach, where suspected data are designated as failed. For tests 1 to 5, the tests are carried out for each cell with the binary condition: 0=pass; 1=fail. The results are summed, and if the sum is larger than 2 (i.e. the cell has failed 2 out of 5 tests) the cell is removed. Test 6 (the echo amplitude) is a surface detection test to remove surface data from each cell. Thus, rejection of cells can occur for one or two reasons:

- **Two out of the five tests that comprise the sum of tests 1 to 5 fail (OTfails)**
- **Failure of the echo amplitude test 6 (EAfail)**

Relevant ADCP raw data (i.e. pitch, roll, pressure and temperature) are firstly checked to identify strong horizontal and/or vertical displacements over time. Comments about dates when there are obvious problems in the record of the ADCP raw data are gathered into a separate table for each mooring, associated with some basics statistics. A particular attention is given to pitch and roll variations, as potential damages can be induced to the ADCP data.

Table 1 – Tests and associated thresholds used to quality control the moored ADCP velocity fields.

Tests:	Error Velocity ($m.s^{-1}$)	Percent Good	Correlation Magnitude	Vertical Velocity ($m.s^{-1}$)	Horizontal Velocity ($m.s^{-1}$)	Echo Amplitude (counts)
$RDI300$[1] kHz	0.15	>80%	>110	<0.2	<2	30
$RDI75$[1] kHz	0.15	>50%	>64	<0.2	<2	25
$RDI75$[2] kHz	0.15	>50%	>110	<0.2	<2	25

[1]Standard

[2]Vitiaz Strait

3 Implementation of QC Procedure

3.1 Case 1: Solomon Strait M1 (upward RDI 300 kHz)

- Instrument type: RDI 300 kHz
- Instrument target depth: 80 m
- Instrument Serial Number: 5307
- Instrument vertical bin size: 4 m
- Instrument Deployment Date/Time (UTC): 07/21/2012 01:30
- Instrument Recovery Date/Time (UTC): 03/06/2014 23:01

The RDI 300 kHz in Solomon Strait M1 are 40 bins for 14253 time realizations. Pitch and roll variations (Figure 1a,b) are lower than 10 to 15 degrees over time, but strong vertical variations occurred in pressure (from 100 to 400 dbar, Figure 1c) and temperature (from 10° to 30°C, Figure 1d) are observed. The average, standard deviation, and range values for the different parameters used in each QC test (Figure 2), were used to preliminary choose corresponding thresholds.

The echo amplitude (EA) test 6 contributes to 45-54% of total fails in bins 25-40 for the different threshold values (20, 25, 30 and 35 counts). The EAfail increases to 50-60% in bins 21-25 for each threshold and no EAfail below bin 21, where the surface is likely detected (see the discontinuity of the echo amplitude mean profile, Figure 2f).

The percent good, correlation magnitude and error velocity parameters are not independent of other tests, they are related. For all threshold values of 10%, 30%, 50% and 80%, the percent good contributes nearly 100% to OTfails in all bins, as the correlation magnitude with thresholds of 50, 64, 75 and 110. Both Percent good and correlation magnitude contribute to ∼50% of total failures in upper bins.

The error velocity test shows little differences between each threshold value in bins 30 to 40 with minor contributions (1-10%) to OTails. Highest contributions to OTfails are observed in bins 19-20. For the vertical velocity test, there are negligible differences between the threshold values, contributing 1-3% to OTfails above bin 20. For the horizontal velocity test, negligible contributions (5-15%) to OTfails are also observed, impacting mostly bins 19-23.

We suggest to use similar QC thresholds than those used during INSTANT for the Workhorse 300 kHz ADCPs. The recommended thresholds for the six QC tests are shown in Table 1, where bad bins are mostly observed between bins 30-40. A comparison of the zonal velocity before and after QC is shown in Figure 3a,b with significant differences occurring in bins 20-40.

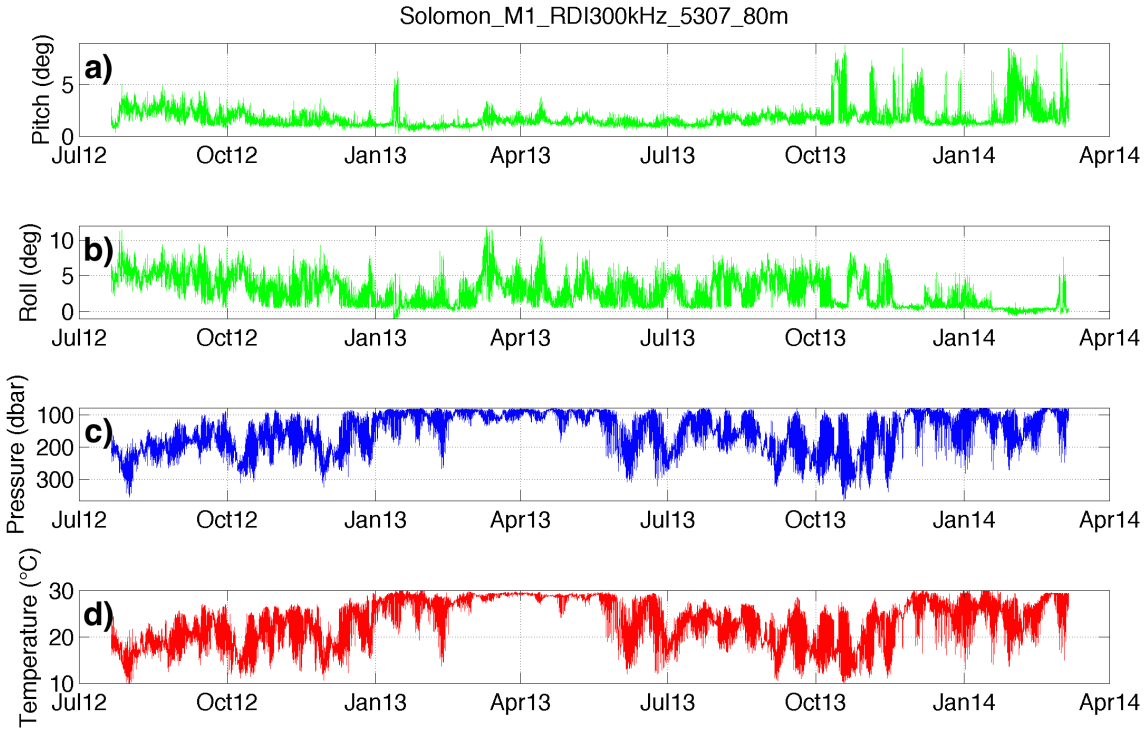

Figure 1 – Solomon Strait M1 RDI 300 kHz (upward) raw data of (a) pitch; (b) roll; (c) pressure and (d) temperature timeseries.

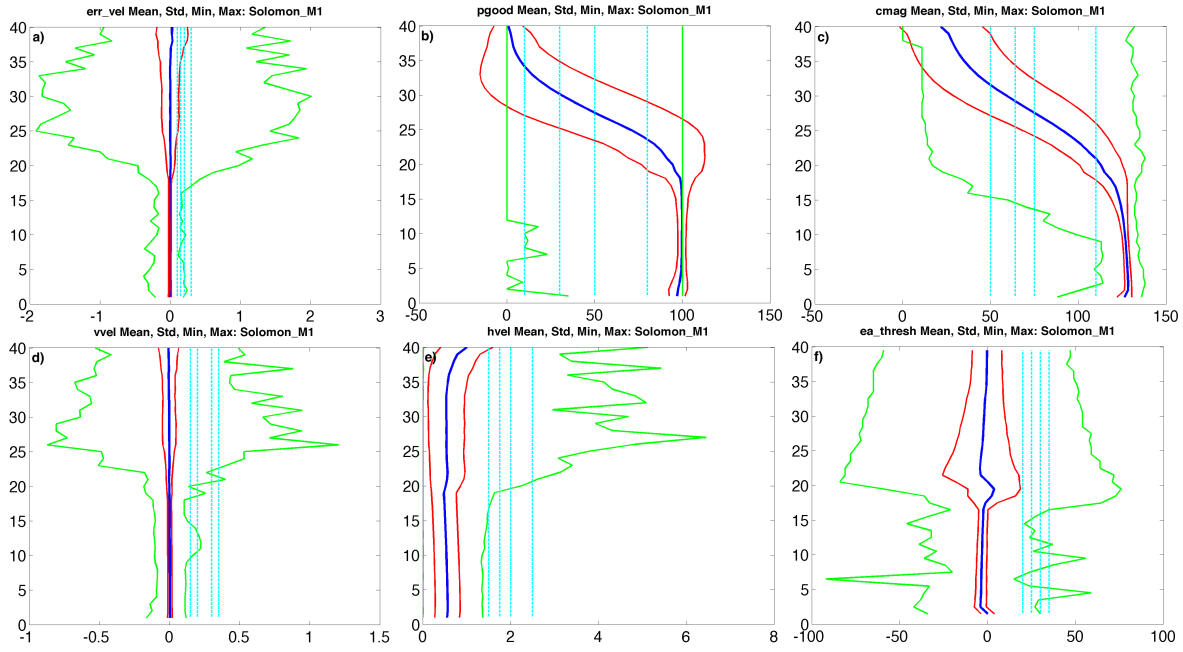

Figure 2 – Mean (thick blue line), standard deviation (red lines) and minimum and maximum (green lines) of the (a) error velocity ($m.s^{-1}$); (b) percent good; (c) correlation magnitude; (d) vertical velocity ($m.s^{-1}$); (e) horizontal velocity ($m.s^{-1}$) and (f) echo amplitude (counts) for the Solomon Strait M1 RDI 300 kHz ADCP versus bin. The four threshold values used in each QC test are marked by cyan lines in panels (a) to (f).

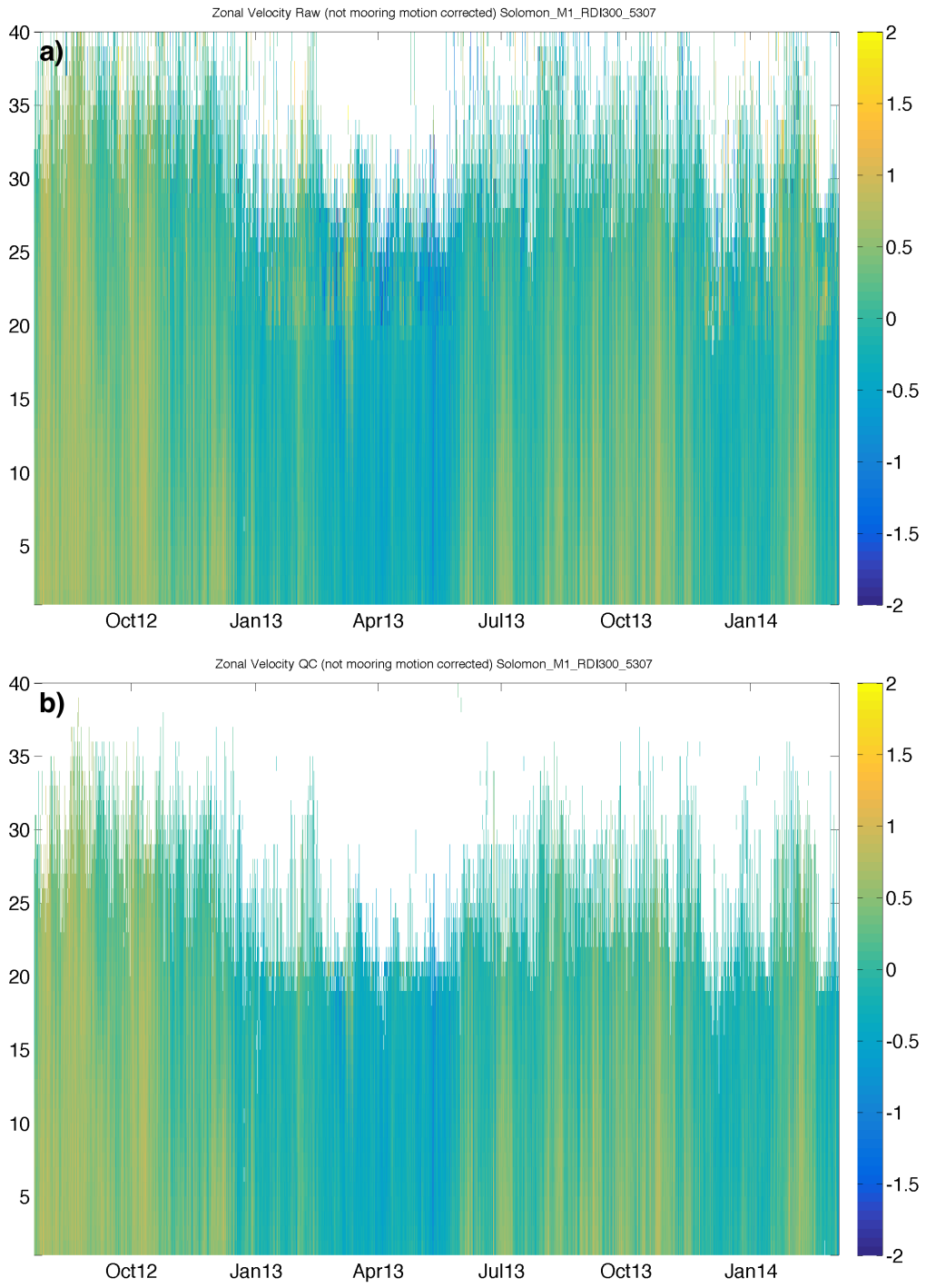

Figure 3 – Comparisons of zonal velocity ($m.s^{-1}$) in Solomon Strait M1, (a) raw zonal velocity and (b) QC zonal velocity of the RDI 300 kHz ADCP.

3.2 Case 2: Solomon Strait M1 (downward RDI 75 kHz)

- Instrument type: RDI 75 kHz
- Instrument target depth: 102 m
- Instrument Serial Number: 3427
- Instrument vertical bin size: 20 m
- Instrument Deployment Date/Time (UTC): 07/21/2012 01:30
- Instrument Recovery Date/Time (UTC): 03/06/2014 23:01

The RDI 75 kHz in Solomon Strait M1 are 30 bins for 14431 time realizations. Pitch and roll variations (Figure 4a,b) are lower than 10 to 20 degrees. Similar vertical variations are observed in pressure (Figure 4c) and temperature (Figure 4d) than those with the upward RDI 300 kHz. The average, standard deviation, and range values for the different parameters used in each QC test are shown in Figure 5.

The EA test contributes ∼100% to total fails in bins 16-26, representing few cells in term of absolute numbers for thresholds of 20 (∼50 cells) and 25 (∼10 cells). No EAfail is found for thresholds 30 and 35. We suggest that an appropriate threshold is 25 counts, as used in INSTANT QC for all RDI 75 kHz.

The percent good and correlation magnitude stay at 100% in most upper bins for the different threshold values in OTfails. The failure rate appear to be insensitive to the choice of thresholds for both percent good (from 10% to 80%) and correlation magnitude (from 50 to 110), suggesting that the rejected values are likely near zero for the percent good and below 50 for the correlation magnitude, and hence bad values. Due to this threshold insensitivity, we decide to follow INSTANT choices for the RDI 75 kHz. Percent good and correlation magnitude thresholds are set to 50% and 64, respectively.

For the error velocity and the vertical velocity, few cells in term of absolute numbers are rejected in OTfails, and no cells are rejected for the horizontal error velocity test. Hence, we stick with INSTANT recommended thresholds of 0.15, 0.2 and 2 $m.s^{-1}$, respectively.

The new QC parameters are shown in Table 1. No significant cell removal was detected, as the sum of the OTfails is mostly lower than 2 and only few cells are rejected through the EA test. Hence, no major differences are found between the zonal or meridional velocities before and after QC (Figure 6a,b).

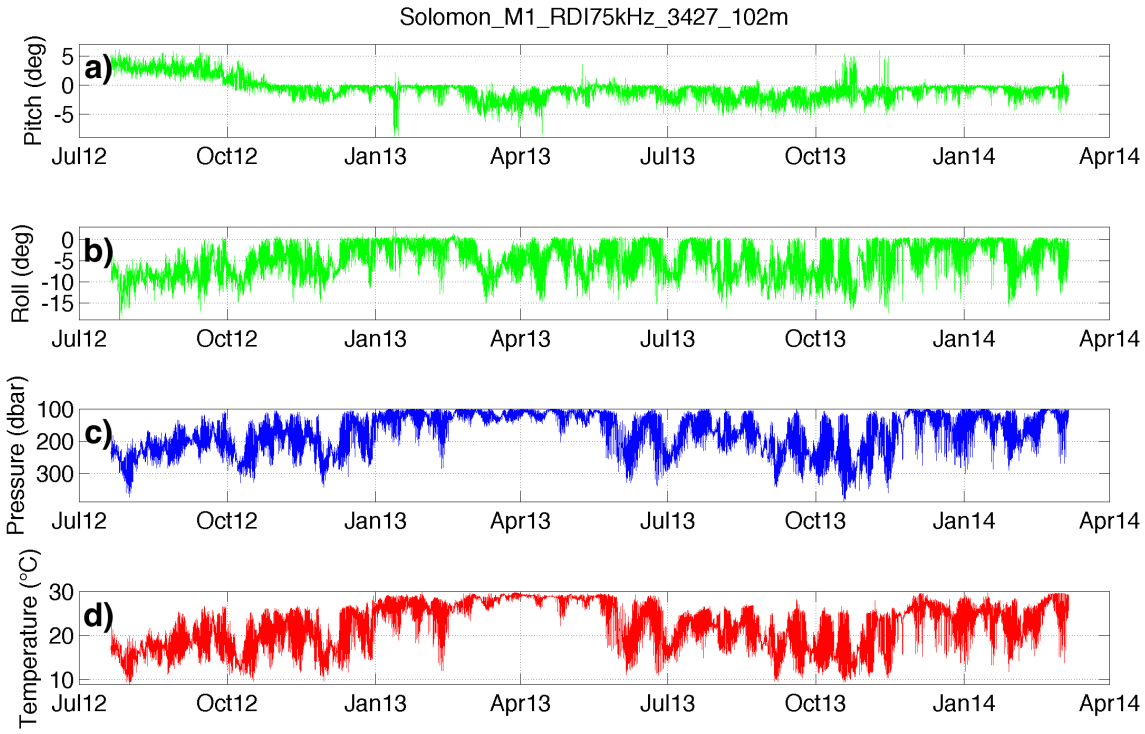

Figure 4 – Solomon Strait M1 RDI 75 kHz (downward) raw data of (a) pitch; (b) roll; (c) pressure and (d) temperature timeseries.

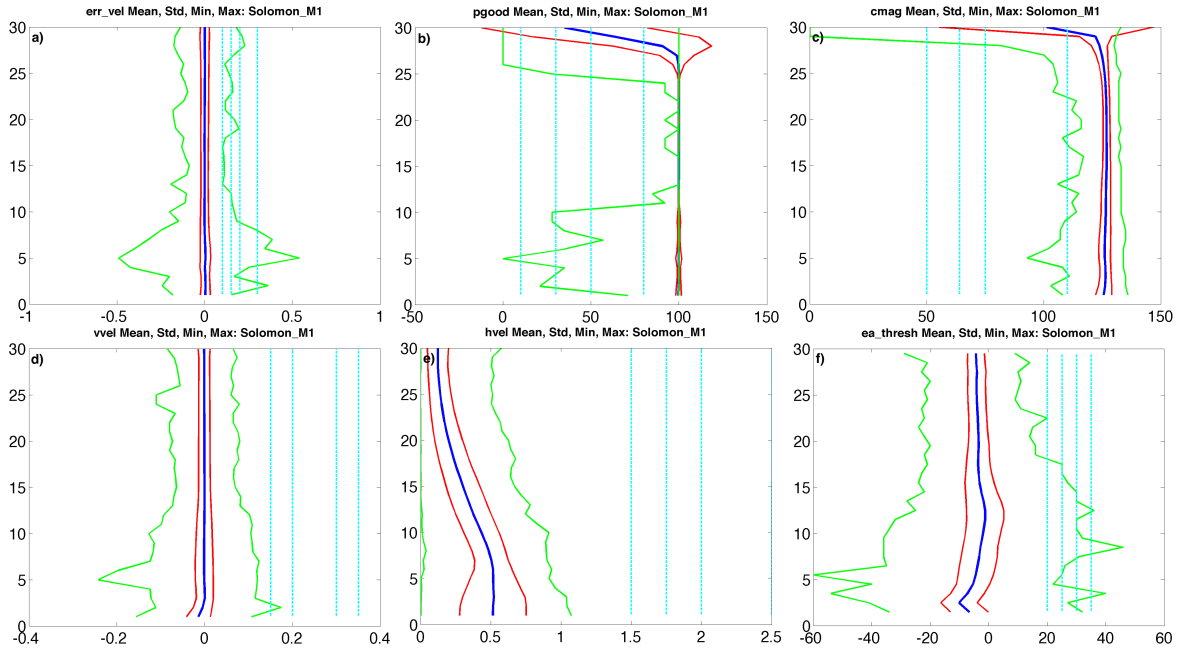

Figure 5 – Mean (thick blue line), standard deviation (red lines) and minimum and maximum (green lines) of the (a) error velocity ($m.s^{-1}$); (b) percent good; (c) correlation magnitude; (d) vertical velocity ($m.s^{-1}$); (e) horizontal velocity ($m.s^{-1}$) and (f) echo amplitude (counts) for the Solomon Strait M1 RDI 75 kHz ADCP versus bin. The four threshold values used in each QC test are marked by cyan lines in panels (a) to (f).

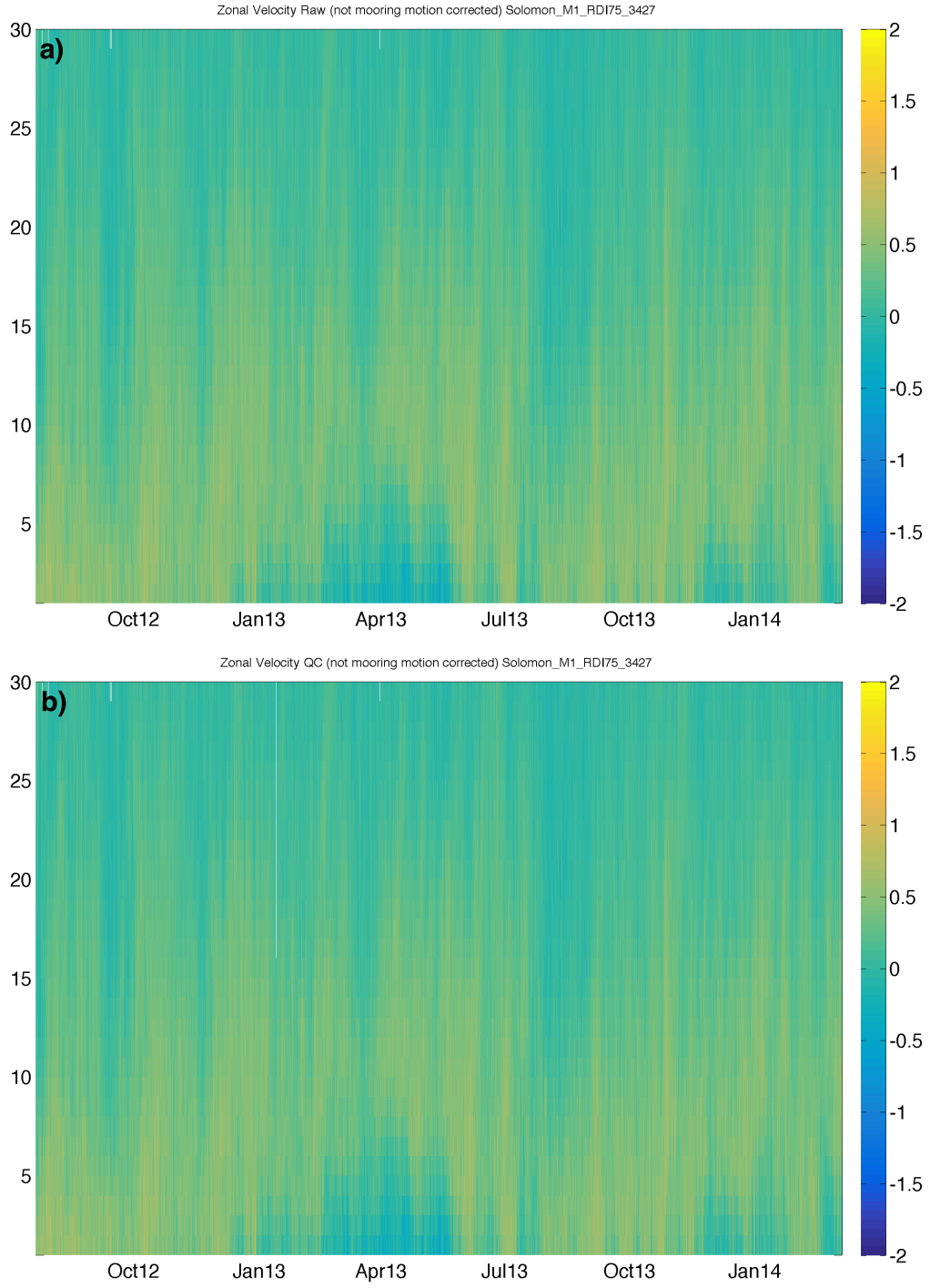

Figure 6 – Comparisons of zonal velocity ($m.s^{-1}$) in Solomon Strait M1, (a) raw zonal velocity and (b) QC zonal velocity of the RDI 75 kHz ADCP.

3.3 Case 3: Solomon Strait M2a (upward FlowQuest 300 kHz)

- Instrument type: FlowQuest 300 kHz
- Instrument target depth: 80 m
- Instrument Serial Number: 40005
- Instrument Deployment Date/Time (UTC): 07/16/2012 04:17
- Instrument Recovery Date/Time (UTC): 03/06/2014 01:45

The upward FlowQuest 300 kHz data could not be retrieved because of technical problems, and so no quality control was performed on this instrument.

3.4 Case 4: Solomon Strait M2b (upward RDI 75 kHz)

- Instrument type: RDI 75 kHz
- Instrument target depth: 400 m
- Instrument Serial Number: 1066
- Instrument vertical bin size: 20 m
- Instrument Deployment Date/Time (UTC): 07/15/2012 22:11
- Instrument Recovery Date/Time (UTC): 03/06/2014 02:24

The RDI 75 kHz in Solomon Strait M2b are 30 bins for 14356 time realizations. Pitch and roll variations (Figure 7a,b) are lower than 5 degrees. Vertical variations in pressure (<100 dbar, Figure 7c) and temperature (<5°C, Figure 7d) are observed with the downward RDI 75 kHz. The average, standard deviation, and range values for the different parameters used in each QC test are shown in Figure 8.

For the EA test, the EAfail stay at 100% in bins 18-30 and no EAfail is found in bins 1-15 for the different threshold values. Differences are found in percent failure in bin 16 (12-73%) and bin 17 (23-77%) for each threshold (20, 25, 30 and 35), where high EAfail is associated with low threshold values. A QC threshold of 25 counts is found to be appropriate for the RDI 75 kHz in Solomon Strait M2b, as in INSTANT for the RDI 75 kHz cases.

As in Solomon Strait M1, the percent good and the correlation magnitude stay mostly at 100% in upper bins 18 to 30, where both percent good and correlation magnitude contribute only to ∼1% of total fails. Percent failures appear to be again, insensitive to the choice of threshold values. Thus, we stick with the Solomon Strait M1 criteria used for the RDI 75 kHz in Solomon Strait M2b.

For the error velocity, cell rejection is mostly occurring in bins 19-30 in OTfails for each threshold values, with significant differences in term of absolute numbers. The percent failure drops off ∼50% from the threshold values of 0.15 $m.s^{-1}$ to 0.2 $m.s^{-1}$. We decide to use 0.15 threshold, as the RDI 75 kHz in Solomon Strait M1. The vertical velocity test exhibits few rejected cells in OTfails in terms of absolute numbers with highest values for the 0.15 threshold criterion. The horizontal velocity test exhibits also few rejected cells, except at the middle bins 19-21 for each threshold value. We stick with previous thresholds for both vertical and horizontal tests (0.2 $m.s^{-1}$ and 2 $m.s^{-1}$, respectively).

The corresponding QC parameters are shown in Table 1, and the zonal velocities before and after QC are shown in Figure 9a,b. Obvious differences occur in bins 18-30, where the revised thresholds retain more cells.

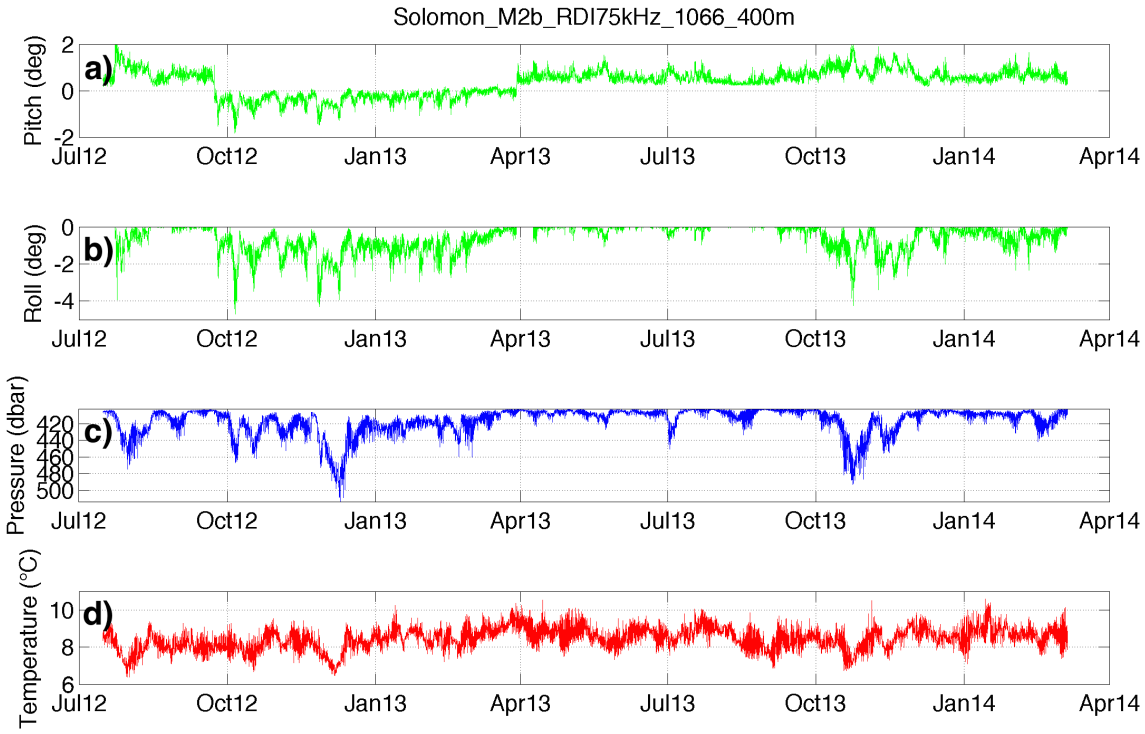

Figure 7 – Solomon Strait M2b RDI 75 kHz (downward) raw data of (a) pitch; (b) roll; (c) pressure and (d) temperature timeseries.

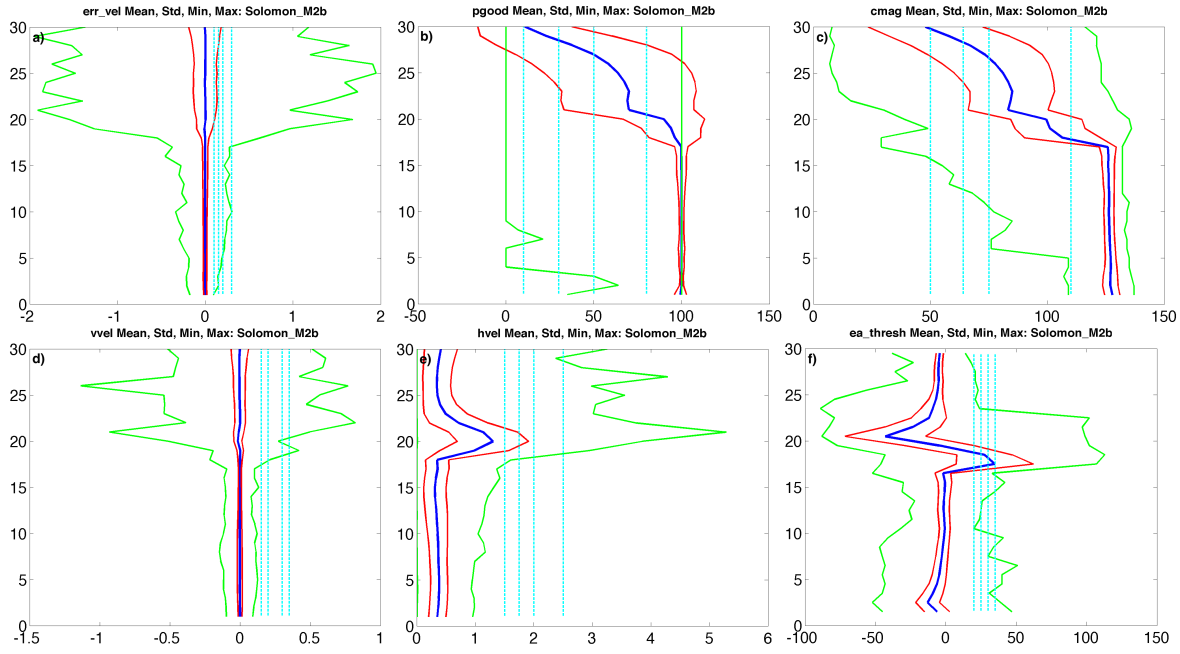

Figure 8 – Mean (thick blue line), standard deviation (red lines) and minimum and maximum (green lines) of the (a) error velocity ($m.s^{-1}$); (b) percent good; (c) correlation magnitude; (d) vertical velocity ($m.s^{-1}$); (e) horizontal velocity ($m.s^{-1}$) and (f) echo amplitude (counts) for the Solomon Strait M2b RDI 75 kHz ADCP versus bin. The four threshold values used in each QC test are marked by cyan lines in panels (a) to (f).

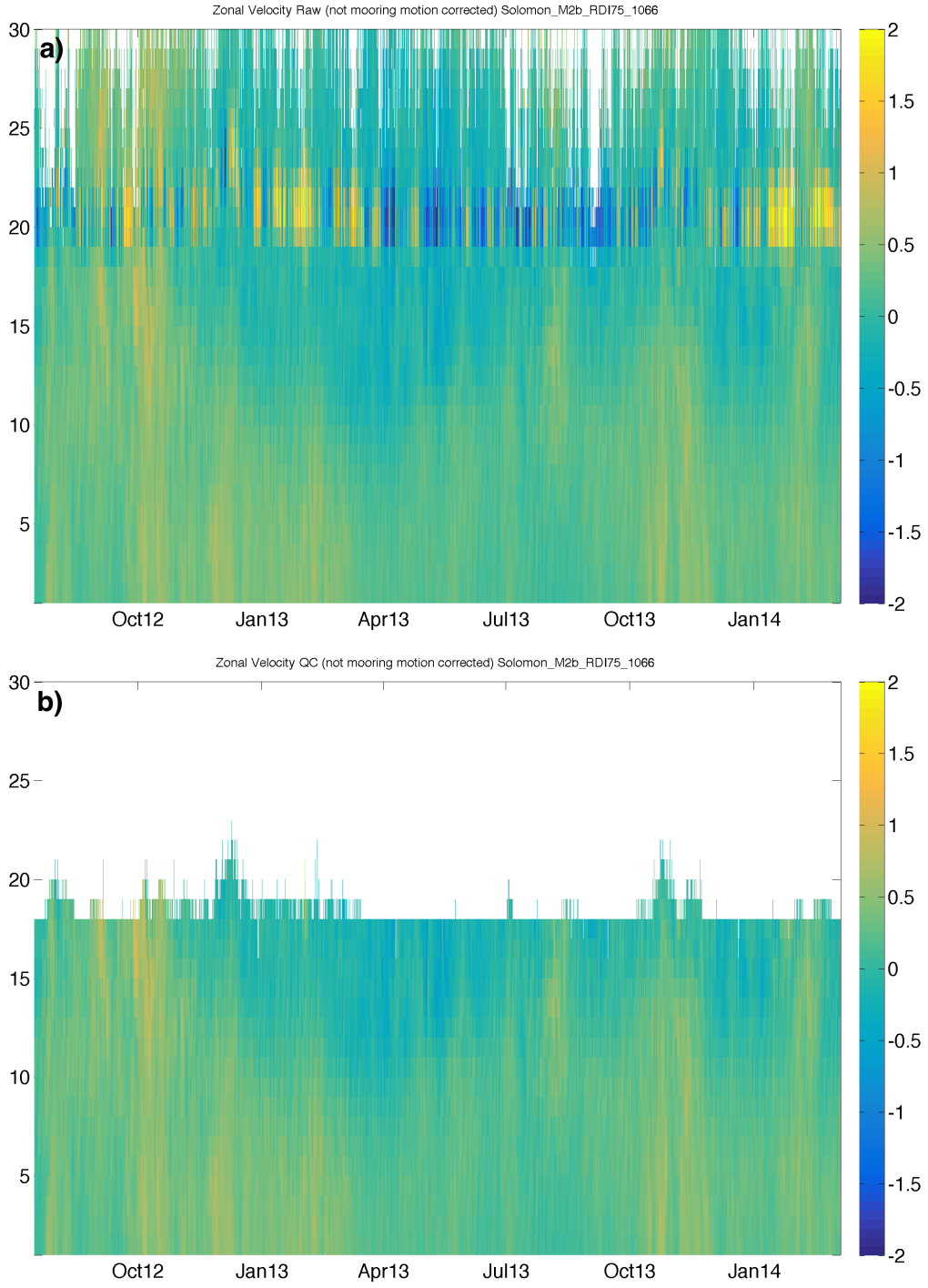

Figure 9 – Comparisons of zonal velocity ($m.s^{-1}$) in Solomon Strait M2b, (a) raw zonal velocity and (b) QC zonal velocity of the RDI 75 kHz ADCP.

3.5 Case 5: Solomon Strait M3 (upward RDI 300 kHz)

- Instrument type: RDI 300 kHz
- Instrument target depth: 80 m
- Instrument Serial Number: 12143
- Instrument vertical bin size: 4 m
- Instrument Deployment Date/Time (UTC): 07/18/2012 01:52
- Instrument Recovery Date/Time (UTC): 03/04/2014 20:35

The RDI 300 kHz in Solomon Strait M3 are 40 bins for 14331 time realizations. Pitch and roll variations (Figure 10a,b) are lower than 5 degrees over time, and some punctual vertical variations in pressure (<50 dbar, Figure 10c) and temperature (<5°C, Figure 10d) are observed. The average, standard deviation, and range values for the different parameters used in each QC test are shown in Figure 11.

The EA test results in 2-5% failure in middle bins 20-30 for each threshold value, and no EAfail below bin 20, where the surface is likely detected (see strong discontinuity of the mean profile, Figure 11f). A 30 threshold that was found appropriate for the RDI 300 kHz used in Solomon Strait M1, is also suitable for this RDI 300 kHz used in Solomon Strait M3.

The percent good contributes 100% to OTfails for each threshold value in upper bins 25-40, which is nearly similar to the correlation magnitude. Both tests contribute to ∼90% of the total fail in most upper bins. As for the RDI 300 kHz in Solomon Strait M1, we suggest to use a 80 percent good and a 110 correlation magnitude.

The error velocity test exhibits rejected cells mostly in bins 18-28 for each threshold value in OTfails. The vertical and horizontal velocity tests rejects cells mostly around bin 25 for the different thresholds in OTfails. As in Solomon Strait M1, the QC threshold criteria that were found appropriate for the RDI 300 kHz (Table 1), are also suitable for the RDI 300 kHz in Solomon Strait M3.

The zonal velocities are shown before and after QC (Figure 12a,b). The differences occur mostly above bin 18, where the revised thresholds retain most of the cells near the sea surface.

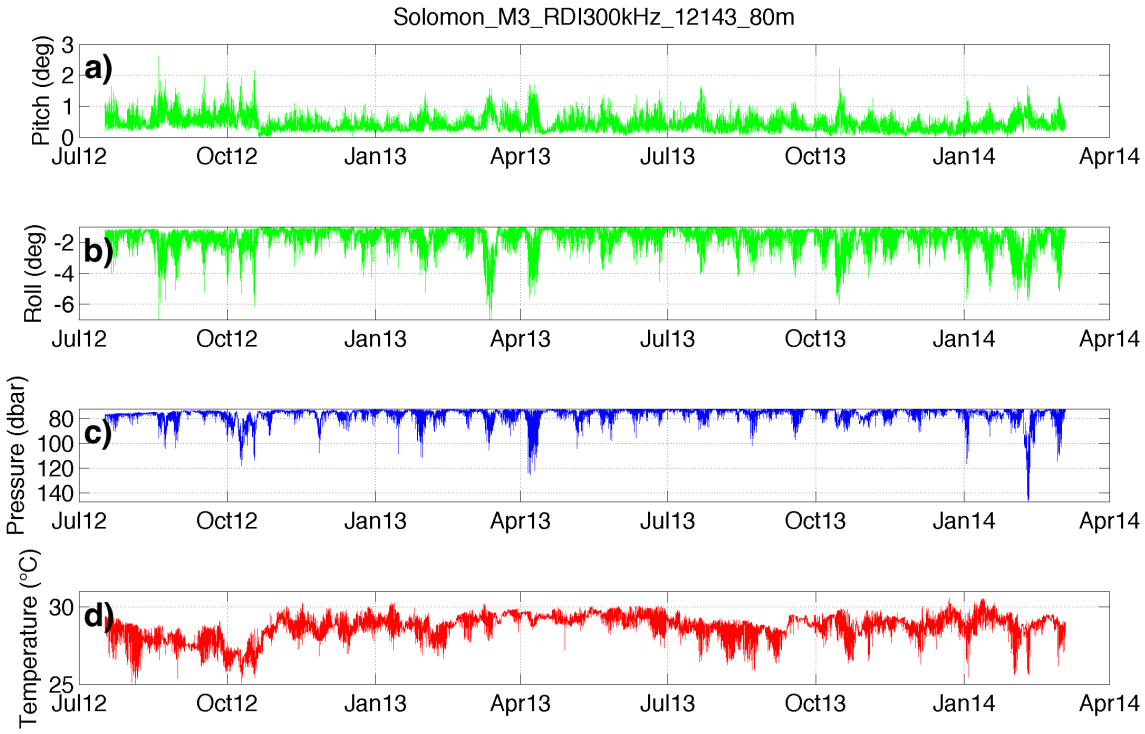

Figure 10 – Solomon Strait M3 RDI 300 kHz (upward) raw data of (a) pitch; (b) roll; (c) pressure and (d) temperature timeseries.

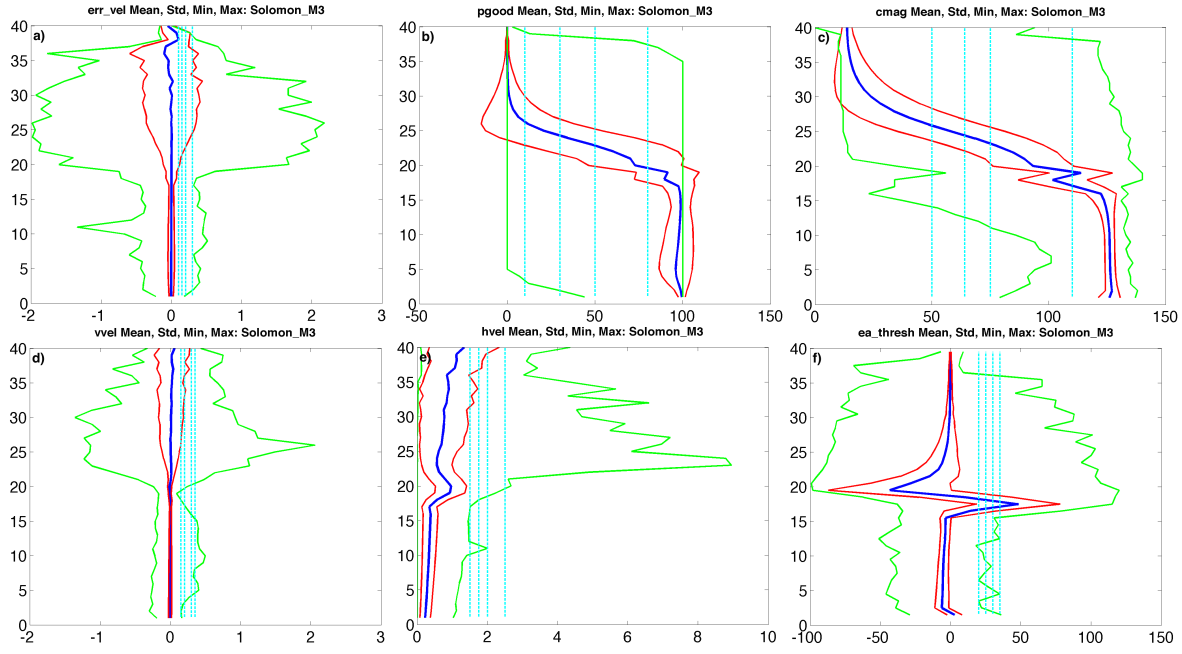

Figure 11 – Mean (thick blue line), standard deviation (red lines) and minimum and maximum (green lines) of the (a) error velocity ($m.s^{-1}$); (b) percent good; (c) correlation magnitude; (d) vertical velocity ($m.s^{-1}$); (e) horizontal velocity ($m.s^{-1}$) and (f) echo amplitude (counts) for the Solomon Strait M3 RDI 300 kHz ADCP versus bin. The four threshold values used in each QC test are marked by cyan lines in panels (a) to (f).

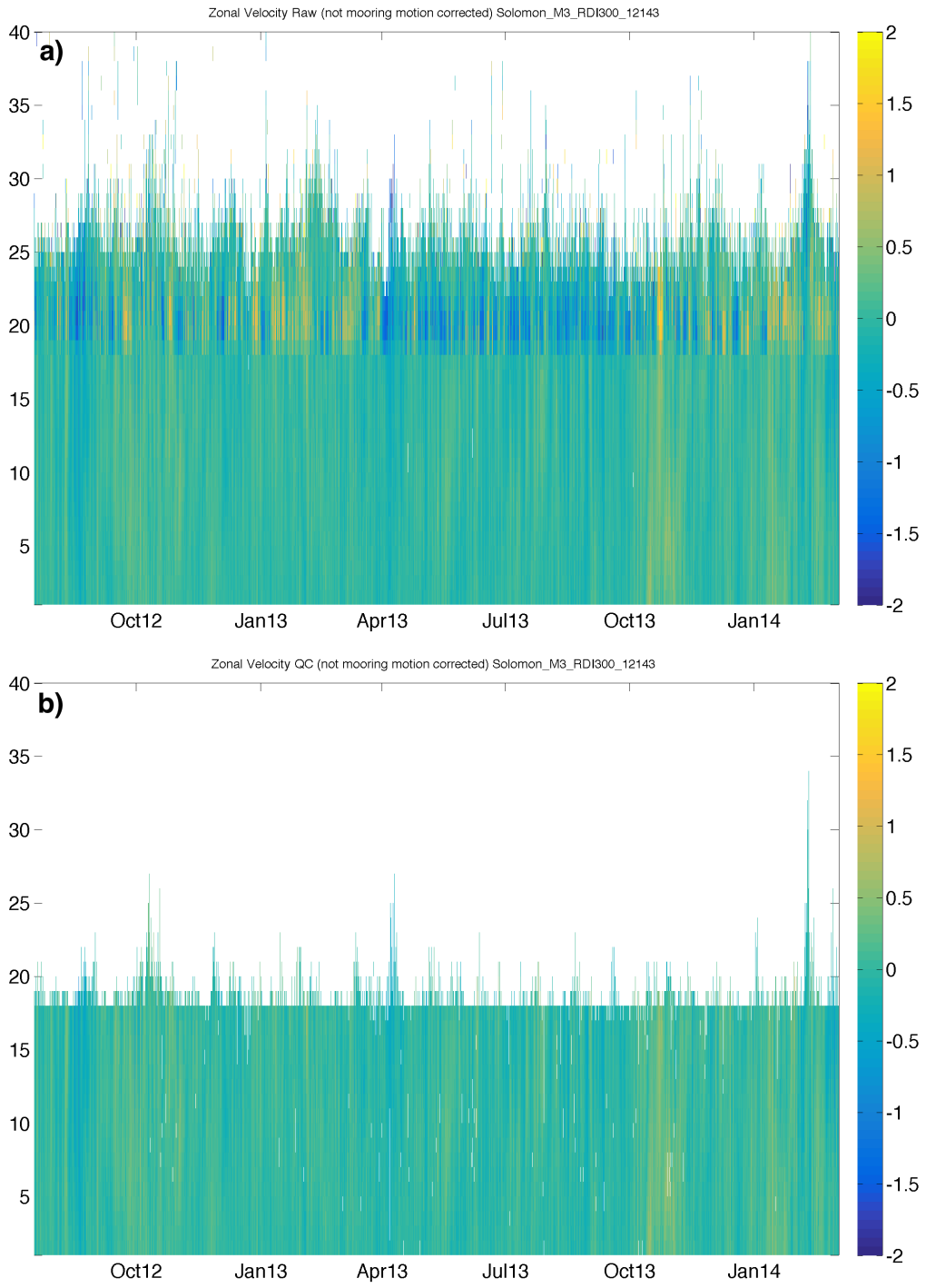

Figure 12 – Comparisons of zonal velocity ($m.s^{-1}$) in Solomon Strait M3, (a) raw zonal velocity and (b) QC zonal velocity of the RDI 300 kHz ADCP.

3.6 Case 6: Solomon Strait M3 (downward RDI 75 kHz)

- Instrument type: RDI 75 kHz
- Instrument target depth: 102 m
- Instrument Serial Number: 14215
- Instrument vertical bin size: 20 m
- Instrument Deployment Date/Time (UTC): 18/07/2012 01:52
- Instrument Recovery Date/Time (UTC): 04/03/2014 20:35

The RDI 75 kHz in Solomon Strait M3 are 30 bins for 10625 time realizations. Pitch and roll variations (Figure 13a,b) are lower than 5 and 10 degrees respectively. Vertical variations in pressure (<50 dbar, Figure 13c) and temperature (<5°C, Figure 13d) are observed with the downward RDI 75 kHz. The average, standard deviation, and range values for the different parameters used in each QC test are shown in Figure 14.

The EA test shows percent failures in bins 20-30 to total fails, rejecting few cells in terms of absolute numbers for thresholds 20, 25 and 30, but no EAfail is found for the 35 threshold. We suggest an appropriate threshold of 25, consistent with those for RDI 75 kHz in Solomon M1 and M2b.

The percent good contributes 100% to OTfails and the correlation magnitude occurs in nearly 100% of cases for the different threshold values in upper bins. For the error velocity test, few cells in term of absolute numbers are rejected in OTfails, and no cells are rejected for the vertical and horizontal velocity tests.

The QC threshold criteria previously used in M1 and M2b for the RDI 75 kHz (Table 1), are also used for the RDI 75 kHz in Solomon Strait M3. The zonal velocities before and after QC (Figure 15a,b) exhibit little differences, as the sum of OTfails is moslty lower than two and only few bad cells are detected through the EA test. Similar results are found with the meridional velocity field, and so are not shown.

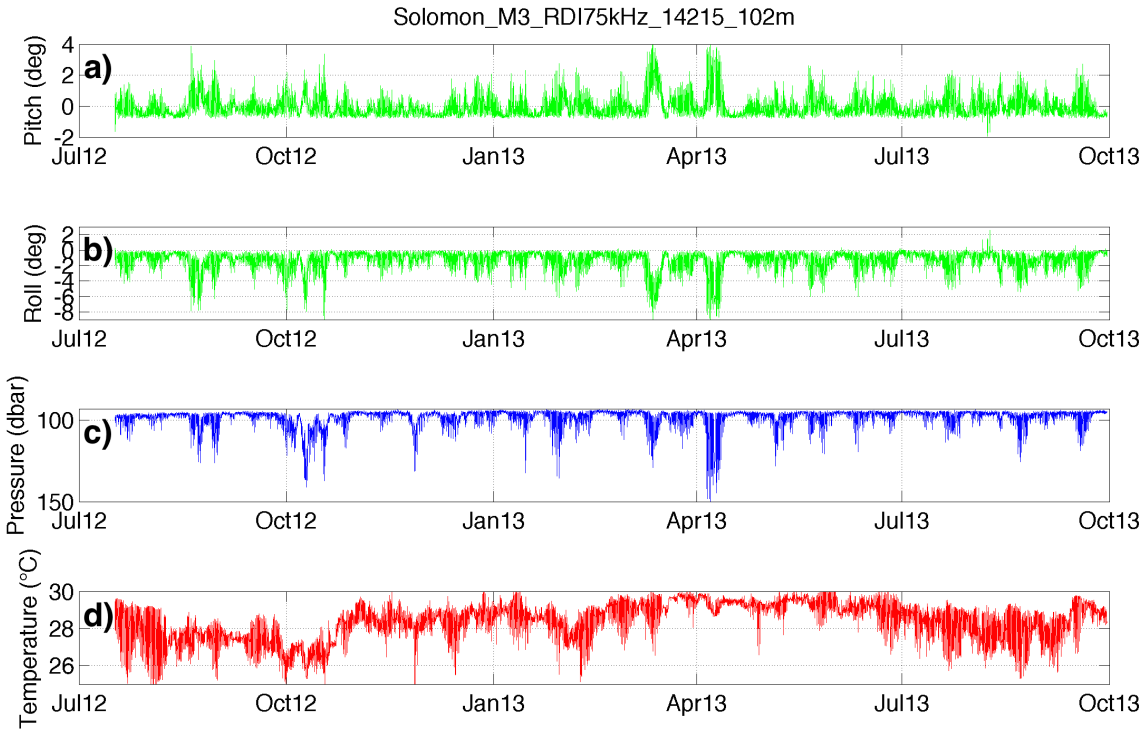

Figure 13 – Solomon Strait M3 RDI 75 kHz (downward) raw data of (a) pitch; (b) roll; (c) pressure and (d) temperature timeseries.

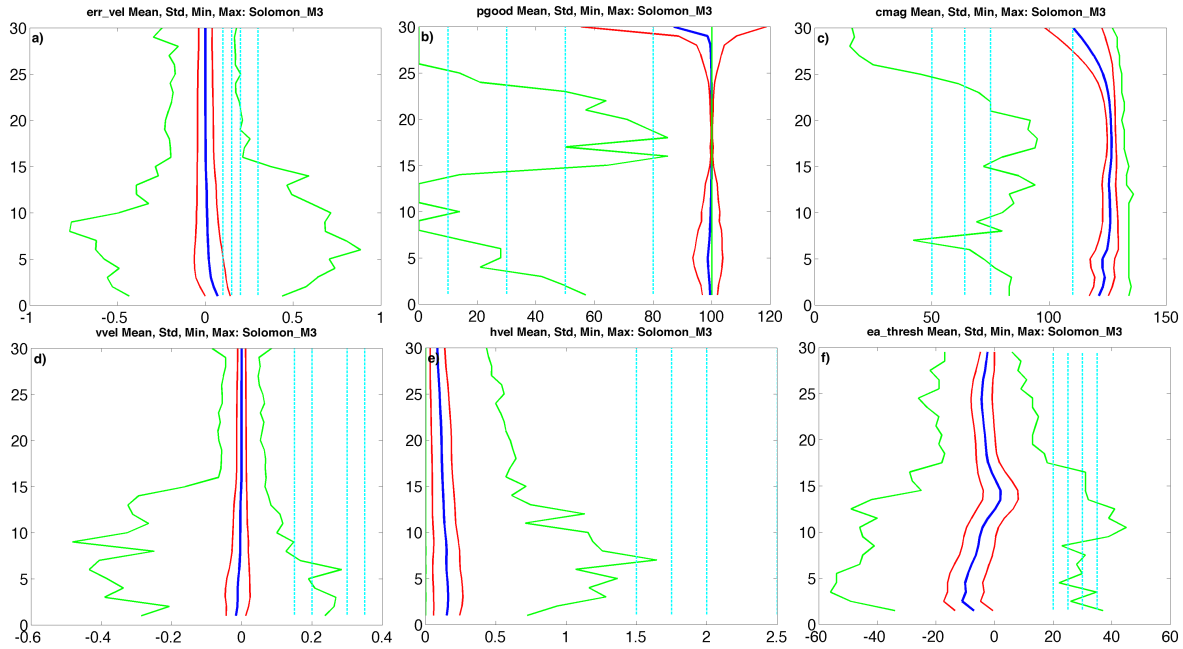

Figure 14 – Mean (thick blue line), standard deviation (red lines) and minimum and maximum (green lines) of the (a) error velocity ($m.s^{-1}$); (b) percent good; (c) correlation magnitude; (d) vertical velocity ($m.s^{-1}$); (e) horizontal velocity ($m.s^{-1}$) and (f) echo amplitude (counts) for the Solomon Strait M3 RDI 75 kHz ADCP versus bin. The four threshold values used in each QC test are marked by cyan lines in panels (a) to (f).

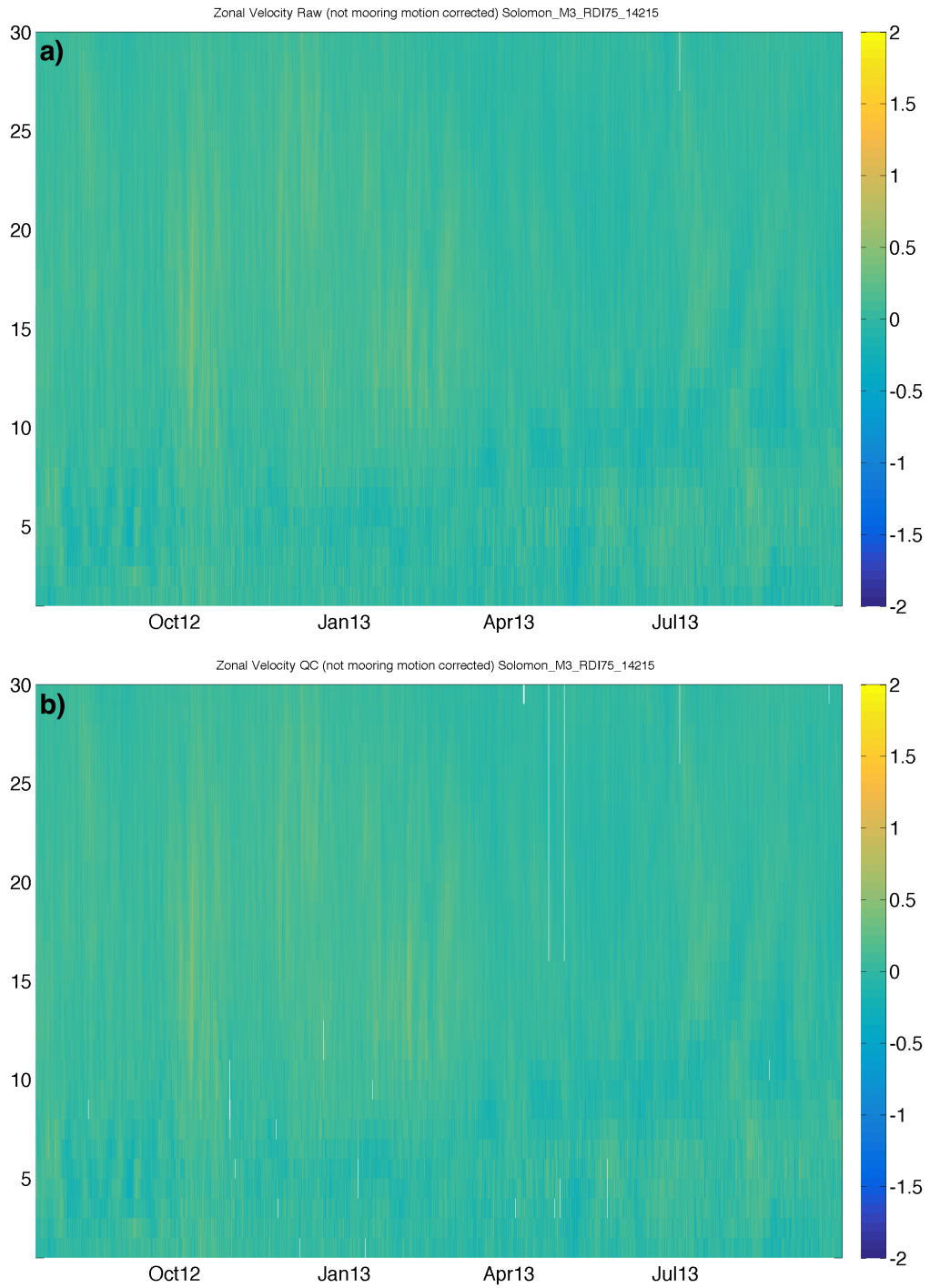

Figure 15 – Comparisons of zonal velocity ($m.s^{-1}$) in Solomon Strait M3, (a) raw zonal velocity and (b) QC zonal velocity of the RDI 75 kHz ADCP.

3.7 Case 7: St Georges East (upward RDI 300 kHz)

- Instrument type: RDI 300 kHz
- Instrument target depth: 152 m
- Instrument Serial Number: 16832
- Instrument vertical bin size: 8 m
- Instrument Deployment Date/Time (UTC): 07/20/2012 05:55
- Instrument Recovery Date/Time (UTC): 03/08/2014 06:35

The RDI 300 kHz in St Georges East are 23 bins for 28834 time realizations. Pitch and roll show strong variations lower than 25 degrees (Figure 16a,b), except between February and April 2013, where strong variations of ±20 degrees are observed. Special attention will be dedicated to ADCP data between February-April 2013 to identify potential damages. Vertical variations in pressure can reach 500 dbar, especially between April-July 2013 (Figure 16c). Temperature variations (Figure 16d) are mostly lower than 10°C, and they can reach 20°C between April-July 2013. The average, standard deviation, and range values for the different parameters used in each QC test are shown in Figure 17.

The EA test results in 6-35% failure to total fails in bins 19-23 for the different threshold values, and EAfail contributes ∼1% below bin 19. The percent good stays at 100% for each threshold value in all bins. The correlation magnitude occurs in nearly 100% cases of OTfails, except in bin 13 for a 50 threshold. Due to relative insensitivity, we stick again with a 80% percent good and a 110 correlation magnitude.

As for the error velocity test, little differences are found between the different thresholds, contributing ∼1-7% to OTfails in all bins. Vertical and horizontal tests reject few bins with percent failures of 0-2% for each threshold. Thus, we suggest using the QC criteria that were found suitable for M1 and M3 RDI 300 kHz (Table 1).

The zonal velocities are shown before and after QC in Figure 18a,b. The differences occur mostly in bins 13-23, where the revised thresholds retain more cells. Between February-April 2013, strong raw zonal velocities (>100 $cm.s^{-1}$) are observed in most upper bins but are retained after QC. Similar strong meridional velocities are observed during February-April 2013 in raw data, but there are also retained after QC (not shown).

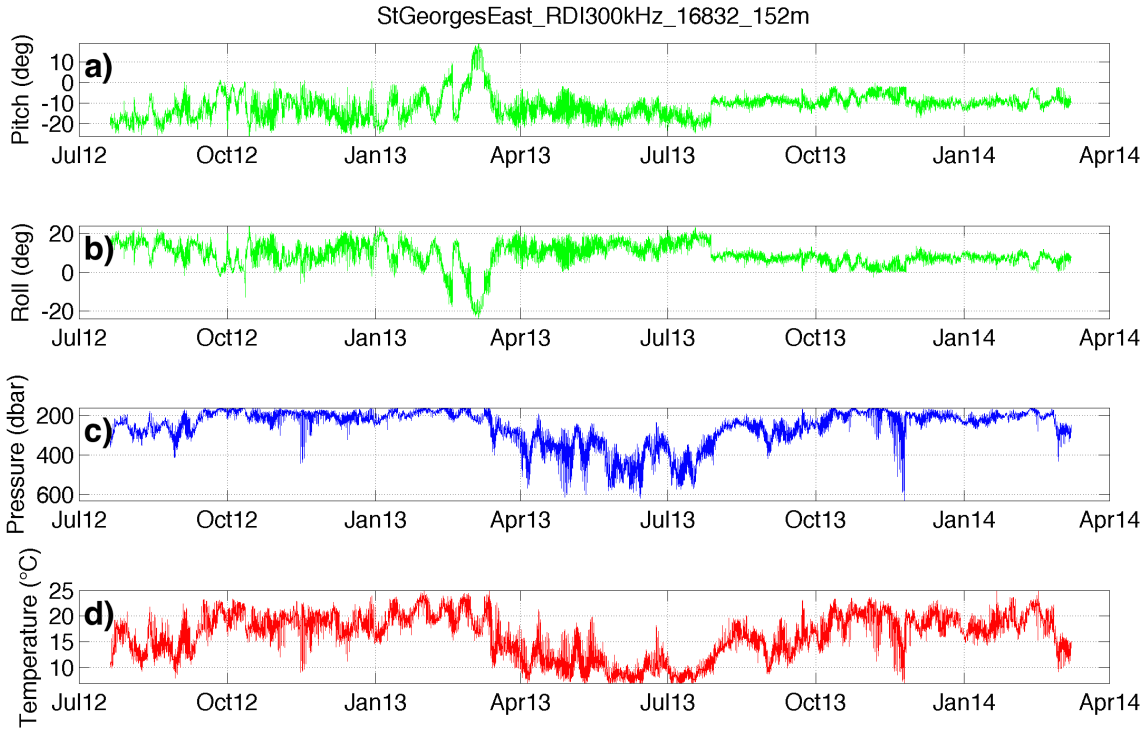

Figure 16 – St Georges Channel East RDI 300 kHz (upward) raw data of (a) pitch; (b) roll; (c) pressure and (d) temperature timeseries.

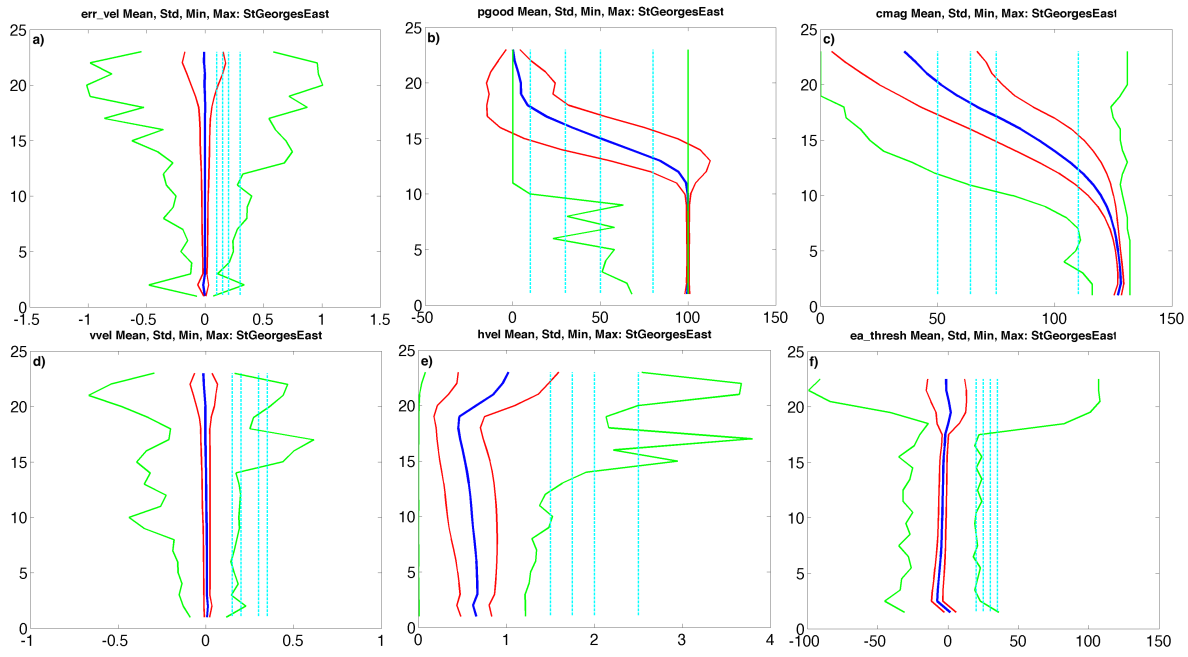

Figure 17 – Mean (thick blue line), standard deviation (red lines) and minimum and maximum (green lines) of the (a) error velocity ($m.s^{-1}$); (b) percent good; (c) correlation magnitude; (d) vertical velocity ($m.s^{-1}$); (e) horizontal velocity ($m.s^{-1}$) and (f) echo amplitude (counts) for the Solomon Strait M3 RDI 75 kHz ADCP versus bin. The four threshold values used in each QC test are marked by cyan lines in panels (a) to (f).

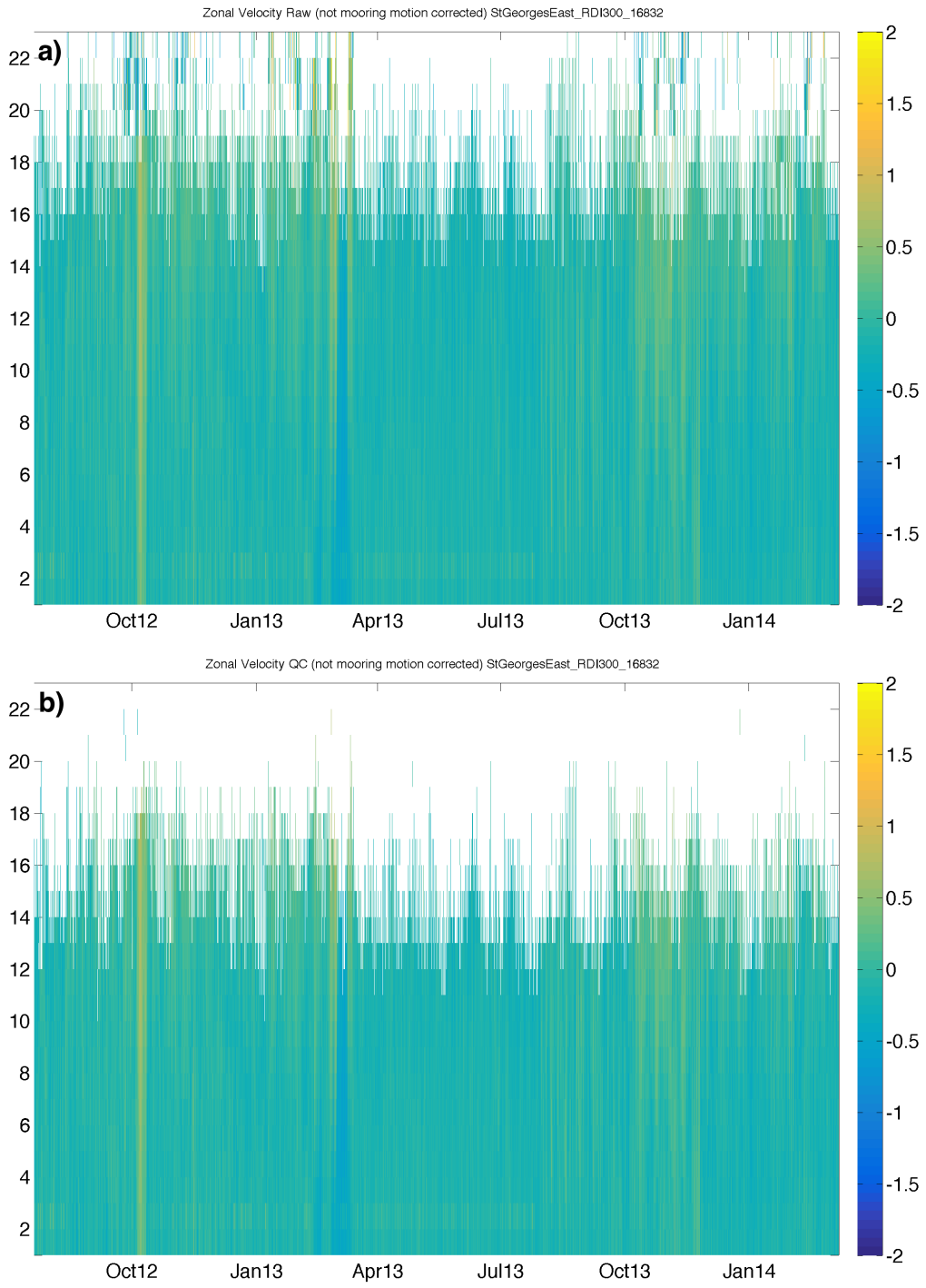

Figure 18 – Comparisons of zonal velocity ($m.s^{-1}$) in St Georges Channel East, (a) raw zonal velocity and (b) QC zonal velocity of the RDI 300 kHz ADCP.

3.8 Case 8: St Georges East (downward RDI 75 kHz)

- Instrument type: RDI 75 kHz
- Instrument target depth: 154 m
- Instrument Serial Number: 16768
- Instrument vertical bin size: 20 m
- Instrument Deployment Date/Time (UTC): 07/20/2012 05:55
- Instrument Recovery Date/Time (UTC): 03/08/2014 06:35

The RDI 75 kHz in St Georges East are 35 bins for 14445 time realizations. Pitch and roll show variations lower than 25 degrees (Figure 19a,b), except between February and April 2013, where strong variations of ±20 degrees are observed. Special attention will be again, dedicated to ADCP data between February-April 2013 to identify potential damages. Vertical variations in pressure can reach 500 dbar from April-July 2013 (Figure 19c). Temperature varies less than 10°C (Figure 19d) but variations can reach 20°C between April-July 2013. The average, standard deviation, and range values for the different parameters used in each QC test are shown in Figure 20.

The EA test shows percent failures of 1% to total fails in all bins for a threshold of 20 counts, and EAfail of 1% only in bin 35 for a 25 threshold. No EAfail is found for the 30 and 35 threshold values. Percent good contributes 100% to OTfails in all bins for each threshold value. The correlation magnitude test contributes also ∼100% to OTfails in all bins.

For the error velocity test, percent failure contributes 1-11% in all bins to OTfails for a threshold of 0.1 $m.s^{-1}$. Only few cells in term of absolute numbers are rejected (0 to 40 cells) for the other threshold values (i.e. 0.15, 0.2 and 0.3 $m.s^{-1}$). The vertical velocity test rejects only one cell in OTfails with a threshold of 0.15 $m.s^{-1}$ from bins 31 to 34, and no cells in all bins with the other thresholds. As for the horizontal velocity test, no cells are rejected for the different cases.

Thus, the relative insensitivity to the choice of thresholds for the different tests, lead us to use the same QC criteria that were previously found appropriate for the RDI 75 kHz in Solomon Strait M1, M2b and M3 (Table 1). Zonal velocities before and after QC (Figure 21a,b) show few differences, although few cells were retain mostly between bins 25-35. Between February-April 2013, zonal and meridional velocities are lower than 50 $cm.s^{-1}$ in most upper bins, similar to those observed during dates without strong pitch and roll.

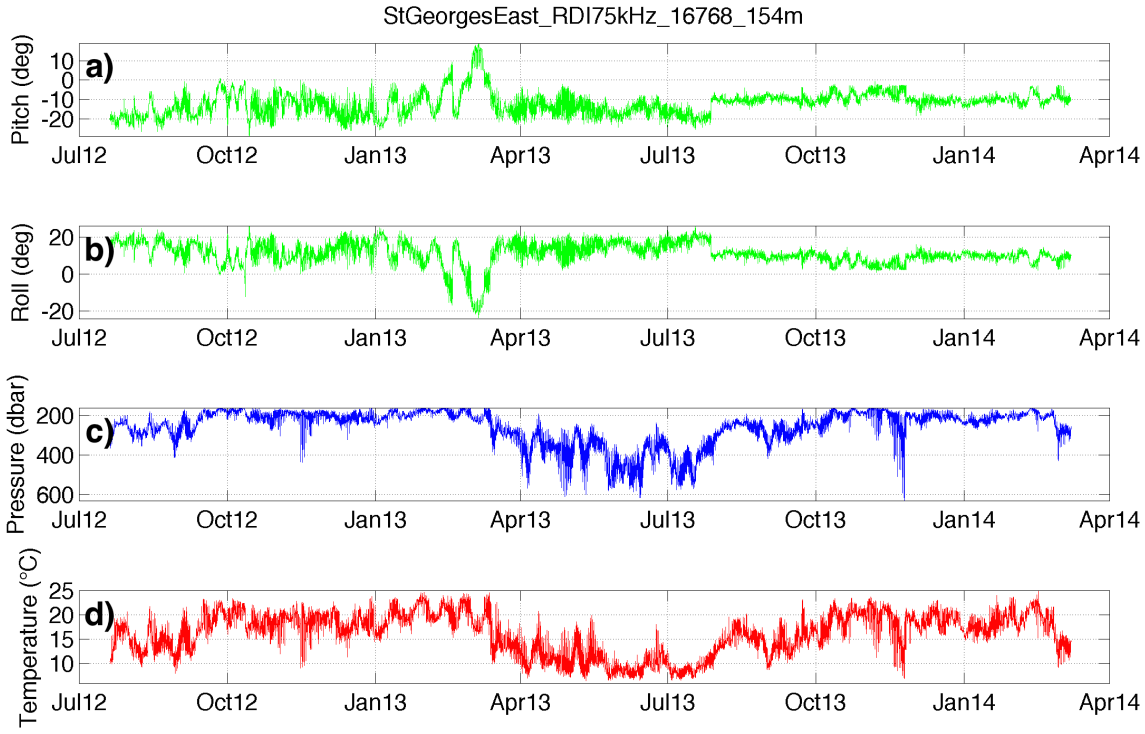

Figure 19 – St Georges Channel East RDI 75 kHz (downward) raw data of (a) pitch; (b) roll; (c) pressure and (d) temperature timeseries.

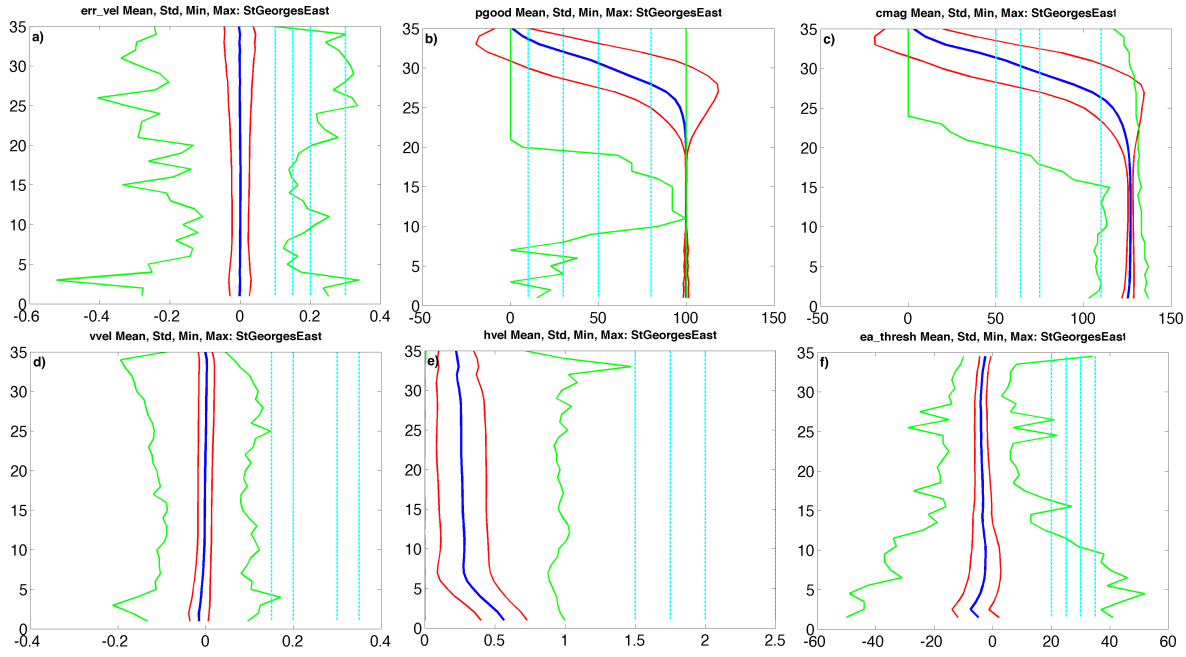

Figure 20 – Mean (thick blue line), standard deviation (red lines) and minimum and maximum (green lines) of the (a) error velocity ($m.s^{-1}$); (b) percent good; (c) correlation magnitude; (d) vertical velocity ($m.s^{-1}$); (e) horizontal velocity ($m.s^{-1}$) and (f) echo amplitude (counts) for the St Georges Channel East RDI 75 kHz ADCP versus bin. The four threshold values used in each QC test are marked by cyan lines in panels (a) to (f).

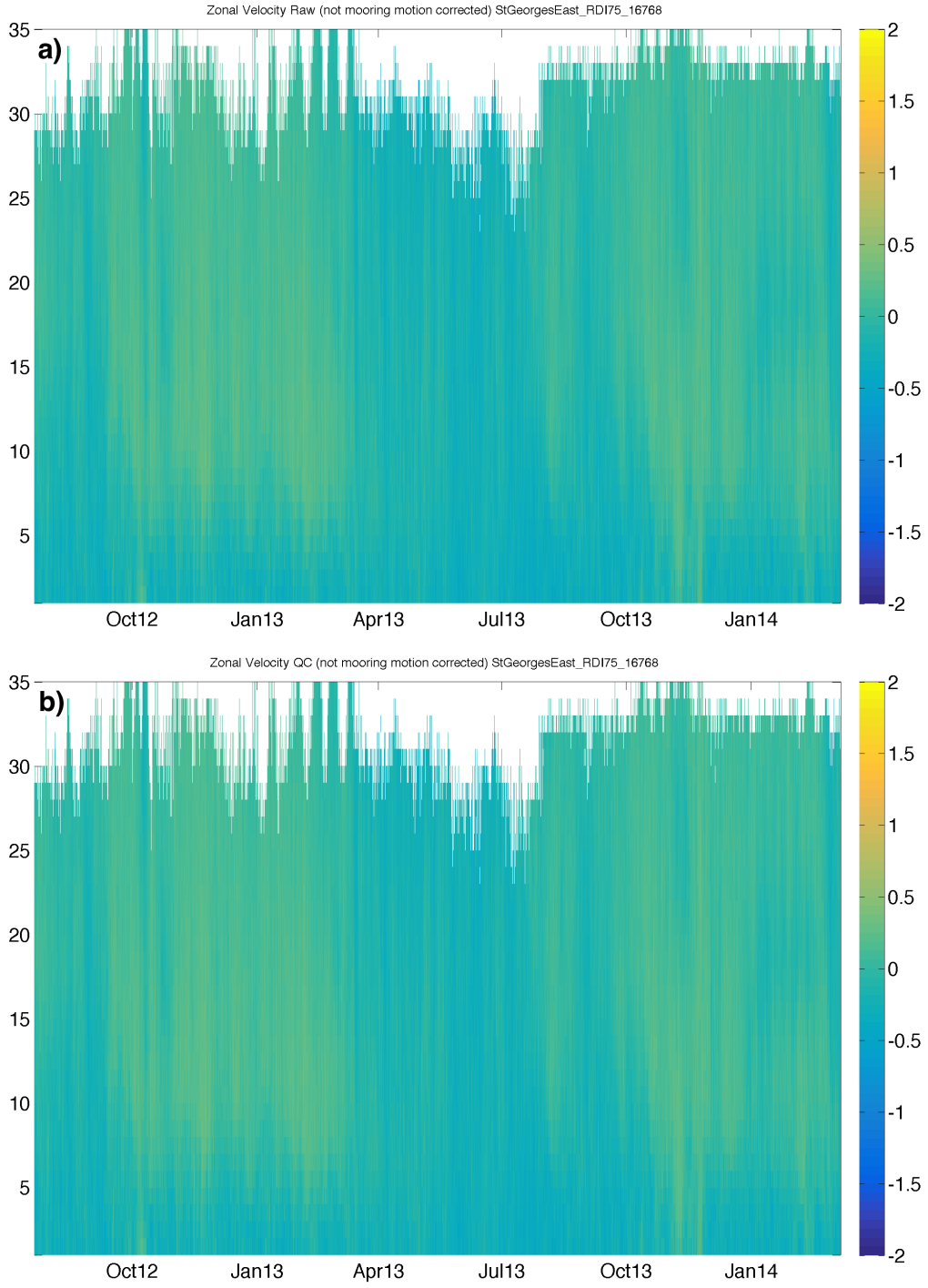

Figure 21 – Comparisons of zonal velocity ($m.s^{-1}$) in St Georges Channel East, (a) raw zonal velocity and (b) QC zonal velocity of the RDI 75 kHz ADCP.

3.9 Case 9: St Georges West (upward RDI 300 kHz)

- Instrument type: RDI 300 kHz
- Instrument target depth: 152 m
- Instrument Serial Number: 16833
- Instrument vertical bin size: 8 m
- Instrument Deployment Date/Time (UTC): 07/20/2012 00:47
- Instrument Recovery Date/Time (UTC): 03/07/2014 23:53

The RDI 300 kHz in St Georges West are 23 bins for 28835 time realizations. Pitch and roll variations (Figure 22a,b) are lower than 25 and 10 degrees, respectively. Pitch looks suspicious, it seems to have a threshold of 0 and does not want to be positive! Data might require further investigation, and need to be handle cautiously. Vertical variations in pressure can reach 500 dbar between April-August 2013 (Figure 22c). Temperature can vary from 5° to 25°C (Figure 22d), mostly from March to July 2013. The average, standard deviation, and range values for the different parameters used in each QC test are shown in Figure 23.

The EA test exhibits percent failures (∼10-50%) in bins 19-23 to total fails for each threshold, and no EAfail is found below bin 19. Percent good contribution to OTfails stays at ∼100% in all bins, for each threshold value. The correlation magnitude test contributes to ∼100% in all bins for threshold values of 75 and 110. As for the error velocity test, little contributions of 1-9% to OTfails are found in all bins for the different threshold values. Vertical and horizontal tests, are responsible for 1-3% of OTfails in all bins.

We decide to use similar QC threshold criteria than those used for the RDI 300 kHz in Solomon Straits and St Georges East (Table 1). Zonal velocities are shown before and after QC (Figure 24a,b). The differences occur mostly in bins 16-23, where the revised thresholds retain some higher velocities, especially when pitch looks clearly suspicious (i.e. between July 2012 to February 2013). However, high zonal velocities ($\sim 1\ m.s^{-1}$) remain in all bins during October 2012, and so likely require further investigation.

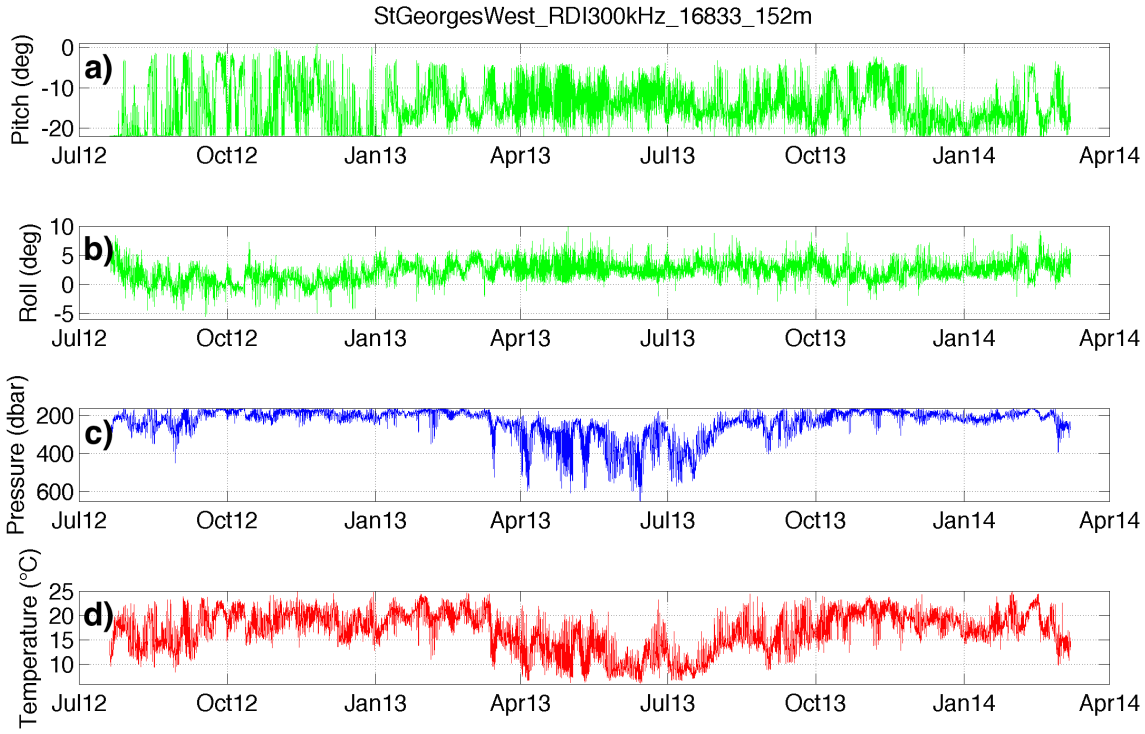

Figure 22 – St Georges Channel West RDI 300 kHz (upward) raw data of (a) pitch; (b) roll; (c) pressure and (d) temperature timeseries.

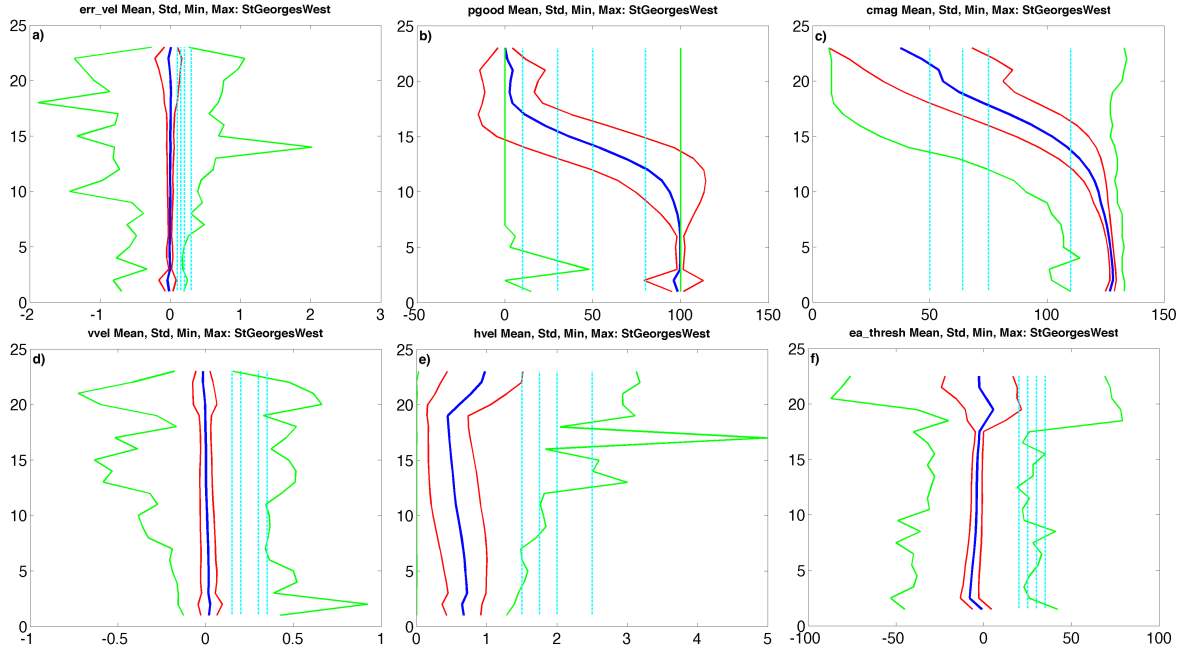

Figure 23 – Mean (thick blue line), standard deviation (red lines) and minimum and maximum (green lines) of the (a) error velocity ($m.s^{-1}$); (b) percent good; (c) correlation magnitude; (d) vertical velocity ($m.s^{-1}$); (e) horizontal velocity ($m.s^{-1}$) and (f) echo amplitude (counts) for the St Georges Channel West RDI 300 kHz ADCP versus bin. The four threshold values used in each QC test are marked by cyan lines in panels (a) to (f).

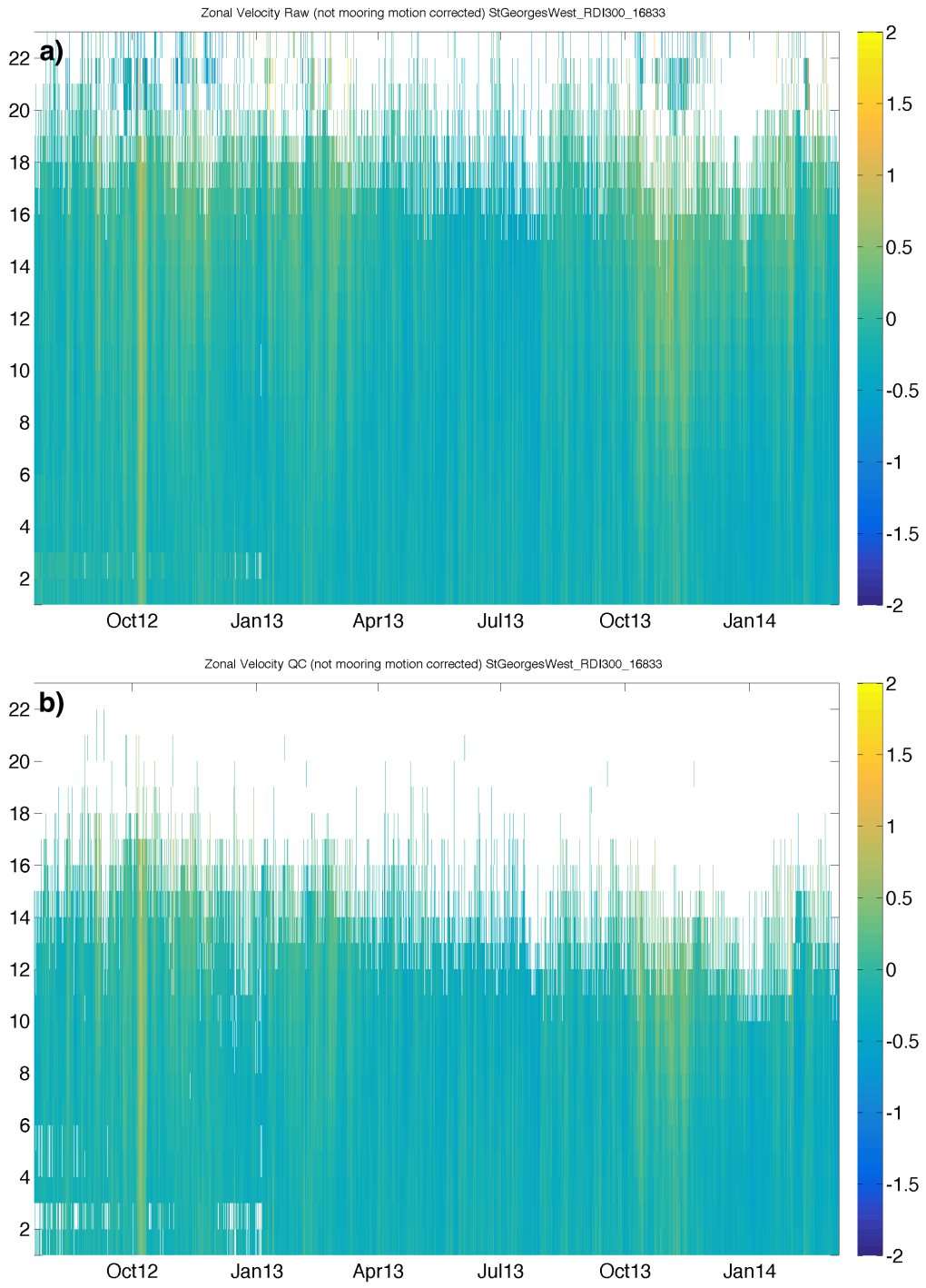

Figure 24 – Comparisons of zonal velocity ($m.s^{-1}$) in St Georges Channel West, (a) raw zonal velocity and (b) QC zonal velocity of the RDI 300 kHz ADCP.

3.10 Case 10: St Georges West (downward RDI 75 kHz)

- Instrument type: RDI 75 kHz
- Instrument target depth: 154 m
- Instrument Serial Number: 8866
- Instrument vertical bin size: 20 m
- Instrument Deployment Date/Time (UTC): 07/20/2012 00:47
- Instrument Recovery Date/Time (UTC): 03/07/2014 23:53

The RDI 75 kHz in St Georges West are 35 bins for 14450 time realizations. Pitch and roll variations (Figure 25a,b) are again, lower than 25 and 10 degrees, respectively. Pitch looks also suspicious, with a threshold of 0. Vertical variations in pressure can reach 400 dbar between April-August 2013 (Figure 25c). Temperature variations are lower than 20°C (Figure 25d), mostly between March-April 2013. The average, standard deviation, and range values for the different parameters used in each QC test are shown in Figure 26.

The EA test exhibits an EAfail of 3-6% in most upper bins 30-35 for the different thresholds. The EAfail can vary from 8% (for a threshold of 35) to 43% (for a threshold of 20) in lower bins. We decide to use a threshold of 25, as in Solomon Straits and St Georges East for the RDI 75 kHz. Percent good contributes ∼100% in OTfails in all bins for the different thresholds, as the correlation magnitude test with a threshold value set to 110. For the error velocity test, all thresholds result in little percent failures of 0-7% in bins 28-35, and 21-56% in most lower bins. The vertical test is associated with only cell rejected in bin 27 for a threshold of 0.15 $m.s^{-1}$, and no cell are rejected with the horizontal velocity test for the different threshold values.

We decide to stick with the QC threshold criteria established in Solomon Straits and St Georges East for the RDI 75 kHz (Table 1). Zonal velocities before and after QC (Figure 27a,b) show few differences, and few cells are retained in bins 25-35. The strong pitch variations do not seem to impact both zonal and meridional velocity fields.

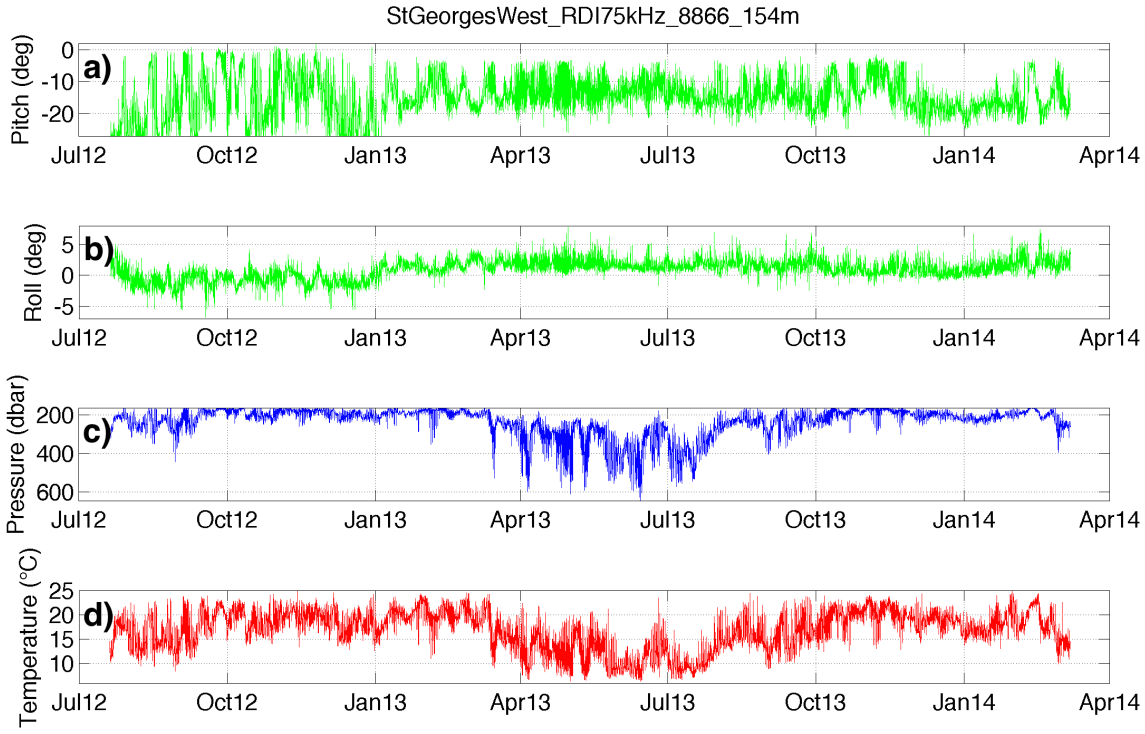

Figure 25 – St Georges Channel West RDI 75 kHz (downward) raw data of (a) pitch; (b) roll; (c) pressure and (d) temperature timeseries.

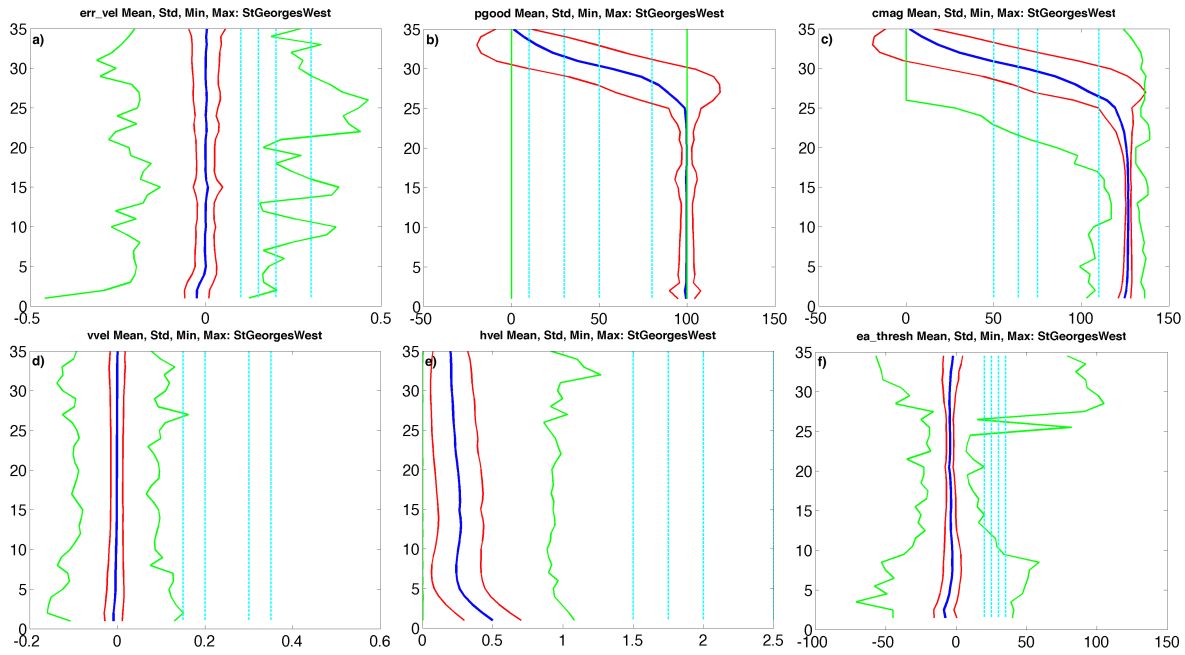

Figure 26 – Mean (thick blue line), standard deviation (red lines) and minimum and maximum (green lines) of the (a) error velocity ($m.s^{-1}$); (b) percent good; (c) correlation magnitude; (d) vertical velocity ($m.s^{-1}$); (e) horizontal velocity ($m.s^{-1}$) and (f) echo amplitude (counts) for the St Georges Channel West RDI 75 kHz ADCP versus bin. The four threshold values used in each QC test are marked by cyan lines in panels (a) to (f).

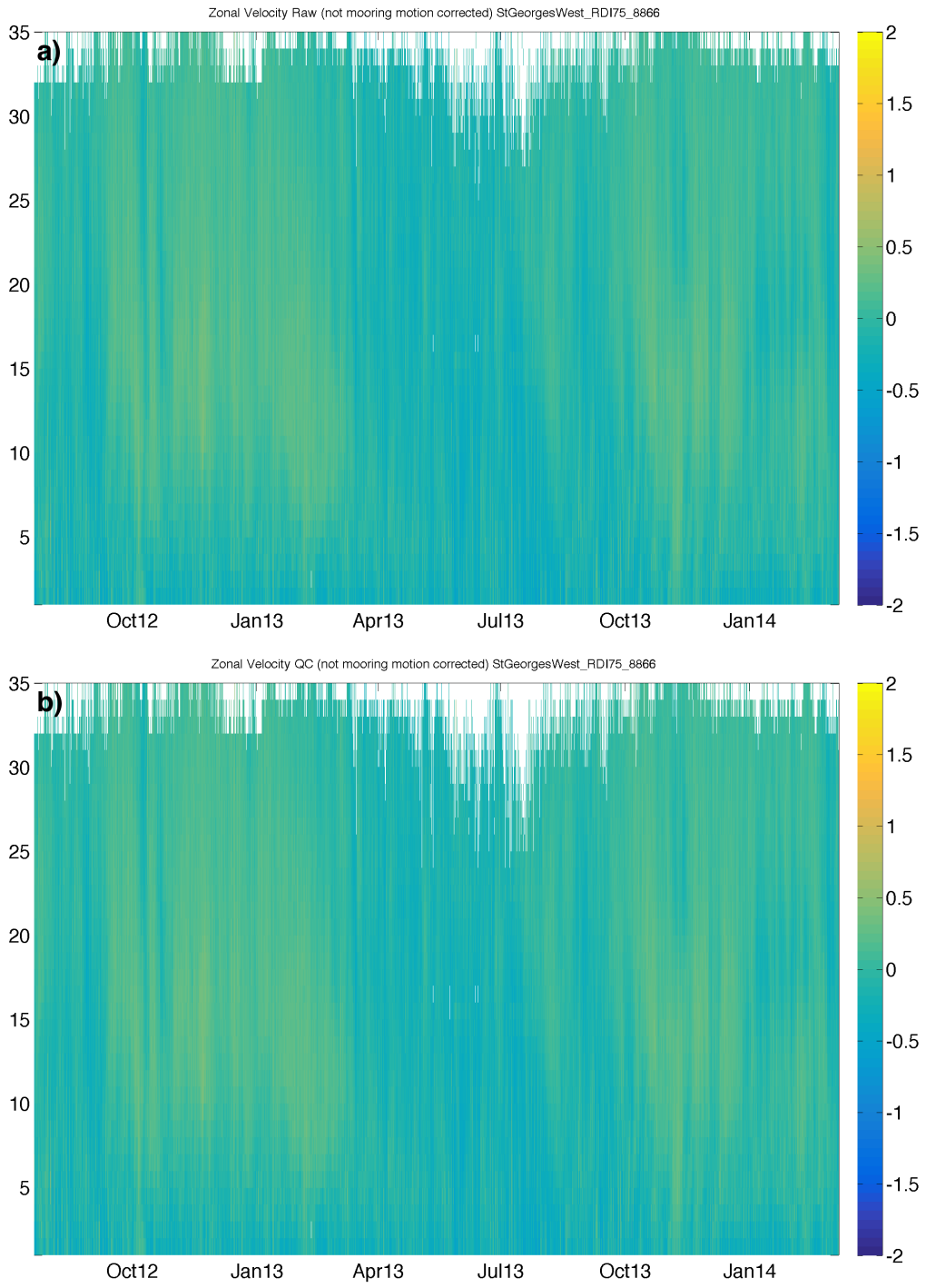

Figure 27 – Comparisons of zonal velocity ($m.s^{-1}$) in St Georges Channel West, (a) raw zonal velocity and (b) QC zonal velocity of the RDI 75 kHz ADCP.

3.11 Case 11: Vitiaz Strait Middle (upward RDI 75 kHz)

- Instrument type: RDI 75 kHz
- Instrument target depth: 332 m
- Instrument Serial Number: 8998
- Instrument vertical bin size: 4 m
- Instrument Deployment Date/Time (UTC): 28/07/2012 13:06
- Instrument Recovery Date/Time (UTC): 15/03/2014 02:15

The upward RDI 75 kHz in Vitiaz Strait Middle are 109 bins for 27283 time realizations. Pitch and roll variations (Figure 28a,b) are lower than 10 and 30 degrees, respectively. Strong roll is mostly observed during August-November 2012, where data might warrant further investigation. Vertical variations in pressure can reach 200 dbar (Figure 28c), mostly from April to August 2013. Temperature variations are lower than 10°C (Figure 28d). The average, standard deviation, and range values for the different parameters used in each QC test are shown in Figure 29.

The EA test exhibits an EAfail of 65-87% in upper bins 90-110, but it appears to be relatively insensitive to the choice of threshold values. As for the percent good test, percent failures contribute $sim100\%$ to OTfails for each threshold. The correlation magnitude is responsible for ∼100% of OTfails in the top most upper bins 105-109 for thresholds 50, 64 and 75, and in bins 95-109 for a 110 threshold.

For the error velocity test, all thresholds result in percent failures of 0-25% to OTfails in bins 90-109. Percent failures are ranged from 30-60% in bins 70-89 (for a 0.15 threshold), and 30-50% (for a 0.2 threshold). The vertical velocity test shows little differences between the different threshold values with minor contributions (1-10%) to OTfails, mainly in most lower bins. As for the horizontal velocity test, few percent failures are found for each threshold, mostly in middle bins 85-95.

Most of the QC criteria used for the previous RDI 75 kHz are found to be appropriate for the upward RDI 75 kHz in Vitiaz Strait, except for the correlation magnitude. A 110 threshold is found to be more suitable (based on mean profile from Figure 29c). The new QC parameters are shown in Table 1, and the zonal velocities are shown before and after QC in Figure 30a,b. Some of the higher velocities are retained in surface bins, but also between bins 60 to 90 from August to November 2012, where strong roll variations have been observed.

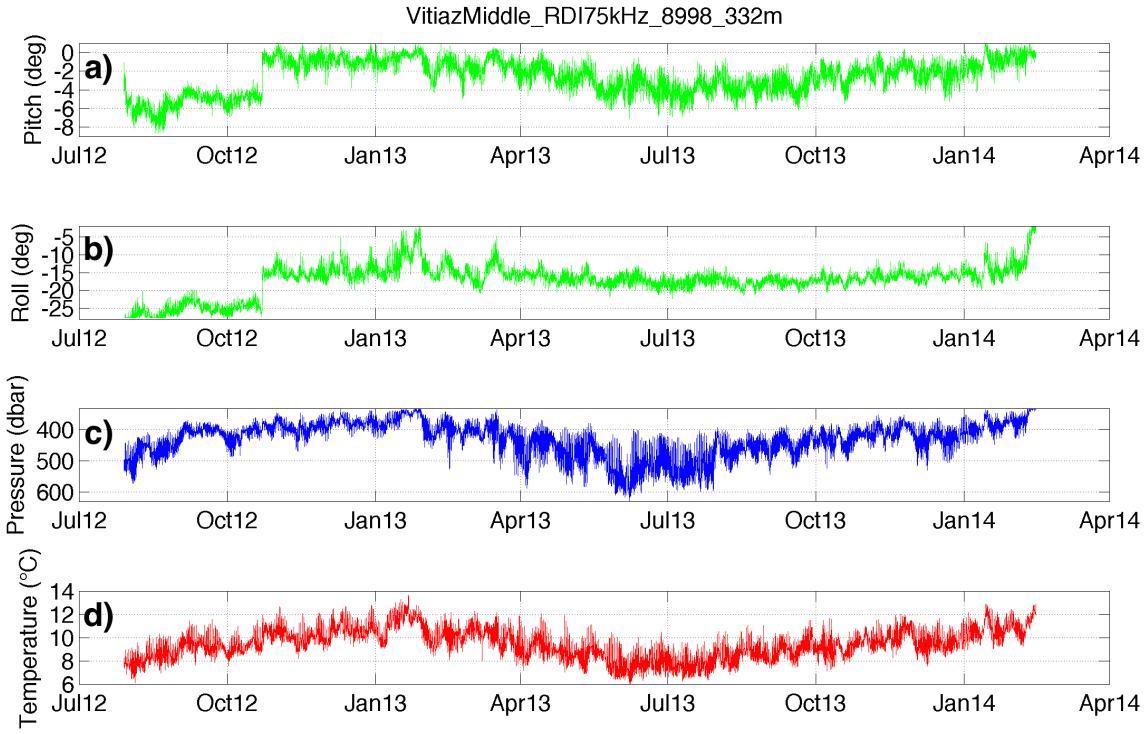

Figure 28 – Vitiaz Strait Middle RDI 75 kHz (upward) raw data of (a) pitch; (b) roll; (c) pressure and (d) temperature timeseries.

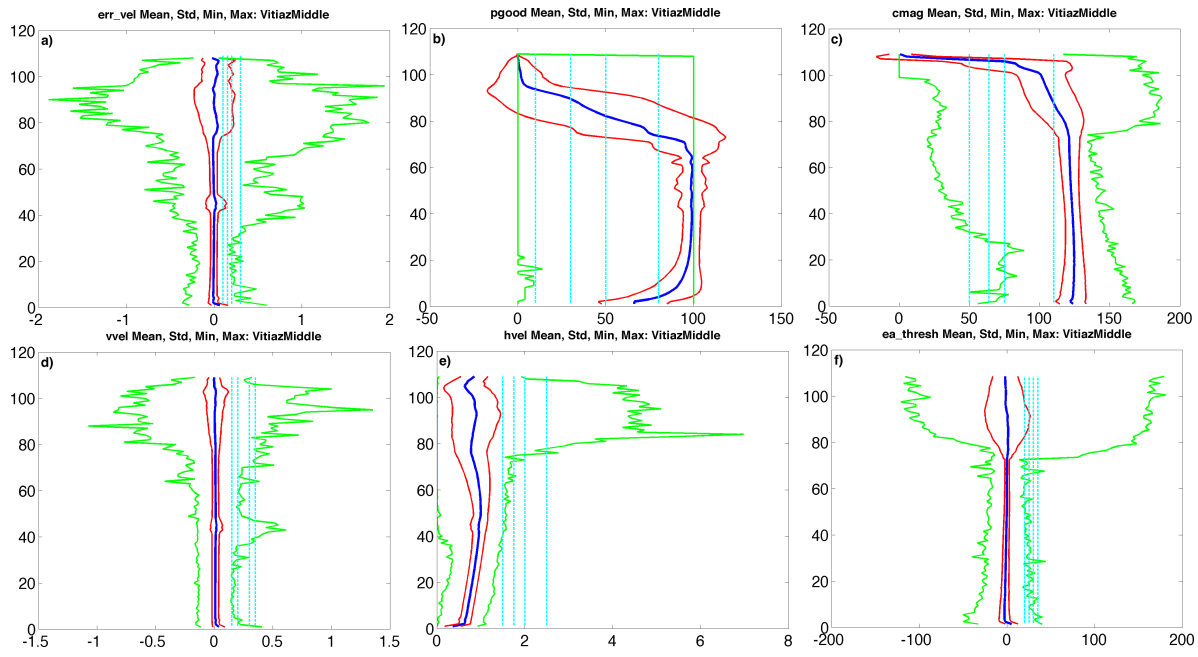

Figure 29 – Mean (thick blue line), standard deviation (red lines) and minimum and maximum (green lines) of the (a) error velocity ($m.s^{-1}$); (b) percent good; (c) correlation magnitude; (d) vertical velocity ($m.s^{-1}$); (e) horizontal velocity ($m.s^{-1}$) and (f) echo amplitude (counts) for the Vitiaz Strait Middle upward RDI 75 kHz ADCP versus bin. The four threshold values used in each QC test are marked by cyan lines in panels (a) to (f).

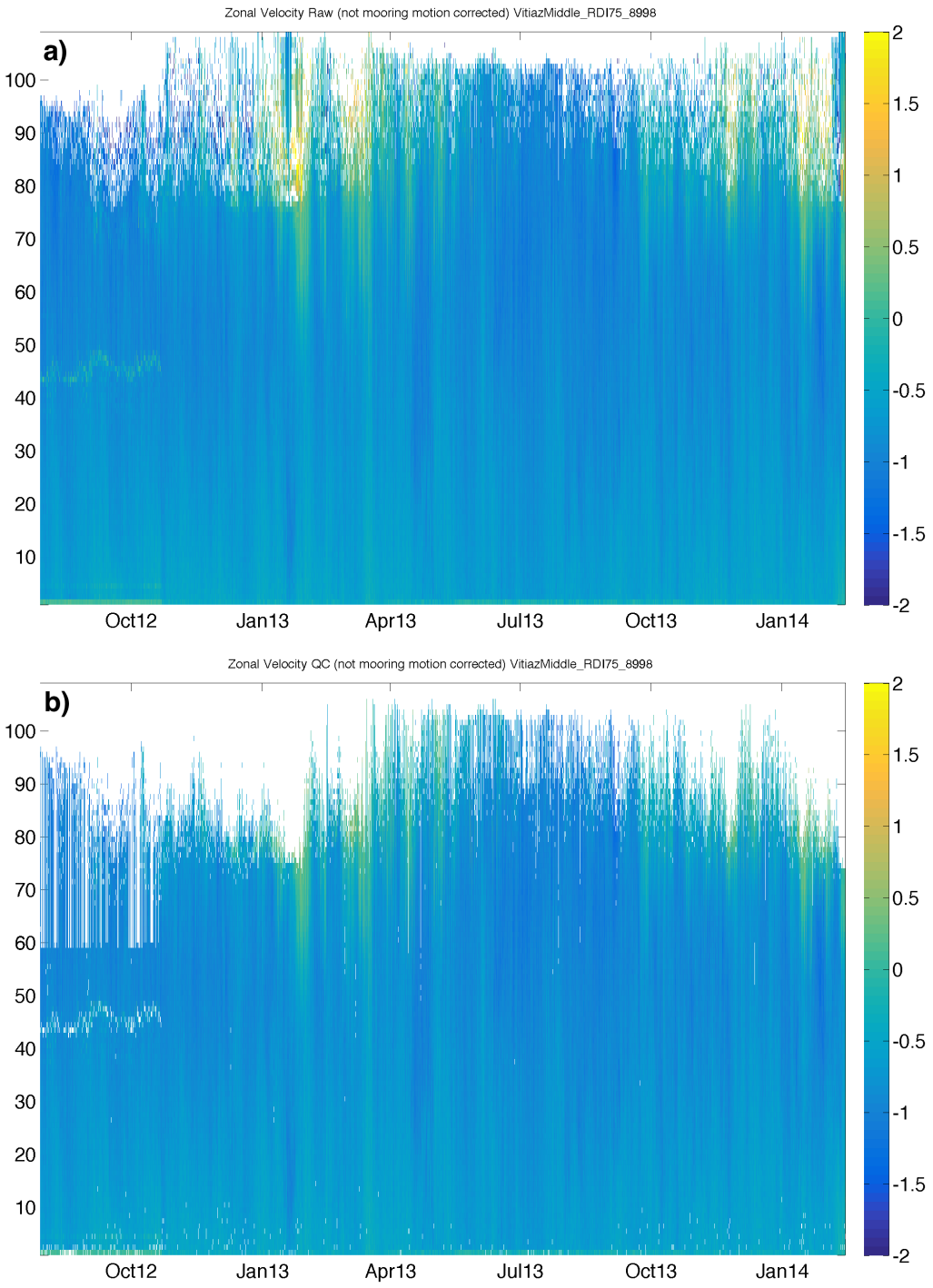

Figure 30 – Comparisons of zonal velocity ($m.s^{-1}$) in Vitiaz Strait Middle, (a) raw zonal velocity and (b) QC zonal velocity of the upward RDI 75 kHz ADCP.

3.12 Case 12: Vitiaz Strait Middle (downward RDI 75 kHz)

- Instrument type: RDI 75 kHz
- Instrument target depth: 334 m
- Instrument Serial Number: 16811
- Instrument vertical bin size: 20 m
- Instrument Deployment Date/Time (UTC): 07/28/2012 13:06
- Instrument Recovery Date/Time (UTC): 03/15/2014 02:15

The downward RDI 75 kHz in Vitiaz Strait Middle are 35 bins for 14408 time realizations. Pitch and roll variations (Figure 31a,b) are lower than 10 and 30 degrees, respectively. Strong roll is also observed during August-November 2012, and data might warrant further investigation. Vertical variations in pressure can reach 200 dbar (Figure 31d), and temperature variations are lower than 10°C (Figure 31c). The average, standard deviation, and range values for the different parameters used in each QC test are shown in Figure 32.

The EA test exhibits an EAfail of 47-94% in upper bins 31-35 for the different thresholds. EAfail can vary from 33-52% in bins 25-31, but EAfail is again, relatively insensitive to the choice of threshold values. Percent good contribution to OTfails stays at 100% in all bins for each threshold value. The correlation magnitude is only responsible for 100% of OTfails in most upper bins, for thresholds of 50, 64 and 75. However, OTfails occur in nearly 100% cases in all bins for a threshold of 110.

The error velocity results mostly in percent failures in bins 25-31 ranging from 3% to 38% (for a 0.15 threshold) and 2-28% (for a 0.2 threshold). The vertical velocity and horizontal tests are responsible for ∼1% of OTfails in all bins, and are insensitive to the choice of threshold values.

We found appropriate to use similar QC criteria than those previously used for the upward RDI 75 kHz in Vitiaz Strait Middle (Table 1). Zonal velocities before and after QC are shown in Figure 33a,b. The differences occur in most upper bins 30-35, where the revised thresholds retain more cells. Between August-November 2012, zonal and meridional velocities are lower than 50 $cm.s^{-1}$ in most upper bins, similar to those observed at time where roll variations are higher than 20 degrees.

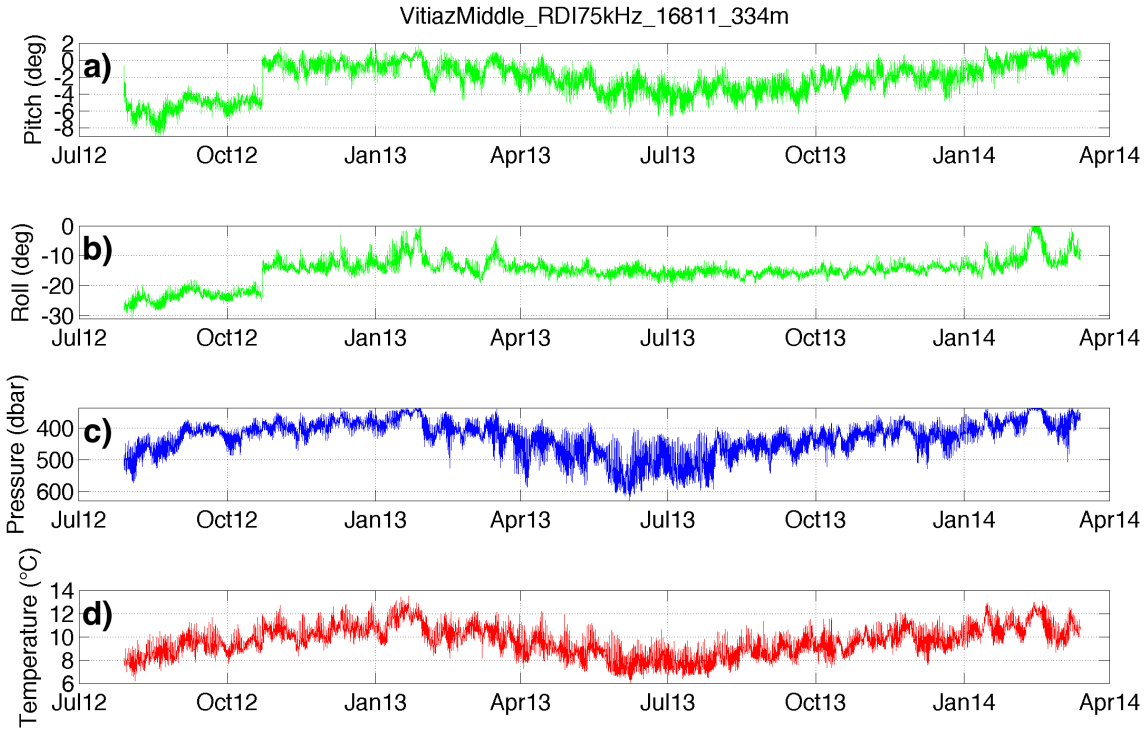

Figure 31 – Vitiaz Strait Middle RDI 75 kHz (downward) raw data of (a) pitch; (b) roll; (c) pressure and (d) temperature timeseries.

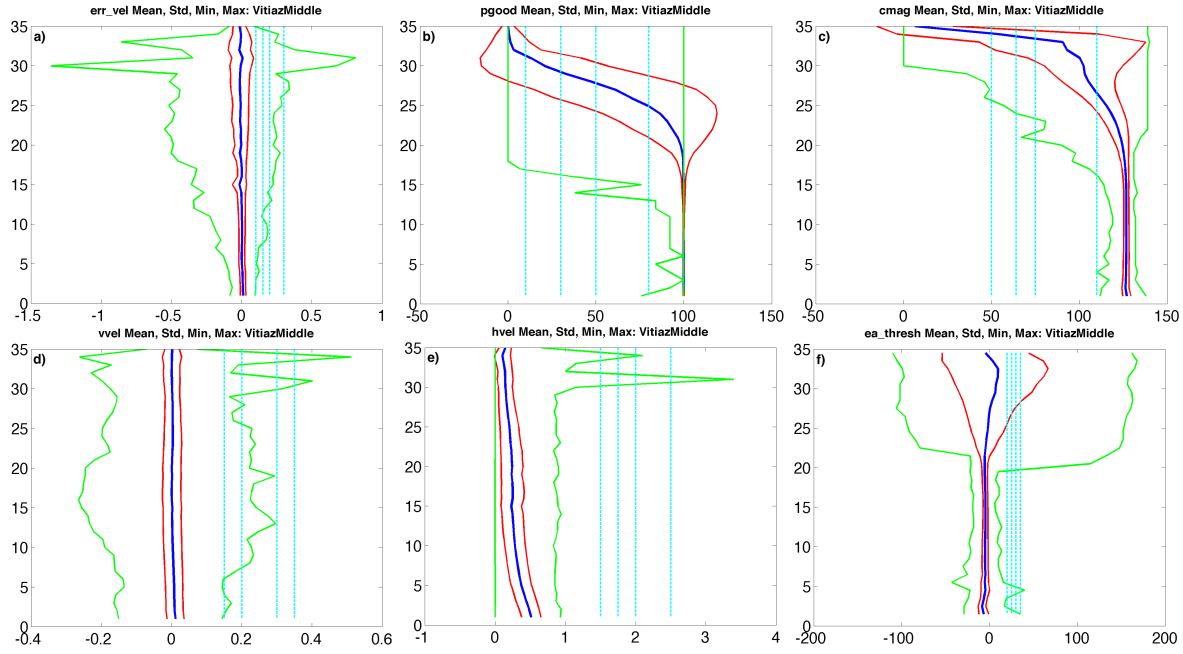

Figure 32 – Mean (thick blue line), standard deviation (red lines) and minimum and maximum (green lines) of the (a) error velocity ($m.s^{-1}$); (b) percent good; (c) correlation magnitude; (d) vertical velocity ($m.s^{-1}$); (e) horizontal velocity ($m.s^{-1}$) and (f) echo amplitude (counts) for the Vitiaz Strait Middle downward RDI 75 kHz ADCP versus bin. The four threshold values used in each QC test are marked by cyan lines in panels (a) to (f).

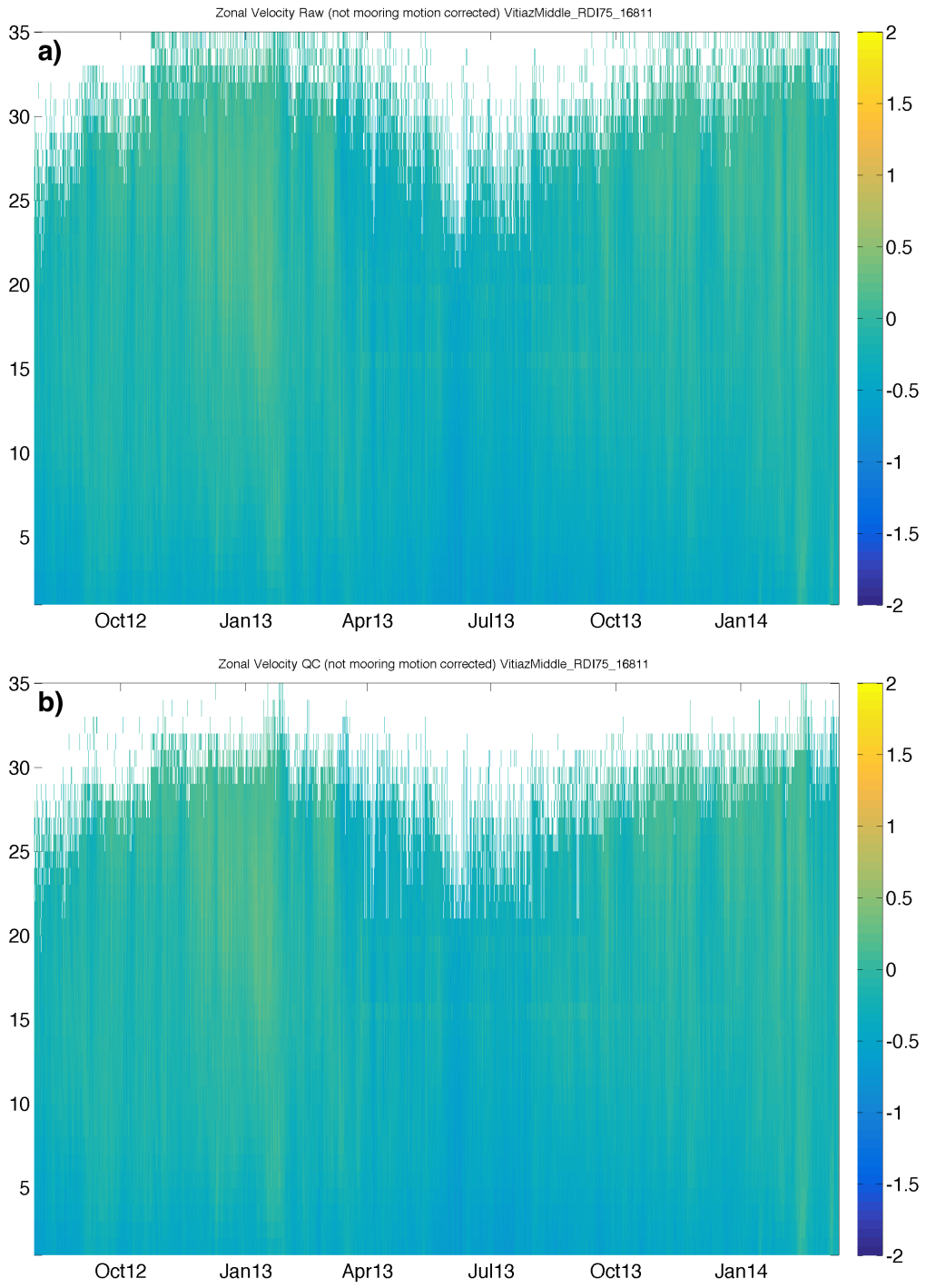

Figure 33 – Comparisons of zonal velocity ($m.s^{-1}$) in Vitiaz Strait Middle, (a) raw zonal velocity and (b) QC zonal velocity of the downward RDI 75 kHz ADCP.

4 Conclusions

The moored ADCPs were deployed between the two SPICE cruises, Pandora (July-August 2012) and MoorSPICE (March 2014), were quality controlled using six tests associated with specific thresholds. Similar set of thresholds than during INSTANT were found to be appropriate in the Solomon Sea straits, except at Vitiaz Strait Middle for the correlation magnitude test (see Table 1). These new QC parameters retain spurious velocities in both velocity fields, especially those due to surface reflection in the surface bins.

References

Cowley, R., Heaney, B., Wijffels, S., Pender, L., Sprintall, J., Kawamoto, S., and Molcard, R. (2008). Instant sunda data report: Description and quality control.

Crout, R., Conlee, D., Gilhousen, D., Bouchard, R., Garcia, M., Demarco, F., Livingston, M., Cooper, C., and Raye, R. (2006). Real-time oil platform ocean current data in the gulf of mexico: An ioos industry partnership success story. In *22nd International Conference on Interactive Information Processing Systems for Meteorology, Oceanography, and Hydrology.*

Ganachaud, A., Cravatte, S., Melet, A., Schiller, A., Holbrook, N. J., Sloyan, B. M., Widlansky, M. J., Bowen, M., Verron, J., Wiles, P., Ridgway, K., Sutton, P., Sprintall, J., Steinberg, C., Brassington, G., Cai, W., Davis, R., Gasparin, F., Gourdeau, L., Hasegawa, T., Kessler, W., Maes, C., Takahashi, K., Richards, K. J., and Send, U. (2014). The Southwest Pacific Ocean circulation and climate experiment (SPICE). *Journal of Geophysical Research: Oceans*, 119(11):7660–7686.

Appendix F

Article submitted to Elementa: Two oceanographic cruises explore the Solomon Sea circulation, chemistry, geochemistry and biology

In this appendix, the article presenting the general context and key results of the Pandora and MoorSPICE cruises is shown. This article benefited from significant improvements after the redaction of this thesis, and was resubmitted in early 2017. For convenient purposes, supplemental material is not shown.

Two oceanographic cruises explore the Solomon Sea: circulation, chemistry, geochemistry and biology

A. Ganachaud[1*], Cravatte Sophie[1,2], Sprintall Janet[3], Germineaud Cyril[1], Alberty Marion[3], Jeandel Catherine[1], Eldin Gerard[1], Metzl Nicolas[5], Bonnet Sophie[4], Benavides Mar[4], Heimburger Lars-Eric[4], Lefèvre Jérôme[2], Michael Susanna[6], Resing Joseph[6], Quéroué Fabien[7], Sarthou Géraldine[7], Rodier Martine[8], Berthelot Hugo[9], Baurand François[10], Grelet Jacques[10], Hasegawa Takuya[11], Kessler, William[12], Kilepak Moyep[13], Lacan François[1], Privat Emilien[1], Send Uwe[3], Van Beek, Pieter[1], Souhaut Marc[1], Jeroen E. Sonke[14]

[1]LEGOS, UMR5566, University of Toulouse, IRD, CNRS, UPS, CNES, Toulouse, France

[2]IRD, LEGOS, UMR5566, IRD, CNRS, UPS, CNES, Nouméa, New Caledonia

[3]Scripps Institution of Oceanography, La Jolla, CA, USA

[4]Mediterranean Institute of Oceanography (MIO), Aix Marseille Université, CNRS/INSU, Université de Toulon, IRD, UM 110, Noumea, New Caledonia

[5]Sorbonne Universités (UPMC, Univ Paris 06) CNRS-IRD-MNHN, LOCEAN/IPSL, Paris, France

[6]Joint Institute for the Study of the Atmosphere and Ocean (JISAO) and Pacific Marine Environmental Laboratory (PMEL), Seattle, WA

[7]Laboratoire des Sciences de l'Environnement Marin, UMR CNRS-IRD-UBO-IFREMER 6539/LEMAR/IUEM, Technopole Brest Iroise, Place Nicolas Copernic, Plouzané, France

[8]Ecosystèmes Insulaires Océaniens, UMR IRD-Université de la Polynésie Française-Institut Malarmé-Ifremer, Centre IRD de Tahiti, French Polynesia

[9]Mediterranean Institute of Oceanography (MIO), Aix Marseille Université, CNRS/INSU, Université de Toulon, IRD, UM 110, Marseille, France

[10]US-IMAGO, IRD, Centre IFREMER, Plouzané, France

[11]Japan Agency for Marine-Earth Science and Technology, Yokosuka, Japan

[12]Pacific Marine Environmental Laboratory, National Oceanic and Atmospheric Administration, Seattle, WA, USA

[13]University of Papua New Guinea, Port Moresby, PNG

[14]GET, UMR5563, University of Toulouse, IRD, CNRS, UPS, CNES, Toulouse, France

[*]Alexandre.Ganachaud@legos.obs-mip.fr

Abstract

The semi-enclosed Solomon Sea in the southwestern tropical Pacific is on the pathway of a major oceanic circuit connecting the subtropics to the equator via energetic western boundary currents. Waters transiting through this area replenish the Pacific Warm Pool and ultimately feed the equatorial current system, in particular the equatorial undercurrent. In addition to dynamical transformations, water masses undergo nutrient and micronutrient enrichment when coming in contact with the coasts, impacting the productivity of the downstream equatorial region. Broadscale observing systems are not well suited for describing the fine-scale currents and water masses properties in the Solomon Sea, leaving it relatively unexplored. Two multidisciplinary oceanographic cruises were conducted in the Solomon Sea region, the first in July-August 2012, and the second in March 2014, by investigators from France and United States. The experimental approach combined physical, chemical, geochemical and biogeochemical analyses, providing access to a wide range of space and time scales of the circulation. This collection of data allow describing the fine-scale structure of the currents and the water properties, transformations and mixing from the surface to the sill depth in the Solomon Sea and in the straits connecting it to the equator. Ocean-margins exchanges were documented through a comprehensive sampling of Trace Elements and Isotopes as efficient tracers of natural fertilization processes. As air chemistry is largely impacted by the regional volcanic plumes, rainwater pH was also sampled. Dinitrogen fixation rates were measured and found to be among the highest in the global ocean, highlighting this region as a hot spot of nitrogen fixation. This study provides an overview of the climatic context during both cruises, of the physical circulation and water masses properties. It provides a comprehensive description of all measurements made onboard, and presents preliminary results, aiming to serve as a reference for further physical, geochemical and biogeochemical studies.

Introduction

The Solomon Sea is a semi-enclosed sea located at the western boundary of the equatorial Southwest Pacific Ocean, between Papua New Guinea and the Solomon Islands (Figure 2). Suspecting the importance of the Solomon Sea circulation to the general Pacific circulation, Lindstrom et al. (1987) made two surveys in 1985 and 1986 that revealed large and vigorous transports toward the equator. This region appeared as an essential pathway for waters originating from mid-to high latitudes and joining the western equatorial Pacific and the equatorial current system. Water properties indicated that the Solomon Sea was in particular the major source of the Equatorial Undercurrent (Tsuchiya et al., 1989), and thereby of the downstream surface waters of the cold tongue in the eastern equatorial Pacific. Since then, the area had essentially only been surveyed by underway shipboard current profilers during research vessel transits or geophysical cruises (Cravatte et al., 2011).

Recently, the CLIVAR Southwest Pacific Ocean Circulation and Climate Experiment (SPICE) pinpointed the region as a key passageway for the low-latitude western boundary currents, and so providing important components for the oceanic and climatic variability of the equatorial Pacific at interannual and decadal time scales (Ganachaud et al., 2014). Water masses mixing, and geochemical and biogeochemical enrichments in the Solomon Sea may indeed impact the downstream surface waters and the productivity of the equatorial cold tongue.

The oceanic conditions in the Solomon Sea are distinctive in several ways. First, strong currents interacting with numerous islands and straits impact water properties (Melet et al., 2011). Then, water masses coming in contact with the coasts undergo not only dynamical transformations but also macro- and micro-nutrients and trace element enrichments through land/sea exchange, or *boundary exchange* (Grenier et al., 2011), including river discharge, shelf inputs and submarine groundwater discharges. Trace elements and their isotopes that are injected from *boundary exchange* provide information on transformation and fate of particles and on water masses as well as mixing. Quantifying these *boundary exchanges* (BE) is a priority of the international GEOTRACES program (e.g. Grenier et al., 2014).

In the context of the SPICE program, two major multidisciplinary cruises were organized inside the Solomon Sea: the Pandora cruise in July-August 2012, and the MoorSPICE cruise in March 2014. Pandora documented the physics, geochemistry, biology and chemistry of the area (Figures 1a; 1b) for full cruise track from New Caledonia. MoorSPICE partly repeated the hydrographic measurements, then explored the Bismarck Sea to the North (Figures 1; 1b). The main objectives of these two cruises were 1) to document the circulation, mixing, and to understand possible water mass transformations and pathways through the Solomon Sea, and 2) to document the chemistry, geochemistry in the area, and the enrichment of the waters. In addition, it has been recently shown that the Solomon Sea is a place of large, and essentially undocumented nitrogen fixation: these cruises were an opportunity to better document N_2 fixation. They also allowed the first evaluation of both anthropogenic carbon and ocean acidification in the region.

The objectives of this paper are to present the general context of these cruises, to provide an initial overview for subsequent more detailed analyses by physical oceanographers, geochemists and biologists. The scientific rationale for these cruises, and the measurements made are presented. The climatic context is provided, and a presentation of key results inferred from observations made during these cruises are also summarized.

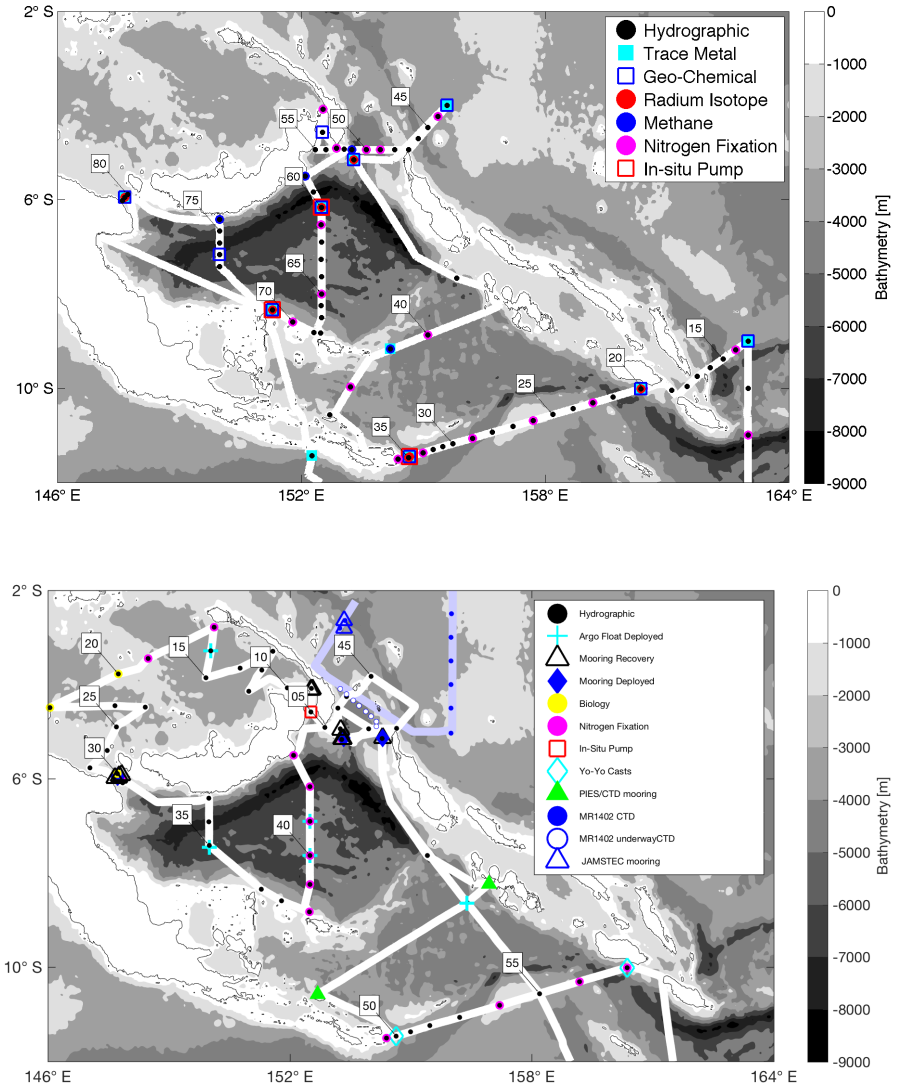

Figure 1: Hydrographic cruises (a) Pandora, June-August 2012, R/V L'Atalante, French Oceanographic Fleet and (b) MoorSPICE, February-March 2014 R/V Thompson, USA. Both cruises departed and arrived in New Caledonia. Each station / cast had specific protocols and characteristics, as indicated in the legends. For clarity, mooring position are reported only on panel b). Station numbers are indicated every 5th station.

Background

Circulation and water characteristics

Recent targeted efforts in the context of the SPICE program have helped to understand aspects of the mean oceanic circulation within the Solomon Sea from a diverse source of observations (vessel mounted current profiler compilations, gliders, drifters and hydrological data) and modeling studies (Ganachaud et al., 2014). All previous works agree on the following mean circulation pattern: the bulk of thermocline transport into the Solomon Sea enters through the southern opening of the Solomon Sea where the Gulf of Papua Current joins the North Vanuatu Jet (NVJ) in forming the low latitude western boundary current called the New Guinea Coastal Undercurrent (NGCU) (Figure 2); (e.g., Melet et al., 2010; Gasparin et al., 2012; Kessler and Cravatte, 2013). The NGCU travels equatorward, splitting around Woodlark Island then rejoins before it bifurcates just south of New Britain. The westward branch exits the Solomon Sea through Vitiaz Strait while the eastward branch travels along the coast of New Britain as the New Britain Coastal Undercurrent (NBCU) (Cravatte et al., 2011). The majority of the NBCU exits through Solomon Strait and the remainder passes through St. Georges Channel. In the near surface, the mean circulation is slightly different, with water entering the Solomon Sea through Solomon Strait and exiting southward through the southern entrance (Melet et al., 2010; Hristova and Kessler, 2012). Surface velocities can also be weaker than subsurface, with strong seasonal variations (Cravatte et al., 2011). At deeper levels, the circulation in the Solomon Sea and straits is quasi unknown.

Mean total transport through the Solomon Sea is estimated to be ~ 30 Sv above 1300 m (Gasparin et al., 2012). The strength of the currents varies on a seasonal timescales with the strongest equatorward flows from June to September during the southeasterly monsoon (Cravatte et al., 2011; Hristova and Kessler, 2012). Currents also vary on El Niño Southern Oscillation (ENSO) timescale in the upper 250 m, with transports increasing during El Niño events and decreasing-or even reversing- during La Nina events (Davis et al., 2012; Melet et al., 2013). Additionally, surface and subsurface mesoscale eddies and submesoscale features dominate instantaneous current fields (Djath et al., 2014; Hristova et al., 2014; Gourdeau et al., 2014).

Water masses, currents, their variation and the partition of their transports between the different straits have therefore been inferred from numerical simulations and scattered measurements mainly confined to the upper 300 m. However, we have not as yet had simultaneous measurements of physics and geochemistry, and our understanding of the internal and deep Solomon Sea is extremely limited by the lack of measurements.

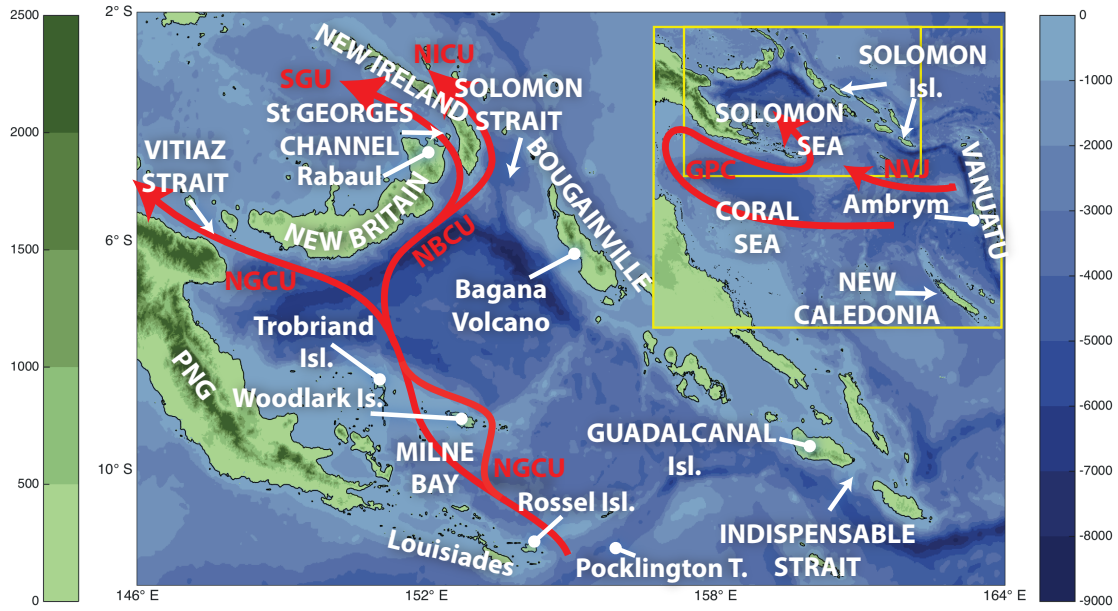

Figure 2: Solomon Sea topography and bathymetry, main islands and points of interest (white text) and large average oceanic currents (red text). (Inset): Southwest Pacific topography. Currents are as follows: NGCU (New Guinea Coastal Undercurrent); NBCU (New Britain Coastal Undercurrent); SGU (St Georges Channel Undercurrent); NICU (New Ireland Coastal Undercurrent); GPC (Gulf of Papua Current); NVJ (North Vanuatu Jet). PNG stands for Papua New Guinea.

N_2 fixation and primary production

The Solomon Sea is an interesting site for its specific biology and chemistry, in particular, atmospheric dinitrogen (N_2) fixation. N_2 fixation is the process by which N_2 is reduced to ammonia by specialized microbes termed diazotrophs. This process is the major external source of nitrogen for the ocean, even more important than riverine and atmospheric inputs (Gruber, 2004). N_2 fixation thus provides nitrogenous nutrients for phytoplankton communities and contributes to carbon dioxide (CO_2) uptake and climate regulation (Karl et al., 2002). The South Pacific Ocean has been ranked as the second major basin contributing to global N_2 fixation after the Indian Ocean (Luo et al., 2012), although the number of studies performed in the South Pacific is much less numerous than those performed for example in the Indian (Luo et al., 2012), in the North Atlantic (Benavides and Voss, 2015) and the North Pacific Oceans (Dore et al., 2002; Karl et al., 1997).

The tropical Pacific is characterized by a strong zonal gradient in nutrient distribution, with the eastern basin affected by the cold equatorial tongue where nutrient availability is higher but trace metals limit primary production (Aufdenkampe et al., 2002; Le Bouteiller, 2003), and the western basin dominated by a warm pool where metals are available through land runoff, hydrothermalism, and volcanic activity (Labatut et al., 2014). In the western Pacific, the permanent water column stratification inhibits nutrient upwelling (Pena et al., 1994) and N_2 fixation appears as the main source of nitrogenous nutrients for primary production (Yoshikawa et al., 2005; Bonnet et al., 2009). This zonal pattern is also reflected in N_2 fixation activity and in the diversity of diazotrophs, with low N_2 fixation rates in the eastern side of the South Pacific (Raimbault and Garcia, 2008) dominated by heterotrophic diazotrophs (Bonnet et al., 2008; Halm et al., 2012), and potentially high rates provided by autotrophic diazotrophs on the western side (Bonnet et al., 2009; Moisander et al., 2010). However, very few studies have quantified N_2 fixation in the Southwest Pacific, in particular in the Solomon Sea, which presents ideal temperature conditions for diazotrophs to bloom extensively.

Trace elements and sulfure

Numerous processes that could affect water properties are occurring at the land-ocean interface and within the water column. These include advective, diffusive and turbulent transports, biological uptake, remineralization, river runoff, dissolution of lithogenic minerals and precipitation of authigenic ones (i.e. precipitated locally within the water column), and adsorption on particles followed by scavenging or desorption from particles followed by the release of the chemical species. Understanding the sources of these trace elements is fundamental for their integration in any model coupling circulation and biogeochemistry. Chemical elements and isotopes identified that help to constrain the nature and rate of these processes are considered as “oceanic tracers” and part of the GEOTRACES core

parameters (GEOTRACES science plan, online at http://www.geotraces.org). The Coral and Solomon Seas are of particular interest to provide indications of these processes, because of their energetic dynamics, where boundary exchange is suspected to be of importance (Grenier et al., 2013; Lacan and Jeandel, 2005; Jeandel and Oelkers, 2015).

The surface deposition from volcanic plumes is also a potential source of various species. Papua New Guinea (PNG), the Solomon Islands and Vanuatu form the Melanesian volcanic arc with large emitters of volcanic species and sulfate precursors (Bani et al., 2012; McCormick et al., 2012). Air chemistry of the marine boundary layer and free troposphere of the Solomon Sea is largely impacted by volcanic plumes from PNG volcanoes (i.e. Rabaul and Bagana, located in New Britain and Bougainville Islands respectively, Figure 2) but also from remote volcanic plumes. The Vanuatu Ambrym volcano is ranked as one of the top emitters, producing between 8% and 17% of global volcanic fluxes of SO_2, HCl, HF, HBr, Hg and ^{210}Po (Allard et al., 2015).

Data sets on cloud chemistry and pH in wet deposition are very limited in the region. Nagamoto et al. (1990) provided the first survey of cloud chemistry across the Western Pacific and recorded rainwater pH values in the range 5 to 6 in the equatorial and remote island region north of Solomon Islands. They suggested a role of the biogenic source (dimethyl sulfide) in rain composition. But over Vanuatu, Vetch and Haefeli (1997) measured a pH of 2 in rainwater 4 km away from Ambrym's crater (Figure 2). Lefevre et al. (2015) showed that Ambrym is the main source of sulfur species in the Coral and Solomon Seas, with a similar contribution to the regional sulfur budget as dimethyl sulfide (DMS) emitted from marine organisms.

The Methylmercury (MeHg) cycle is also unclear; in particular we do not know whether MeHg is primarily produced in marine sediments and subsequently advected into the open ocean or whether it is produced *in situ* in the oceanic water column, during the remineralization of sinking organic matter (Fitzgerald et al., 2007; Mason et al., 2012).

Carbon cycle

The global ocean absorbs about 30% of the annually-emitted anthropogenic carbon (Le Quéré et al., 2015) slowing the rapid accumulation of CO_2 in the atmosphere that has recently reached 400 ppm (Global CO_2 mean in March 2015). But the ocean carbon uptake leads to a decrease in pH, the so-called "other" CO_2 problem of ocean acidification, that will have a harmful impact on marine organisms and ecosystems. Since pre-industrial times, the mean pH in the surface ocean has dropped by about 0.1 units. In order to follow both the anthropogenic CO_2 penetration in the ocean and acidification changes, observations are needed to be regularly conducted in open oceans, marginal seas and coastal zones. Very few observations of the inorganic carbon system have been previously conducted in the Coral and Solomon Seas (Suzuki et al., 2013; Lauvset et al., 2016; Olsen et al., 2016).

It is thus interesting to explore the CO_2 system in this area (also referred as south-eastern part of the Coral Triangle), including the anthropogenic CO_2 penetration and associated ocean acidification and compare our new observations with previous analysis conducted in open ocean tropical and subtropical zones (e.g. Alvarez et al., 2009). Interestingly, this region, part of the so-called North Australia region in MARCATS (MARgins and CATchments Segmentation) presents large uncertainty in air-sea CO_2 fluxes estimates depending on data-based method (CO_2 source) or ocean biogeochemical models (CO_2 sink) (Bourgeois et al., 2016). A recent study using data-based reconstruction (Lenton et al., 2016) also suggests low pH in this region ($8.03-8.05$) and authors also concluded that at present the Coral Sea is not experiencing marginal conditions with respect to ocean acidification (values of the aragonite saturation state < 3.5).

Data and Methods

Most data analyzed in this paper originate from the two research cruises: Pandora carried out aboard the French research vessel *L'Atalante* (also recorded as GEOTRACES cruise GP12), and the MoorSPICE cruise aboard US research vessel *Thomas G. Thompson*. As part of the Tropical Ocean Climate Study (TOCS) project, a cruise took place aboard the R/V Mirai (MR14-02) in February 2014, around the New Ireland (Figure 1b). This cruise was conducted by the Japan Agency for Marine-Earth Science and Technology (JAMSTEC) in order to explore the oceanic leakage between the Solomon Sea and the western equatorial Pacific through the NICU pathways (Figure 1b). Data acquired during this cruise are not discussed here.

Pandora Cruise, June-August 2012

The R/V L'Atalante departed Nouméa, New Caledonia, on 28 June 2012, and returned to port on 6 August (Figure 1a; see Figure S1a for a larger-scale map). Scientific equipment included two SBE-911+ CTD/Rosette systems. The primary, *standard*, rosette was used at all stations outfitted with duplicated temperature-conductivity-oxygen SBE sensors, a Chelsea Aqua3 fluorometer, a Wetlab C-star transmissometer and a pair of RDI built Lowered-Acoustic Doppler Current Profilers (L-ADCP) attached to the CTD frame (150kHz and 300kHz, down- and up-looking, respectively) to measure currents along the rosette profile. The rosette was fitted with 22×12L Niskin bottles to obtain water samples for the standard parameters (see below).

The secondary, *clean*, rosette was designed for obtaining uncontaminated samples for trace metals, with a titanium CTD body and epoxy coated frame and included one set of SBE temperature-conductivity-oxygen sensors, a Wetlab Westar fluorometer and 12L Go-Flo bottles. A set of 7 Maclane or Challenger *In Situ Pumps* for sampling of particulate matter was deployed at 5 stations on a hydrography wire. Underway continuous recordings are summarized in Table S1 as well as specific discrete sampling.

The Pandora cruise track included a meridional section along 163°E, from 18°S and to 9°S to sample incoming waters from the SEC (Figure 1a) followed by a section across the southern entrance of the Solomon Sea that closely followed a 2007 cruise track (Gasparin et al., 2012). Three more sections across the Solomon Sea were conducted to follow the paths and transformations of water masses (Figure 1a). Other sections included one on the eastern side of the Solomon Islands, and two across Solomon and Vitiaz Straits. Details of the parameters sampled during stations are given in Table S2. Along the cruise track, eleven long duration stations with repeated casts (3-39h, Table S2, last row) allowed the necessary large volume water samplings required for geochemistry analyses. Moreover, the repeated CTD casts during these stations provided additional information on the high frequency variability of properties and currents. Overall, measurements were made at 83 stations, for a total of 170 casts, including 30 clean sample casts, and 6 *In Situ Pumps* deployments (Figure 1a).

A total of 9 moorings were deployed over the northern exit channels of Vitiaz and Solomon straits, and in St Georges Channel from 2012 to March 2014 (MoorSPICE cruise), and two CTD moorings on either side of the southern mouth of the Solomon Sea since 2012. These later two moorings were combined with bottom Pressure Inverted Echosounders (PIES) to capture the geostrophic transport between these two endpoint moorings. They will remain deployed (with some intermediate servicing) until summer 2017, and are part of a boundary current transport monitoring system measuring the inflow into the Solomon Sea using gliders (Davis et al., 2012).

MoorSPICE Cruise, February-March 2014

The MoorSPICE cruise aboard the R/V Thomas G. Thompson was carried out from 28 February 2014 to 31 March 2014. Scientific equipment included a dual set of temperature-conductivity-oxygen SBE-911+ CTD, a Wetlab ECO fluorometer, a Wetlab C-star transmissometer and a pair of RDI L-ADCPs attached to the CTD frame (300 kHz down- and up-looking). The rosette was fitted with 24 12-L Niskin bottles.

The ship directly sailed from Nouméa to the Solomon Strait and St Georges Channel to recover the moorings previously deployed during the Pandora cruise; and a number of CTD stations were reoccupied. A saw-tooth pattern across the Bismarck Sea was then performed, in an area with poor in-situ data coverage. The cruise continued through Vitiaz

Strait, where mooring work was done. Then the track closely followed that of Pandora across the northern section of the Solomon Sea (in a reversed pattern). At the entrance to the Solomon Sea, most of the Pandora stations were reoccupied. Upon reaching Guadalcanal the ship sailed back to Nouméa. Overall, 57 stations were surveyed, some of them repeated, for a total of 78 casts (Figure 1b). Details of underway and on-station sampled parameters are given in Tables S1 to S3 (Section *Supplemental Material*). There were 6 Argo deployments and 9 moorings were recovered that were deployed during Pandora with 4 additional moorings re-deployed.

Physical parameters

For both cruises, data processing followed the GO-SHIP guidelines (online at http://www.go-ship.org/HydroMan.html). Temperature and conductivity sensors were calibrated by the manufacturer soon after the cruises. Calibration parameters were applied after checking agreement with salinity bottle samples. Every CTD cast was checked for spikes that might be due to particulate matter in the sensor circuits or electrical problems, and flagged accordingly. Dissolved oxygen sensor data were adjusted by comparison with a Winkler titration determination of water samples (Langdon, 2010; Uchida et al., 2010; Saout-Grit et al., 2015).

Shipboard ADCP velocity data were processed and calibrated using the CODAS software (online at http://currents.soest.hawaii.edu). LADCP velocity data was processed using the GEOMAR/LDEO software v10.8 (Visbeck, 2002). Continuous surface temperature and salinity as well as basic meteorological data were recorded by both ships using the underway thermosalinograph and meteorological systems, respectively.

Moorings

During the July 2012 cruise, nine moorings were deployed in Vitiaz and Solomon straits, and St Georges Channel (Figure 1b). Moorings in the straits were recovered and four of them were redeployed in Vitiaz Strait and Solomon Strait during the March 2014 cruise, and recovered in August 2015. They provided continuous measurements of near full-depth temperature, salinity and velocity. Two subsurface ADCP moorings were also deployed off the eastern coast of New Ireland Island in August 2012 during TOCS MR12-03 cruise. Then they were recovered in February 2014 during TOCS MR14-02 cruise. They provided continuous current velocity data from near surface to subsurface. Two moorings were also deployed on either side of the southern entrance of the Solomon Sea in 2012 (Figure 1b). Those were part of a boundary current heat transport monitoring system also using gliders and Pressure Inverted EchoSounders (PIES) (Davis et al., 2012). This data will be presented in further studies.

Nutrients

Dissolved nutrients (N, P, Si) were sampled and analyzed at high precision following the GO-SHIP guidelines (Hydes et al., 2010) but based on pasteurization (Aminot and Kerouel, 1995; Daniel et al., 2012). Pasteurized samples are analyzed on a SEAL-AA3 automated Segmented Flow Analysis, following (Hydes et al., 2010; Aminot and Kerouel, 2007).

Carbonates

Discrete samples for Total Dissolved Inorganic Carbon (DIC) and Total Alkalinity (TA) were collected (poisoned with $HgCl_2$ after sampling) at selected stations and measured back at LOCEAN laboratory in Paris-France using a potentiometric titration (e.g. Metzl et al., 2010). For calibration, we used Certified Reference Material (CRM, Batch #119) provided by Prof A. Dickson (Scripps Institution of Oceanography, San Diego, USA). The accuracy of DIC and TA are estimated to be $\pm$ 2.6 μmol.kg^{-1} and $\pm$ 2.1 μmol.kg^{-1} respectively. Using DIC/TA pairs, other inorganic carbon properties can be calculated (Pierrot et al., 2011) such as the fugacity of CO_2 (fCO_2), carbonates ions, calcium carbonate solubility (for aragonite and calcite), or pH.

For all derived calculations we used recommended constants K1, K2 from Mehrbach et al. (1973) refit by Dickson and Millero (1987; 1989) and pH is seawater scale.

Acid precipitation

The presence of volcanogenic acidic sulfur was monitored using 30 rainwater samples during Pandora. pH and temperature in rainwater were measured using a rain gauge fixed on the fore deck, which provided a simple and affordable measurement. A glass electrode was used to determine pH values in rain samples immediately after collection (WTW 3110 pHmeter). The pH readings were standardized with commercial buffer solutions.

N_2 fixation, primary production

The abundance of different diazotroph phylotypes was assessed through quantitative polymerase chain reaction (qPCR) counts of the *nifH* gene (encoding for a subunit of the nitrogenase enzyme, responsible for the N_2 fixation activity) as previously described (Church et al., 2005; Moisander et al., 2008). For the purpose of this study, only the main phylotypes are reported (i.e., *Trichodesmium* and the sum of unicellular diazotrophic cyanobacteria, UCYN). N_2 fixation and primary production were measured at four depths (5, 50, 100, 150 m during Pandora, Table S2 and 5, 15, 30, 70 m during MoorSPICE, Table S3) using $^{15}N/^{13}C$ dual isotopic labeling and in situ-simulated 24-h incubation as described in Bonnet et al. (2015); Berthelot et al. (2017).

Trace elements

During Pandora (also GEOTRACES GP12), a comprehensive group of trace element samples and some isotopes (TEIs) were collected and are currently being measured. They are listed in Appendix together with their role as geochemical tracers. Many of those are not available at the time of publication of the present work, except for Al, Mn, Hg speciation and dissolved Fe, which sampling and analytical protocols are briefly presented below, while results are discussed in the following section.

Dissolved iron (dFe) samples were collected using a trace metal clean rosette and Go-Flo bottles with a slight N2 overpressure to force filtration through 0.2 μm filter cartridges (Sartrobran-300, Sartorius). They were acidified to pH 2.0 with ultrapurQR hydrochloric acid (HCl, Merck) and analyzed on board after at least 24h by flow injection with chemiluminescence detection (Sarthou et al., 2007). Samples for total and dissolved aluminum (Al) and manganese (Mn) were collected into 100mL LDPE bottles. Total samples were collected directly into the sample bottle, while dissolved samples were collected after their passage through 0.2μm cellulose acetate Sartobran-300 capsule filters. Samples were acidified to pH < 7 with 12 N Optima HCl at least one week prior to analysis. Al and Mn were determined by flow injection analysis using fluorimetric (Resing and Measures, 1994), and spectrophotometric (Resing and Mottl, 1992) detection respectively. The manganese chemistry was modified by adding 4g of Nitrilo Tri-acetic acid per liter of reaction buffer.

Total Hg (tHg) and methylmercury (MeHg) were measured according to Heimburger et al. (2015). The 9 profiles sampled during the Pandora cruise consisted of 89 unfiltered acidified (HCl 0.4%, v/v) samples.

Climatic context during Pandora and MoorSPICE cruises

The Solomon Sea is a region subject to significant annual variability (influenced by the Australian monsoon), interannual variability (linked to El Nino Southern Oscillation cycles), and intraseasonal variability (linked essentially to Madden-Julian Oscillation events, cyclones and synoptic westerly wind events). The Pandora and MoorSPICE cruises sampled two contrasted seasons, associated with significant changes in winds and precipitation. Pandora took place during the dry strong-trade winds season (June-November), in July-August 2012, and MoorSPICE during the wet weak- trade winds season (December-May), in March 2014. At this time of year, the SPCZ is fully developed over the Solomon Sea and the winds weaken or even reverse direction to become northwesterly.

The Pandora cruise occurred following the 2011 La Niña event and coincided with a return to neutral state, also present during the MoorSPICE cruise (Figure 3). The MoorSPICE cruise followed a series of strong equatorial westerly wind bursts and corresponding downwelling eastward Kelvin waves, associated with the onset of the “aborted 2014 El Niño” (Menkes et al., 2014; McPhaden et al., 2015).

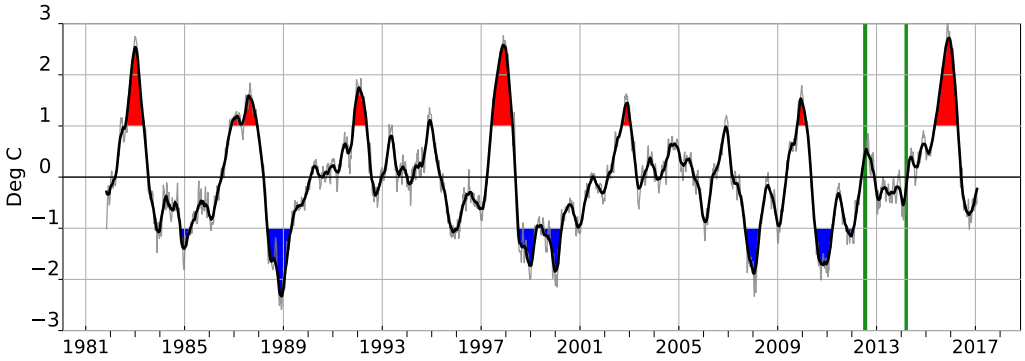

Figure 3: The Niño3.4 SST anomaly index (region bounded by 90°W-150°W and 5°S-5°N) from 1982 through January 2017 (grey line, from http://www.esrl.noaa.gov/psd); overlaid by a 3-month moving average (black line), where red and blue shading indicate El Niños (Niño3.4 anomalies greater than +1) and La Niñas (Niño3.4 anomalies less than -1), respectively. Green lines indicate the dates of the Pandora (July-August 2012) and MoorSPICE (March 2014) cruises.

In general, El Niño periods in the Coral Sea-Solomon Sea region are characterized by stronger south-easterly wind stress anomalies, with clockwise (upwelling) curl north-east of the Solomon Islands where the wind stress anomalies turn westerly (Kessler and Cravatte, 2013).

During Pandora, winds were strongly southeasterly (Figure 4a), July corresponding to the height of the south-east trade season. The warmest Sea Surface Temperature (SST) during Pandora were largely confined equatorward and east of the Solomon Islands, with cooler waters within the Solomon Sea and south toward the winter hemisphere (Figure 4a). In contrast, regional winds were extremely weak during MoorSPICE (Figure 4b), in keeping with the expected change in the seasonal cycle, but also the coinciding transition from a cold phase to a warm phase of ENSO.

During MoorSPICE, SST was largely above 29°C in most of the Solomon Sea. The warmest waters were found in the tropics east of the Solomon Islands, and likely reflected the eastward shift of the western Pacific warm pool in response to westerly wind bursts earlier in the year associated with the El Niño conditions that ultimately failed to materialize (Menkes et al., 2014; McPhaden et al., 2015).

Thus, Solomon Sea SST and winds patterns are tied to the regional scale seasonal cycle are visualized in Figure 4.

On intraseasonal time scales, the air-sea coupling of the western Pacific is influenced by the Madden-Julian Oscillation (MJO), a system of large-scale coupled patterns of atmospheric convection and winds that propagate eastward along the equator (Madden and Julian, 1972). An active MJO is characterized by deep convective anomalies that can block the incoming solar radiation and produce anomalously cool SST. The Wheeler and Hendon (2004) index breaks the MJO cycle into eight phases that correspond to the shifting location of the maximum intraseasonal winds and convection (derived from satellite measurements of Outgoing Longwave Radiation (OLR, $W.m^{-2}$). During Pandora, MJO anomalies based on the Wheeler and Hendon Index suggest an extremely weak active phase of the MJO, while for MoorSPICE, MJO activity was strong in late February, just before the cruise (not shown).

These stable conditions suggest that at least during the time of the cruises, MJO and intraseasonal wind forcing did not likely play a strong role in upper ocean variability or circulation. However, the apparent weak variability during both cruises was fortuitous since four anticyclones migrated south of 10°S during Pandora, nevertheless leaving near stationary conditions over the Solomon Sea. Atmospheric conditions were more unstable during MoorSPICE, promoting the formation of tropical cyclones (TC): weak TC HADI (Category 1 9-11 March south of 10°S) and severe TC LUSI (Category 3, March 9-16, over the north Vanuatu Islands). A third TC (GILLIAN, March 21-26) formed in the Southwest Pacific too, but just outside the Solomon Sea (http://www.bom.gov.au). In the end, none of these TCs directly impacted oceanic conditions in the Solomon Sea during the cruise time of MoorSPICE.

Similar OLR values of around 220-230 $W.m^{-2}$ are found during both Pandora (Figure 4c) and MoorSPICE (Figure 4d). Low OLR (cloudier) is mostly confined north of the equator during Pandora, probably indicating the location of the western Pacific Intertropical Convergence Zone. During MoorSPICE, the minimum in OLR to the east of the Solomon Sea indicates the equatorward axis of the South Pacific Convergence Zone (SPCZ), which is more active during the Southern Hemisphere summer.

The July-August 2012 cruise conditions were therefore mainly representative of the strong-trade wind season, while the March 2014 cruise conditions were representative of the opposite weak-trade wind season. Interannual and intraseasonal variability are not expected to be of major influence.

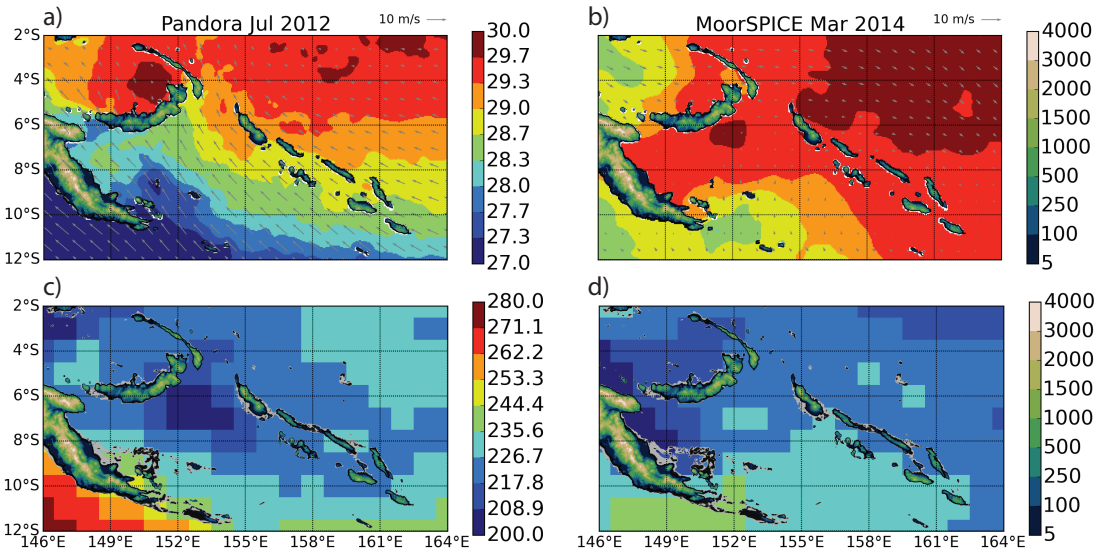

Figure 4: SST (°C) from the Operational Sea Surface Temperature and Sea Ice Analysis °C) overlain by ASCAT wind vectors (m.s^{-1}) averaged over (a) Pandora and (b) MoorSPICE cruise periods. Unit wind vector is found in the upper right. Outgoing Longwave Radiation (OLR from http://www.esrl.noaa.gov/psd (Lee, 2014), W.m^{-2}) also averaged over (c) Pandora and (d) MoorSPICE cruise periods.

Results

Sea surface temperature and salinity

The sea surface conditions during both cruises were assessed using the along-track direct measurements of in situ winds, Sea Surface Salinity (SSS) and SST (Table S1; Figures 5; S3 for complete cruise track). During Pandora, we observed strong ($\sim$ 20 m.s^{-1}) and unidirectional winds oriented equatorward along the prevalent trade wind axis (Figure 5a). During MoorSPICE winds were much weaker ($\sim$ 5 m.s^{-1}) along an identical axis and were poleward to the north of 6°S and equatorward to the south of this latitude (Figure 5b). In situ winds (Figure 5) agree well with the monthly mean satellite winds (Figure 4) for both cruises.

Sea surface waters in the Solomon Sea appear to be saltier and colder during Pandora compared to MoorSPICE (Figure 5) except northeast of Bougainville Island. The SSS is dominated by small scale gradients during Pandora, while during MoorSPICE salinity features were much more cohesive on a large scale, especially within the northern exit straits of the Solomon Sea. The SST exhibits a stronger zonal cross-basin gradient during Pandora compared to MoorSPICE, with lower temperature on the western part of the Solomon Sea (Figure 5c,d). Similar patterns were found in the monthly mean satellite SST for both cruises (Figure 4a,b), consistent in SST and SSS seasonal variability described in Delcroix et al. (2014). These colder and saltier waters are due to northwestward oceanic advection (Figures 5; S3).

Volcanic influences

Results of the pH survey are displayed in Figure 6a. The atmospheric transport and dispersion of acidic species released from Rabaul, Bagana and Ambrym volcanoes were forecast onboard using the atmospheric circulation model WRF-Flexpart (Mari et al., 2014; Lefevre et al., 2015) (Figure 6b). Cloud waters in the pristine marine boundary layer are characterized by pH values ranging from 6 to 7, but large pH decreases of 1 to 2 units were recorded in cloud waters contaminated by the volcanic plumes. A very acidic rainfall (pH = 4.1) was found $>$ 500 km downwind of Ambrym volcano (3 July 2012). The volcanic source of acidifiers was confirmed by air trajectory results (Figure 6b). Six days later (9 July 2012), the volcanic plume was crossed off the Louisiade archipelago (Figure 2), over 1000 km away from Ambrym volcano acid rain with a collected pH of 5.4.

The presence of volcanogenic acidifiers is explained by the long range transport of sulfate precursors from Ambrym discussed in Lefevre et al. (2015): from July 5th to 15th. A strong anticyclone (1030 hPa) in the northern Tasman Sea (http://www.bom.gov.au) drove a rapid and steady south-easterly trade wind flux, promoting the transport of volcanogenic acid species from Ambrym to the sampling site within a couple of days.

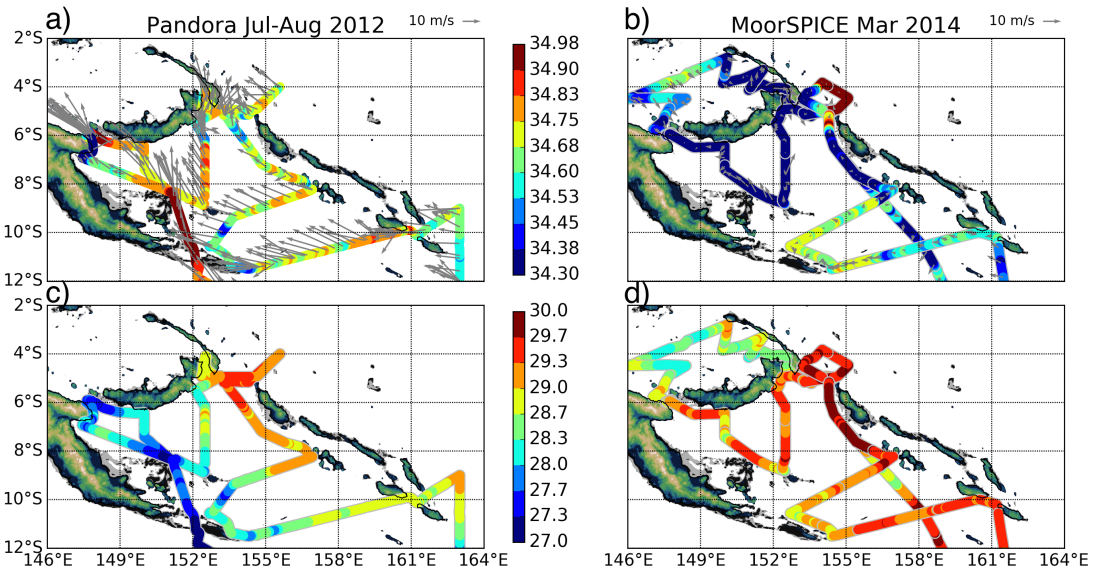

Figure 5: Observed along-track sea surface salinity and in situ winds ($m.s^{-1}$) during (a) Pandora and (b) MoorSPICE. Along-track sea surface temperature (°C) during (c) Pandora and (d) MoorSPICE. Topgraphy is indicated by the colorbar to the right (meters).

It is worth noting that close to Rabaul volcano, cloud chemistry is also influenced by local magma degassing (Figure 6b). Finally, the pH distribution (Figure 6a) is in good agreement with the mean distribution of surface sulfate concentrations and total sulfate (dry + wet) flux deposition displayed in Lefevre et al. (2015, their Figures 13a,b).

Ocean circulation

The observed currents were generally strong with high energy at mesoscale ($\sim$ 100 km) and submesoscale ($\sim$ 10 km) so that snapshots from each cruise contain variability on many time scales. Currents derived from satellite altimetry and drifters suggest that the mean surface circulation during Pandora was dominated by a westward flow in most of the Solomon Sea (Figure 7a). The shipboard ADCP shows a strong and narrow NGCU entering the Solomon Sea (Figure 7c). The NGCU core is located between 500 and 1000 m depth with a surface reversal above 100 m (Germineaud et al., 2016, Figure S4a), as also observed by repeated glider transects (Davis et al., 2012).

As the NGCU splits around Woodlark Island, a strong, shallower stream traveled to the west through the Milne Bay, while the other stream was eastward, and stronger below 100 m (Figure 7c, 153.5°E, 9°S). This asymmetry is likely due to the sill depth of the passage between Woodlark Island and Trobriand (151.5°E, 8.5°S) which is about 350 m (Figure S4a). A moderate ($\sim$ 0.5 m.s^{-1}) surface enhanced flow was observed entering the Solomon Sea through the very narrow Indispensable Strait (Figure 7c). The portion of the NGCU that exited the Solomon Sea through Vitiaz Strait was strong ($>$ 1 m.s^{-1}) over the full depth (Germineaud et al., 2016).

While the bifurcation of the NGCU south of New Britain was not sampled, the resulting NBCU was captured at 152°E with flow along the coast to the northeast at all depths and a portion exiting through St. Georges Channel with the current's core between 100 and 400 m depth (Germineaud et al., 2016, Figure 7c). The circulation at Solomon Strait was stronger near the coast of New Ireland and northward below 100 m as the southward flow was confined to the upper 100 m and to the western half of the Solomon Strait (Figure 7c).

East of Solomon Islands and south of 6°S (Figure 7a), there is a branch of the westward SEC with an eastward current to the north (2°-6°S). Cyclonic circulations occur South of Papua New Guinea (11°S, 148°E) and north-east of Bougainville Island (5°S, 156°E) (Figure 7a). This last feature is related to a strong northwestward surface flow along the east coast of Bougainville Island (Figure 7c, 155°E, 5°S).

During MoorSPICE the surface circulation was dominated by cyclonic eddies at the southern entrance of the Solomon Sea (Figure 7b). The current was southward through Solomon Strait, contributing to a large anti-cyclonic eddy inside the Solomon Sea (8°S, 153°E). East of Solomon Islands, the flow was eastward at 8°S, that is, against the time-mean flow in the SEC with large eddies centered at 6°S and 10°S.

20

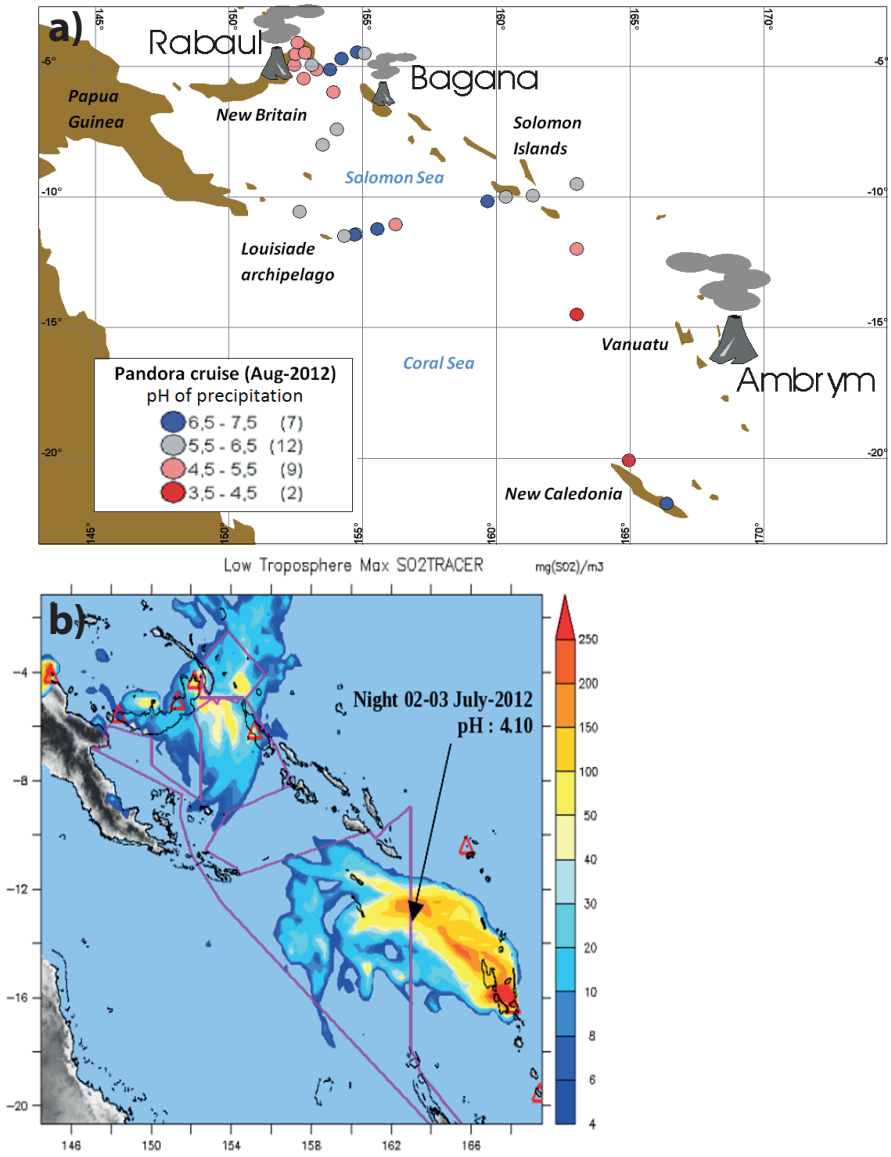

Figure 6: a) Distribution of pH in rainwater during the Pandora cruise, with main volcanic SO_2 emitters superimposed. b) Example of the simulated volcanic plume dispersion (here SO_2 is used as tracer) for the night 2-3 July 2012 using the WRF-Flexpart (right).

Compared to during the Pandora cruise, the NGCU was shallower and wider during MoorSPICE, with no surface reversal as it entered the Solomon Sea (Germineaud et al., 2016, Figures 7d; S4b). No NGCU bifurcation around Woodlark Island was observed during MoorSPICE, with eastward flow east of Milne Bay, that is, opposite to the direction found during Pandora.

This contrast was also observed in drifter climatology during this season (Hristova and Kessler, 2012). However the merging of a very strong and deep NGCU was observed north of the Woodlark Island chain. The outflow through Vitiaz Strait was unexpectedly strong (> 1 m.s^{-1}), and so not consistent with the expected seasonal decrease. Nevertheless, the flow decreases with depth, and the total transport through Vitiaz Strait was much lower (Germineaud et al., 2016). The NBCU had a similar speed and direction to that found during Pandora. Surface flow (0-100 m) in both St. Georges Channel and Solomon Strait was entirely southward into the Solomon Sea to the southwest along the coast of New Britain.

In addition, strong variations in spatial mixing patterns were also detected between both cruises. Observations from Pandora and MoorSPICE cruises, and the Argo database were used to estimate the dissipation of kinetic energy and mixing in the Solomon Sea using the Thorpe scale method and finescale parametrization (Alberty et al., 2017). The mean profile of dissipation in the Solomon Sea is maximum near the surface and decreases with depth. Depth-mean dissipation in the Solomon Sea is elevated by a factor of 8 relative to the rest of the equatorial Pacific and spatial patterns of mixing vary by up to two orders of magnitude along isopycnal layers. The results suggest seasonal variability of mixing with enhancement during strong monsoonal winds, though the full seasonal cycle remains unresolved.

The two cruises therefore show contrasted circulations, which we attribute to the expected seasonal variability as both the intraseasonal and interannual contrasts are low between the two cruises (Section *climatic context*). Pandora was characterized by strong and well defined currents that are typical of austral winter (e.g. Cravatte et al., 2011; Hristova and Kessler, 2012) while MoorSPICE was characterized by weaker currents and a greater activity of cyclonic eddies, typical of early austral summer (Gourdeau et al., 2014; Hristova et al., 2014).

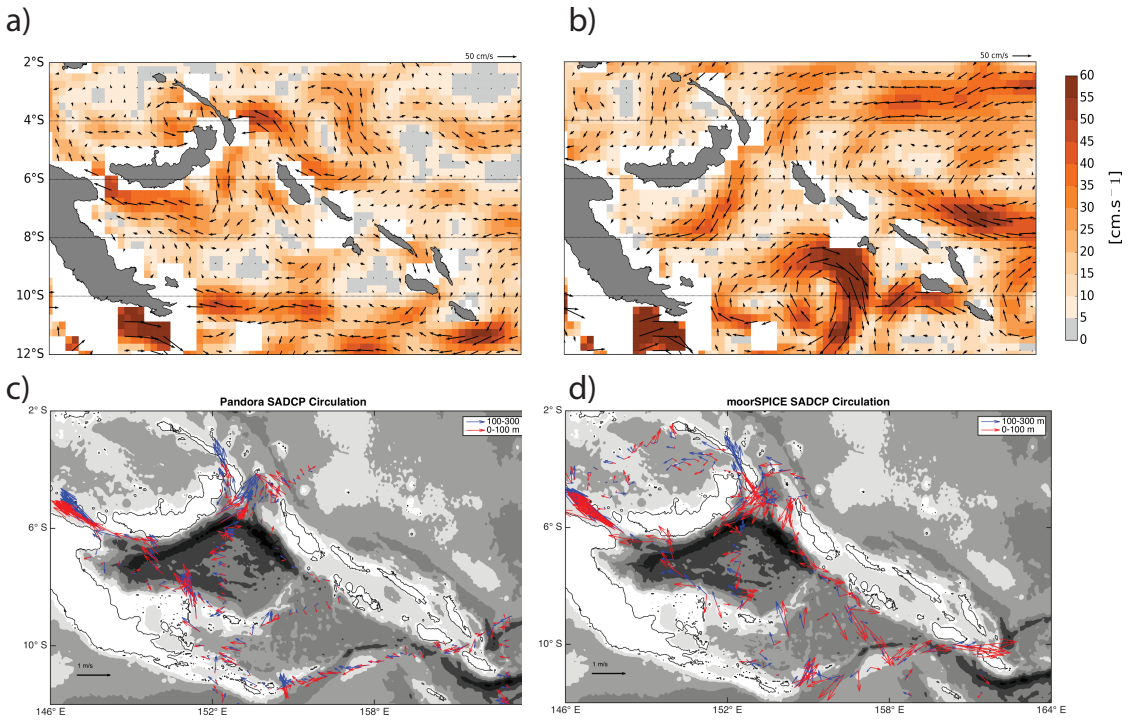

Figure 7: Sea surface currents derived from the AVISO-DUACS14 geostrophic velocity anomalies during a) Pandora (average July-August 2012) and b) MoorSPICE (average March 2014) combined with the annual mean surface current climatology from GDP drifters (1979 through March 2015) (from http://www.aoml.noaa.gov/phod/dac/dacdata.php). Underway currents from the S-ADCP in the layers 0-100 m (red) and 300-500 m (blue) during c) Pandora and d) MoorSPICE.

Water properties

Germineaud et al. (2016) provide a detailed analysis of thermocline and intermediate water properties and we summarize here the main features. Near the surface, water properties have an essentially homogeneous salinity during Pandora (Figure 8a, 34.4-35.4) and a large range during MoorSPICE (Figure 8b, 33.2-35.6 above 28°C).

Below the surface, water masses are identified by marked temperature and salinity extremes. During Pandora, salinities reach a maximum around 200 m depth (> 35.8) at σ_θ = 24.5 (Figure 8a) characterizing the South Pacific Tropical Water (Wyrtki, 1962, SPTW), also referred as the *Upper Salinity Maximum* with south/east Pacific origins (Donguy, 1994; Qu and Lindstrom, 2002). This upper salinity maximum was found at $\sigma_\theta \sim 25$ during MoorSPICE with salinities (< 36) lower than during Pandora (Figure 8b).

Below the SPTW is the Subtropical Mode Water (STMW; σ_θ = 25-26.5 kg.m^{-3}, 12°-20°C) coming from the northern part of the Tasman Sea (Donguy and Henin, 1977; Holbrook and Maharaj, 2008). Deeper, waters in the density range close to σ_θ = 27.0 kg.m^{-3} (5°-8°C, Figure 8a) indicate the Subantarctic Mode Water (SAMW; McCartney, 1977) formed at the northern edge of the Antarctic Circumpolar Current south of Tasmania and then advected northward into the South Pacific (e.g., Grenier et al., 2013; Kessler and Cravatte, 2013).

Near 800 m depth at σ_θ = 27.2 kg.m^{-3}, a salinity minimum (< 34.6) associated with a maximum in oxygen content ($\sim$ 150-200 μmol.kg^{-1}, Figure 8a) identifies the Antarctic Intermediate Water (AAIW) that originates in the southeast Pacific (Qu and Lindstrom, 2004). AAIW is also associated with marked increases in silicate (Figure 8c,d) and nitrate (Figure 8e,f) observed below $\sigma_\theta \sim 27$. Northeast of Bougainville Island ($\sim 5°$ S-155°E; Figure S9), the highest salinities of the intermediate waters indicate the presence of the South Equatorial Pacific Intermediate water (SEqPIW that emanates from the equatorial region, Germineaud et al., 2016; Bostock et al., 2010).

An increase in salinity at σ_θ = 27.4 (> 1000 m) associated with high nutrient content characterizes the Upper Circumpolar Deep Water (UCDW), which is consistent with Sokolov and Rintoul (2000, their Figure 12b). We observed quite low oxygen content associated with high concentrations in nitrate (> 30 μmol.kg^{-1}) and silicate (> 100 μmol.kg^{-1}), with high salinity (> 34.5) during both cruises.

The UCDW emanates southeast of New Zealand, before reaching the anticyclonic gyre in the South Pacific (Tsimplis et al., 1998; Kawabe and Fujio, 2010). Below, the major deep and bottom waters are characterized by the Lower Circumpolar Deep Water (LCDW), which corresponds to an increase in salinity and a decrease in silicate near 2000 m in the Southern Ocean (Orsi et al., 1999). This deep water flows northward across the Southwest Pacific via complex pathways (Kawabe and Fujio, 2010, their Figure 2c), although its presence within the Coral and Solomon Seas remains poorly documented.

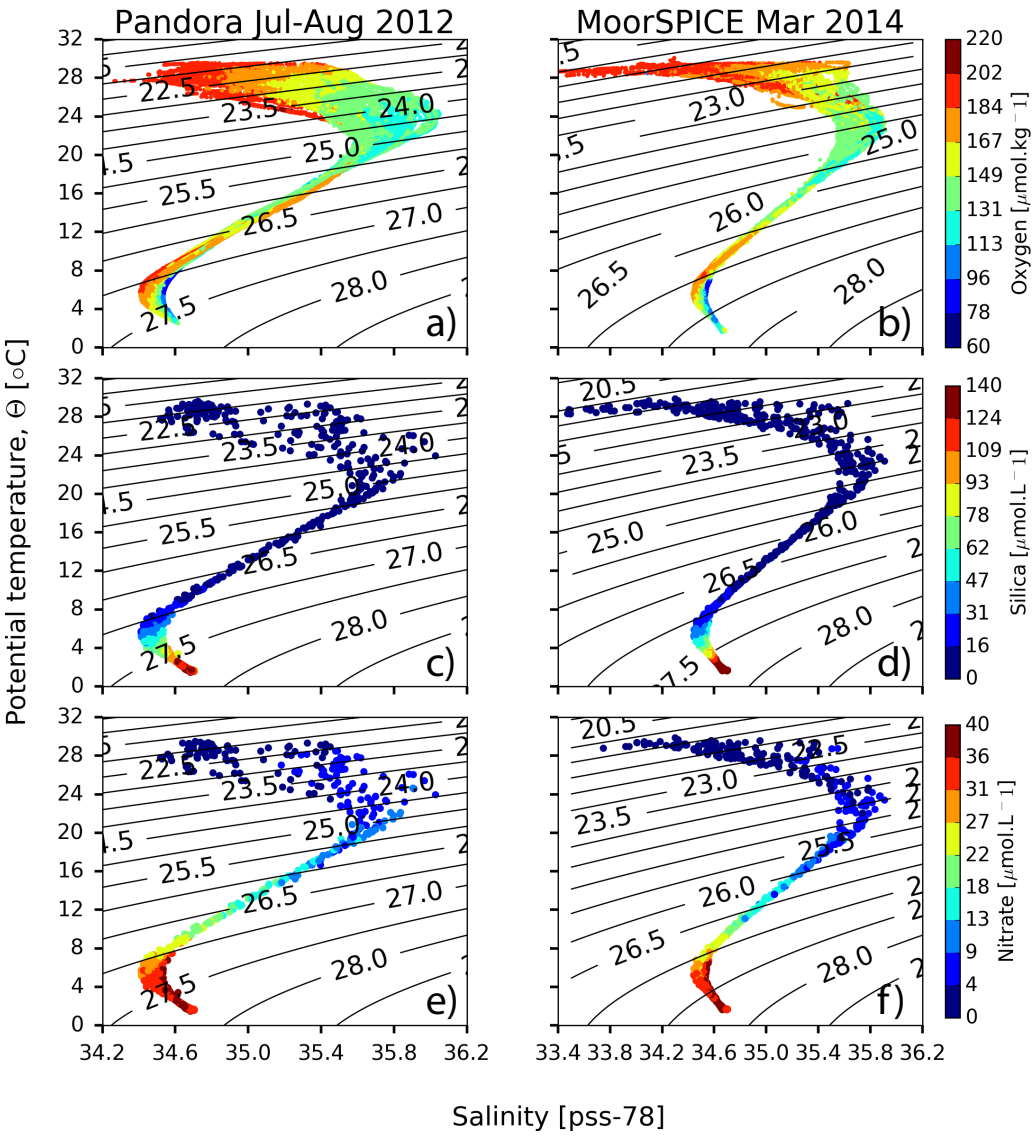

Figure 8: Water properties (left) Pandora; (Right) MoorSPICE color-coded by a),b): oxygen; c),d): silicate; e),f): nitrate concentration. Note that iso-contours indicate potential density.

N_2 fixation, primary production and diazotroph abundances

Bonnet et al. (2015) and Berthelot et al. (2017) provide a detailed quantification of N_2 fixation and diazotrophs in the Solomon Sea and we summarize here the main results and trends. In general, *Trichodesmium* dominate the diazotroph community in the Solomon Sea with up to 8.2×10^{10} *nifH* copies m^{-2} during Pandora and up to 4.8×10^{9} *nifH* copies m^{-2} during MoorSPICE (Figure 9a) (Bonnet et al., 2015). These abundances are in the upper range of *nifH*-derived *Trichodesmium* abundances in the world ocean (Luo et al., 2012). UCYN were the second most abundant phylotypes during Pandora (average of 4.0×10^{9} *nifH* copies m^{-2}; Figure 9). Maxima were observed at the centre of the Solomon Sea (8.0×10^{9} *nifH* copies m^{-2}) during MoorSPICE, with much lower maximum abundances in the Bismarck Sea ($< 1.3 \times 10^{8}$ *nifH* copies m^{-2}) (Figure 9b). *Trichodesmium* dominates over UCYN phylotypes in the Solomon Sea in contrast with other South Pacific areas such as the Coral Sea. This seems to be associated with the meridional temperature gradient between the Solomon and the Coral Sea, as well as the higher trace metal availability in the Solomon Sea (geochemistry section ; Bonnet et al., 2015; Moisander et al., 2010).

In the Solomon Sea, photic N_2 fixation rates ranged from 30 to 5449 (average 624) μmol N m^{-2} d^{-1} during Pandora and 0.2 to 4364 (average 1396) μmol N m^{-2} d^{-1} during MoorSPICE (Figure 9c). They were significantly higher during austral summer conditions (MoorSPICE) than during austral winter conditions (Pandora), suggesting a possible seasonal effect. Nonetheless, rates were at both seasons in the upper range of those reported in the global N_2 fixation MAREDAT database and even surpassed its upper rates (100-1000 μmol N m^{-2} d^{-1}). This suggests that the Solomon Sea is a hot spot of N_2 fixation in the global ocean, although the reasons behind these high rates need to be further investigated. We hypothesize that having SST values $> 27°C$ all year round (i.e. optimal for diazotrophs growth and nitrogenase activity (Breitbarth et al., 2007) associated with significant micro- and macronutrient inputs provide ideal conditions for N_2 fixation. In particular, phosphate turnover times have been reported to be > 2 days (i.e. non-limiting for phytoplankton communities) further south around Melanesian archipelagoes (Moutin et al., 2005), which is likely the case in the Solomon Sea as surface phosphate concentrations were never exhausted during both cruises (always > 0.08 μmol L^{-1}).

In addition, iron, a major component of the nitrogenase enzyme which catalyzes N_2 fixation (Raven, 1988) is continuously provided to the Solomon Sea through land runoff, hydrothermal, and volcanic activity (see paragraph 'Dissolved iron' below and Labatut et al., 2014) and possibly through energetic currents interacting with the islands (Djath et al., 2014; Grenier et al., 2013; 2014). The dissolved Fe measurements performed along a west-east zonal section in the equatorial Pacific (Slemons et al., 2010) confirm that the Solomon Sea is a primary source of iron for the equatorial Pacific.

Altogether, these conditions provide optimal environmental conditions for diazotrophs to bloom extensively and likely explain why this regional sea is a hot spot of N_2 fixation. The basin-scale South Pacific N_2 fixation rate was estimated at 46 Tg N y^{-1} (Luo et al., 2012), equivalent to a daily water column integrated rate of 125 μmol N m^{-2} d^{-1} (considering an area of 72×10^6 km^2 for the South Pacific). The N_2 fixation rates measured during the Pandora and MoorSPICE cruises are larger by a factor of 7 (529 μmol N m^{-2} d^{-1} on average and up to > 5000 μmol N m^{-2} d^{-1}; Figure 9c), confirming that the Solomon Sea contributes importantly to fixed nitrogen inputs in the South Pacific as a whole.

In an attempt to assess the importance of N_2 fixation in this region, we extended the depth-integrated N_2 fixation rates obtained during both cruises to the Solomon Sea surface ($7.2 \times 1011 m^2$). Assuming that diazotrophs fix on average 600 μmol N m^{-2} d^{-1} during the austral winter conditions (Pandora) and 1300 μmol N m^{-2} d^{-1} during austral summer conditions (MoorSPICE), N_2 fixation would introduce 3.5 Tg N y^{-1} to the Solomon Sea. This corresponds to $\sim$ 10% of the total nitrogen fixed for the entire South Pacific Ocean as reported in Luo et al. (2012), while the Solomon Sea represents only 1% of its total area. Consequently, the N_2 fixation budget for the South Pacific needs to be updated by including the recent studies performed in the previously unexplored Solomon Sea.

The nitrogen demand derived from primary production data (Figure 9) (assuming a C:N ratio of 6.6) indicates that N_2 fixation fueled on average 5.5 and 15.1% of total primary production in the Solomon Sea during the Pandora and MoorSPICE cruises, respectively. This contribution is remarkably high compared to other oceanic regions such as the Northwestern Pacific (Shiozaki et al., 2013), Southeastern Pacific (Raimbault and Garcia, 2008), Northeast Atlantic (Benavides et al., 2013) or the Mediterranean Sea (Bonnet et al., 2011; Ridame et al., 2014), where the contribution of N_2 fixation to primary production is generally $< 5\%$. This further confirms the importance of N_2 fixation in supplying new nitrogen to the surface waters of the Solomon Sea.

By using high-resolution nanometer scale secondary ion mass spectrometry (nanoSIMS) coupled with $^{15}N_2$ isotopic labelling and flow cytometry cell sorting, Bonnet et al. (2016) showed during MoorSPICE that 10 % of diazotroph-derived N was quickly (48h) transferred to non-diazotrophic plankton, in particular diatoms, whose abundance increased 3-fold in that time frame. Diatoms are efficient carbon exporters to depth (Nelson et al., 1995), suggesting that N_2 fixation may sustain an indirect export pathway of organic matter in the Solomon Sea. It would be interesting in further studies to quantify the part of exported material sustained by diazotrophy in such a hot spot of N_2 fixation.

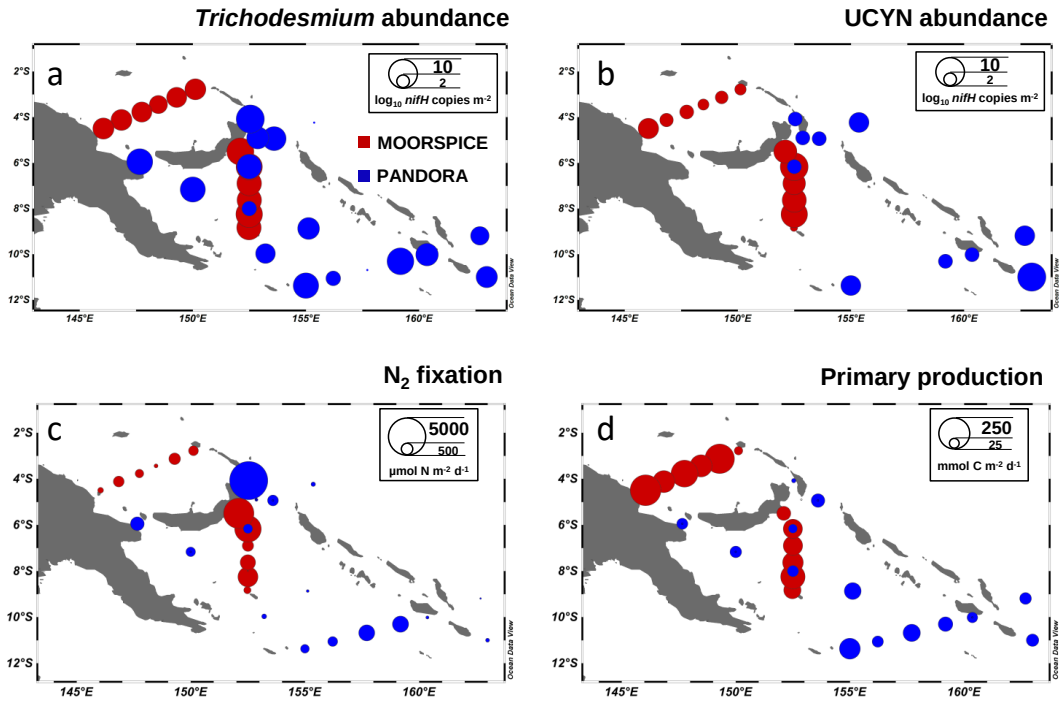

Figure 9: (a) *Trichodesmium* and (b) UCYN abundances (log*nifH* copies m^{-2}), (c) N_2 fixation rates (μmol N m^{-2} d^{-1}), and (d) primary production rates (mmol C $m^{-2}d^{-1}$), during the Pandora (austral winter, blue dots) and MoorSPICE (austral summer, red dots) cruises. All data are integrated over the 0-100 m layer, corresponding approximately to the photic zone.

Inorganic carbon observations, anthropogenic CO_2 and acidification

Although during Pandora samples were taken at contrasted locations, depth profiles for both TA and DIC are relatively depth-independent below 2000 m, as compared to surface gradients (Figure 11a,b). Below the surface, a pronounced TA subsurface maximum around 150 m is clearly recognized in the SPTW (Figure 8). In intermediate waters (500-1000 m), TA and DIC regularly increase with depth.

However, at station 44 (4°S-155°E, i.e. outside the Solomon Sea in the western tropical Pacific) we observed localized DIC maxima around 500-700 m (highlighted in Figure 11b) in the core of the low oxygen layer characterizing old SEqPIW of northern origins (Section *Water properties*). In deep waters ($>$ 1000 m) DIC and TA concentrations present, like nutrients, a maximum around 2000-3000 m. However, lower DIC and TA concentrations (highlighted in Figure 11a,b) are found around 3000 m at station 29 (11°S, 156°E) associated with lower nutrient concentrations, high salinity and high oxygen (11.5°S, 155.7°E).

In surface waters, the range for TA (2270-2290 μmol.kg^{-1}), for DIC (1920-1955 μmol.kg^{-1}), for pH (8.06-8.09) and Aragonite saturation state (3.8-4) are typical values observed in the eastern Indian and western Pacific tropical zones (Takahashi et al., 2014; Lenton et al., 2016). Sea surface fCO_2 (calculated) was around 350 μatm at 14°S-162°E and higher at 370 μatm around 4°S-152°E, a difference that could be explained by warming in the north. The fCO_2 range derived from surface DIC/TA data is coherent with underway fCO_2 measurements conducted in this region during July-August 2012 (Trans-Future 5 cruise, Figure 10, available on SOCAT-V3 data-base, online at www.socat.info, Bakker et al. (2016)).

In July 2012 the global mean atmospheric concentration was about 392 ppm (or 378 μatm when converting to fCO_2) (Le Quéré et al., 2015) Therefore, during the cruise the region was a CO_2 sink (oceanic fCO_2 was lower than in the air). To understand how the oceanic carbon uptake propagates in the water column, we evaluated the anthropogenic CO_2 concentrations (C_{ant}) using the method based on the TrOCA tracer (a combination of TA/DIC pairs, temperature, salinity and oxygen data) previously applied in the Indian Ocean along several WOCE sections (Touratier et al., 2007; Alvarez et al., 2009). The new TrOCA method proposed by Touratier et al. (2007) was considered the most suitable for the investigated region because no transient tracers (e.g. CFCs) were measured during the Pandora cruise. The C_{ant} concentrations are presented only below 200 m (Figure 11b) as the method is not suitable to evaluate C_{ant} in surface layers.

The C_{ant} vertical gradient suggests a significant penetration of anthropogenic CO_2 down to about 1500 m. Between 200 and 1000 m C_{ant} concentrations decrease sharply from about 50 μmol.kg^{-1} to 10 μmol.kg^{-1}. Below 1500 m, the C_{ant} concentrations are low and within the error of the method ($\pm 7\mu$mol.kg^{-1}).

We also estimated the anthropogenic pH (pH-ant= pH2012-pHpreindustrial) by calculating the difference between modern pH (based on DIC and TA concentrations) and pre-industrial pH values (based on DIC-C_{ant} and TA concentrations). As expected, the pH-ant profiles mirror the C_{ant} penetration (Figure 11b). A large pHant value of about -0.1 units is estimated in upper layers (200 m) and is also significant at depth (-0.05 units at 500 m).

The DIC and TA observations obtained during the Pandora cruise enable the first evaluation of both anthropogenic carbon and ocean acidification in the Solomon Sea. Added to historical observations conducted in the Western Tropical Pacific ocean (Suzuki et al., 2013), these data can be used to investigate in more detail the oceanic inorganic carbon system and its variability in a broader context.

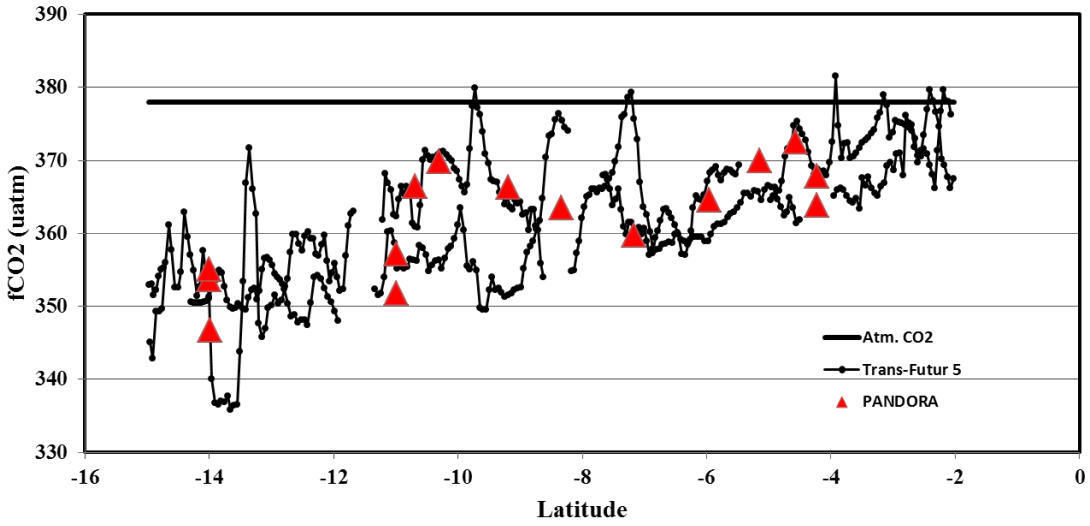

Figure 10: Sea surface fCO_2 calculated with DIC/TA from Pandora (red triangles) and underway fCO_2 measurements (black dots, Trans-Future cruises in July-August 2012 in North Coral Sea and Solomon Sea, from SOCAT-V3, (Bakker et al., 2016). Both observations show lower sea surface fCO_2 compared to atmospheric fCO_2 (black line). During this period, the region was a CO_2 sink.

30

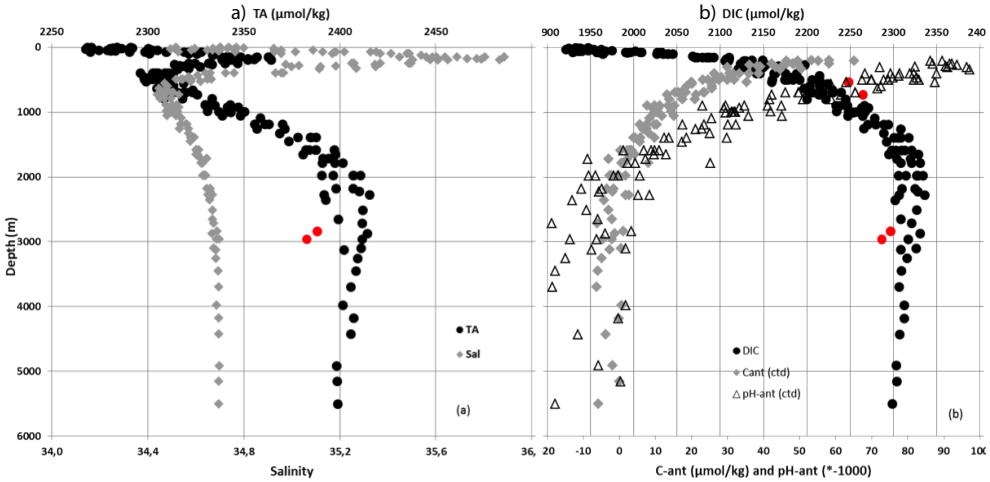

Figure 11: (a) Salinity (grey) and TA (black) (μmol.kg^{-1}) profiles; (b) DIC (black, μmol.kg^{-1}), C$_{ant}$ (grey, μmol.kg^{-1}) and pH-ant profiles (triangles). For scaling purpose in (b), pH-ant values are multiplied by -1000 (i.e. 100 = -0.1 unit pH change). In (a) and (b) red dots highlight anomalies observed at a few locations. Uncertainty on C$_{ant}$ estimate is about $\pm$ 7μmol.kg^{-1}.

Trace elements

We present below a preliminary examination of Fe, Al, Hg and Mn.

Dissolved Iron

Dissolved Fe (dFe) presents nutrient-like profiles, with low concentrations at the surface and an increase with depth (Figure 12a). The surface dFe concentrations range from 0.11 to 0.44 nmol.L^{-1} (Figure 12b) and show significantly ($p < 0.05$) higher dFe concentrations near the islands (0.35 ± 0.06 nmol.L^{-1}) than in the Coral Sea (0.23 ± 0.07 nmol.L^{-1}) in the first 150 m. Similar concentrations have been observed by Labatut et al. (2014) off the Papua New Guinea coast due to river runoff. Volcanic inputs from the Rabaul volcano (close to station 42) could also be involved. This enrichment is confined near islands and offshore, dFe concentrations (0.19 ± 0.02 nmol.L^{-1}) are not significantly ($p > 0.05$) different to those in the Coral Sea. High primary production and Trichodesmium abundance could explain the similar dFe stocks (Bonnet et al., 2015). The deep water dFe concentrations range from 0.62 to 1.29 nmol.L^{-1} (Figure 12c) and suggest a sedimentary and/or hydrothermal source of dFe in the Solomon Strait (Labatut et al., 2014).

Al and Mn

Enrichments in Al and Mn concentrations in the region relative to the open ocean indicate that coastal and sedimentary input is important in this region and that this *boundary exchange* (BE) is likely driven by strong currents scouring the coastal margin. However, quantification of BE requires the coupling of REE concentrations and Nd isotopes measurements, currently underway (Lacan and Jeandel, 2005; Grenier et al., 2013). The evolution of Al concentration along the NGCU pathways near the shallow shelf (< 500 m) of the Rossel Island (station 34) suggests a noticeable source at about 400 m depth (Figure 13), at the core of the NGCU (Germineaud et al., 2016). There is a strong Mn gradient in the upper water column, also suggestive of sediment flux from the shelf (Figure 13). These stations also show evidence of enrichment at depth from deep sedimentary input.

The NGCU flows near the shallow sill along the Woodlark and Trobriand Islands (station 71) before it bifurcates into the NBCU. Here, there is an increase in aluminum and manganese at depth, as well as a peak in aluminum (but not manganese) around 500 m. This could either be the signal from the Louisiades, or a lateral input from the nearby shallow sill. The absence of Mn enrichment at this depth suggests that the aluminum is from a more distant source like the Louisiades and that the Mn has been scavenged during transport. There is also deep water enrichment off of New Britain (station 60). In the Solomon Strait (station 42), the enrichment from the Louisiades is overwhelmed by the strong continental inputs through the strait.

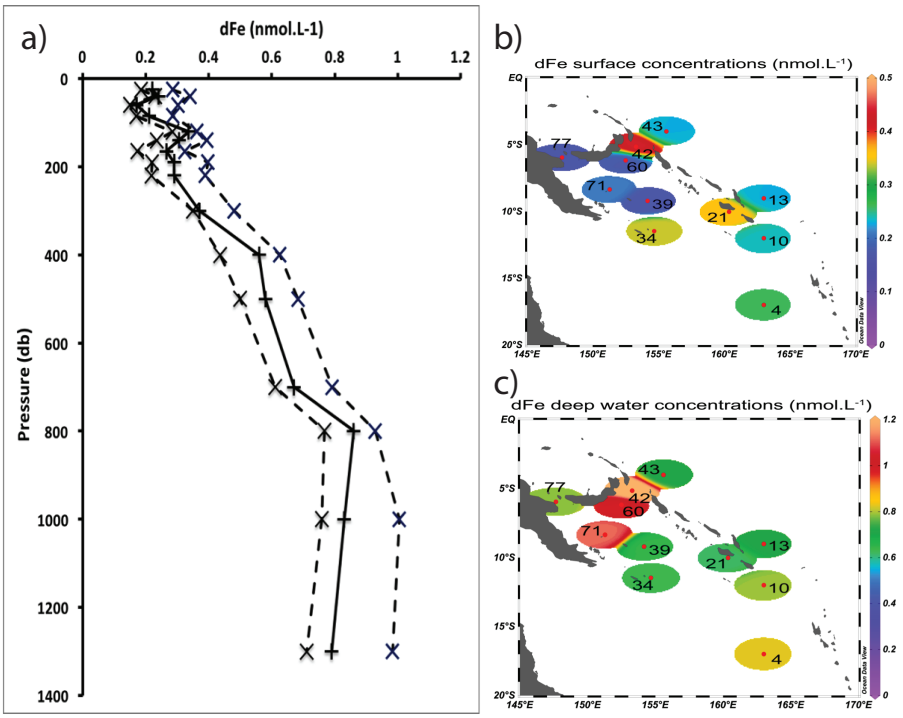

Figure 12: a) Vertical distribution of dFe concentrations measured during the Pandora cruise showing the median dFe (solid line with crosses). The interquartile range, defined as the range around the median containing 50% of the data, is given between the two dotted lines. (b) Concentrations of dFe in surface waters measured during the Pandora cruise at 25 m for all the stations except station 34 (45 m) and 77 (80 m). (c) Same as b), but at 1300 m.

Based on the Al profile, as the NBCU flows through the Solomon Strait it entrains both deep sedimentary inputs and lateral input from coastal margins. Continuing along the NGCU through the Vitiaz Strait (station 77), there are lateral inputs from the shelves, as well as enrichment at depth. Sites located adjacent to each other in the Solomon Strait (station 42) and northeast of Bougainville (station 43) are remarkably different. The Solomon Strait is enriched in aluminum and manganese relative to the Bougainville coast, suggesting that as water exits the Solomon Strait it flows more northwards than eastwards (Figure 7). This is consistent with ADCP findings, which show no flow between these neighboring sites. Rather, the Solomon Islands Coastal Undercurrent flows north, and there is some concurrence between this station and the south side of the Solomon Islands (station 13): they have similar manganese distributions, and similar Al distributions deep in the water column.

In the Coral Sea, upstream the Solomon Sea, station 4 located within the North Caledonian Jet (NCJ) have similar distribution of aluminum and manganese to those of station 82, further north. Lateral inputs from the shelf off New Caledonia enrich station 4 in both aluminum and manganese, relative to station 82. Based on these data, the predominant inputs of trace metals to the Solomon Sea are from coastal margin fluxes at depth, as well as lateral inputs in straits, where water is in contact with sediment at both the seafloor and along the coasts. There are high surface concentrations at many stations that reach thermocline depths ($\sim$ 300 m). In general, average aluminum and manganese concentrations ($\sim$ 12 nM and $\sim$ 0.5 nM, respectively) are elevated relative to open ocean values. The most elevated concentrations in aluminum are found at station 77, along the outflow of the Vitiaz Strait, suggesting high terrestrial inputs in the surface waters.

The Solomon Sea is, in many locations, enriched in Al and Mn relative to open ocean values, suggesting that the interaction between strong currents and coastal boundaries is an important mechanism by which Al and Mn concentrations are enriched in this area. Such hypothesis will be confirmed, or not when REE and Nd will be analyzed.

Mercury (Hg)

We present 9 vertical profiles (to 1300 m-depth) for tHg and MeHg that were sampled during the Pandora cruise. Total Hg concentrations vary only little, both vertically and horizontally (mean = 0.90$\pm$0.18 pM, range = 0.55-1.69 pM, n = 87). The vertical tHg profiles show neither a clear surface enrichment nor indications for sedimentary sources (Figure 14), and correspond to concentrations generally observed in the open ocean (Lamborg et al., 2014). The MeHg vertical distributions show a similar pattern at all stations (mean = 0.17$\pm$0.14 pM, range = DL-0.42 pM, DL = 0.01 pM, n = 89).

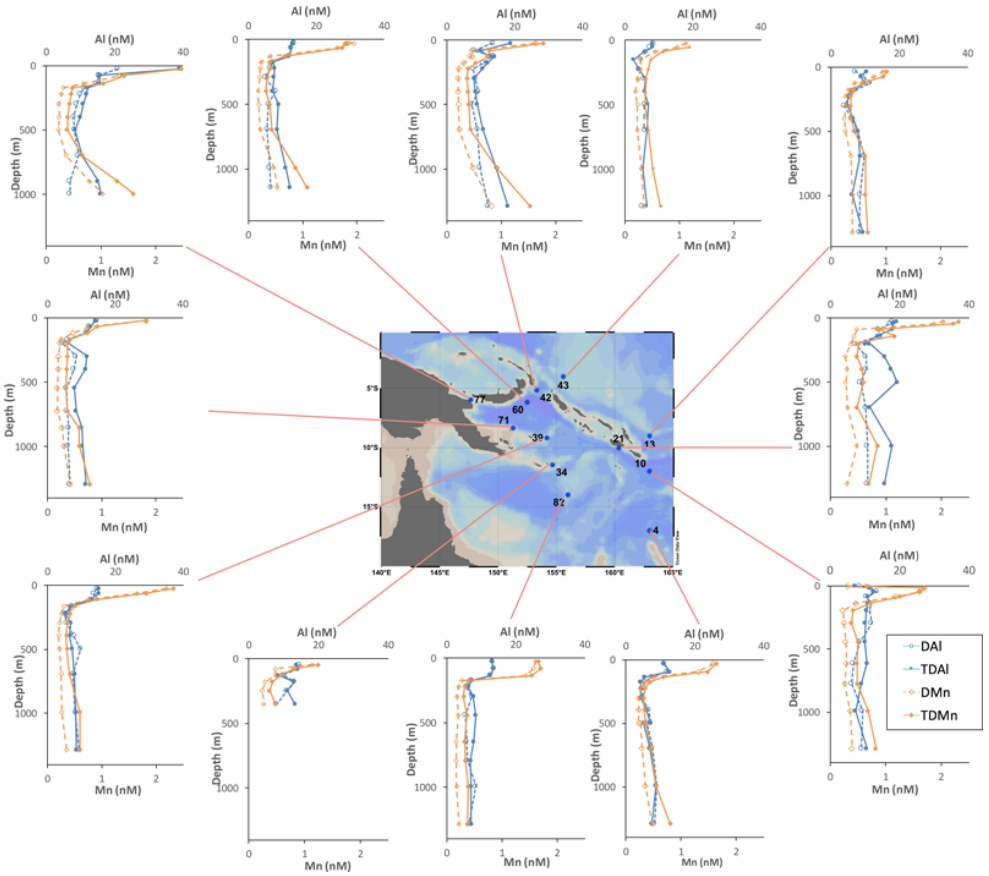

Figure 13: Aluminum and manganese distributions across the Solomon Sea. DAl and DMn represent the dissolved fraction ($< 0.2\ \mu$m), while TDAl and TDMn represent the whole water fraction.

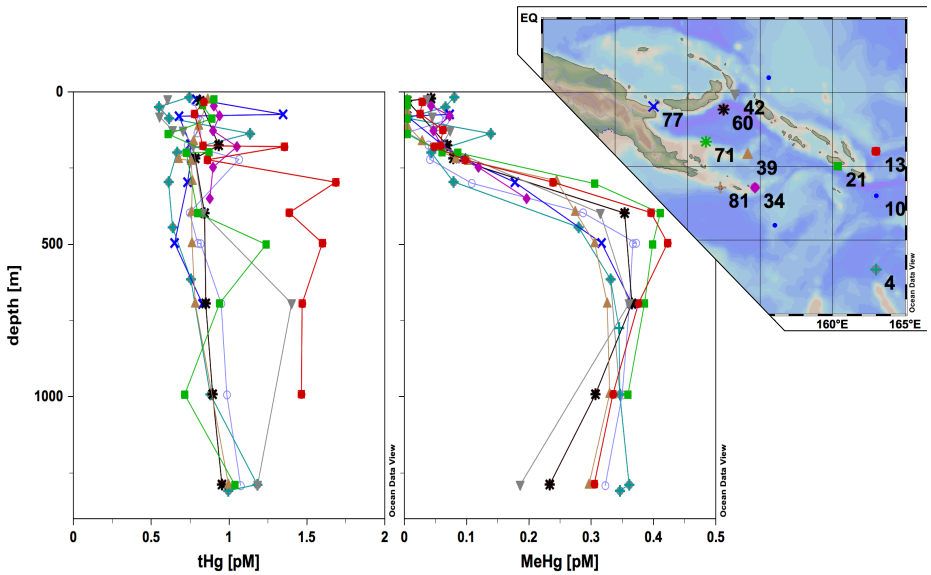

Figure 14: Total Hg (tHg) and methylmercury (MeHg) distributions in picomoles per liter (pM) across the Solomon Sea

MeHg concentrations are generally low (0.043±0.021pM, n = 39) at the surface (0-200 m), increase gradually from 200 to 400 m-depth (0.195±0.103 pM, n = 21) to reach their maximum below 400 m-depth, (0.337±0.034 pM, n = 29). The fact that MeHg and tHg distributions are relatively homogeneous in this dynamic zone and comparable to what is observed eastward in the open Equatorial Pacific (Mason and Fitzgerald, 1990; Munson et al., 2015) suggests that MeHg is formed in situ in the oceanic water column and that boundary exchange has little or no influence. Concurrent near margin Hg scavenging (Cossa et al., 2004) and Hg release from margin sediments could indeed result in zero net effect on tHg concentrations. It is however very unlikely that those boundary exchange processes would not affect MeHg distributions.

Conclusions

The Pandora and MoorSPICE multidisciplinary cruises documented the Solomon Sea and part of the Coral and Bismarck Seas during two contrasted seasons, in austral winter (July-August 2012) and austral summer (March 2014). This paper presents the climatic context of the cruises, explains the scientific rationales behind all measurements made and describes the data acquisition. It presents an ensemble view of available observations and some preliminary results on physics, biogeochemistry and geochemistry so that those can be used as a reference for further, refined physical, geochemical and biogeochemical studies and hopefully stimulate multidisciplinary analyses.

Both cruises took place during neutral or weak ENSO conditions, and during weak active phases of MJO, precluding a strong influence of these phenomena on observed conditions. It is more likely that seasonal variability is the main driver of observed differences between the two cruises. Pandora took place during austral winter, and was associated with colder sea surface temperature, strong regional monsoonal wind forcing, and well-defined currents, whose transports were in the upper range of what had been previously estimated. In contrast, MoorSPICE took place in austral summer, and was associated with warm SSTs, much weaker winds, weaker currents and a greater activity of cyclonic eddies.

Measurements of temperature, salinity, oxygen, nutrients and currents allowed an unprecedented description of the fine-scale structure of water mass pathways, properties and mixing at different densities. Special attention was paid to the entrance and exits of the Solomon Sea, and these sections were sampled from top to bottom. Waters enter the Solomon Sea through the southern entrance in the narrow and deep NGCU confined to the western boundary, joining a weaker branch in mid-basin. This strong current further splits around islands and bifurcates on the New Britain coast, ultimately exiting the Solomon Sea through three narrow exits. The main branch exits northwestward through Vitiaz Strait, where the flow is found to extend to the bottom during both cruises. Other branches exit through St. Georges Channel and Solomon Strait. In the surface, waters also enter the Sea through Solomon Strait. Unexpected features include the deep extension of the currents, and strong contrasts between the interior of the Solomon Sea and conditions east of the Solomon Strait (Germineaud et al., 2016).

These energetic currents and the complex topography make this area potentially key for water mixing. Spatial patterns of mixing have been analyzed using CTD and LADCP profiles and reveal high seasonal dependence dissipation, which is much higher in the Solomon Sea than in other equatorial Pacific regions.

Biogeochemical measurements revealed new and important results. The Solomon Sea appears as a hot spot of N_2 fixation in the global ocean. Trichodesmium were quite abundant during both cruises and dominated the diazotroph community. N_2 fixation rates measured were among the highest of the global ocean, especially in the narrow exits of the Solomon Sea where diazotrophs accumulate. The Pandora cruise carbon measurements also enabled the first evaluation of anthropogenic carbon and oceanic acidification in the Solomon Sea. Anthropogenic carbon signal penetrates deep in the water column, down to 1500 m, and acidification, large in the surface layer, was still found to be significant at 500 m depth.

Trace elements and isotopes were collected at selected locations along the water pathways; though many tracers are still currently being analyzed, the first results clearly reveal land to ocean inputs. A surface dissolved iron enrichment, probably due to river runoff or volcanic inputs, is confined close to the coasts (Labatut et al., 2014). Dissolved iron concentrations in deep waters suggest the existence of a deep sedimentary and/or hydrothermal source. Aluminum and manganese concentrations also suggest significant sediment flux from the shelf, in shallow and deep waters, and lateral inputs in the straits. Surprisingly, total mercury and methylmercury vertical distributions are similar to those in open ocean, and did not reveal any substantial surface enrichment, nor sedimentary sources. These results suggest that boundary exchange has little or no influence on MeHg formation. Further analyses of other tracers (more specifically REE concentrations and Nd isotopes) will help to constrain the nature and rate of the boundary exchanges at the land-ocean interface. The question of how these micronutrients elements will be transported downstream toward the equator remains open.

The data collected during these two cruises provide snapshots of the Solomon Sea conditions. They give unprecedented detailed information, but have inherent limitations, since a snapshot view of the currents can be strongly impacted by variability on many timescales, in particular by mesoscale eddies, intraseasonal or interannual variability. To complement these cruises, moorings have been deployed at the entrance and exits of the Solomon Sea (in Vitiaz Strait, St-Georges Channel and Solomon Strait) for a period of 18 months to 3 years. They sampled velocity, temperature and salinity at high frequency from top to bottom. Together with the repeated glider sections at the entrance of the Solomon Sea, with the PIES end points moorings, they will provide estimates of mass and heat transport variability from the tropics to the equator via the low-latitude western boundary current.

We hope to learn much from these observations about the scales of variability of this transport, which is a key element of the meridional subtropical cells supplying waters of mid to high latitude origin into the western equatorial Pacific. It is recognized that sustained boundary current observations are primary missing elements of the ocean observing system, and that their transport of mass, heat and freshwaters should be monitored through dedicated observations (TPOS2020, report available online at http://tpos2020.org/first-report/). We also hope to learn from these measurements how to effectively built a sustained observing system for this region.

Appendix: List of the trace elements and their isotopes for which samples were taken in the framework of Pandora cruise

During Pandora (also GEOTRACES GP12), a comprehensive group of trace element samples were collected and are currently being measured. They are listed below, along with their scientific application:

1) Dissolved and particulate trace metal concentrations (Fe, Co, Mn, Cu, Zn, Pb, Cd...) and some of their isotope distributions (Fe, Zn, Cu, Pb, Cd) will be used to assess the flux of trace elements provided to the water masses by their contact with the adjacent continent to the Solomon Sea. In addition, some of them as for example Fe, Co, Cu, or Zn are essential to the phytoplankton development and considered as micro-nutrients.
2) Concentrations and isotopic composition of these micronutrients help to constrain their origin, fate and cycling in seawater. For example, hydrothermal sources can provide iron that is isotopically light compared to the simple dissolution of erosion products, allowing the differentiation of the element sources (Radic et al., 2011; Conway and John, 2014; Labatut et al., 2014; Klar et al., 2017). Lead isotopes are good tracers of the lead sources in the different water masses.
3) Being conservative lithogenic tracers, particulate Al and ^{232}Th allow discrimination the terrestrial from the biogenic fraction of the suspended material pool.
4) Radium and actinium isotopes (^{226}Ra, $T_{1/2}$ =1602 years; ^{228}Ra, $T_{1/2}$ =5.75 years; ^{224}Ra, $T_{1/2}$=3.66 day; ^{223}Ra, $T_{1/2}$=11.4 day) are all decay products of insoluble elements. Soluble, they often show high activity in shallow water overlying continental shelves via epibenthic outflux, and decrease in abundance by natural radioactive decay and mixing. Because of their chronometer properties, Ra isotopes provide information on water transit time and mixing processes (van Beek et al., 2008; Sanial et al., 2015). ^{227}Ac (half-life 21.8 years) is produced in the bottom sediments. ^{227}Ac will be analyzed on the same samples as for Ra and will help in constraining the vertical mixing on a longer time-scale (Geibert et al., 2002).

5) Rare Earth (REE) concentrations and Nd isotopes: The continental margins surrounding the world ocean display different isotopic signatures, reflecting their different geological origin: old granitic sediments display low $^{143}Nd/^{144}Nd$ ratios while the volcanic sediment have high $^{143}Nd/^{144}Nd$ ratios. This property allows the quantification of the fraction of weathered material that dissolves at the continent/ocean interface (Arsouze et al., 2009; Jeandel and Oelkers, 2015).
6) Thorium and protactinium isotopes: Thorium is insoluble in seawater. ^{228}Th, ^{230}Th are used as tracers of particle scavenging rates, settling rates, dissolved/particulate exchange (Henderson, 2003; Venchiarutti et al., 2008; Hayes et al., 2013; 2014). ^{231}Pa is also insoluble (but slightly more soluble than Th) and also produced in the water column by the decay of a soluble father. Although more soluble than Th, ^{231}Pa is still particle reactive. Coupled with ^{230}Th isotope data, its distribution provides a powerful means to estimate dissolved/particle exchange rate, boundary scavenging and ventilation rates (Henderson, 2003; Venchiarutti et al., 2008; Hayes et al., 2013; 2014).
7) Stable Li and Pb isotopes: hydrothermal fluids have a characteristic stable Pb isotope signatures (as do Nd) that is altered near a vent. Li concentrations and Li isotopic signatures are also good specific tracers of hydrothermalism because seawater has an isotopic signature of about $\delta 7\text{Li} = +33‰$ whereas hydrothermal fluids are close to $\delta 7\text{Li} = +5 - 10‰$.
8) Total Hg (tHg) and methylmercury (MeHg) are contaminants, the last one being accumulated and toxic for the trophic chain (Heimburger et al., 2015).

References

Alberty MS, Sprintall J, MacKinnon J, Ganachaud A, Cravatte S, et al. 2017. Spatial patterns of mixing in the Solomon Sea. *J Geophys Res* **Submitted**.

Allard P, Aiuppa A, Bani P, Metrich N, Bertagnini A, et al. 2015. Prodigious emission rates and magma degassing budget of major, trace and radioactive volatile species from Ambrym basaltic volcano, Vanuatu island Arc. *Journal of Volcanology and Geothermal Research* ISSN 03770273.

Alvarez M, Lo Monaco C, Tanhua T, Yool A, Oschlies A, et al. 2009. Estimating the storage of anthropogenic carbon in the subtropical Indian Ocean: a comparison of five different approaches. *Biogeosciences* **6**(4): 681–703. ISSN 1726-4189.

Aminot A, Kerouel R. 1995. Reference material for nutrients in seawater: stability of nitrate, nitrite, ammonia and phosphate in autoclaved samples. *Marine Chemistry* **49**(2-3): 221–232. ISSN 03044203.

Aminot A, Kerouel R. 2007. *Dosage automatique des nutriments dans les eaux marines: méthodes en flux continu*. France: Ifremer. ISBN 9782759200238.

Arsouze T, Dutay JC, Lacan F, Jeandel C. 2009. Reconstructing the Nd oceanic cycle using a coupled dynamical – biogeochemical model. *Biogeosciences Discussions* **6**(3): 5549–5588. ISSN 1810-6285.

Aufdenkampe AK, McCarthy JJ, Navarette C, Rodier M, Dunne J, et al. 2002. Biogeochemical controls on new production in the tropical Pacific. *Deep Sea Research Part II: Topical Studies in Oceanography* **49**(13-14): 2619–2648. ISSN 09670645.

Bakker DCE, Pfeil B, Landa CS, Metzl N, O'Brien KM, et al. 2016. A multi-decade record of high-quality fCO2 data in version 3 of the Surface Ocean CO2 Atlas (SOCAT). *Earth System Science Data* **8**(2): 383–413. ISSN 1866-3516.

Bani P, Oppenheimer C, Allard P, Shinohara H, Tsanev V, et al. 2012. First estimate of volcanic SO2 budget for Vanuatu island arc. *Journal of Volcanology and Geothermal Research* **211-212**: 36–46. ISSN 03770273.

Benavides M, Arístegui J, Agawin NS, Álvarez-Salgado XA, Álvarez M, et al. 2013. Low contribution of N2 fixation to new production and excess nitrogen in the subtropical northeast Atlantic margin. *Deep Sea Research Part I: Oceanographic Research Papers* **81**: 36–48. ISSN 09670637.

Benavides M, Voss M. 2015. Five decades of N2 fixation research in the North Atlantic Ocean. *Frontiers in Marine Science* **2**. ISSN 2296-7745.

Berthelot H, Benavides M, Moisander PH, Grososo O, Bonnet S. 2017. Extremely high Nitrogen fixation rates in the particulate and dissolved pools in the Southwestern Pacific. *Geophys Res Lett* **Submitted**.

Bonnet S, Berthelot H, Turk-Kubo K, Cornet-Barthaux V, Fawcett S, et al. 2016. Diazotroph derived nitrogen supports diatom growth in the South West Pacific: A quan-

941 titative study using nanoSIMS: Transfer of diazotrophic N into plankton. *Limnology*
942 *and Oceanography* **61**(5): 1549–1562. ISSN 00243590.
943 Bonnet S, Biegala IC, Dutrieux P, Slemons LO, Capone DG. 2009. Nitrogen fixation in
944 the western equatorial Pacific: Rates, diazotrophic cyanobacterial size class distribu-
945 tion, and biogeochemical significance. *Global Biogeochemical Cycles* **23**(3): n/a–n/a.
946 ISSN 08866236.
947 Bonnet S, Grosso O, Moutin T. 2011. Planktonic dinitrogen fixation along a longitudinal
948 gradient across the Mediterranean Sea during the stratified period (BOUM cruise).
949 *Biogeosciences* **8**(8): 2257–2267. ISSN 1726-4189.
950 Bonnet S, Guieu C, Bruyant F, Prasil O, Van Wambeke F, et al. 2008. Nutrient limitation
951 of primary productivity in the Southeast Pacific (BIOSOPE cruise). *Biogeosciences*
952 **5**(1): 215–225. ISSN 1726-4189.
953 Bonnet S, Rodier M, Turk-Kubo KA, Germineaud C, Menkes C, et al. 2015. Contrasted
954 geographical distribution of N2 fixation rates and nif H phylotypes in the Coral and
955 Solomon Seas (southwestern Pacific) during austral winter conditions. *Global Bio-*
956 *geochemical Cycles* pp. n/a–n/a. ISSN 08866236.
957 Bostock HC, Opdyke BN, Williams MJ. 2010. Characterising the intermediate depth wa-
958 ters of the Pacific Ocean using 13C and other geochemical tracers. *Deep Sea Research*
959 *Part I: Oceanographic Research Papers* **57**(7): 847–859. ISSN 09670637.
960 Bourgeois T, Orr JC, Resplandy L, Terhaar J, Ethé C, et al. 2016. Coastal-ocean uptake of
961 anthropogenic carbon. *Biogeosciences* **13**(14): 4167–4185. ISSN 1726-4189.
962 Breitbarth E, Oschlies A, LaRoche J. 2007. Physiological constraints on the global distri-
963 bution of Trichodesmium effect of temperature on diazotrophy. *Biogeosciences* **4**(1):
964 53–61. ISSN 1726-4189.
965 Church M, Jenkins B, Karl D, Zehr J. 2005. Vertical distributions of nitrogen-fixing phylo-
966 types at Stn Aloha in the oligotrophic North Pacific Ocean. *Aquatic Microbial Ecol-*
967 *ogy* **38**: 3–14. ISSN 0948-3055, 1616-1564.
968 Conway TM, John SG. 2014. Quantification of dissolved iron sources to the North Atlantic
969 Ocean. *Nature* **511**(7508): 212–215. ISSN 0028-0836, 1476-4687.
970 Cossa D, Cotte-Krief MH, Mason RP, Bretaudeau-Sanjuan J. 2004. Total mercury in the
971 water column near the shelf edge of the European continental margin. *Marine Chem-*
972 *istry* **90**(1-4): 21–29. ISSN 03044203.
973 Cravatte S, Ganachaud A, Duong QP, Kessler WS, Eldin G, et al. 2011. Observed circu-
974 lation in the Solomon Sea from SADCP data. *Progress In Oceanography* **88**(1-4):
975 116–130. ISSN 00796611.
976 Daniel A, Kérouel R, Aminot A. 2012. Pasteurization: A reliable method for preservation
977 of nutrient in seawater samples for inter-laboratory and field applications. *Marine*
978 *Chemistry* **128-129**: 57–63. ISSN 03044203.

Davis RE, Kessler WS, Sherman JT. 2012. Gliders Measure Western Boundary Current Transport from the South Pacific to the Equator. *Journal of Physical Oceanography* **42**(11): 2001–2013. ISSN 0022-3670, 1520-0485.

Delcroix T, Radenac MH, Cravatte S, Alory G, Gourdeau L, et al. 2014. Sea surface temperature and salinity seasonal changes in the western Solomon and Bismarck Seas. *Journal of Geophysical Research: Oceans* **119**(4): 2642–2657. ISSN 21699275.

Dickson A, Millero F. 1987. A comparison of the equilibrium constants for the dissociation of carbonic acid in seawater media. *Deep Sea Research Part A Oceanographic Research Papers* **34**(10): 1733–1743. ISSN 01980149.

Dickson A, Millero F. 1989. Corrigenda. *Deep Sea Research Part A Oceanographic Research Papers* **36**(6): 983.

Djath B, Melet A, Verron J, Molines JM, Barnier B, et al. 2014. A 1/36 model of the Solomon Sea embedded into a global ocean model: On the setting up of an interactive open boundary nested model system. *Journal of Operational Oceanography* **7**(1): 34–46.

Djath B, Verron J, Melet A, Gourdeau L, Barnier B, et al. 2014. Multiscale dynamical analysis of a high-resolution numerical model simulation of the Solomon Sea circulation. *J Geophys Res Oceans* ISSN 2169-9291.

Donguy J, Henin C. 1977. Origin of the surface tropical water in the Coral and Tasman Seas. *Mar Freshwater Res* **28**(3): 321–332.

Donguy JR. 1994. Surface and subsurface salinity in the tropical Pacific Ocean relations with climate. *Progress In Oceanography* **34**(1): 45–78. ISSN 0079-6611.

Dore JE, Brum JR, Tupas LM, Karl DM. 2002. Seasonal and interannual variability in sources of nitrogen supporting export in the oligotrophic subtropical North Pacific Ocean. *Limnology and Oceanography* **47**(6): 1595–1607. ISSN 00243590.

Fitzgerald WF, Lamborg CH, Hammerschmidt CR. 2007. Marine Biogeochemical Cycling of Mercury. *Chemical Reviews* **107**(2): 641–662. ISSN 0009-2665, 1520-6890.

Ganachaud A, Cravatte S, Melet A, Schiller A, Holbrook NJ, et al. 2014. The Southwest Pacific Ocean circulation and climate experiment (SPICE). *Journal of Geophysical Research: Oceans* **119**(11): 7660–7686. ISSN 21699275.

Gasparin F, Ganachaud A, Maes C, Marin F, Eldin G. 2012. Oceanic transports through the Solomon Sea: The bend of the New Guinea Coastal Undercurrent. *Geophysical Research Letters* **39**(15). ISSN 0094-8276.

Geibert W, Rutgers van der Loeff M, Hanfland C, Dauelsberg HJ. 2002. Actinium-227 as a deep-sea tracer: sources, distribution and applications. *Earth and Planetary Science Letters* **198**(1-2): 147–165. ISSN 0012821X.

Germineaud C, Ganachaud A, Sprintall J, Cravatte S, Eldin G, et al. 2016. Pathways and water mass properties of the thermocline and intermediate waters in the Solomon Sea.

Journal of Physical Oceanography ISSN 0022-3670, 1520-0485.

Gourdeau L, Verron J, Melet A, Kessler W, Marin F, et al. 2014. Exploring the mesoscale activity in the Solomon Sea: A complementary approach with a numerical model and altimetric data. *Journal of Geophysical Research: Oceans* **119**(4): 2290–2311. ISSN 21699275.

Grenier M, Cravatte S, Blanke B, Menkes C, Koch-Larrouy A, et al. 2011. From the western boundary currents to the Pacific Equatorial Undercurrent: Modeled pathways and water mass evolutions. *Journal of Geophysical Research* **116**(C12): C12044.

Grenier M, Jeandel C, Cravatte S. 2014. From the subtropicss to the equator in the Southwest Pacific: Continental material fluxes quantified using neodymium data along modeled thermocline water pathways. *Journal of Geophysical Research: Oceans* **119**(6): 3948–3966. ISSN 21699275.

Grenier M, Jeandel C, Lacan F, Vance D, Venchiarutti C, et al. 2013. From the subtropics to the central equatorial Pacific Ocean: Neodymium isotopic composition and rare earth element concentration variations. *Journal of Geophysical Research* ISSN 0148-0227.

Gruber N. 2004. The Dynamics of the Marine Nitrogen Cycle and its Influence on Atmospheric CO2 Variations, in Follows M, Oguz T, eds., *The Ocean Carbon Cycle and Climate*. Dordrecht: Springer Netherlands: pp. 97–148. ISBN 978-1-4020-2086-5, 978-1-4020-2087-2. DOI: 10.1007/978-1-4020-2087-2_4.

Halm H, Lam P, Ferdelman TG, Lavik G, Dittmar T, et al. 2012. Heterotrophic organisms dominate nitrogen fixation in the South Pacific Gyre. *The ISME Journal* **6**(6): 1238–1249. ISSN 1751-7362, 1751-7370.

Hayes CT, Anderson RF, Fleisher MQ, Serno S, Winckler G, et al. 2014. Biogeography in 231Pa/230Th ratios and a balanced 231Pa budget for the Pacific Ocean. *Earth and Planetary Science Letters* **391**: 307–318. ISSN 0012821X.

Hayes CT, Anderson RF, Jaccard SL, François R, Fleisher MQ, et al. 2013. A new perspective on boundary scavenging in the North Pacific Ocean. *Earth and Planetary Science Letters* **369-370**: 86–97. ISSN 0012821X.

Heimburger LE, Sonke JE, Cossa D, Point D, Lagane C, et al. 2015. Shallow methylmercury production in the marginal sea ice zone of the central Arctic Ocean. *Scientific Reports* **5**: 10318. ISSN 2045-2322.

Henderson GM. 2003. The U-series Toolbox for Paleoceanography. *Reviews in Mineralogy and Geochemistry* **52**(1): 493–531. ISSN 1529-6466.

Holbrook NJ, Maharaj AM. 2008. Southwest Pacific subtropical mode water: A climatology. *Progress in Oceanography* **77**(4): 298–315. ISSN 00796611.

Hristova HG, Kessler WS. 2012. Surface Circulation in the Solomon Sea Derived from Lagrangian Drifter Observations. *Journal of Physical Oceanography* **42**(3): 448–458. ISSN 0022-3670, 1520-0485.

Hristova HG, Kessler WS, McWilliams JC, Molemaker MJ. 2014. Mesoscale variability and its seasonality in the Solomon and Coral Seas. *Journal of Geophysical Research: Oceans* ISSN 21699275.

Hydes DJ, M Aoyama, A Aminot, K Bakker, S Becker, et al. 2010. Recommendations for the Determination of Nutrients in Seawater to High Levels of Precision and Inter-Comparability using Continuous Flow Analysers. version 1: GO-SHIP.ORG.

Jeandel C, Oelkers EH. 2015. The influence of terrigenous particulate material dissolution on ocean chemistry and global element cycles. *Chemical Geology* **395**: 50–66. ISSN 00092541.

Karl D, Letelier R, Tupas L, Dore J, Christian J, et al. 1997. The role of nitrogen fixation in biogeochemical cycling in the subtropical North Pacific Ocean. *Nature* **388**(6642): 533–538. ISSN 0028-0836.

Karl D, Michaels A, Bergman B, Capone D, Carpenter E, et al. 2002. Dinitrogen fixation in the world's oceans. *Biogeochemistry* **57-58**(1): 47–98. ISSN 0168-2563.

Kawabe M, Fujio S. 2010. Pacific ocean circulation based on observation. *Journal of Oceanography* **66**(3): 389–403. ISSN 0916-8370, 1573-868X.

Kessler WS, Cravatte S. 2013. Mean circulation of the Coral Sea. *Journal of Geophysical Research: Oceans* **118**(12): 6385–6410. ISSN 21699275.

Klar JK, James RH, Gibbs D, Lough A, Parkinson I, et al. 2017. Isotopic signature of dissolved iron delivered to the Southern Ocean from hydrothermal vents in the East Scotia Sea. *Geology* .

Labatut M, Lacan F, Pradoux C, Chmeleff J, Radic A, et al. 2014. Iron sources and dissolved-particulate interactions in the seawater of the Western Equatorial Pacific, iron isotope perspectives. *Global Biogeochemical Cycles* **28**(10): 1044–1065. ISSN 08866236.

Lacan F, Jeandel C. 2005. Neodymium isotopes as a new tool for quantifying exchange fluxes at the continent–ocean interface. *Earth and Planetary Science Letters* **232**(3-4): 245–257. ISSN 0012821X.

Lamborg CH, Hammerschmidt CR, Bowman KL, Swarr GJ, Munson KM, et al. 2014. A global ocean inventory of anthropogenic mercury based on water column measurements. *Nature* **512**(7512): 65–68. ISSN 0028-0836, 1476-4687.

Langdon C. 2010. Determination of dissolved oxygen in Seawater by Winkler Titration using the Amperometric Technique. version 1: GO-SHIP.ORG.

Lauvset SK, Key RM, Olsen A, van Heuven S, Velo A, et al. 2016. A new global interior ocean mapped climatology: the $1^\circ \times 1^\circ$ GLODAP version 2. *Earth System Science Data Discussions* pp. 1–30. ISSN 1866-3591.

Le Bouteiller A. 2003. Primary production, new production, and growth rate in the equatorial Pacific: Changes from mesotrophic to oligotrophic regime. *Journal of Geophysi-*

cal Research **108**(C12). ISSN 0148-0227.

Le Quéré C, Moriarty R, Andrew RM, Canadell JG, Sitch S, et al. 2015. Global Carbon Budget 2015. *Earth System Science Data* **7**(2): 349–396. ISSN 1866-3516.

Lee HT. 2014. Climate Algorithm Theoretical Basis Document (C-ATBD): Outgoing Longwave Radiation (OLR) - Daily. NOAA.

Lefevre J, Menkes C, Bani P, Marchesiello P, Curci G, et al. 2015. Distribution of sulfur aerosol precursors in the SPCZ released by continuous volcanic degassing at Ambrym, Vanuatu. *Journal of Volcanology and Geothermal Research* ISSN 03770273.

Lenton A, Tilbrook B, Matear RJ, Sasse TP, Nojiri Y. 2016. Historical reconstruction of ocean acidification in the Australian region. *Biogeosciences* **13**(6): 1753–1765. ISSN 1726-4189.

Lindstrom E, Lukas R, Fine RA, Godfrey JS, Meyers G, et al. 1987. The Western Equatorial Pacific Ocean Circulation Study. *Nature* **330**: 533–537.

Luo YW, Doney SC, Anderson LA, Benavides M, Berman-Frank I, et al. 2012. Database of diazotrophs in global ocean: abundance, biomass and nitrogen fixation rates. *Earth System Science Data* **4**(1): 47–73. ISSN 1866-3516.

Madden RA, Julian PR. 1972. Description of Global-Scale Circulation Cells in the Tropics with a 40-50 Day Period. *J Atmos Sci* **29**(6): 1109–1123. ISSN 0022-4928.

Mari X, Lefèvre J, Torréton JP, Bettarel Y, Pringault O, et al. 2014. Effects of soot deposition on particle dynamics and microbial processes in marine surface waters. *Global Biogeochemical Cycles* **28**(7): 662–678. ISSN 08866236.

Mason RP, Choi AL, Fitzgerald WF, Hammerschmidt CR, Lamborg CH, et al. 2012. Mercury biogeochemical cycling in the ocean and policy implications. *Environmental Research* **119**: 101–117. ISSN 00139351.

Mason RP, Fitzgerald WF. 1990. Alkylmercury species in the equatorial Pacific. *Nature* **347**(6292): 457–459. ISSN 0028-0836.

McCartney M. 1977. Subantarctic Mode Water. *Deep Sea Research, supplement* **24**: 103–119.

McCormick BT, Edmonds M, Mather TA, Carn SA. 2012. First synoptic analysis of volcanic degassing in Papua New Guinea: Volcanic degassing in Papua New Guinea. *Geochemistry, Geophysics, Geosystems* **13**(3). ISSN 15252027.

McPhaden MJ, Timmermann A, Widlansky MJ, Balmaseda MA, Stockdale TN. 2015. The Curious Case of the EL Nino That Never Happened: A Perspective from 40 Years of Progress in Climate Research and Forecasting. *Bulletin of the American Meteorological Society* **96**(10): 1647–1665. ISSN 0003-0007, 1520-0477.

Mehrbach C, Culberson CH, Hawley JE, Pytkowicx RM. 1973. Measurement of the apparent dissociation constants of carbonic acid in seawater at atmospheric pressure. *Limnology and Oceanography* **18**(6): 897–907. ISSN 00243590.

Melet A, Gourdeau L, Kessler WS, Verron J, Molines JM. 2010. Thermocline Circulation in the Solomon Sea: A Modeling Study. *J Phys Oceanogr* **40**(6): 1302–1319. ISSN 0022-3670.

Melet A, Gourdeau L, Verron J, Djath B. 2013. Solomon Sea circulation and water mass modifications: response at ENSO timescales. *Ocean Dynamics* **63**(1): 1–19. ISSN 1616-7341, 1616-7228.

Melet A, Verron J, Gourdeau L, Koch-Larrouy A. 2011. Equatorward Pathways of Solomon Sea Water Masses and Their Modifications. *Journal of Physical Oceanography* **41**: 810–826.

Menkes CE, Lengaigne M, Vialard J, Puy M, Marchesiello P, et al. 2014. About the role of Westerly Wind Events in the possible development of an El Nino in 2014. *Geophysical Research Letters* **41**(18): 6476–6483. ISSN 00948276.

Metzl N, Corbiere A, Reverdin G, Lenton A, Takahashi T, et al. 2010. Recent acceleration of the sea surface CO2 growth rate in the North Atlantic subpolar gyre (1993-2008) revealed by winter observations. *Global Biogeochemical Cycles* **24**(4): n/a–n/a. ISSN 08866236.

Moisander PH, Beinart RA, Hewson I, White AE, Johnson KS, et al. 2010. Unicellular Cyanobacterial Distributions Broaden the Oceanic N2 Fixation Domain. *Science* **327**(5972): 1512–1514. ISSN 0036-8075, 1095-9203.

Moisander PH, Beinart RA, Voss M, Zehr JP. 2008. Diversity and abundance of diazotrophic microorganisms in the South China Sea during intermonsoon. *The ISME Journal* **2**(9): 954–967. ISSN 1751-7362, 1751-7370.

Moutin T, Van Den B B, Beker B, Dupouy C, Rimmelin P, et al. 2005. Phosphate availability controls Trichodesmium spp. biomass in the SW Pacific Ocean. *Marine Ecology Progress Series* **297**: 15–21. ISSN 0171-8630, 1616-1599.

Munson KM, Lamborg CH, Swarr GJ, Saito MA. 2015. Mercury species concentrations and fluxes in the Central Tropical Pacific Ocean. *Global Biogeochemical Cycles* **29**(5): 656–676. ISSN 08866236.

Nagamoto C, Parungo F, Kopcewicz B, Zhou MY. 1990. Chemical analysis of rain samples collected over the Pacific Ocean. *Journal of Geophysical Research* **95**(D13): 22343. ISSN 0148-0227.

Nelson DM, Tréguer P, Brzezinski MA, Leynaert A, Quéguiner B. 1995. Production and dissolution of biogenic silica in the ocean: Revised global estimates, comparison with regional data and relationship to biogenic sedimentation. *Global Biogeochemical Cycles* **9**(3): 359–372. ISSN 1944-9224.

Olsen A, Key RM, van Heuven S, Lauvset SK, Velo A, et al. 2016. The Global Ocean Data Analysis Project version 2 (GLODAPv2) – an internally consistent data product for the world ocean. *Earth System Science Data* **8**(2): 297–323. ISSN 1866-3516.

1169 Orsi AH, Johnson GC, Bullister JL. 1999. Circulation, mixing and production of Antarctic
1170 Bottom Water. *Prog Oceanogr* **43**(1): 55–109.
1171 Pena MA, Lewis MR, Cullen JJ. 1994. New production in the warm waters of the tropical
1172 Pacific Ocean. *Journal of Geophysical Research* **99**(C7): 14255. ISSN 0148-0227.
1173 Pierrot DE, Lewis A, Wallace D. 2011. MS Excel Program Developed for CO2 System
1174 Calculations. ORNL/CDIAC-105a. Oak Ridge, Tennessee: Oak Ridge National Lab-
1175 oratory, U.S. Department of Energy.
1176 Qu T, Lindstrom EJ. 2002. A Climatological Interpretation of the Circulation in the West-
1177 ern South Pacific. *J Phys Oceanogr* **32**(9): 2492–2508. ISSN 0022-3670.
1178 Qu T, Lindstrom EJ. 2004. Northward Intrusion of Antarctic Intermediate Water in the
1179 Western Pacific. *J Phys Oceanogr* **34**(9): 2104–2118. ISSN 0022-3670.
1180 Radic A, Lacan F, Murray JW. 2011. Iron isotopes in the seawater of the equatorial Pa-
1181 cific Ocean: New constraints for the oceanic iron cycle. *Earth and Planetary Science*
1182 *Letters* **306**(1–2): 1–10. ISSN 0012-821X.
1183 Raimbault P, Garcia N. 2008. Evidence for efficient regenerated production and dinitrogen
1184 fixation in nitrogen-deficient waters of the South Pacific Ocean: impact on new and
1185 export production estimates. *Biogeosciences* **5**(2): 323–338. ISSN 1726-4189.
1186 Raven JA. 1988. The iron and molybdenum use efficiencies of plant growth with different
1187 energy, carbon and nitrogen sources. *New Phytologist* **109**(3): 279–287. ISSN 0028-
1188 646X, 1469-8137.
1189 Resing JA, Measures CI. 1994. Fluorometric Determination of Al in Seawater by Flow
1190 Injection Analysis with In-Line Preconcentration. *Anal Chem* **66**(22): 4105–4111.
1191 ISSN 0003-2700.
1192 Resing JA, Mottl MJ. 1992. Determination of manganese in seawater using flow injection
1193 analysis with on-line preconcentration and spectrophotometric detection. *Anal Chem*
1194 **64**(22): 2682–2687. ISSN 0003-2700.
1195 Ridame C, Dekaezemacker J, Guieu C, Bonnet S, L'Helguen S, et al. 2014. Contrasted
1196 Saharan dust events in LNLC environments: impact on nutrient dynamics and primary
1197 production. *Biogeosciences* **11**(17): 4783–4800. ISSN 1726-4189.
1198 Sanial V, van Beek P, Lansard B, Souhaut M, Kestenare E, et al. 2015. Use of Ra isotopes
1199 to deduce rapid transfer of sediment-derived inputs off Kerguelen. *Biogeosciences*
1200 **12**(5): 1415–1430. ISSN 1726-4189.
1201 Saout-Grit C, Ganachaud A, Maes C, Finot L, Jamet L, et al. 2015. Calibration of CTD
1202 oxygen data collected in the Coral Sea during the 2012 bifurcation cruise. *Mercator*
1203 *Ocean-Coriolis Quarterly Newsletter Special Issue* **52**(3): 27–33.
1204 Shiozaki T, Kodama T, Kitajima S, Sato M, Furuya K. 2013. Advective transport of di-
1205 azotrophs and importance of their nitrogen fixation on new and primary production
1206 in the western Pacific warm pool. *Limnology and Oceanography* **58**(1): 49–60. ISSN

00243590.

Slemons LO, Murray JW, Resing J, Paul B, Dutrieux P. 2010. Western Pacific coastal sources of iron, manganese, and aluminum to the Equatorial Undercurrent: WESTERN PACIFIC METAL SOURCES TO THE EUC. *Global Biogeochemical Cycles* **24**(3): n/a–n/a. ISSN 08866236.

Sokolov S, Rintoul S. 2000. Circulation and water masses of the southwest Pacific: WOCE section P11, Papua New Guinea to Tasmania. *Journal of marine research* **58**(2): 223–268.

Suzuki T, Ishii M, Christian J. 2013. PACIFICA Data Synthesis Project. ORNL/CDIAC-159, NDP-092. Environmental Sciences Division, Oak Ridge National Laboratory,Tennessee: Carbon Dioxide Information Analysis Center (CDIAC).

Takahashi T, Sutherland S, Chipman D, Goddard J, Ho C, et al. 2014. Climatological distributions of pH, pCO2, total CO2, alkalinity, and CaCO3 saturation in the global surface ocean, and temporal changes at selected locations. *Marine Chemistry* **164**: 95–125. ISSN 03044203.

Touratier F, Azouzi L, Goyet C. 2007. CFC-11, 14 C and 3H tracers as a means to assess anthropogenic CO2 concentrations in the ocean. *Tellus B* **59**(2): 318–325. ISSN 0280-6509, 1600-0889.

Tsimplis MN, Bacon S, Bryden HL. 1998. The circulation of the sub-Tropical South Pacific derived from hydrographic data. *J Geophys Res* **103**(C10): 21,443–21,468.

Tsuchiya M, Lukas R, Fine RA, Firing E, Lindstrom E. 1989. Source waters of the Pacific Equatorial Undercurrent. *Progress In Oceanography* **23**(2): 101–147. ISSN 0079-6611.

Uchida H, Johnson CG, McTaggart KE. 2010. CTD oxygen sensor calibration procedures. version 1: GO-SHIP.ORG.

van Beek P, Bourquin M, Reyss JL, Souhaut M, Charette M, et al. 2008. Radium isotopes to investigate the water mass pathways on the Kerguelen Plateau (Southern Ocean). *Deep Sea Research Part II: Topical Studies in Oceanography* **55**(5-7): 622–637. ISSN 09670645.

Venchiarutti C, Jeandel C, Roy-Barman M. 2008. Particle dynamics study in the wake of Kerguelen Island using thorium isotopes. *Deep Sea Research Part I: Oceanographic Research Papers* **55**(10): 1343–1363. ISSN 09670637.

Vetch P, Haefeli S. 1997. August visit reveals lava fountains, Strombolian explosions, Ambrym. *Bull Global Volc Network* **22**: 11.

Visbeck M. 2002. Deep velocity profiling using Acoustic Doppler Current Profilers : Bottom tracks and inverse solutions. *J Atm Oc Tech* **19**: 794–807.

Wheeler MC, Hendon HH. 2004. An All-Season Real-Time Multivariate MJO Index: Development of an Index for Monitoring and Prediction. *Mon Wea Rev* **132**(8): 1917–

1932. ISSN 0027-0644.

Wyrtki K. 1962. The subsurface water masses in the western South Pacific Ocean. *Marine and Freshwater Research* **13**(1): 18–47.

Yoshikawa C, Nakatsuka T, Kawahata H. 2005. Transition of low-salinity water in the Western Pacific Warm Pool recorded in the nitrogen isotopic ratios of settling particles. *Geophysical Research Letters* **32**(14): n/a–n/a. ISSN 00948276.

Contributions

AG, SC, JS, CJ, and GE coordinated the projects, cruises and article writing. CG and MA contributed to the physical analysis and produced corresponding figures; MB, SB, HB, MR lead the biological analyses; JL the volcanic aspects. The geochemistry aspects were analyzed by NM (carbonates); L-EH (Hg); SM, JR (Al/Mn); FQ, GS, FL (Fe). Cruise data acquisition and treatment was ensured by JG and FB. TH lead the JAMSTEC cruise; WK, MK, EP, US, PV-B, MS and JES were involved at different stages of the results presented here.

Acknowledgements

This work is a contribution to the CLIVAR/SPICE and GEOTRACES International programmes. We are grateful to the ship crews (RV L'Atalante, RV Thompson and RV Mirai) who made possible the various in situ measurements, thereby requiring skills and care. The collaboration with SOPAC/SPC, PI-GOOS, and University of Papua New Guinea was greatly appreciated. We thank the technical division of INSU (DT-INSU, O. Desprez de Gesincourt, L. Fichez, E., F. Perault, E. de SaintLeger); US-IMAGO (D. Lopez, L. Jamet), IRD Center Noumea (J. Carso, V. Perrin, C. Hartmann, J.-L. Fuda, D. Varillon), LEGOS support staff (B. Cournou, N. Lacroux, A. Baritaud, M. Mena) for their efforts to ensure a timely delivery of instruments/air tickets or participation at different stages of the cruise organization. We thank the Hydraulics Laboratory at SIO for their mooring expertise (P. Harvey, S. Kawamoto). We thank Patrick Raimbault (MIO) who did the mass spectrometric analyses related to biology. The Pandora data processing followed the US-IMAGO (IRD) information system (online at http://www.ird.fr/us191/spip.php?article66). Dissolved Fe analyses were funded by Labex Mer. Most geochemical graphics were made under ODV (Schlitzer, R., Ocean Data View, http://odv.awi.de, 2015). MoorSPICE data can be found through Cruise DOI: 10.7284/903044. Also thank C. Schmechtig who ensured the Pandora and MoorSPICE data delivery through the LEFE-CYBER Database (online at http://www.obs-vlfr.fr/proof/).

Funding information

The accomplishments were made possible through concurrent contributions of national funding agencies.The MoorSPICE and Pandora cruises have been co-funded by NSF grant OCE1029487, and by ANR project ANR- 09-BLAN-0233-01 and INSU/LEFE project Solwara (IDAO and CYBER). Carbonate measurements were supported by European program FP7/CARBOCHANGE (grant 264879). NM thanks the Service National dAnalyses des Paramètres Océaniques du CO_2 (SNAPO-CO_2) supported by CNRS/INSU and UPMC (OSU ECCE-Terra). CG was supported by a PhD scholarship from the French Ministry of Research and Education. South Solomon Sea endpoint moorings (US NOAA funded CORC project grant NA10OAR432015) Mercury analyses were funded by ERC-2010-StG_20091028 grant from the European Research Council to JES.

Competing interests

None

Supplemental material

Available online

Abstract

The Low Latitude Western Boundary Currents (LLWBCs) of the Southwest Pacific establish a major connection between the subtropics and the equator. They are believed to play a key role in heat and mass budgets of the equatorial Pacific and cross, as a final passage, the Solomon Sea southeast of Papua New Guinea. As part of a France-U.S. collaboration, two oceanographic multidisciplinary cruises were conducted in the Solomon Sea during contrasting trade wind seasons, in July-August 2012 and March 2014 to characterize currents, water properties and their modifications. During July-August 2012, the season of strong southeasterly trade winds, an intense flow of 36 $\pm$ 3 Sv from the surface down to 1000 m is entering the Solomon Sea, that falls by 70% to 11 $\pm$ 3 Sv in March 2014 when the winds over the sea are weaker. The LLWBCs are associated with distinct water mass properties across the Solomon Sea that can be tracked along their pathways, and undergo significant modifications between the southern entrance and the northern exits of the sea. Below 2000 m, the Upper Circumpolar Deep Water (UCDW) has been traced from the New Caledonia Trench and the South Fiji Basin into the Solomon Sea, associated with a volume transport of 2-3 $\pm$ 2 Sv. Preliminary analyses of the mooring array in each major exit channel indicate large time variability of the LLWBCs in both intensity and vertical extent, where thermocline pathways vary in most cases, coherently and in phase at intraseasonal to seasonal time scales.

Résumé

Dans le Pacifique sud-ouest, le cheminement des eaux depuis la gyre subtropicale vers l'équateur est réalisé via les courants de bord ouest (WBCs), associés à des changements de température ou de quantité d'eau à différentes échelles de temps. La mer des Salomon située au sud de la Papouasie Nouvelle-Guinée est considérée comme une région clé pour étudier les WBCs juste avant qu'ils rejoignent l'équateur. Dans le cadre d'une collaboration internationale, deux campagnes en mer ont été réalisées en mer des Salomon pendant deux périodes contrastées de la saison des alizés (Juillet-Août 2012 et Mars 2014). En Juillet-Août 2012, pendant la saison de forts alizés, les WBCs transportent 36 $\pm$ 3 Sv à travers l'entrée sud de la mer des Salomon depuis la surface jusqu'à 1000 m de profondeur, mais seulement 11 $\pm$ 3 Sv en Mars 2014 (réduction de 70%) quand les alizés faiblissent. Les WBCs sont associés à des propriétés de masses d'eau distinctes qui subissent d'importantes modifications au cours de leur passage en mer des Salomon. En dessous de 2000 m de profondeur, l'Upper Circumpolar Deep Water (UCDW) est tracée depuis le bassin de Fidji et la fosse de la Nouvelle-Calédonie avant d'entrer en mer des Salomon, associée à un transport de masse de 2 à 3 $\pm$ 2 Sv. L'étude préliminaire des mouillages au niveau des détroits de sortie a permis d'identifier une modulation de l'intensité et de la structure verticale des WBCs en relation avec la variabilité saisonnière des alizés. Les eaux de thermocline entre les différents mouillages varient généralement de manière cohérente et en phase à l'échelle intra-saisonnière et saisonnière.

Keywords - Mots clés

Ocean Circulation and Variability, Water mass property, Western Boundary Currents
Circulation océanique et variabilité, Propriétés des masses d'eau, Courants de bord ouest